Experimental and Modeling Studies of Passive NO_x Adsorbers

by
Mugdha Ambast

A thesis submitted to the Department of Chemical and Biomolecular Engineering,
University of Houston
in partial fulfillment of the requirements for the degree of

DOCTOR OF PHILOSOPHY

in Chemical Engineering

Chair of Committee: Dr. Michael P Harold

Committee Member: Dr. Vemuri Balakotaiah

Committee Member: Dr. Lars C Grabow

Committee Member: Dr. Stanko R Brankovic

Committee Member: Dr. William S Epling

University of Houston
May 2021

Acknowledgment

I acknowledge the financial support of this research by the Department of Energy (DE- EE0008233) and FCA US LLC (Auburn Hills, Michigan). I also had useful interactions with Dr. Yang Zheng (FCA).

I would like to express my sincere gratitude to my guide Dr. Michael P Harold, for his guidance and encouragement. I would also like to thank Kyle Karinshak, Sam A Malamis and Zhiyu Zhou for training me on various experimental setups.

Abstract

To meet the future more stringent regulations for nitrogen oxides (NO_x) emission from vehicle's exhaust, improved technologies which can further reduce NO_x emissions during cold start period are needed. The passive NO_x adsorbers (PNA) have been gaining attention recently as a technology that has the potential to abate cold-start NO_x emissions.

A combined experimental and modeling study of the PNA is presented that advances the understanding and prediction of the effects of various operating parameters and material properties of H-ZSM-5, Pd/H-ZSM-5 and Pd/SSZ-13. Experiments reveal that the presence of H_2O in the feed significantly lowers NO_x uptake at lower temperatures as a result of competition for sites between H_2O and NO_x species and the extent of inhibition is a function of temperature. A one-dimensional two-phase transient monolith model is developed to predict and validate NO_x uptake and temperature programmed desorption (TPD) data for H-ZSM-5, Pd/H-ZSM-5 and Pd/SSZ-13. The model is extended for NO uptake and release over Pd/SSZ-13 with H_2O, CO, C_2H_4 and $C_{12}H_{26}$ in the feed. The microkinetic schemes for each of the feeds involves multi-site NO adsorption on multiple types of Pd cations: $Z^-[PdOH]^+$, $Z^-Pd^{2+}Z^-$, and Z^-Pd^+, with a key feature being the reduction of a pair of $Z^-[PdOH]^+$ sites to two Z^-Pd^+ sites. The reduced sites bind NO the strongest. The Pd(II) to Pd(I) reduction generates NO_2, CO_2 or C_2H_4O depending on the feed constituents. For NO-only feed, this endothermic reaction occurs at temperature ~120℃ and generates NO_2. In the presence of CO and C_2H_4 the exothermic reduction occurs at lower temperatures and generates CO_2 and C_2H_4O respectively. The presence of $C_{12}H_{26}$ is shown to impact the NO uptake and/or release despite its own limited uptake. When a co-feed containing $C_{12}H_{26}$ and NO is supplied to an unsaturated (with $C_{12}H_{26}$) sample, the NO

uptake is unaffected but during the subsequent temperature ramp the release of trapped NO is delayed from 175℃ to over 220℃. The release delay is beneficial for PNA performance as the primary NO_x aftertreatment technology Selective Catalytic Reduction (SCR) is ineffective at temperatures below 200℃. Oxidation of $C_{12}H_{26}$ leads to the generation of partial oxidation product CO at lower temperatures (< 250℃) and complete oxidation product CO_2 at higher temperatures. Carbon monoxide binds strongly to Pd sites and can delay NO release.

Model tuning utilizes a combination of diffuse reflective infrared Fourier transform spectroscopy (DRIFTS) data, density functional theory (DFT) estimates of energy barriers and a fit of constant temperature uptake and temperature-ramped desorption and conversion data. The tuned model is validated at different uptake temperatures, desorption ramp rates, and feed flowrates. The model helps to interpret the data features and trends and is used to identify operating conditions to meet application-relevant performance metrics including NO_x trapping efficiency and NO_x release temperature.

Table of Contents

ACKNOWLEDGEMENR ..... **ii**

ABSTRACT ..... **iii**

TABLE OF CONTENTS ..... **v**

LIST OF TABLES ..... **vii**

LIST OF FIGURES ..... **viii**

NOMENCLATURE ..... **xiii**

CHAPTER 1 INTRODUCTION **1**

1.1 MOTIVATION 1
1.2 PASSIVE NOX ADSORBERS 1
1.3 LITERATURE REVIEW 2
1.4 OBJECTIVE AND APPROACH 5

CHAPTER 2 PASSIVE NO_X ADSORPTION ON Pd/H-ZSM-5: EXPERIMENTS AND MODELING **7**

2.1 EXPERIMENTAL 7
2.1.1 Catalyst Preparation 7
2.1.2 Monolith Washcoating 7
2.1.3 Bench-scale Reactor System 8
2.1.4 Flow Reactor Experiments 9
2.1.5 Catalyst Characterization 10
2.1.6 Characterization 11
2.1.7 Effect of Temperature and Pd-loading for Dry Feed 15
2.1.8 Effect of Temperature and Pd-loading for Wet Feed 18
2.1.9 Washcoat Diffusion Limitations 20
2.1.10 Effect of Feed Flowrate 21
2.2 MODELING 23
2.2.1 One-Dimensional Two-Phase Transient Model 23
2.2.2 Model Tuning and Validation Procedure 25
2.2.3 Microkinetic Model for H-ZSM-5 28
2.2.4 Reaction Mechanism Development and Microkinetic Models for Pd/H-ZSM-5 36
2.3 CONCLUSIONS 56

CHAPTER 3 NO_X ADSORPTION WITH CO AND C_2H_4 ON Pd/SSZ-13: EXPERIMENTS AND MODELING **58**

3.1 EXPERIMENTAL 58
3.1.1 Catalyst properties 58

3.1.2 Reactor setup and experimental protocol 58
3.1.3 Characterization 59
3.2 MODELING 62
3.2.1 Transient monolith model 62
3.2.2 Model tuning and validation procedure 62
3.2.3 Microkinetic model for NO-only feed 64
3.2.4 NO + CO feed 78
3.2.5 NO+C_2H_4 feed 85
3.2.6 NO+CO+C_2H_4 feed validation 95
3.2.7 Integral trapping efficiency 97
3.2.8 Cold-start simulation: Comparison of reductants 98
3.2.9 Comparison of NO uptake on Pd/SSZ-13 and Pd/ZSM-5 99
3.3 DEGREE OF UPTAKE CONTROL 104
3.4 CONCLUSIONS 106

CHAPTER 4 COUPLED UPTAKE AND CONVERSION OF $C_{12}H_{26}$ AND NO ON Pd/SSZ-13: EXPERIMENTS AND MODELING 108

4.1 EXPERIMENTAL 108
4.1.1 Catalyst properties 108
4.1.2 Reactor setup and experimental protocol 108
4.2 RESULTS AND DISCUSSION 109
4.2.1 Experimental 109
4.2.2 Modeling 119
4.2.3 Model application 138
4.3 CONCLUSIONS 142

CHAPTER 5 EFFECTS OF LOW PD LOADING, O2 AND CO ON NO UPTAKE 143

5.1 NO UPTAKE FOR LOW PD LOADING PNA CATALYST 143
5.2 EFFECTS OF OXYGEN 145
5.3 ALTERNATE MECHANISM FOR CO UPTAKE 150

CHAPTER 6 CONCLUSIONS 152

CHAPTER 7 FUTURE WORK 155

REFERENCES 156

APPENDIX 162

List of Tables

Table 2.1 Catalyst composition 8
Table 2.2 IR peaks assignments 13
Table 2.3 Parameters used in model 27
Table 2.4 Reaction mechanism for H-ZSM-5 29
Table 2.5 Kinetic Parameters for H-ZSM-5 model 32
Table 2.6 Reaction Mechanism for Pd/H-ZSM-5 (Scheme I) 38
Table 2.7 Reaction Mechanism for Pd/H-ZSM-5 (Scheme II) [..... 39
Table 2.8 Kinetic Parameters for Pd/H-ZSM-5 model- Scheme I 41
Table 2.9 Kinetic Parameters for Pd/H-ZSM-5 model- Scheme II 55
Table 3.1 Parameters used in model 62
Table 3.2 Reaction mechanism for simple NO feed 68
Table 3.3 Kinetic Parameters for simple NO feed model 69
Table 3.4 Reaction Mechanism for NO+CO feed 80
Table 3.5 Kinetic Parameters for NO+CO feed model 82
Table 3.6 Reaction Mechanism for NO+C_2H_4 feed 88
Table 3.7 Kinetic Parameters for NO+C_2H_4 feed model 89
Table 4.1 Parameters used in model 119
Table 4.2 Reaction mechanism for $C_{12}H_{26}$ feed 124
Table 4.3 Kinetic parameters for $C_{12}H_{26}$ feed 125
Table 4.4 Reaction mechanism for NO + $C_{12}H_{26}$ feed 129
Table 4.5 Kinetic parameters for NO + $C_{12}H_{26}$ feed 129
Table 5.1 Reaction mechanism for simple NO feed for low Pd loading 145
Table 5.2 Alternate reaction mechanism for CO uptake on Pd(1%)/SSZ-13 150
Table 5.3 Alternate reaction mechanism for CO uptake on Pd(1%)/SSZ-13 in the presence of O_2 151
Table 5.4 Alternate reaction mechanism for CO uptake on Pd(1%)/SSZ-13 in the absence of O_2 151

List of Figures

Figure 2.1 XPS spectra acquired on Pd/H-ZSM-5 12

Figure 2.2 H_2-TPR curve of Pd(1%)/H-ZSM-5 12

Figure 2.3 (a) DRIFTS spectra obtained during dry NO+O_2 exposure to H-ZSM-5, 1% Pd/H- ZSM-5 and 2% Pd/H-ZSM-5 at 50°C (b) zoomed-in DRIFTS spectra showing NO uptake. 14

Figure 2.4 NO_x adsorption profile for (a) H-ZSM-5, (b) Pd(1%)/H-ZSM-5 and (c) Pd(2%)/H-ZSM-5 at uptake temperatures of 50°C, 80°C, and 150°C for dry feed. 16

Figure 2.5 NO_x TPD profiles for (a) H-ZSM-5, (b) Pd(1%)/H-ZSM-5 and (c) Pd(2%)/H-ZSM-5 for uptake conducted at temperatures of 80°C for dry feed. 17

Figure 2.6 Comparison of moles of NO per mole of Pd at different uptake temperatures in presence of 7% H_2O in the feed as well as model predictions are shown by black points. 19

Figure 2.7 Comparison of moles of NO_x adsorbed per gram zeolite for different Pd loading in the feed comprised of NO_2 (5ppm)/ NO (400ppm)/ O_2 (2%)/ H_2O (7%)/ balance Ar during uptake. 20

Figure 2.8 (a) Comparison of NO_x adsorption profile for dry feed at uptake temperature of 80°C (b) Dependence of trapping efficiency on volume of gas contacting the catalyst for total feed flowrates of 1500 sccm and 2500 sccm. 22

Figure 2.9 Experimental and modeling results of NO_x uptake at 80°C and TPD on H-ZSM-5 for dry feed with a flowrate of 1500 sccm. 33

Figure 2.10 (a)Experimental and modeling results of NO_x uptake at 150°C and TPD on H-ZSM-5 for dry feed with a flowrate of 1500 sccm (b) Enlarged view of TPD profile. 34

Figure 2.11 Experimental and modeling results of NO_x uptake at 80°C and TPD on H-ZSM-5 for dry feed with a flowrate of 2500 sccm. 35

Figure 2.12 Comparison of TPD profiles for NO uptake on Pd(1%)/H-ZSM-5 (blue) and H-ZSM-5 (red) at uptake at temperature of 80°C for dry feed. 40

Figure 2.13 Experimental and modeling results of NO_x uptake at 80°C and TPD on Pd(1%)/H-ZSM-5 for wet-feed (7% H_2O) and feed flowrate of 1500 sccm. 46

Figure 2.14 Coverage of different species on site (a) $Z-Pd2+Z-$, (b) $Z-[PdIIOH]+$, and (c) $Z-Pd+$ during uptake of NO_x at 80°C and TPD for feed flow rate of 1500 sccm in presence of 7% H_2O in the feed. 48

Figure 2.15 Experimental and modeling results of NO_x uptake at 150°C and TPD on Pd(1%)/H-ZSM-5 for wet-feed (7% H_2O) and feed flowrate of 1500sccm. 50

Figure 2.16 Experimental and modeling results of NO_x uptake at 80°C and TPD on Pd(1%)/H-ZSM-5 for wet-feed (7% H_2O) and feed flowrate of 2500sccm. 50

Figure 2.17 Experimental and modeling results of NO_x uptake at 80°C and TPD on Pd(2%)/H-ZSM-5 for wet-feed (7% H_2O) and feed flowrate of 1500. 51

Figure 2.18 Experimental and modeling results of NO_x uptake at 80°C and TPD on Pd(1%)/H-ZSM-5 for wet-feed (7% H_2O) and feed flowrate of 1500 sccm (Scheme II). 56

Figure 3.1 XPS spectra acquired on Pd(1%)/SSZ-13 and Pd(2%)/H-ZSM-5 60

Figure 3.2 DRIFTS spectra for (a) SSZ-13 and (b) Pd(1%)/SSZ-13..... 61

Figure 3.3 Uptake and TPD profile for feed comprising of (a) 200 ppm NO/ 12% $O2$/ 6% CO_2/ 6% $H2O$ / balance N_2, (b) 200 ppm NO/ 500 ppm CO/ 12% $O2$/ 6% $H2O$ / balance N_2, (c) 200 ppm NO/ 200 ppm C_2H_4/ 12% $O2$/ 6% $H2O$ / balance N_2 on Pd(1%)/SSZ-13. 66

Figure 3.4 Experimental and model results of NO_x uptake at 95°C and TPD on Pd(1%)/SSZ-13 for a feed comprising of 200 ppm NO/ 12% $O2$/ 6% CO_2/ 6% $H2O$ / balance N_2 and feed flowrate of 30 khr^{-1}. 72

Figure 3.5 Coverage of different species on site (a) $Z-[PdOH]+$, (b) $Z-Pd+$, and (c) $Z-Pd2+Z-$, during uptake of NO_x at 95°C and TPD for a feed comprising of 200 ppm NO/ 12% $O2$/ 6% CO_2/ 6% $H2O$ / balance N_2 and feed flowrate of 30 khr^{-1}..... 74

Figure 3.6 Experimental and model results of NO_x uptake at 75°C and TPD on Pd(1%)/SSZ-13 for a feed comprising of 200 ppm NO/ 12% $O2$/ 6% CO_2/ 6% $H2O$ / balance N_2 and feed flowrate of 30 khr^{-1}. 77

Figure 3.7 Experimental and model results of NO_x uptake at 88°C and TPD on Pd(1%)/SSZ-13 for a feed comprising of 200 ppm NO/ 12% $O2$/6% CO_2/ 6% $H2O$ / balance N_2 and feed flowrate of 30 khr^{-1}. 77

Figure 3.8 Experimental and model predicted values of NO/Pd for the two NO adsorption regimes at different uptake temperatures. 78

Figure 3.9 (a)Experimental and model results for uptake at 98°C and TPD on Pd(1%)/SSZ-13 for a feed comprising of 200 ppm NO/500 ppm CO/ 12% O2/ 6% H2O / balance N_2 and feed flowrate of 30 khr^{-1}. 81

Figure 3.10 Coverage of different species on site (a) Z − [PdOH] +, (b) Z − Pd +, and (c) Z − Pd2 + Z −, during uptake of NO at 98°C and TPD for a feed comprising of 200 ppm NO/ 500 ppm CO/ 12% O2/ 6% H2O / balance N_2 and feed flowrate of 30 khr^{-1}... 86

Figure 3.11 (a)Experimental and model results for uptake at 105°C and TPD on Pd(1%)/SSZ-13 for a feed comprising of 200 ppm NO/200 ppm C_2H_4/ 12% O2/ 6% H2O / balance N_2 and feed flowrate of 30 khr^{-1}, (b) Enlarged view of NO_x profile. 91

Figure 3.12 Coverage of different species on site (a) Z − [PdOH] +, (b) Z − Pd +, and (c) Z − Pd2 + Z −, during uptake of NO at 105°C and TPD for a feed comprising of 200 ppm NO/ 200 ppm C_2H_4/ 12% O2/ 6% H2O / balance N_2 and feed flowrate of 30 khr^{-1}. 94

Figure 3.13 Experimental and model results for uptake at 120°C and TPD on Pd(1%)/SSZ-13 for a feed comprising of 200 ppm NO/200 ppm C_2H_4/ 12% O2/ 6% H2O / balance N_2 and feed flowrate of 30 khr^{-1}..... 95

Figure 3.14 Experimental and model results for uptake at 118°C and TPD on Pd(1%)/SSZ-13 for a feed comprising of 200 ppm NO/ 200 ppm CO/ 200 ppm C_2H_4/ 12% O2/ 6% H2O / balance N_2 and feed flowrate of 30 khr^{-1}. 96

Figure 3.15 Integral trapping efficiency vs time plot for simple NO feed, NO+CO feed, and NO+C_2H_4 feed..... 98

Figure 3.16 Model prediction of NO profile for simple NO feed, NO+CO feed and NO+C_2H_4 feed with a continuous temperature ramping of 40°C/min starting from 30°C to 600°C..... 100

Figure 3.17 Model prediction of integral trapping efficiency and uptake profile for Pd(1%)/SSZ-13 and Pd(1%)/H-ZSM-5 for feed comprising of 400 ppm NO/ 2% O2/ 7% H2O / balance Ar 101

Figure 3.18 Model prediction of NO profile for Pd(1%)/SSZ-13 and Pd(1%)/ZSM-5 for a feed of 400 ppm NO/ 2% O2/ 7% H2O / balance Ar at 30k hr^{-1} feed flowrate with a continuous temperature ramping from 30°C to 600°C at the rate of (a) 20°C/min and (b) 40°C/min. 103

Figure 3.19 Sensitivity analysis of different reactions as a function of uptake temperature. 106

Figure 4.1 Experimental profiles for uptake at 115°C and TPD on Pd(1%)/SSZ-13 for a feed comprising of 395 ppm NO/55 ppm $C_{12}H_{26}$/ 2% O_2/ 2% H_2O/ balance Ar during uptake and 2% O_2/ Ar during TPD. 110

Figure 4.2 NO uptake profiles for NO only feed, co-feed of NO and $C_{12}H_{26}$ and pre-adsorption of $C_{12}H_{26}$ followed by co-feed of NO and $C_{12}H_{26}$ at uptake temperatures of (a) ~115°C and (b) ~135°C. 111

Figure 4.3 NO TPD profiles for NO only feed and co-feed of NO and $C_{12}H_{26}$ at uptake temperatures of ~115°C. 112

Figure 4.4 (a) Experimental profiles for pre-adsorption of $C_{12}H_{26}$ and H_2O followed by co-feed of NO and $C_{12}H_{26}$ at 115°C and TPD on Pd(1%)/SSZ-13; b) Enlarged view of uptake and TPD profiles. 113

Figure 4.5 NO uptake profiles for H_2O pre-adsorption and dry $C_{12}H_{26}$ pre-adsorption followed by uptake of NO at uptake temperatures of (a) ~110°C and (b) ~125°C. 115

Figure 4.6 (a) Experimental profiles for uptake at 105°C and TPD on Pd(1%)/SSZ-13 for a feed comprising of 395 ppm NO/ 2% O_2/ 2% H_2O/ balance Ar during uptake and 25 ppm CO/ 2% O_2/ Ar during TPD (b) Enlarged species vs temperature profile. 118

Figure 4.7 (a) Langmuir isotherms generated with the three concentration and three temperature combinations; (b) Arrhenius plot of the ratio of rate constants. 123

Figure 4.8 Experimental and model results for uptake at 135°C and TPD on Pd(1%)/SSZ-13 for a feed comprising of (a) 103 ppm $C_{12}H_{26}$/ balance Ar during uptake and only Ar during TPD; (b) 56 ppm $C_{12}H_{26}$/ 2%H_2O/ balance Ar during uptake and only Ar during TPD. 125

Figure 4.9 (a) Experimental and model results for uptake at 115°C and TPD on Pd(1%)/SSZ-13 for a feed comprising of 380 ppm NO/ 2% O_2/ 2% H_2O/ balance Ar during uptake and 2% O_2/ Ar during TPD; (b) Enlarged NO TPD profile. 127

Figure 4.10 (a) Experimental and model results for uptake at 135°C and TPD on Pd(1%)/SSZ-13 for a feed comprising of 395 ppm NO/ 58 ppm $C_{12}H_{26}$/ 2% O_2/ 2% H_2O/ balance Ar during uptake and 2% O_2/Ar during TPD; (b) Enlarged uptake and TPD profiles. 131

Figure 4.11 Experimental and modeling NO uptake profiles for H_2O pre-adsorption followed by NO uptake at uptake temperatures of (a) ~125°C and (b) ~110°C..... 134

Figure 4.12 Experimental and modeling NO uptake profiles for $C_{12}H_{26}$ and H_2O pre-adsorption followed by NO uptake at uptake temperatures of (a) ~135°C and (b) ~115°C. 136

Figure 4.13 Model prediction of NO profile for feed comprising of 400 ppm NO/ 2% O2/ 2% H2O/ balance Ar with a continuous temperature ramping from 30ºC to 600ºC at the rate of 20ºC/min and with and without 60 ppm $C_{12}H_{26}$ at feed flowrate of 2500 sccm .138

Figure 4.14 Modeling results of NO uptake at 95°C and TPD on Pd(1%)/SSZ-13 for a feed comprising of 200 ppm NO/ 12% O2/ 6% CO_2/ 6% H2O / balance N_2 with and without 60 ppm of $C_{12}H_{26}$. 140

Figure 0.15 Model prediction of NO profile for a feed comprising of 200 ppm NO/ 12%O_2/ 6% H_2O/ balance Ar with and without 60 ppm of $C_{12}H_{26}$ and a continuous temperature ramping of 20ºC/min starting from 30ºC to 600ºC..... 141

Figure 5. 1 Experimental results of NO_x uptake at 95°C and TPD on Pd(0.36%)/SSZ-13 for a feed comprising of 390 ppm NO/ 5 ppm NO_2 / 2% O2 / 2% H2O / balance Ar. ... 144

Figure 5. 2 (a) Experimental profiles for uptake at 95°C and TPD for a feed comprising of 386 ppm NO/ 5 ppm NO_2/ 2% O_2/ 2% H_2O/ balance Ar during uptake and TPD on catalyst pre-treated with 5% O_2/ 2% H_2O/ balance Ar; (b) Enlarged view of NO_2 TPD profile. 147

Figure 5.3 (a) Experimental profiles for uptake at 95°C and TPD for a feed comprising of 386 ppm NO/ 5 ppm NO_2/ 2% H_2O/ balance Ar during uptake and TPD on Pd(1%)/SSZ-13 pre-treated with 5% O_2/ 2% H_2O/ balance Ar; (b) Enlarged view of NO_2 TPD profile. 148

Figure 5.4 (a) Experimental profiles for uptake at 95°C and TPD for a feed comprising of 386 ppm NO/ 5 ppm NO_2/ 2% H_2O/ balance Ar during uptake and TPD on Pd(1%)/SSZ-13 pre-treated with 2% H_2O/ balance Ar; (b) Enlarged view of NO_2 TPD profile..... 149

Nomenclature

C_{Tm} = total molar concentration (mol/m^3)

C_x = concentration of adsorption site x (mol/m^3 washcoat)

C_{in} = inlet concentration (mol/m^3)

$k_{mo,j}$ = overall mass transfer coefficient of species j (m/s)

$k_{mi,j}$ = internal mass transfer coefficient of species j (m/s)

$k_{me,j}$ = external mass transfer coefficient of species j (m/s)

$\widehat{K}$ = equilibrium constant

α = repulsion coefficient

$\in$ = porosity of washcoat

$R_{\Omega 1}$ = effective transverse length scale (m)

$R_{\Omega 2}$ = effective washcoat thickness (m)

X_{jm} = dimensionless cup mixing concentration of species j in fluid

$X_{j,wc}$= dimensionless concentration of species j at fluid-washcoat interface

$R_{ad,j}$ = adsorption rate of specious j (mol/ m^3 washcoat s)

$R_{des,j}$= desorption rate of species j (mol/ m^3 washcoat s)

<u> = average gas velocity in gas phase (m/s)

$R_{v,l}$ = rate of reaction l (mol/ m^3 washcoat s)

θ_{jX} = fraction surface coverage of species j on adsorption site x

ν_{lj} = stoichiometric coefficient of species j in reaction l

$D_{f,j}$ = diffusivity in fluid phase of species j (m^2/s)

$D_{e,j}$= diffusivity in washcoat phase of species j (m^2/s)

R_g = universal gas constant (J mol^{-1} K^{-1})

β = heating rate (K/s)

Chapter 1

Introduction

1.1 Motivation

The transportation sector is a major source of NO_x (x = 1, 2) emissions. There has been a continued improvement in the performance of the emission control systems in response to more stringent emission standards since the Clean Air Act passed by U.S. Congress in 1970. Vehicle emissions during the startup period are a large contributor to the overall emissions due to the ineffectiveness of emission control catalysts [1-2]. For example, the three-way catalyst (TWC) for stoichiometric gasoline vehicles is inactive at low temperature due primarily to CO inhibition on precious metal sites [3-5], while selective catalytic reduction (SCR) for diesel vehicles is ineffective at temperatures below 200℃ due to constraints imposed by the urea injection system for NH_3 supply [6-8]. In these and other cases adsorption technologies are needed that trap pollutants at low temperature and release them at higher temperature. That way the aforementioned TWC and SCR units positioned downstream can be used to provide the requisite abatement.

1.2 Passive NO_x Adsorbers

The PNA was introduced in recent years by researchers at Johnson Matthey Inc. as a technology to abate cold-start NO_x emissions [9-11]. Materials used in the PNA are generally noble metals such as Pd supported by rare earth oxides or zeolites; for instance, ZSM-5, BEA, or SSZ-13. These materials adsorb NO and NO_2 at low temperatures (< 150℃) and release the NO_x species at higher temperatures, enabling their reduction by

downstream SCR or NSR. Although PNAs have the potential to tackle cold-start NO_x emissions, a relatively small number of studies have been reported to date.

1.3 Literature Review

Recent studies done by both automotive and catalyst companies along with academic institutions have examined the effectiveness of PNAs for NO_x adsorption at low temperatures. Reviews by Lee et al. [12] and Gu and Epling [13] provide a comprehensive assessment of PNA. Johnson Matthey Inc. patents [9-11] proposed Pd/H-zeolite (BEA, ZSM-5, CHA) as an effective PNA material. Chen et al. [14] reported the low temperature adsorption of NO_x on Pd/H-zeolites, including their sulfur tolerance. The PNA technology concept builds on earlier studies of NO adsorption on related materials have inspired follow-up studies. These are highlighted next.

Descorme et al. [15] conducted a surface infrared study of NO adsorption on Pd-exchanged ZSM-5. They reported that the adsorption of NO at ambient temperatures leads to the reduction of Pd^{2+} cations bound to the $[Si\text{-}O\text{-}Al]^-$ site, in the form of $[Pd(OH)]^+$, to Pd^+, generating NO_2 and H_2O. More recently, Lee et al. [16] investigated the effects of Pd loading and Silica to Alumina ratio ($Si:Al_2$) on NO adsorption and reported that an optimal Pd:Al molar ratio exists for Pd/ZSM-5. They also reported the effects of high-temperature hydrothermal treatment on Pd/H-ZSM-5 and found that cationic Pd species are associated with NO adsorption at low temperatures. Murata et al. [17] studied a combined NO_x trap and three-way catalyst (TWC) and demonstrated a reduction in cold-start NO_x and hydrocarbon emissions. Okumura et al. [18] used EXAFS and XANES to study the formation of highly dispersed PdO over ZSM-5 and investigated the changes in Pd structure upon adsorption of NO. A shift of the edge energy in the XANES region to values

between those of bulk PdO and metallic Pd^0 evidenced a valence change in Pd consistent with Pd^+ induced by exposure to NO. Pommier et al. [19] used infrared measurements during NO adsorption on Pd/H-ZSM-5 to infer the reduction of dispersed Pd^{2+} to Pd^+ cations with subsequent formation of Pd^+ mononitrosyl complexes. Zheng et al. [20] studied the structure, performance, and adsorption chemistry of Pd-exchanged zeolites and reported the existence of multiple Pd species in those materials, including atomically dispersed Pd in cationic sites of zeolite and PdO_2 and PdO particles on external surfaces. Porta et al. [21] conducted NO_x adsorption on several Pd-exchanged zeolites under dry and wet conditions and reported that water strongly suppresses NO_x storage.

Other components like CO, C_2H_4 and $C_{12}H_{26}$ are also present in vehicle exhaust and can affect PNA behavior. Vu et al. [22] studied the effects of CO on Pd/BEA and reported an improvement in the amount of stored NO_x at low temperatures in the presence of excess CO in the feed. Chakarova et al. [23] also studied the co-adsorption of CO and NO on Pd/H-ZSM-5 and reported the formation of mixed Pd^{2+}(CO)(NO) species. Khivantsev et al. [24] showed that O_2 and CO improve NO_x storage on Pd/SSZ-13. They reported the shielding of Pd^{2+} from excess H_2O and selective formation of the mixed carbonyl-nitrosyl complex Pd^{2+}(CO)(NO) in the presence of CO.

Study by Ryou et al. [25] shows that Pd/SSZ-13 has considerable NO adsorption ability even after hydrothermal aging at 800℃ for 25 h. The problem arises when reductants such as CO and H_2 are present in the feed. Reductants will always be present in a real scenario. Multiple researchers have studied the effects of H_2 exposure on Pd/zeolite [19,26-28] and have reported the formation of Pd metal. This weakens the electronic bond between palladium and tetrahedrally coordinated Al in the zeolite structure. The zeolite can no

longer stabilize Pd, resulting in catalyst deactivation. Ryou et al. [29] studied the effects of exposure of CO and H_2 on Pd/SSZ-13 and reported the changes in Pd and SSZ-13 using XRD, EXAFS, H_2-TPR, HAADF-STEM, and NMR analysis. They reported that CO treatment induced more severe sintering of Pd species than H_2 at the same reduction temperature. After re-oxidation at 500°C, H_2-treated sample generated more Pd ion species than the CO-treated one, reason being facile sintering behavior due to the high mobility of Pd-carbonyl complex upon the treatment with CO. They concluded Pd sintering as the main deactivation mechanism of Pd/SSZ-13 passive NO_x adsorber.

Hydrocarbons (HCs) also need to be trapped during cold start period. Higher molecular weight alkanes can be effectively trapped on zeolites at low temperatures due to their pore structure and acidity [30-35]. Aromatics and lower molecular weight olefins and alkanes require dispersed metals for adsorption. For example, Ag^+ promoted ZSM-5 was shown to be effective for trapping C_2H_4 [36]. Exhaust components H_2O, CO, low molecular weight olefins, and aromatics may affect NO uptake and release behavior on PNA materials. Thus, it is important to study their impact as single components and in mixtures. Several PNA studies have been conducted to study the effects of trapping HCs on different zeolites such as Pd/ZSM-5, BEA, SSZ-13, etc. [37-43]. Comparatively fewer studies have been reported for trapping and oxidation of long chain HCs (C_{10}-C_{24}) which are common components of diesel exhaust. Peng et al. studied the trapping and oxidation of dodecane on a Pt/Pd/BEA monolith and applied a low dimensional model to predict the performance [44]. Malamis et al. [45] studied the trapping, release and conversion of NO_x, n-$C_{12}H_{26}$ and C_3H_6 on a Lean Hydrocarbon NO_x Trap (LHCNT) using sequential and dual-layer configurations of Pd/SSZ-13 and Pt/Pd/BEA, identifying the Pd/SSZ-13 + Pt/Pd/BEA

sequential configuration as most effective in simultaneously trapping C_{12} and NO. They also reported that addition of n-$C_{12}H_{26}$ and C_3H_6 delays NO desorption. Gupta et al. [38] studied NO uptake and release on Pd/SSZ-13 with and without H_2O, C_2H_4 and CO in the feed and reported that NO uptake approaches NO/Pd ~ 1 for a range of conditions, along with the generation of NO_2 during NO feed and CO_2 (CH_3CHO) during NO + CO (NO + C_2H_4) co-feed, suggesting reduction of well-dispersed Pd cations. Chen et al. conducted NO uptake on Pd supported on ZSM-5, BEA and SSZ-13 in the presence of decane [46]. They reported that NO is adsorbed on dispersed Pd at exchange sites of zeolites.

1.4 Objective and Approach

The objective of the current study is to develop a mechanistically rooted PNA model that can deepen our understanding and lead to optimized PNA materials and operating strategies. In the experimental part of study, the effects of feed parameters and material properties including uptake temperatures, feed flowrates, feed components (H_2O, CO, C_2H_4, $C_{12}H_{26}$), and Pd-loading on NO_x uptake and release are studied. DRIFTS data are also presented to provide guidance in the interpretation of the data and in the establishment of prospective mechanisms for microkinetic scheme development. In the modeling part a transient monolith model is described, which incorporates the microkinetic schemes for NO_x adsorption on H-ZSM-5 and Pd/H-ZSM-5.

The approach was extended to the development of a PNA model for NO uptake on Pd/SSZ-13 in the presence of H_2O, along with exhaust components CO and C_2H_4. The model is used to predict and to elucidate recently reported NO uptake and release data of

Gupta et al. [38]. The model was also used to compare NO uptake of Pd/SSZ-13 and Pd/ZSM-5.

Next the model is further extended to include the impact of $C_{12}H_{26}$ on NO uptake and release. Systematic experiments are conducted with mechanistic-based modeling to elucidate the underlying mechanism for coupled $C_{12}H_{26}$ and NO uptake on Pd/SSZ-13. The tuned and validated PNA monolith model is used to evaluate, understand, and optimize the PNA composition and operating strategy.

Chapter 2
Passive NO_x Adsorption on Pd/H-ZSM-5: Experiments and Modeling

2.1 Experimental

2.1.1 Catalyst Preparation

Ammonium (NH_4)-ZSM-5 with SAR (Si/Al ratio) of 15 was procured from Zeolyst International. Synthesis of H-ZSM-5 involved calcination of NH_4-ZSM-5 at 80°C for 12 hours, followed by 120°C for 2 hours, and finally 550°C for 4 hours. During the transition between each temperature a heating rate of 5°C/min was used. Pd/H-ZSM-5 was prepared by incipient wetness impregnation using Palladium nitrate dihydrate (PNDH) as the precursor (Sigma Aldrich). The required amount of PNDH was dissolved in deionized (DI) water in an amount equal to the pore volume of the H-ZSM-5 crystallites. The precursor solution was added dropwise to H-ZSM-5 while mixing rigorously. The impregnated sample was calcined following the same steps used for (NH_4)-ZSM-5. Following the washcoating step described below, a high temperature calcination at 550°C for 4 hours enabled dispersion of a fraction of Pd cations to occupy anionic $[Al\text{-}O\text{-}Si]^-$ zeolitic sites, which will be represented as Z^-. Catalyst composition data including the actual loading in wt.%, Pd dispersion, and the nominal Al:Pd ratio for the Pd(1%)/H-ZSM-5 and Pd(2%)/H-ZSM-5 samples are provided in Table 2.1.

2.1.2 Monolith Washcoating

Washcoating of the monolith was done by a two-step process of milling and dip-coating. The zeolitic powder was mixed with deionized water to form a 10 wt.% slurry. Alumina binder was added in the form of colloidal alumina sol (20% alumina) to give an 18 wt.% alumina + 82 wt.% zeolite mixture. After mixing, the solution was poured into a

plastic bottle filled 2/3rd with 5 mm silicon beads and ball-milled for 1.5 days. After ball milling, the slurry was poured into a glass beaker and continuously stirred at 200-400 rpm to give a uniform solution. A cordierite monolith of 400 cpsi, 4 cm in length, having 49 channels, was dipped into the catalyst solution for 20-25 seconds. Air was then blown into the channels to avoid blocking of the channels. The coated monolith was then kept in an oven for 1 hour at 80°C. This step was repeated until the desired washcoat loading was achieved. After finishing the washcoating process, the monolith was calcined using the same procedure mentioned above.

Table 2.1 Catalyst composition

	Pd(1%)/H-ZSM-5	**Pd(2%)/H-ZSM-5**
Actual Pd wt.%	1.00	2.00
Actual Pd(moles/g zeolite)	9.49×10^{-5}	1.88×10^{-4}
Pd Dispersion	41%	22%
Al/Pd (total)	7.06	3.50
Al/Pd (dispersed)	17.24	15.98

2.1.3 Bench-scale Reactor System

The experiments were conducted in a bench reactor system. Monoliths coated with Pd/H-ZSM-5 + Al_2O_3 were wrapped in ceramic paper and loaded in a quartz tube of 0.58 inch I.D. by 0.75 inch O.D. The quartz tube was inserted into a temperature-controlled furnace. Flowrates of various feed gases were metered by MKS mass flow controllers. There were three lines for gas flow: lines one, two, and main. A four-way valve enabled switching between the two feed lines. The NO feed contained a small amount of NO_2 (~5 ppm for 400 ppm NO feed) which was accounted for in the data analysis. The monolith temperature was measured by a thermocouple placed inside and at the middle of the

monolith channel. A FTIR measured the NO and NO_2 effluent concentrations. A syringe pump and heated injection syringe system was employed to add water into the feed.

2.1.4 Flow Reactor Experiments

The tested monolith samples were pretreated in 5% O_2 and balance Ar at 550°C for 30 minutes prior to each experiment. Following a high temperature treatment of Pd/H-ZSM-5 in a net oxidizing atmosphere, most of the dispersed Pd is expected to have a +2 oxidation state, following Descorme et al. [15]. Confirmation of these species by XPS and H_2-TPR is described below. The identity of TPD peaks utilizes a combination of DRIFTS and DFT calculated binding energies, also described later. The monolith was cooled to ambient temperature and then heated again to the desired temperature (50°C, 80°C, 100°C, or 150°C). Experiments were carried out at space velocities in the range 28-48k hr^{-1} (monolith volume basis; at 298K, 1 bar). The experiment involved exposure to NO_2 (5ppm)/ NO (400ppm)/ O_2 (2%)/ balance Ar at the prescribed temperature and duration, followed by exposure to O_2 (2%) in balance Ar, under a temperature ramp from the prescribed temperature to 550°C at a ramp rate of 22°C/min. When water was added, the feed contained 7% H_2O. Each NO uptake experiment was repeated to check for reproducibility; the reported data are the average of three runs. The amount of NO_x adsorbed was comparable to amount of NO_x desorbed within the 10% for all the experimental results used here. A blank tube experiment was carried out at each flowrate to estimate the time delay. The NO uptake is reported with two metrics: NO/Pd ratio and moles NO/g zeolite. The nitrogen balance was calculated for uptake and desorption and was found to be within 10% error limit for all the results presented in this study.

2.1.5 Catalyst Characterization

A combination of X-ray photoelectron spectroscopy (XPS), H_2 temperature programmed reduction (H_2-TPR), diffuse reflectance infrared Fourier transform spectroscopy (DRIFTS) and CO chemisorption were used to characterize the materials.

The XPS analysis of Pd(1%)/H-ZSM-5 was conducted with a PHI model 5700 X-ray photoelectron spectrometer. The powder sample was placed on the Mo cover plate which accommodated a sample area of up to 1 in^2. The effects of charging were corrected with reference to Si-2p binding energy of 103.3 eV. The instrument was able to analyze the sample up to ~5 nm depth.

The H_2-TPR analysis used 0.1 g of the Pd(1%)/H-ZSM-5 powder. The sample was pelletized, crushed and sieved to 50-70 mesh and loaded into a quartz tube of 4 mm ID and 6.35 mm OD. Prior to the H_2 exposure, the catalyst was pretreated at 550℃ for 1 h in an oxidative atmosphere (5% O_2/ balance Ar). The catalyst was then cooled to ambient temperature and subjected to 50 sccm total feed flowrate containing ~1.2% H_2 and balance Ar. The temperature was increased from 25℃ to 700℃ at a ramp rate of 40℃/min. The gases were detected using a mass-spectrometer (HIDEN analytic, HPR 20).

CO chemisorption was conducted to measure the Pd dispersion of the two samples, Pd(1%)/H-ZSM-5 and Pd(2%)/H-ZSM-5. The testing of 0.2 g of pre-calcined catalyst (550°C) was performed in Micromeritics Accelerated Surface and Porosity System (ASAP2020). Evacuation was done by using He gas to remove any adsorbed species. Finally, CO was fed to the system to conduct the chemisorption measurements.

Diffuse reflectance infrared Fourier transform spectroscopy (DRIFTS) was used for identification of surface species for the same (dry) feed compositions in the reactor

experiments. The DRIFTS system had a gas cell equipped with Cadmium Telluride windows and a KBr beam splitter and a Praying Mantis^{TM} design (Harrick Scientific Inc.). Details of the system are provided elsewhere [47]. Powder catalyst samples were pressed into pellets and loaded into the gas cell. The feed gas metered by MKS mass flow controllers was directed through the catalyst sample. Gas lines into the cell are heated to prevent any condensation. DRIFTS experiments were carried out at three temperatures: 50°C, 150°C, and 300°C for H-ZSM-5, Pd(1%)/H-ZSM-5, and Pd(2%)/H-ZSM-5. Approximately 50 mg of powder catalyst was pressed into a pellet (3 mm radius, 2 mm thickness) and set inside the flow-through cell. Samples were pretreated for an hour at 500°C with a feed mixture containing 5% O_2 in He. Samples were then cooled to the desired temperature under the same flowing gases and were held at the desired temperature for 1-2 hours to allow equilibration of atmospheric water before measuring the background IR spectrum. The IR spectra was recorded at a resolution of 4 cm^{-1} with every 16 measurements averaged into a single output. Several baseline measurements were taken before 0.1% NO was introduced into the system.

Experimental Results

2.1.6 Characterization

The XPS analysis results for Pd(1%)/H-ZSM-5 are shown in Figure 2.1. The duplet peaks ~337 eV ($3d_{5/2}$) and ~342 eV ($3d_{3/2}$) are associated with Pd in +2 state [16,20]. Thus, the XPS result shows the existence of Pd(II) in the catalyst surface. The corresponding H_2-TPR data for Pd(1%)/H-ZSM-5 is shown in Figure 2.2 corroborate the XPS findings. Lee et al. [16] reported that PdO is reduced to Pd at ~0℃ while ionic Pd species are reduced at ~50-150℃. According to Adelman et al. [48] PdO is reduced to Pd at ~0℃ while Pd^{+2}

cations are reduced at ~90-250℃. These studies show that reduction of Pd cations occurs above 50℃ [16,48]. The H_2 consumption has a dip at ~25℃ which appears at the start of the experiment when the temperature is at ambient ~25 ºC. This dip is attributed to the reduction of bulk PdO while a second broader dip spanning 50 to 200℃ is attributed to the reduction of Pd(II) species [16,48]. Collectively, the XPS and H_2-TPR results shows the existence of Pd(II).

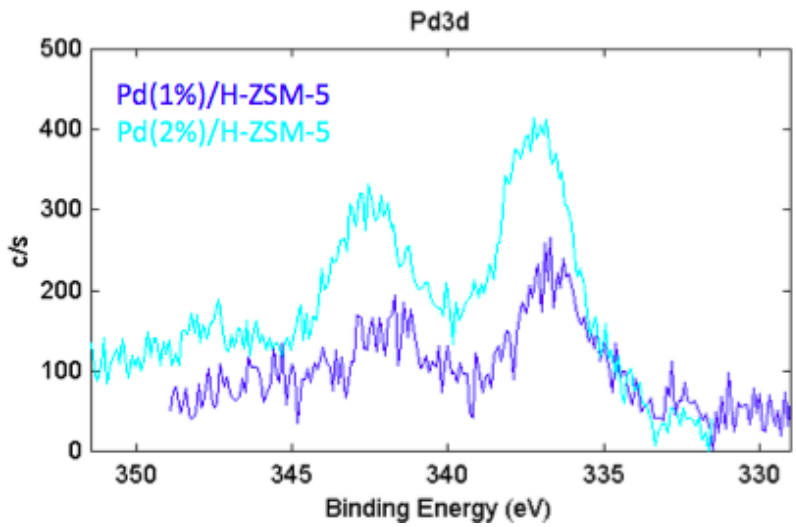

Figure 2.1 XPS spectra acquired on Pd/H-ZSM-5

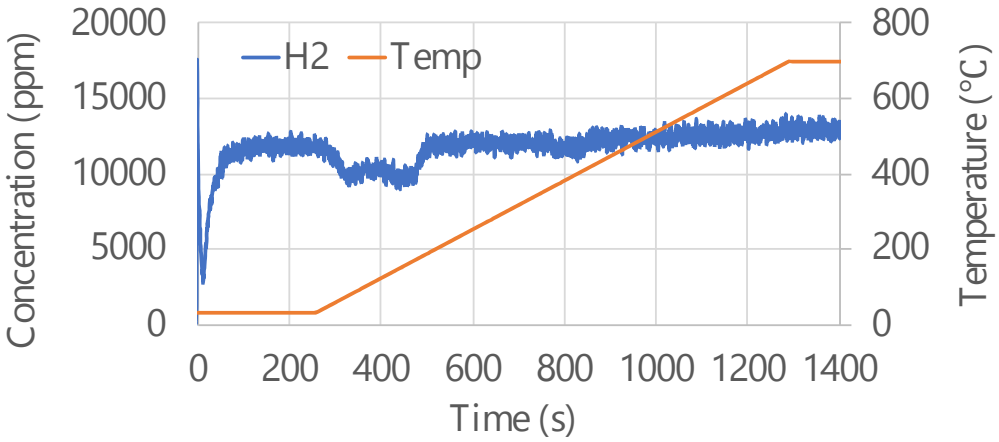

Figure 2.2 H_2-TPR curve of Pd(1%)/H-ZSM-5

The chemisorption measurements give a fractional Pd dispersion of 0.41 and 0.22 for Pd(1%)/H-ZSM-5 and Pd(2%)/H-ZSM-5, respectively.

The DRIFTS measurements were conducted using a feed containing 5% O_2, 0.1% NO, with He as balance. Figure 2.3 shows DRIFTS results for NO adsorption at 50°C during exposure of the feed gas to H-ZSM-5, Pd(1%)/H-ZSM-5 and Pd(2%)/H-ZSM-5. Table 2.2 lists the key IR peaks of interest along with their reported identities. This information is used for the development of uptake mechanisms discussed later.

Table 2.2 IR peaks assignments

IR Peak cm^{-1}	**Assignment**
1643	Nitrate species on H-ZSM-5 [15,27]
1805	NO adsorbed on Pd^+ for Pd/H-SSZ-13[24]
1836	NO adsorbed on Pd^+ for Pd/H-ZSM-5[21]
1865	NO adsorbed on Pd^{2+} for Pd/H-SSZ-13[24]
1880	NO adsorbed on Pd^{2+} for Pd/H-ZSM-5[21]
2136	Z^-NO^+ [21,23] and NO_2 interacting with hydroxyls of zeolite [15,49]
3610	Acid hydroxyls of the zeolite structure being consumed [15]

The H-ZSM-5 data show a prominent peak at 2136 cm^{-1}, which is attributed to NO_2 interacting with H-ZSM-5 acidic hydroxyls [15,49] and NO^+ species interacting with zeolitic oxygen; i.e., Z^-NO^+ [25-27, 50]. The smaller peak at 1643 cm^{-1} is attributed to surface nitrate species [15,50]. The negative peak at 3610 cm^{-1} reveals consumption of acidic hydroxyls during the NO_x uptake [15,49]. The 2136 cm^{-1} and 1643 cm^{-1} peaks suggest that NO is oxidized by O_2 to NO_2 and that further oxidation to NO_3^- is possible. The two broad peaks spanning ~2300 to ~3300 cm^{-1} are a result of atmospheric water that could not be eliminated in the system [25].

The Pd(1%)/H-ZSM-5 and Pd(2%)/H-ZSM-5 data show no qualitative differences. The presence of peaks at 1836 and 1880 cm^{-1} confirms that NO adsorbs onto Pd cations [15,24]. These findings corroborate the data reported by Descorme et al. [15] who proposed the aforementioned two-step Pd^{2+} reduction mechanism. We expand on that and the other steps in the modeling section.

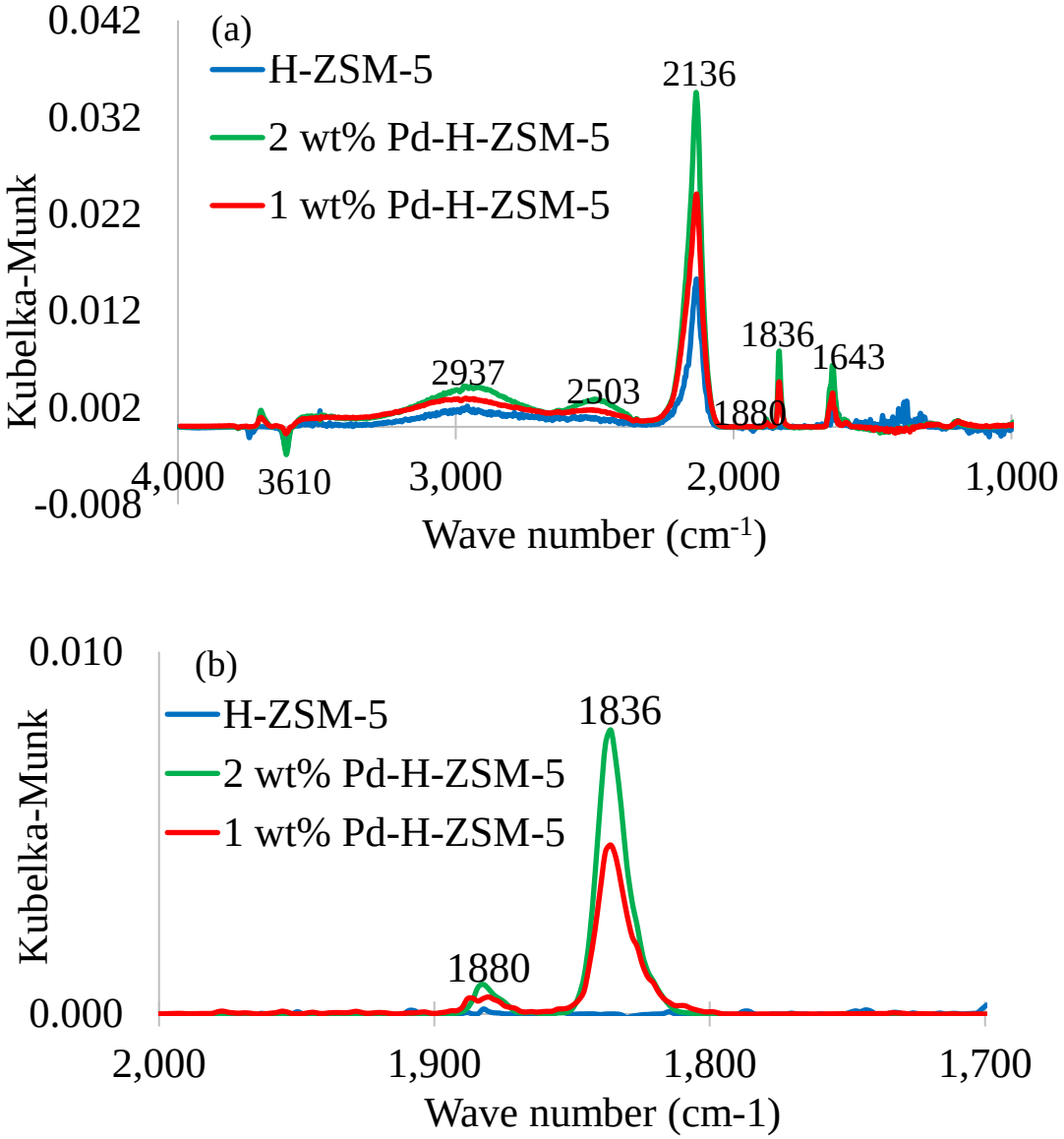

Figure 2.3 (a) DRIFTS spectra obtained during dry $NO+O_2$ exposure to H-ZSM-5, 1% Pd/H-ZSM-5 and 2% Pd/H-ZSM-5 at 50°C (b) zoomed-in DRIFTS spectra showing NO uptake.

2.1.7 Effect of Temperature and Pd-loading for Dry Feed

NO_x uptake experiments were conducted over on protonated and Pd-exchanged ZSM-5 samples for a range of uptake temperatures. The feed was devoid of water. Figure 2.4 (a) - (c) show the NO_x uptake profiles for H-ZSM-5, Pd(1%)/H-ZSM-5, and Pd(2%)/H-ZSM-5, respectively, each at the three uptake temperatures 50°C, 80°C, and 150°C. The area under the uptake curve was subtracted from the feed area to calculate the amount of NO_x adsorbed. The amount of NO_x adsorbed expectedly decreases with an increase in temperature. Consistent with the uptake trend is a decrease in the breakthrough time with increasing temperature; e.g., ~40, ~25 and ~4 seconds for 50°C, 80°C and 150°C, respectively, for Pd(1%)/H-ZSM-5.

The corresponding TPD profiles for NO_x uptake at 80°C for H-ZSM-5, Pd(1%)/H-ZSM-5, and Pd(2%)/H-ZSM-5 are shown in Figure 2.5(a) - (c), respectively. For H-ZSM-5, the Figure 2.5(a) data show that there are two TPD peaks for NO_2 and one low temperature peak of NO. The two NO_2 peaks indicate that NO_2 binds to at least two different sites having distinct binding energies. The low temperature NO_2 peak is proposed to be associated with NO_2 adsorbed on Brønsted acid sites while high temperature peak is likely associated with nitrate species [15,49-50]. The low temperature NO peak is attributed to NO^+ interacting with the anionic zeolite site, forming Z^-NO^+ [25-26].

In contrast, the TPD data for Pd(1%)/H-ZSM-5 in Figure 2.5(b) reveals two peaks for both NO and NO_2. Since the high temperature NO peak is absent in the H-ZSM-5 data, it is associated with a Pd site. Comparison of the NO_x uptake and TPD profiles of the Pd(1%)/H-ZSM-5 and H-ZSM-5 indicates a higher NO_x uptake for the former than the latter which is also shown in Figure A. 1. This increase is noted from the increase in area under the TPD curves of Pd(1%)/H-ZSM-5 when compared to H-ZSM-5.

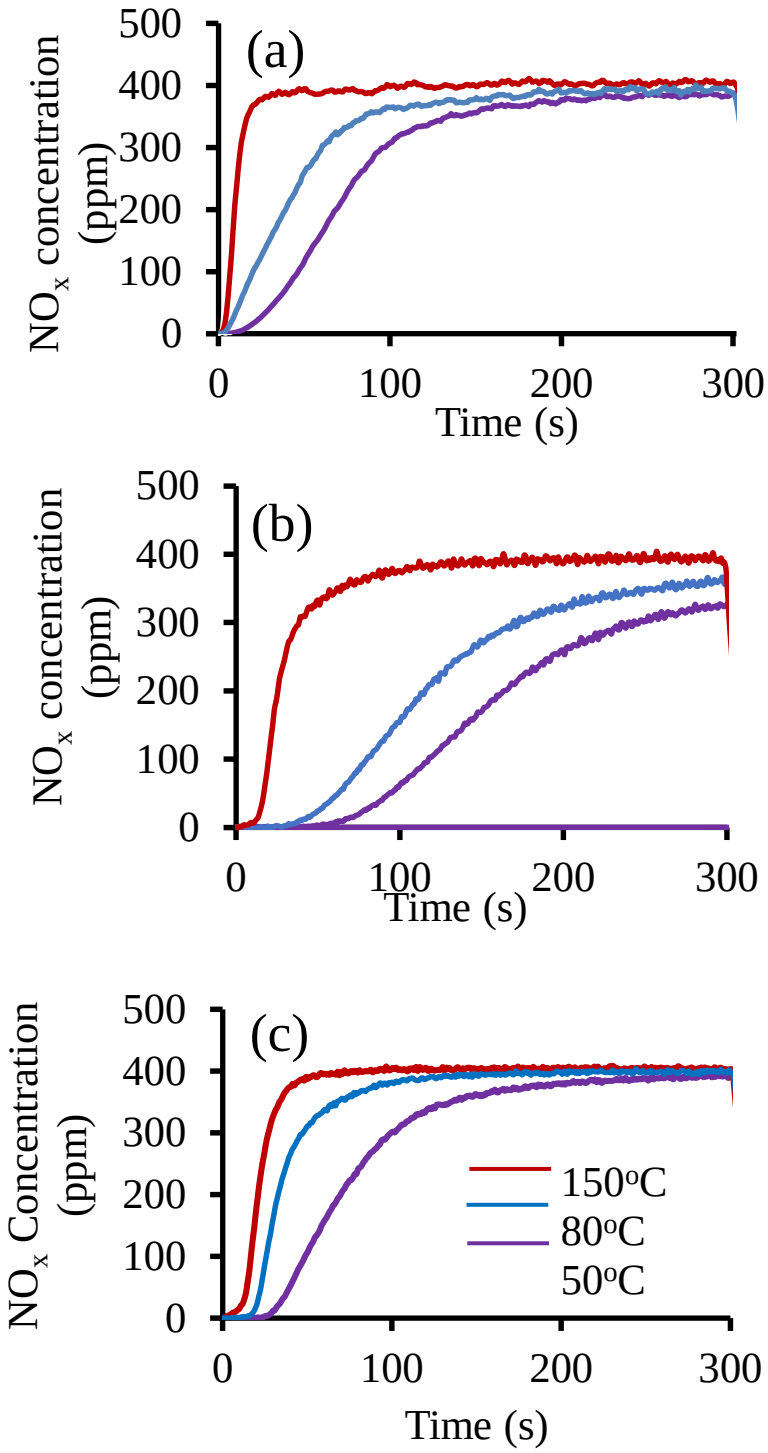

Figure 2.4 NO_x adsorption profile for (a) H-ZSM-5, (b) Pd(1%)/H-ZSM-5 and (c) Pd(2%)/H-ZSM-5 at uptake temperatures of 50°C, 80°C, and 150°C for dry feed.

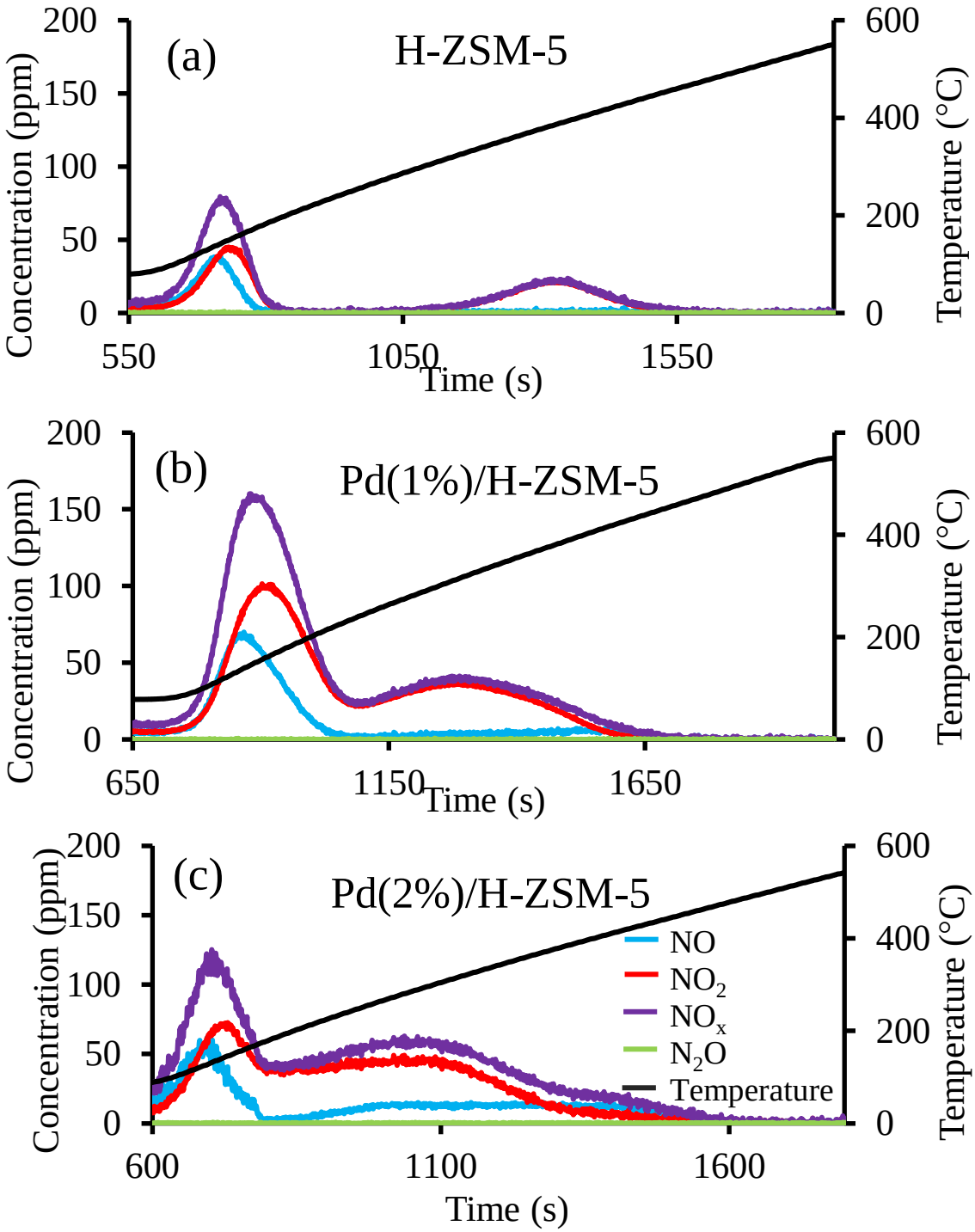

Figure 2.5 NO_x TPD profiles for (a) H-ZSM-5, (b) Pd(1%)/H-ZSM-5 and (c) Pd(2%)/H-ZSM-5 for uptake conducted at temperatures of 80°C for dry feed.

Multiple Pd species may coexist in the zeolite framework; these include PdO_x clusters and Pd cations, described in more detail below. Comparison of the NO_x uptake and TPD profiles during exposure of Pd(1%)/H-ZSM-5 and Pd(2%)/H-ZSM-5 to the dry feed (Figure 2.5(b-c)) indicates a higher NO_x uptake for the former than the latter. The aforementioned Pd dispersion measurements of 0.41 (Pd(1%)/H-ZSM-5) and 0.22 (Pd(2%)/H-ZSM-5) are consistent with the comparative NO_x uptakes. In the absence of H_2O in the feed, both dispersed Pd and Brønsted acid sites contribute to NO_x uptake. Dispersed Pd as well as PdO nanoclusters require two Brønsted sites for stabilization [12]. Also, Pd(2%) has higher percentage of Pd clusters which blocks the Brønsted sites which would have otherwise contributed for NO_x uptake. Collectively this results in the higher NO_x uptake for Pd(1%)/H-ZSM-5 compared to Pd(2%)/H-ZSM-5 for the dry feed.

2.1.8 Effect of Temperature and Pd-loading for Wet Feed

Water significantly inhibits NO_x uptake, while the extent of inhibition is a function of temperature. The effect of H_2O on the NO_x uptake was examined using the same feed mixture but with 7% H_2O added. The same uptake and TPD steps were followed. NO_x uptake on H-ZSM-5 at 80°C and TPD profiles for the experiment are shown in Figure A. 2 of Appendix. The data show that in the presence of H_2O, H-ZSM-5 does not adsorb any measurable NO_x. This fact is presumably a result of site blockage by adsorbed H_2O.

Similar experiments containing H_2O in the feed were conducted for Pd(1%)/H-ZSM-5. The total NO_x uptake at 80°C dramatically decreases from ~1.95×10^{-4} mole NO_x/ g zeolite (NO/Pd ~1.98) for the dry feed to ~0.35×10^{-4} mole NO_x/ g zeolite (NO/Pd~0.36) when 7% H_2O is present (Figure A. 1). The decrease is attributed to inhibition of NO_x uptake by H_2O adsorbed on the H-ZSM-5 Brønsted acid sites and on the Pd cations.

Brønsted acid sites do not adsorb NO_x in the presence of H_2O as shown in Figure A. 2. The measured NO uptakes for temperatures of 80°C, 100°C, 150°C and 170°C are shown in Figure 2.6 In contrast to the dry feed experiments, the NO uptake for the wet feed increases with temperature up to a maximum value at 150°C. The model described later is able to predict this trend shown in Figure 2.6, which is attributed to the decreasing coverage of H_2O with increasing temperature, thereby freeing up sites for NO_x adsorption.

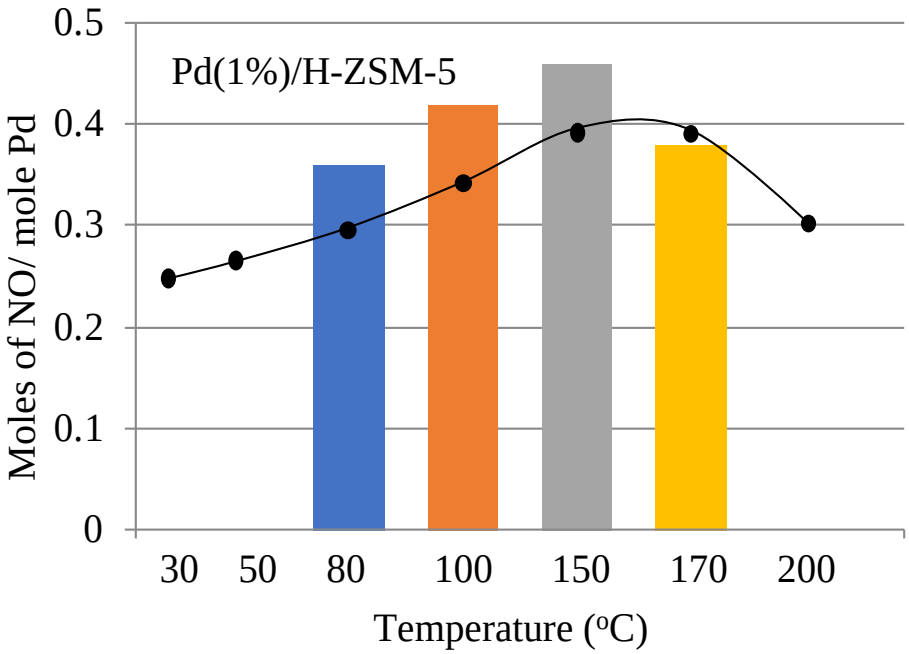

Figure 2.6 Comparison of moles of NO per mole of Pd at different uptake temperatures in presence of 7% H_2O in the feed as well as model predictions are shown by black points.

Experiments were conducted with Pd(1%)/H-ZSM-5 and Pd(2%)/H-ZSM-5 to examine the effect of Pd loading using a wet feed. Conditions such as temperature (50°C, 80°C, and 150°C) and composition (5ppm NO_2/ 400ppm NO/ 2% O_2/ 7% H_2O/ balance Ar) were fixed. A comparison of the NO_x uptake for Pd(1%)/H-ZSM-5 and Pd(2%)/H-ZSM-5 is shown in Figure 2.7 The total NO_x uptake (mole NO_x/g zeolite) is only ~10%

higher on the Pd(2%)/H-ZSM-5. The minor increase in the NO_x uptake on Pd(2%)/H-ZSM-5 (4.15×10^{-5} mole NO_x/g zeolite) compared to Pd(1%)/H-ZSM-5 (3.5×10^{-5} mole NO_x /g zeolite) is attributed to the slightly higher Pd disperstion which provides additional NO_x sorption sites.

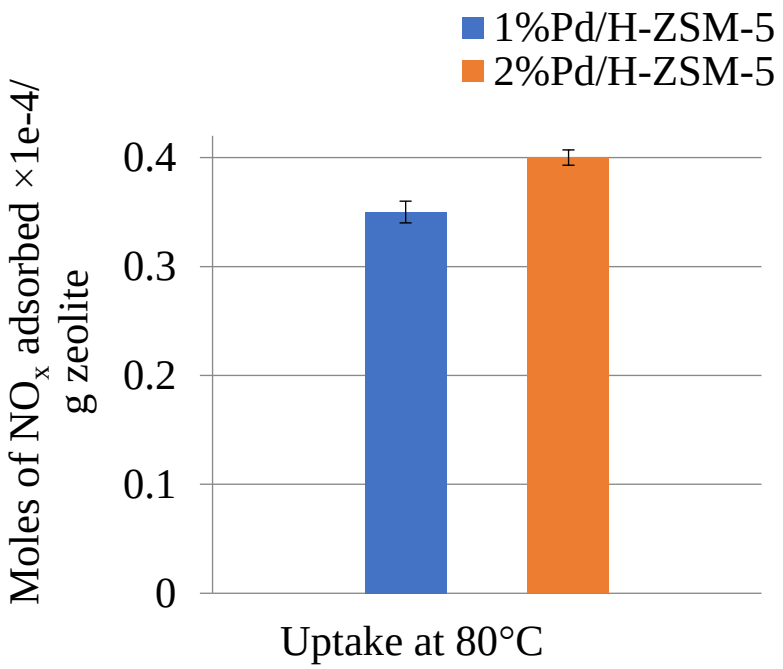

Figure 2.7 Comparison of moles of NO_x adsorbed per gram zeolite for different Pd loading in the feed comprised of NO_2 (5ppm)/ NO (400ppm)/ O_2 (2%)/ H_2O (7%)/ balance Ar during uptake.

2.1.9 Washcoat Diffusion Limitations

The potential impact of washcoat diffusion was examined for Pd(1%)/H-ZSM-5 by using two different lengths of monolith (2 cm, 4 cm) while fixing the total amount of washcoat (mass). The premise is that the 4 cm long monolith has a shorter diffusion length due to its thinner washcoat. In addition, the feed gas contact time was fixed, accomplished by a doubling of the flow rate for the longer sample. The experiment involved exposure to dry NO_2 (5ppm)/ NO (400ppm)/ O_2 (2%)/ balance Ar at the prescribed temperature and duration, followed by exposure to O_2 (2%) in balance Ar, under a temperature ramp from

experimental temperature to 550°C at a ramp rate of 22°C/min. The results reveal a nearly equal NO_x uptake on both monolith samples at the same three temperatures (Figure A. 3). These results show that the washcoat diffusion is not the limiting rate process for NO_x uptake in the range of temperatures used in this study.

2.1.10 Effect of Feed Flowrate

Experiments were conducted for both H-ZSM-5 and Pd(1%)/H-ZSM-5 at two different feed flowrates, 28.5k hr^{-1} and 47.5k hr^{-1}. NO feed durations of 5 and 3 minutes were used for the 28.5 and 47.5 hr^{-1} flowrates, respectively. The different uptake times were used to ensure that the same quantity of NO was fed to the reactor at the two flowrates. The uptake temperature (50°C, 80°C, and 150°C) and dry feed composition (5ppm NO_2/ 400ppm NO/ 2% O_2/ balance Ar) were fixed.

NO_x adsorption profiles at an uptake temperature of 80°C for both the flowrates are shown in Figure 2.8(a). The data show that with increasing total feed flowrate the amount of NO_x adsorbed decreases. Specifically, the NO_x uptake at 80°C is ~1.95×10^{-4} mole NO_x/g zeolite at 1500 sccm and ~1.17×10^{-4} mole NO_x/g zeolite at 2500 sccm. Figure 2.8(b) shows the dependence of the integral NO_x trapping efficiency η_T on the total volume of gas contacting the catalyst where η_T is given by

$$\eta_T = 100\left(1 - \frac{1}{t^* F_{NOx}^o}\int_0^{t^*} F_{NOx}(t)dt\right). \quad (2.1)$$

Here F_{NOx}^o and F_{NOx} are the NO_x feed and effluent molar flow rates and t^* is the exposure time. For a fixed amount of feed gas, η_T decreases with increasing flowrate.

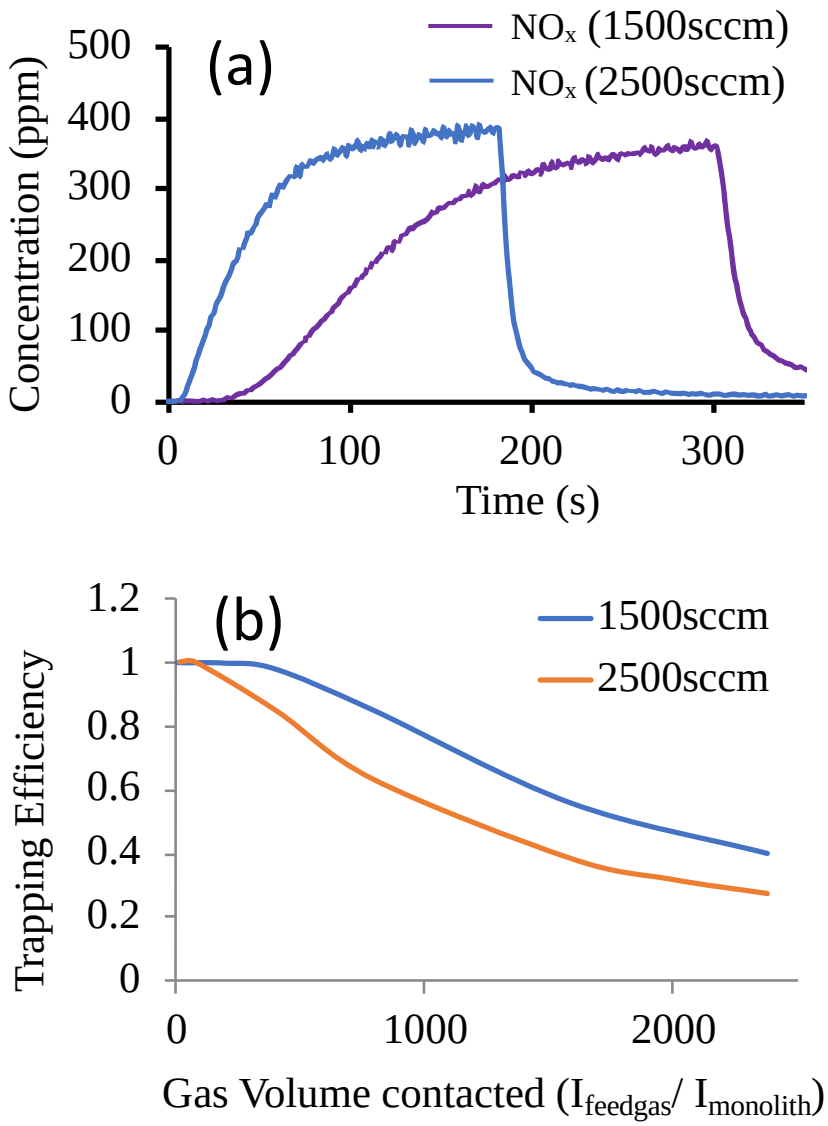

Figure 2.8 (a) Comparison of NO_x adsorption profile for dry feed at uptake temperature of 80°C (b) Dependence of trapping efficiency on volume of gas contacting the catalyst for total feed flowrates of 1500 sccm and 2500 sccm.

These results show that the uptake rate is a function of the contact time and is therefore kinetically limited. The earlier-described experiments carried out to assess potential washcoat diffusion limitations showed negligible transport resistance. Taken together, the decrease in the amount of NO_x adsorbed with increasing gas flowrate is attributed to limitations associated with the adsorption process.

2.2 Modeling

2.2.1 One-Dimensional Two-Phase Transient Model

A one-dimensional, two-phase transient, single channel monolith model containing a mechanistic-based microkinetic scheme is used to predict the effluent gas concentration profiles spanning uptake through conversion and release. The low dimensional model formulation used here follows the approach developed by Joshi et al. [19]. The following assumptions are made: (i) pressure drop is negligible; (ii) thicknesses of wall and washcoat are small compared to the channel hydraulic radius; (iii) axial diffusion in the fluid phase is negligible compared to convection justified by a high Pe number ($\langle u\rangle L/D_m$ is in the range of ~ 254-819); (iv) flow is laminar (channel Reynolds number ($4R_{\Omega 1}\langle u\rangle/\nu$) ~ 4-36) and fully developed; (v) isothermal condition during the uptake; (vi) hydraulic diameter of the channel is much smaller than the length of the channel; (vii) uniform washcoat activity and thickness; (viii) each channel is identical.

The model equations containing species balance in the fluid and solid phase (washcoat) are as follows:

$$\frac{\partial X_{jm}}{\partial t} = -\langle u\rangle \frac{\partial X_{jm}}{\partial z} - \frac{k_{mo,j}}{R_{\Omega 1}} (X_{jm} - X_{j,wc}), \tag{2.2}$$

$$\frac{\partial X_{j,wc}}{\partial t} = \frac{k_{mo,j}}{\in R_{\Omega 2}} (X_{jm} - X_{j,wc}) + \frac{1}{\in C_{rm}} \left(\sum_{l=1}^{rxn} [\, \nu_{lj}\, R_{v,l}(\theta, X_{wc})] - R_{ad,j} + R_{des,j}\right), \tag{2.3}$$

$$\frac{\partial \theta_{jX}}{\partial t} = \frac{1}{C_x} (R_{ad,j} - R_{des,j}), \tag{2.4}$$

and $\frac{\partial T}{\partial t} = \beta.$ (2.5)

The entrance boundary condition is $X_{jm} = X_{jm,in}$ at z = 0 while the initial condition is $X_{jm} = 0$, $X_{j,wc} = 0$ at t = 0.

The parameters and variables are defined in the List of Notation. Key variables and parameters are described here. Mole-fractions of species j in the flowing gas and in the washcoat are shown by X_{jm} and $X_{j,wc}$, respectively. The hydraulic radius $R_{\Omega 1}$ is defined as the ratio of open channel area to channel perimeter. The effective transverse diffusion length in the washcoat $R_{\Omega 2}$, is defined as ratio of washcoat cross-sectional area to fluid-washcoat interfacial perimeter. Ramanathan et al. [28] provided expressions to estimate $R_{\Omega 1}$and $R_{\Omega 2}$ using the SEM images of the washcoat (Figure A. 4). The parameter β is the temperature ramp rate. The overall mass transfer coefficient of species j that is $k_{mo,j}$ is defined as follows:

$$\frac{1}{k_{mo,j}} = \frac{1}{k_{mi,j}} + \frac{1}{k_{me,j}}, \tag{2.6}$$

$$k_{me,j} = \frac{D_{f,j} Sh_e}{4\, R_{\Omega 1}}, \tag{2.7}$$

$$k_{mi,j} = \frac{D_{e,j} Sh_{i,\infty}}{R_{\Omega 2}}, \tag{2.8}$$

and $\lambda = \frac{D_{f,j}}{D_{e,j}}$. (2.9)

The external and internal mass transfer coefficients are shown by $k_{me,j}$ and $k_{mi,j}$ respectively. The diffusivities of species j in fluid phase and washcoat, are shown by $D_{f,j}$ and $D_{e,j}$ respectively. The values of $D_{f,j}$ are given in Table A. 1. Following Metkar et al. [51] the value of λ for ball-milled ZSM-5 is in the range of 80-100; a value 80 is used here. The value of external Sherwood Sh_e is taken from Ramanathan et al. [52]. The value of asymptotic internal Sherwood number $Sh_{i,\infty}$depends on the values of $R_{\Omega 1}$and $R_{\Omega 2}$ [52]. C_{Tm} is total gas phase concentration approximated by the ideal gas law and neglecting pressure drop in the channel [$C_{Tm} = \frac{P_o}{R_g T}$; P_o = 101,325 Pa].

2.2.2 Model Tuning and Validation Procedure

Our approach in developing microkinetic schemes was to include a level of detail that is mechanistically complete and able to capture trends in data from the current study and selected literature data. In this section we describe the overall approach. In the following two sections we explain the reaction steps, for H-ZSM-5 and Pd/H-ZSM-5.

A systematic procedure was followed to develop and tune the PNA model for H-ZSM-5 and Pd/H-ZSM-5 using a combination of NO uptake and desorption data, DRIFTS measurements, and density functional theory calculations [30]. For some of the reactions DFT estimates for CHA and BEA were available but not for ZSM-5. Since the pore size of ZSM-5 lies between that of CHA and BEA, the binding energy values (ΔH) for BEA and CHA were taken as the lower and upper bounds for the ZSM-5 ΔH values. After parameter fitting, all estimated values lie between the lower and upper bounds and the final model was found to be insensitive to the limiting values, including those adopted from various DFT sources.

The first step in the microkinetic model development was to propose a reaction scheme for NO_x uptake on H-ZSM-5 in the absence of H_2O. Next, using data with H_2O in the feed, H_2O adsorption step on the Brønsted acid sites was added. Pd/H-ZSM-5 data in the absence of H_2O were then used to propose steps associated with NO_x uptake and release on Pd-associated sites for a dry feed. Parameter estimation for the Pd/H-ZSM-5 model was accomplished while keeping the parameters associated with H-ZSM-5 fixed. The final step was to add steps for NO_x uptake on Pd/H-ZSM-5 with H_2O in the feed. Again, parameter estimation was accomplished while keeping all previously estimated parameters fixed. At each stage the model was validated for different conditions, including uptake temperature,

feed composition, ramp rate, Pd-loading and total flowrate. In the final stage the model was validated for a different Pd loading.

The model contains both non-kinetic and kinetic parameters. Values of non-kinetic parameters are provided in Table 2.3 and are primarily concerned with the monolith geometry and operating conditions. Where possible, values of kinetic parameters available from the literature or from DFT calculations were used. The remaining unknown kinetic parameters were estimated by fitting selected data using a parameter estimation algorithm (MATLAB *fmincon*) interfaced with the monolith reactor model containing the microkinetic scheme. This involved defining an objective function comprising the sum of squared differences between the experimental and predicted NO_x (NO, NO_2) concentrations spanning the uptake and release. The four stages (reference sets) of the model tuning involved the following number of data points (N_d) and estimated parameters (N_p):

- NO + O_2 on H-ZSM-5: $N_d = 3420$; $N_p = 30$
- NO + O_2 + H_2O on H-ZSM-5: $N_d = 2019$; $N_p = 2$
- NO + O_2 on Pd/H-ZSM-5: $N_d = 2786$; $N_p = 18$
- NO + O_2 + H_2O on Pd/H-ZSM-5: $N_d = 1946$; $N_p = 21$ (Scheme I)
  $N_p = 31$(Scheme II)

More details of parameter estimation are provided in the next section and in the Supplemental Material section.

Table 2.3 Parameters used in model

Parameter	Value
L	0.04 m
<u>	0.316*(T/273.15) m/s
$C_{\tau m}$	$(12187.3/T)$ mol/m^3
ε_{wc}	0.4
$R_{\Omega 1}$	3×10^{-4} m
$R_{\Omega 2}$	1.5×10^{-5} m
Sh_e	4.36
$Sh_{i,\infty}$	2.37
λ	50
C_S	1406 mole-sites/m^3 of washcoat
C_{S1}	1250 mole-sites/m^3 of washcoat
C_{S2}	49 mole-sites/m^3 of washcoat
C_{S3}	29 mole-sites/m^3 of washcoat

The enthalpy change for any step i is given by $-\Delta H_i$, and the corresponding equilibrium constant is given by

$$K_i(T) = \frac{k_{fi}}{k_{bi}} = \left(A_{fi}/A_{bi}\right)e^{-\left(\frac{\Delta Hi}{R_g T}\right)}, \tag{2.10}$$

with $\Delta H_i = E_{fi} - E_{bi}$ the heat of adsorption for step i. Forward and reverse rate constants are given by

$$k_{fi}(T) = A_{fi}e^{-\frac{E_{fi}}{R_g T}} \tag{2.11}$$

and $k_{bi}(T) = A_{bi}e^{-\frac{E_{bi}}{R_g T}}$. (2.12)

Where A_{fi} and A_{bi} are pre-exponential factors, and E_{fi} and E_{bi} are activation energies for the forward and reverse steps, respectively. To maintain thermodynamic consistency, the combination of selected ΔH values were constrained. For example, the combination of reactions R2.1, R2.2, and R2.3 or of R2.6, R2.8, R2.9, and R2.11 give NO oxidation which has a known ΔH. Where possible, binding energies for NO, NO_2, and H_2O on the Brønsted acid and Pd cation sites were estimated using literature data or DFT-calculated values. For

the latter, DFT calculations for binding energies on Pd/H-SSZ-13 from [30] and Pd/H-BEA from Mei et al. [53] were used. With the nominal pore size of medium-pore size ZSM-5 zeolite (0.56 nm) between that of large-pore BEA zeolite (0.65 nm) and small-pore SSZ-13 zeolite (0.32 nm), the estimated binding energies were fixed at values bounded by the SSZ-13 and BEA values. This approach ensures a mechanistic underpinning while limiting the number of unknown parameters. The values of activation energies for adsorption of different species on active sites are assumed to be zero. The activation energy for reverse reaction is obtained such that $E_f - E_b$ matches the corresponding ΔH value for each step.

The model partial differential equations (PDEs) were discretized using a second-order finite difference method. The reactor length was discretized into 50 elements as a compromise between simulation time and simulation accuracy. The resulting set of ordinary differential equations (ODEs) were solved by the MATLAB routine *ODE23s*.

2.2.3 Microkinetic Model for H-ZSM-5

The first set of reactions in the microkinetic description to be developed is for NO_x uptake on H-ZSM-5 in the absence of H_2O in the feed. Table 2.4 lists the proposed 11 steps [R2.1-R2.11]; also included are the rate expressions for each of the steps. Justification for selecting these steps is provided below and is based on the NO uptake and release data, DRIFTS measurements, and selected literature. NO uptake at 80°C (reference data set) and accompanying NO and NO_2 TPD data was used to estimate the unknown kinetic parameters as explained above.

Table 2.4 Reaction mechanism for H-ZSM-5 (s – $O_z^-H^+$)

Reaction no.	Reaction step	Rate expression (R_f - R_b)
R2.1	$2NO \leftrightarrow ONNO^*$	$k_{1f}X_{NO}^2C_s^2$- $k_{1b}C_{ONNO*}$
R2.2	$ONNO^* + O_2 \leftrightarrow N_2O_4^*$	$k_{2f}C_{ONNO*}X_{O_2}C_s$ - $k_{2b}C_{N_2O_4^*}$
R2.3	$N_2O_4^* \rightarrow 2NO_2$	$k_{3f}C_{N_2O_4^*}$
R2.4	$NO_2 + Z^-H^+ \leftrightarrow Z^-H^+ - NO_2$	$k_{4f}X_{NO_2}\theta_{vs}C_s$- $k_{4b}\theta_{NO_2-s}C_s$
R2.5	$NO_2 + Z^-H^+ - NO_2 \leftrightarrow Z^-H^+ - (NO_3^-NO^+)$	$k_{5f}X_{NO_2}\theta_{NO_2-s}C_s$- $k_{5b}\theta_{(NO_3^-NO^+)-s}C_s$
R2.6	$NO + NO_2 + 2Z^-H^+ \leftrightarrow Z^-NO^+ + Z^-H^+ - HNO_2$	$k_{6f}X_{NO}X_{NO_2}\theta_{vs}^2C_s^2$- $k_{6b}\theta_{NO^+S^-}\theta_{HNO_2-s}C_s^2$
R2.7	$2NO_2 + 2Z^-H^+ \leftrightarrow Z^-NO^+ + Z^-H^+ - HNO_3$	$k_{7f}X_{NO_2}^2\theta_{vs}^2C_s^2$- $k_{7b}\theta_{NO^+S^-}\theta_{HNO_3-s}C_s^2$
R2.8	$Z^-NO^+ + O_2 \leftrightarrow Z^-NO_3^+$	$k_{8f}\theta_{NO^+s^-}X_{O_2}C_s$- $k_{8b}\theta_{NO_3^+s^-}C_s$
R2.9	$NO + Z^-NO_3^+ \leftrightarrow Z^-NO_2^+ + NO_2$	$k_{9f}X_{NO}\theta_{NO_3^+s^-}C_s$- $k_{9b}\theta_{NO_2^+s^-}X_{NO_2}C_s$
R2.10	$2Z^-H^+ - HNO_3 \leftrightarrow 2NO_2 + H_2O + 0.5O_2 + 2Z^-H^+$	$k_{10f}\theta_{HNO_3-s}^2C_s^2$- $k_{10b}X_{NO_2}^2X_{H_2O}X_{O_2}^{0.5}\theta_{vs}^2C_s^2$
R2.11	$Z^-H^+ - HNO_2 + Z^-NO_2^+ \leftrightarrow 2NO_2 + 2Z^-H^+$	$k_{11f}\theta_{HNO_2-s}\theta_{NO_2^+s^-}C_s^2$- $k_{11b}X_{NO_2}^2\theta_{vs}^2C_s^2$
R2.12	$H_2O + Z^-H^+ \leftrightarrow Z^-H^+ - H_2O$	$k_{12f}X_{H_2O}\theta_{vs}C_s$- $k_{12b}\theta_{H_2O-s1}C_s$

According to Artioli et al. [26], siliceous zeolites with non-porous voids of molecular dimensions (less than ~0.6 nm) catalyze NO oxidation by O_2 at near ambient temperatures (263-473K) following a mechanism that is consistent with the homogeneous reaction pathway. The reaction exhibits a negative apparent activation energy and the reaction orders of NO and O_2 are consistent with the formation of ONNO* as intermediate confined in a void, as indicated by *. The heat of reaction for NO oxidation given by half

of $\Delta H^{\circ}_{R2.1+R2.2+R2.3}$ is 57.05 kJ/mol. The value of $\Delta H^{\circ}_{R2.1+R2.2}$, the heat of formation of $N_2O_4^*$, was measured by Artioli et al. [26] to be 35.8 ± 2.1kJ/mole and -41.2 ± 1.4 kJ/mole for on siliceous BEA and CHA samples, respectively. For the current study, we adopted the same chemistry for the H-ZSM-5; i.e., reactions R2.1 (formation of ONNO*) and R2.2 (oxidation of ONNO*). Since the pore size of ZSM-5 lies between that of CHA and BEA, the $\Delta H^{\circ}_{R2.1+R2.2}$values for BEA and CHA were taken as the lower and upper bounds for the $\Delta H^{\circ}_{R2.1+R2.2}$for H-ZSM-5. The value of $\Delta H^{\circ}_{R2.3}$ was calculated from the values of $\Delta H^{\circ}_{R2.1+R2.2+R2.3}$ and $\Delta H^{\circ}_{R2.1+R2.2}$.

DRIFTS measurements provide evidence for selected surface species. NO_2 that is formed from NO oxidation interacts with the BAS, denoted here by Z^-H^+. BAS are known to adsorb NO and NO_2 in the absence of water [15,25,26,49]. Descorme et al. [15] used IR to study the interaction of NO_2 on H-ZSM-5 and reported the 2136 cm^{-1} band to be associated with the weak interaction of NO_2 with BAS. A second peak at 1643cm^{-1} is associated with strongly adsorbed nitrate (NO_3^-) species. Our DRIFTS data corroborate these findings (Figure 2.3).

Reactions steps R2.4 and R2.5 were added to the scheme; they respectively represent NO_2 adsorption on Z^-H^+ and NO_2 coupling to form an adsorbed $NO_3^-NO^+$ complex [50]. The low temperature NO_2 TPD peak in ~120-160ºC range is associated with adsorbed NO_2 formed by hydrogen bonding between NO_2 and BAS, described by reaction R2.4. Differences in the binding strength of the two species lead to the two independent NO_2 peaks during the TPD. The NO_2 peak at ~150°C (Figure 2.5(a)) is associated with NO_2 bound to the BAS, while the peak at ~370°C is associated with nitrate species [15,49].

Loiland et al. [27] measured NO oxidation rates as a function of temperature from 298 to 623 K over H-, Na-, and siliceous CHA materials. The materials exhibit two reaction regimes as a function of temperature. Below a temperature of ~423 K, the NO oxidation occurs by confinement mechanism and has a negative activation energy [26]. For temperatures above ~423 K the NO oxidation rate over H-SSZ-13 and Na-SSZ-13 increases with increasing temperature, signifying a different pathway. The investigators proposed that adsorbed NO^+ plays a direct role in high temperature NO oxidation. To this end, reactions R2.6 and R2.7 are two independent paths to Z^-NO^+; R2.6 involves the coupling of NO and NO_2 on two acid sites, forming HNO_2 adsorbed on a BAS, while R2.7 involves the coupling of two NO_2 on two acid sites, forming adsorbed HNO_3. The coupled desorption of NO and NO_2 at ~150°C is attributed to the reverse of reactions R2.6 and R2.4. Loiland et al. [27] proposed an endothermic pathway that involves the formation of a $Z^-NO_3^+$ intermediate. Reaction R2.8 describes the nitrate formation while R2.9 describes its reduction by NO, producing NO_2. Hadjiivanov et al. [25] investigated the co-adsorption of NO+O_2 on H-ZSM-5 and reported the existence of Z^-NO^+ species. The NO_2 appearing in the 355-455ºC range may also be considered to be the product of HNO_3 and HNO_2 decomposition, reactions R2.10 and R2.11.

Selected heats of reaction in the 11-step scheme were estimated from previous works. The lower and upper bounds for ΔH°_{R1+R2} for H-ZSM-5 are taken from Artioli et al. [26]. Steps R2.4, R2.5, R2.6, and R2.7 which involving NO and NO_2 adsorption are assumed non-activated. The activation energy for the reverse of reaction R2.4 was taken from Olsson et al. [54]. Finally, the activation energies for reactions R2.8 and R2.9 were taken from Loiland et al. [27].

In minimizing the objective function for 3420 data points for the NO uptake (at 80°C) and TPD data estimates were obtained for 30 unknown kinetic parameters. Table 2.5 provides those values along with the pre-assigned values which are denoted by an asterisk (*).

Table 2.5 Kinetic Parameters for H-ZSM-5 model

Reaction no.	Pre-exponential factor		Activation Energy (kJ mol^{-1})	
R2.1	A_{1f} A_{1b}	3.034e2 7.11e1	E_{1f} E_{1b}	10 20
R2.2	A_{2f} A_{2b}	1.97e-3 3e13	E_{2f} E_{2b}	10 39.5*
R2.3	A_{2f}	4e-2	E_{3f}	-74.64*
R2.4	A_{4f} A_{4b}	5 2e10	E_{4f} E_{4b}	0 92.8*
R2.5	A_{5f} A_{5b}	18.07 2e11	E_{5f} E_{5b}	0 160
R2.6	A_{6f} A_{6b}	0.284 5.04e18	E_{6f} E_{6b}	0 168.34*
R2.7	A_{7f} A_{7b}	101.3 2e9	E_{7f} E_{7b}	0 170
R2.8	A_{8f} A_{8b}	4e16 8.04e3	E_{8f} E_{8b}	142.8* 47.6*
R2.9	A_{9f} A_{9b}	401.7 5.02e9	E_{9f} E_{9b}	31* 122*
R2.10	A_{10f} A_{10b}	5.04e9 1e2	E_{10f} E_{10b}	160 20
R2.11	A_{11f} A_{11b}	1e14 1e8	E_{11f} E_{11b}	150 100
R2.12	A_{12f} A_{12b}	6e2 2e18	E_{12f} E_{12b}	0 180.7*

Overall the agreement between measurement and prediction is satisfactory (Figure 2.9). In addition to predicting the NO breakthrough and approach to the ~380 ppm asymptotic level, the model predicts the sustained generation of NO_2 during the uptake, reaching a level of ~20 ppm after ~500 s. The model captures the location and magnitude of the NO and NO_2 desorption peaks. NO_2 was also observed for lower uptake temperatures

of 30ºC and 50ºC, which shows low temperature NO oxidation, well predicted by the model. The model predicts most of the NO_x is adsorbed in form of NO_2 and nitrates evidenced by larger TPD peaks for NO_2 than NO.

The H-ZSM-5 (without H_2O) microkinetic scheme was validated for different uptake temperatures (95ºC and 150ºC). Experimental and modeling results of uptake and TPD profiles for uptake experiments at 150ºC are shown in Figure 2.10. It can be seen that uptake at 150ºC results in a single TPD peak of NO_2. The model predicts this feature, which is a result of uptake occurring at a temperature exceeding the desorption temperature of NO from Z^-NO^+ and NO_2 adsorbed on BAS. The results of the 95ºC validation are shown in Figure A. 5.

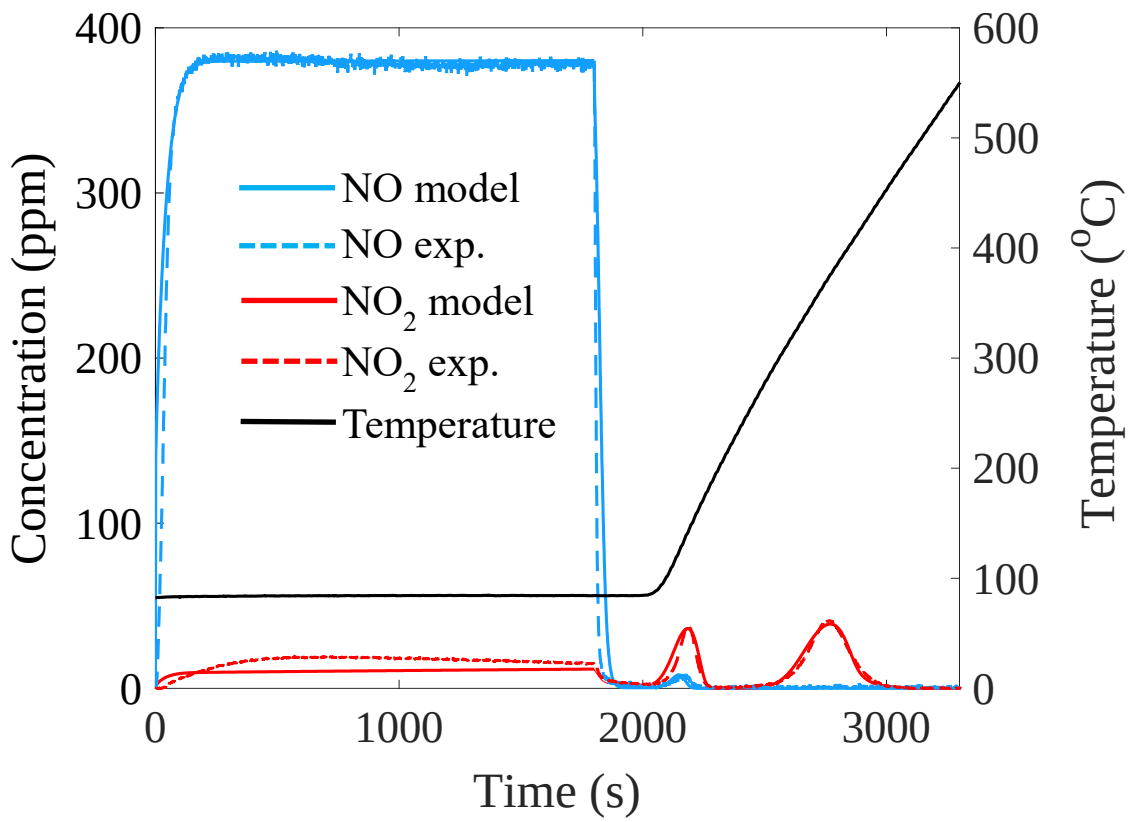

Figure 2.9 Experimental and modeling results of NO_x uptake at 80°C and TPD on H-ZSM-5 for dry feed with a flowrate of 1500 sccm.

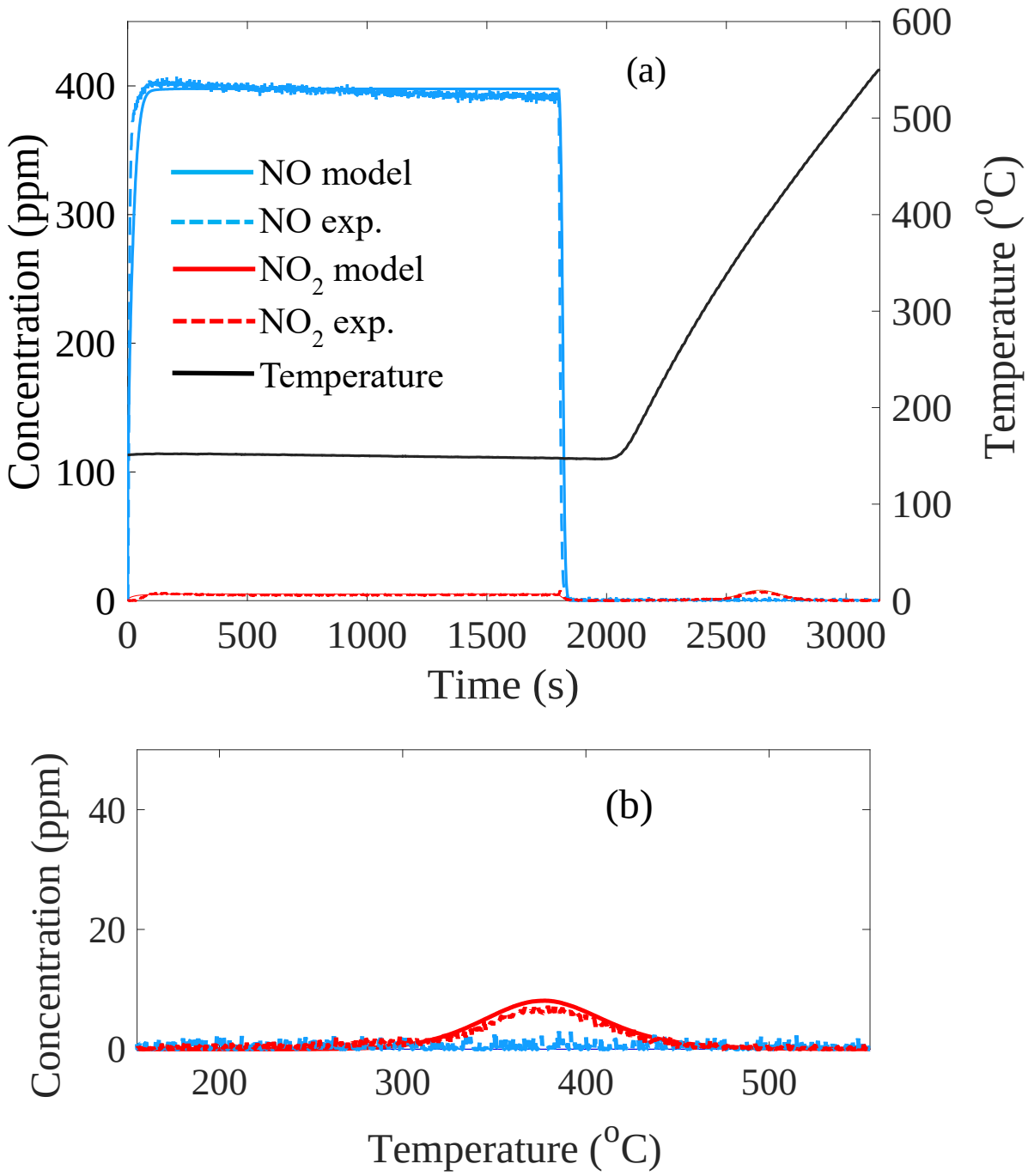

Figure 2.10 (a)Experimental and modeling results of NO_x uptake at 150°C and TPD on H-ZSM-5 for dry feed with a flowrate of 1500 sccm (b) Enlarged view of TPD profile.

As discussed earlier, in the absence of H_2O in the feed, NO_x uptake on H-ZSM-5 decreases with increase in the uptake temperatures which results in decrease in area under

the TPD peaks. Model-predicted NO_x uptake at 80ºC (Figure 2.9) and 95ºC (Figure A. 5) shows the model predicts this feature. Further, it was observed experimentally that with increase in flowrate the NO_x uptake decreases. Model validation was done for a feed flowrate of 2500 sccm. Figure 2.11 shows that the model is able to predict decrease in NO_x uptake with increase in feed flowrate.

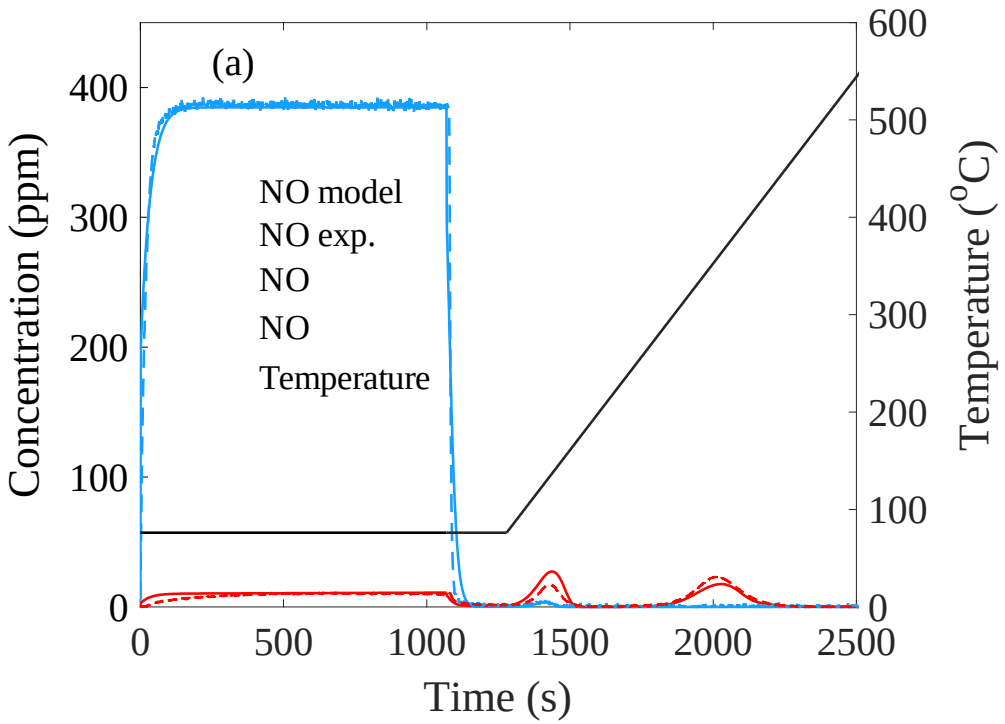

Figure 2.11 Experimental and modeling results of NO_x uptake at 80°C and TPD on H-ZSM-5 for dry feed with a flowrate of 2500 sccm.

As described earlier, when 7% H_2O is added to the feed a negligible amount of NO_x adsorbs on H-ZSM-5. This is a result of the competition for sites between NO_x and H_2O [21]. Reaction step R2.12 (Table 2.4) was added to account for the adsorption of H_2O on the BAS. The forward and reverse activation energies for adsorption and desorption of H_2O on BAS (R2.12) were adopted from Sjövall et al. [55]. In addition, reaction steps R2.1, R2.2 and R2.3 were turned off with H_2O present in the feed. According to Artioli et al.

[26], low temperature NO oxidation takes place by stabilization of the termolecular state by confinement within the voids mediated by van der Waals interactions. In the presence of excess of H_2O, our experimental results show no NO_2 formation, suggesting that the enthalpic confinement does not occur.

The two pre-exponential factors were estimated through a fit of the NO_x uptake and TPD data with 7% H_2O in the feed. Specifically, 2019 data points were used to estimate the 2 unknown parameters. A comparison of the data and model-predictions is shown in the Figure A. 2.

2.2.4 Reaction Mechanism Development and Microkinetic Models for Pd/H-ZSM-5

In this section we develop the part of the microkinetic scheme associated with the Pd cation sites both in the absence and presence of H_2O. The above-described H-ZSM-5 reaction scheme and associated kinetics, with two exceptions, were not adjusted during this next step in the kinetic model development. The one exception is the adjustment in the BAS concentration to account for the presence of the Pd cations that occupy a fraction of the Z^- sites. The procedure for estimating the Brønsted acid and Pd cation site concentrations is described in the Supplemental Material section. The second exception is the enthalpy for NO oxidation in the voids that will be discussed later in this section.

The NO_x uptake and release data provide key features required by any proposed reaction scheme. In particular, there are multiple binding sites, water inhibition, NO_2 generation, among other features. We propose two prospective schemes that can predict these features. Here we introduce them and expand on their features in the next section.

Table 2.6 provides the proposed Scheme I, which comprises a 15-step mechanism for NO uptake on Pd/H-ZSM-5 both in the absence (R2.13 – R2.20) and presence (R2.21

– R2.27) of H_2O in the feed. Scheme I consider $Z^-[PdOH]^+, Z^-Pd^{2+}Z^-$ and Z^-Pd^+ as the active sites for NO_x adsorption together with the available BAS in Pd/H-ZSM-5. Similar to the H-ZSM-5 reaction scheme, justification for each of the steps follows from the NO uptake and release data, DRIFTS data, selected literature, and DFT calculations.

Table 2.7 provides the proposed Scheme II, which comprises a 12-step mechanism for NO uptake on Pd/H-ZSM-5 both in the absence (R2.28 – R2.34) and presence (R2.35 – R2.39) of H_2O in the feed. Scheme II considers $Z^-Pd^{2+}Z^-$ to be the low temperature NO sorption site and Pd nitrate to be associated with the high temperature NO desorption. Key aspects of Scheme II are the reduction of PdO_2 to PdO along with NO_2 generation and the formation of the $Pd(NO_3)_2$.

Each PNA microkinetic scheme requires estimates of the available sites for both the protonated (H-ZSM-5) and Pd cation exchanged (Pd/H-ZSM-5) materials. In this section we describe the parameter estimation approach for Scheme I. A similar approach was taken for Scheme II with details provided in the Supplemental Material section.

NO_x uptake occurs only on the BAS for H-ZSM-5, and on both the BAS and Pd cation sites for Pd/H-ZSM-5. Further, Pd is assumed to be present in the form of multiple types of Pd cations having +2 valence ($Z^-[PdOH]^+, Z^-Pd^{2+}Z^-$) and +1 valence ($Z^-Pd^+$). The three Pd cation types occupy a fraction of the negatively-charged sites (Z^-) of the framework. Finally, Pd may exist in non-exchanged, dispersed PdO_x clusters which in this model we assume do not bind NO or NO_2 [16]. The procedure uses knowledge of the Pd loading, Pd dispersion, Silica to Alumina ratio (Si/Al_2), and certain features of the TPD profile to estimate C_{S1} (H^+Z^-), and the Pd cation site concentrations C_{S2} (Pd^{2+}) and C_{S3} ($[Pd(OH)]^+$).

Table 2.6 Reaction Mechanism for Pd/H-ZSM-5 (Scheme I) [s_1 - $O_z^-H^+$; s_2 - $Z^-Pd^{2+}Z^-$; s_3 - $Z^-[Pd(II)OH]^+$; s_4 - Z^-Pd^+]

Reaction	Reaction step	Rate expression (R_f - R_b)
R2.13	$NO + Z^-Pd^{2+}Z^- \leftrightarrow Z^-Pd^{2+}Z^- - NO$	$k_{13f}X_{NO}\theta_{vs2}C_{s2}$- $k_{13b}\theta_{NO-s2}C_{s2}$
R2.14	$NO + Z^-Pd^{2+}Z^- - NO \leftrightarrow Z^-Pd^{2+}Z^- - (NO)_2$	$k_{14f}X_{NO}\theta_{NO-s2}C_{s2}$- $k_{14b}\theta_{(NO)_2-s2}C_{s2}$
R2.15	$NO + Z^-Pd^{2+}Z^- - (NO)_2 \leftrightarrow Z^-Pd^{2+}Z^- - (NO)_3$	$k_{15f}X_{NO}\theta_{(NO)_2-s2}C_{s2}$- $k_{15b}\theta_{(NO)_3-s2}C_{s2}$
R2.16	$NO_2 + Z^-Pd^{2+}Z^- \leftrightarrow Z^-Pd^{2+}Z^- - NO_2$	$k_{16f}X_{NO_2}\theta_{vs2}C_{s2}$- $k_{16b}\theta_{NO_2-s2}C_{s2}$
R2.17	$NO + Z^-[Pd(II)OH]^+ \leftrightarrow Z^-[Pd(II)OH]^+ - NO$	$k_{17f}X_{NO}\theta_{vs3}C_{s3}$- $k_{17b}\theta_{NO-s3}C_{s3}$
R2.18	$NO + 2Z^-[Pd(II)OH]^+ \leftrightarrow 2Z^-Pd^+ + NO_2 + H_2O$	$k_{18f}X_{NO}\theta_{vs3}^2C_{s3}^2$- $k_{18b}\theta_{s4}^2X_{NO_2}X_{H_2O}C_{s3}^2$
R2.19	$NO + Z^-Pd^+ \leftrightarrow Z^-Pd^+ - NO$	$k_{19f}X_{NO}\theta_{s4}C_{s3}$- $k_{19b}\theta_{NO-s4}C_{s3}$
R2.20	$2Z^-Pd^+ + Z^-H^+ - H_2O + 0.5O_2 \leftrightarrow 2Z^-[Pd(II)OH]^+ + Z^-H^+$	$k_{20f}\theta_{s4}^2\theta_{H_2O-s1}X_{O_2}^{0.5}C_{s1}C_{s3}^2$- $k_{20b}\theta_{vs1}\theta_{vs3}^2C_{s1}C_{s3}^2$
R2.21	$H_2O + Z^-Pd^{2+}Z^- \leftrightarrow Z^-Pd^{2+}Z^- - H_2O$	$k_{21f}X_{H_2O}\theta_{vs2}C_{s2}$- $k_{21b}\theta_{H_2O-s2}C_{s2}$
R2.22	$H_2O + Z^-[Pd(II)OH]^+ \leftrightarrow Z^-[Pd(II)OH]^+ - H_2O$	$k_{22f}X_{H_2O}\theta_{vs3}C_{s3}$- $k_{22b}\theta_{H_2O-s3}C_{s3}$
R2.23	$H_2O + Z^-Pd^+ \leftrightarrow Z^-Pd^+ - H_2O$	$k_{23f}X_{H_2O}\theta_{s4}C_{s3}$- $k_{23b}\theta_{H_2O-s4}C_{s3}$
R2.24	$NO + Z^-Pd^{2+}Z^- - H_2O \leftrightarrow Z^-Pd^{2+}Z^- - (H_2O)(NO)$	$k_{24f}X_{NO}\theta_{H_2O-s2}C_{s2}$- $k_{24b}\theta_{(H_2O)(NO)-s2}C_{s2}$
R2.25	$NO + Z^-[Pd(II)OH]^+ - H_2O \leftrightarrow [Pd(II)OH]^+ - (H_2O)(NO)$	$k_{25f}X_{NO}\theta_{H_2O-s3}C_{s3}$- $k_{25b}\theta_{(H_2O)(NO)-s3}C_{s3}$
R2.26	$NO + Z^-Pd^+ - H_2O \leftrightarrow Z^-Pd^+ - (H_2O)(NO)$	$k_{26f}X_{NO}\theta_{H_2O-s4}C_{s3}$- $k_{26b}\theta_{(H_2O)(NO)-s4}C_{s3}$
R2.27	$NO_2 + Z^-Pd^{2+}Z^- - H_2O \leftrightarrow Z^-Pd^{2+}Z^- - (H_2O)(NO_2)$	$k_{27f}X_{NO_2}\theta_{H_2O-s2}C_{s2}$- $k_{27b}\theta_{(H_2O)(NO_2)-s2}C_{s2}$

Table 2.7 Reaction Mechanism for Pd/H-ZSM-5 (Scheme II) [$Z^{-}Pd^{2+}Z^{-}$; s_5 - PdO_2; s_6 – PdO]

Reaction	Reaction step	Rate expression (R_f - R_b)
R2.28	$NO + Z^{-}Pd^{2+}Z^{-} \leftrightarrow Z^{-}Pd^{2+}Z^{-} - NO$	$k_{28f}X_{NO}\theta_{vs2}C_{s2}$- $k_{28b}\theta_{NO-s2}C_{s2}$
R2.29	$NO + Z^{-}Pd^{2+}Z^{-} - NO \leftrightarrow Z^{-}Pd^{2+}Z^{-} - (NO)_2$	$k_{29f}X_{NO}\theta_{NO-s2}C_{s2}$- $k_{29b}\theta_{(NO)_2-s2}C_{s2}$
R2.30	$NO + Z^{-}Pd^{2+}Z^{-} - (NO)_2 \leftrightarrow Z^{-}Pd^{2+}Z^{-} - (NO)_3$	$k_{30f}X_{NO}\theta_{(NO)_2-s2}C_{s2}$- $k_{30b}\theta_{(NO)_3-s2}C_{s2}$
R2.31	$NO_2 + Z^{-}Pd^{2+}Z^{-} \leftrightarrow Z^{-}Pd^{2+}Z^{-} - NO_2$	$k_{31f}X_{NO_2}\theta_{vs2}C_{s2}$- $k_{31b}\theta_{NO_2-s2}C_{s2}$
R2.32	$NO + PdO_2 \leftrightarrow PdO + NO_2$	$k_{32f}X_{NO}\theta_{vs5}C_{s5}$- $k_{32b}X_{NO_2}\theta_{vs6}C_{s5}$
R2.33	$2NO + 1.5O_2 + PdO \leftrightarrow Pd(NO_3)_2$	$k_{33f}X_{NO}^2X_{O_2}^{1.5}\theta_{vs6}C_{s5}$- $k_{33b}\theta_{Pd(NO_3)_2}C_{s5}$
R2.34	$2PdO + O_2 \leftrightarrow 2PdO_2$	$k_{34f}X_{O_2}\theta_{vs6}^2C_{s5}^2$- $k_{34b}\theta_{vs5}^2C_{s5}^2$
R2.35	$H_2O + Z^{-}Pd^{2+}Z^{-} \leftrightarrow Z^{-}Pd^{2+}Z^{-} - H_2O$	$k_{35f}X_{H_2O}\theta_{vs2}C_{s2}$- $k_{35b}\theta_{H_2O-s2}C_{s2}$
R2.36	$NO + Z^{-}Pd^{2+}Z^{-} - H_2O \leftrightarrow Z^{-}Pd^{2+}Z^{-} - (H_2O)(NO)$	$k_{36f}X_{NO}\theta_{H_2O-s2}C_{s2}$- $k_{36b}\theta_{(H_2O)(NO)-s2}C_{s2}$
R2.37	$NO_2 + Z^{-}Pd^{2+}Z^{-} - H_2O \leftrightarrow Z^{-}Pd^{2+}Z^{-} - (H_2O)(NO_2)$	$k_{37f}X_{NO_2}\theta_{H_2O-s2}C_{s2}$- $k_{37b}\theta_{(H_2O)(NO_2)-s2}C_{s2}$
R2.38	$H_2O + PdO_2 \leftrightarrow PdO_2 - H_2O$	$k_{38f}X_{H_2O}\theta_{vs5}C_{s5}$- $k_{38b}\theta_{H_2O-s5}C_{s5}$
R2.39	$H_2O + PdO \leftrightarrow Pd(OH)_2$	$k_{39f}X_{H_2O}\theta_{s6}C_{s5}$- $k_{39b}\theta_{H_2O-s6}C_{s5}$

Reaction steps are first described for NO_x uptake on Pd/H-ZSM-5 in the absence of H_2O in the feed. From NO uptake on the Pd(1%)/H-ZSM-5 sample, two TPD peaks for NO and NO_2 are evident in Figure 2.5(b). A comparison of the NO TPD profiles for Pd(1%)/H-ZSM-5 and H-ZSM-5, shown in Figure 2.12, indicates a higher uptake for the former than the latter. The increase in area under the two NO TPD peaks, denoted by $\Delta A_1$and ΔA_2, are associated with an incremental increase in NO uptake on Pd^{2+} +

$[Pd(OH)]^+$, and Pd^{1+} sites, respectively. The areas are used to estimate the site concentrations. The reader is referred to the Supplemental Material for details.

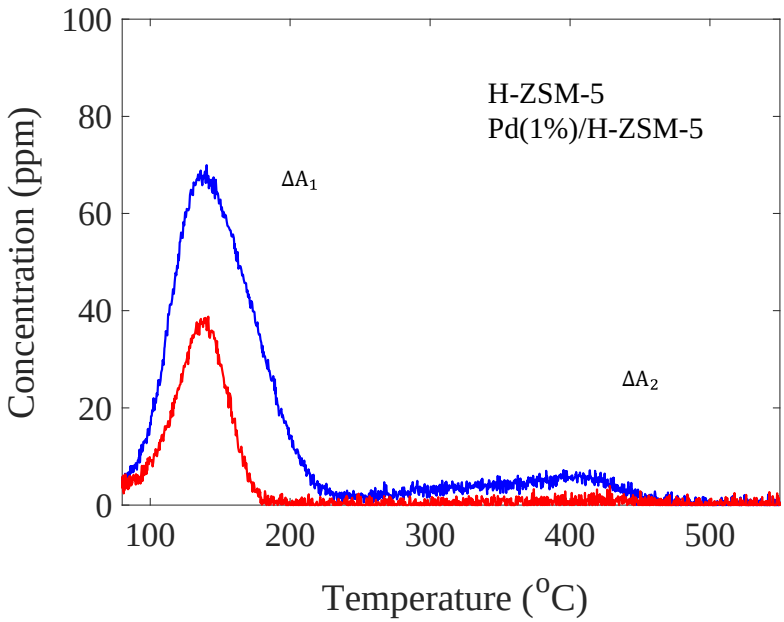

Figure 2.12 Comparison of TPD profiles for NO uptake on Pd(1%)/H-ZSM-5 (blue) and H-ZSM-5 (red) at uptake at temperature of 80°C for dry feed.

Reaction steps R2.13, R2.14, and R2.15 involve the reversible uptake of NO on isolated Pd^{2+} sites in the absence of H_2O. DFT calculations show that multiple NO molecules may be adsorbed by Pd^{2+} [30-53]. The DFT-calculated binding energies for NO_x on Pd/H-BEA and Pd/H-SSZ-13 are shown in Table 2.8 along with estimates used in the current model for the Pd/H-ZSM-5. DFT calculations of Mei et al. [53] show that the NO binding energies changes from -256 to -120 to -70 kJ/mole for one, two and three NO molecules bound to Pd^{2+}. Reaction step R2.16 involves the uptake of NO_2 on Pd^{2+}. DFT calculations also show that NO binds to $Z^-[PdOH]^+$ (R2.17). The addition of steps R2.13 through R2.17 accounts for the NO and NO_2 desorption peaks encountered at lower temperature (< 150°C) as shown in Figure 2.5(b). Their location is a result of their lower

binding energy values on Pd^{2+} sites compared to reduced Pd^{+}. We expand on this point next.

Table 2.8 Kinetic Parameters for Pd/H-ZSM-5 model- Scheme I

Reaction no.	**Pre-exponential factor**		**Activation Energy (10^3*kJ mol^{-1})**		**Binding Energy of species at corresponding site (kJ mol^{-1})**	
					BEA – Mei et al.	**SSZ-13**
R2.2	A_{2f} A_{2b}	1.97e-3 3e13	E_{2f} E_{2b}	6.6 39.5	-	-
R2.3	A_{3f}	4e-2	E_{3f}	-71.24	-	-
R2.13	A_{13f} A_{13b}	8.2e2 1.8e20	E_{13f} E_{13b}	0 160	*-256*	**-120**
R2.14	A_{14f} A_{14b}	1.8e3 2e13	E_{14f} E_{14b}	0 115	*-120*	-
R2.15	A_{15f} A_{15b}	3.23e1 6e6	E_{15f} E_{15b}	0 68	*-70*	-
R2.16	A_{16f} A_{16b}	1e2 1.43e11	E_{16f} E_{16b}	0 140	*-151*	-
R2.17	A_{17f} A_{17b}	1.77e4 3.42e17	E_{17f} E_{17b}	0 136.5	*-164*	-
R2.18	A_{18f} A_{18b}	5.9e14 1.96e5	E_{18f} E_{18b}	95 10	*-39*	**120**
R2.19	A_{19f} A_{19b}	3.42e3 2.73e18	E_{19f} E_{19b}	0 245	*-250*	**-240**
R2.20	A_{20f} A_{20b}	0.46e1 8.17e9	E_{20f} E_{20b}	0 120	-	-
R2.21	A_{21f} A_{21b}	2.8e1 1e14	E_{21f} E_{21b}	0 118	*-120*	-
R2.22	A_{22f} A_{22b}	4.43e2 3.1e15	E_{22f} E_{22b}	0 120	*-122*	-
R2.23	A_{23f} A_{23b}	3e6 3e13	E_{23f} E_{23b}	30 170	-	-
R2.24	A_{24f} A_{24b}	2.2e3 2.25e15	E_{24f} E_{24b}	20 140	-	-
R2.25	A_{25f} A_{25b}	3.43e1 1.15e9	E_{25f} E_{25b}	0 80	-	-
R2.26	A_{26f} A_{26b}	1e6 8e14	E_{26f} E_{26b}	10 184	-	**-205**
R27	$A_{2.27f}$ $A2._{27b}$	1e2 2e11	E_{27f} E_{27b}	0 100	-	-

Reaction steps R2.18 to R2.27 are added to the reaction Scheme to account for involvement of H_2O. Following Descorme et al. [15], step R2.18 is the reduction of two $[PdOH]^+$ to two Pd^+ with the generation of NO_2 and H_2O. Ambast et al. [30] provides a detailed DFT analysis of the sequence of steps and sites involved in this reduction. The sequence involves two $[PdOH]^+$ complexes located in the same zeolite cage. Step R2.19 is the uptake of NO onto the reduced Z^-Pd^+ site, giving the mononitrosyl species Z^-Pd^+-NO. R2.20 is a combined step that involves re-oxidation of Pd^+ by O_2 in the presence of H_2O back to $[PdOH]^+$. Okumura et al. [18] used EXAFS and XANES to study NO_x uptake on Pd/ZSM-5 and reported the reduction of Pd^{2+} to Pd^{+1} upon NO adsorption. R2.21 is the uptake of H_2O on isolated Pd^{2+} cations while steps R2.22 and R2.23 involve H_2O adsorption on $[PdOH]^+$ and Pd^+. Collectively, steps R2.20 – R2.22 involve the competitive adsorption of H_2O on sites that can bind both NO and NO_2. DFT studies show that NO_x may adsorb on Pd sites already occupied by H_2O [30-53]. Consistent with this fact, steps R2.24 and R2.27 respectively account for NO and NO_2 adsorption on $Z^-Pd^{2+}Z^- - H_2O$. R2.25 and R2.26 are similar steps for NO adsorbed on $Z^-[PdOH]^+ - H_2O$ and $Z^-Pd^+ - H_2O$ respectively.

Each of the dispersed Pd cation types can adsorb NO at low temperature based on experimental measurements and DFT calculations [30-53]. As seen in Figure 2.5(b), the TPD profile has two peaks for both NO and NO_2; these occur at ~155°C and ~320°C. Consistent with estimated binding energies, the peak below 200°C is associated with NO bound to $[PdOH]^+$and $Z^-Pd^{2+}Z^-$ while the peak above 250°C is associated NO bound to Z^-Pd^+. DFT estimates by Rahman et al. [30] show that the NO binding energies are of comparable magnitude on $Z^-[PdOH]^+$and $Z^-Pd^{2+}Z^-$ ($\leq$160 kJ/mol), whereas the binding

energy of NO on $Z^{-}Pd^{+}$is in the range of ~250 kJ/mol. Vu et al. [22] also reported that Pd^{2+} is associated with the low temperature NO_x TPD peak whereas Pd^{+} is associated with high temperature NO_x TPD peak.

It is possible that the reduction of $Z^{-}[PdOH]^{+}$to $Z^{-}Pd^{+}$ by NO occurs at temperatures at or below 150ºC [30]. The uptake of NO on $Z^{-}[PdOH]^{+}$ generates NO_2 and H_2O and reduces Pd^{2+} to Pd^{+} in the process (reaction R2.18 in Table 2.6). Evidence for the reduction is the immediate production of NO_2 (~110 ppm) during NO uptake at ~150°C with H_2O in the feed. It is noted that in the presence of H_2O, Brønsted acid sites do not contribute to NO_2 formation nor do they sorb NO_x. Thus, the observed formation of NO_2 may be the result of $Z^{-}[PdOH]^{+}$reduction to $Z^{-}Pd^{+}$. At lower uptake temperatures, the generation of NO_2 occurs during the temperature ramp and in the range of 100-150ºC. Its release indicates either that (i) the Pd reduction occurs at that temperature, or (ii) the reduction occurs at a lower temperature and the NO_2 released during the temperature ramp represented NO_2 that has accumulated on Pd cations during reduction.

The NO uptake at 80ºC and corresponding NO and NO_2 TPD data on Pd(1%)/H-ZSM-5 in the absence of H_2O in the feed (shown in the Figure A. 6) was used as a reference data set to estimate kinetic parameters for the Pd/H-ZSM-5 reaction subset (R2.13-R2.20). The experiment involved exposure to NO_2(~5ppm)/ NO (400ppm)/ O_2 (2%)/ balance Ar at 80ºC for a duration of 5 minutes, followed by exposure to O_2 (2%)/ balance Ar, under a temperature ramp from 80ºC to 550ºC at a ramp rate of 22°C /min.

All kinetic parameters connected with NO_x uptake on H-ZSM-5, except for reaction R2.2 and R2.3, were kept constant in the model tuning for Pd/H-ZSM-5; i.e. reactions R2.1, R2.4-R2.12. Several parameters were assigned values as follows. A minor adjustment in

the ΔH for R2.2 was made, i.e., 2 kJ/mole. ΔH for R2.3 was then adjusted to maintain the thermodynamic consistency; i.e., keep overall ΔH of NO oxidation to be -57.05 kJ/mol. As discussed earlier, low temperature NO oxidation has been attributed to a confinement effect in the zeolite micropores [26]. With the addition of Pd cations into these pores, confinement may increase, resulting in a higher rate of NO oxidation. This is observed by the increase in amount of NO_2 that is generated during the uptake on Pd/H-ZSM-5 (Figure A. 6) compared to H-ZSM-5 (Figure 2.9). The activation energies for adsorption of NO_x species on all Pd sites in reactions R2.13-R2.17 and R2.19 are assumed to be 0 kJ/mole. The values of ΔH (E_f- E_b) for reactions R2.13, R2.18 and R2.19 are available for Pd/BEA and Pd/SSZ-13 from the DFT calculations [30-53]. The assumed ΔH values for reactions R2.13, R2.18 and R2.19 on Pd/ZSM-5 were within the range of the Pd/BEA and Pd/SSZ-13 calculated values. The binding energies for two, and three moles of NO (R2.14 and R2.15) on $Z^{-}Pd^{2+}Z^{-}$ are available for $Z^{-}Pd^{2+}Z^{-}$on BEA but not for $Z^{-}Pd^{2+}Z^{-}$on SSZ-13. With the NO binding energy on $Z^{-}Pd^{2+}Z^{-}$for BEA and SSZ-13 calculated to be -256 and -120 kJ/mole respectively, we have used an estimate for $Z^{-}Pd^{2+}Z^{-}$ on ZSM-5 bounded by these values [30-53]. Thus, it was assumed that the binding energy of one mole of NO on $Z^{-}Pd^{2+}Z^{-}$on ZSM-5 (R2.13) is lower than that of one mole of NO on $Z^{-}Pd^{2+}Z^{-}$on BEA. Following a similar approach, the binding energies for two and three moles of NO on $Z^{-}Pd^{2+}Z^{-}$on ZSM-5 were taken to be slightly lower than that of available DFT-calculated binding energies for $Z^{-}Pd^{2+}Z^{-}$on BEA. A similar process was used to calculate the reverse activation energies of R2.16 and R2.17.

Estimates for the remaining kinetic parameter values are provided in Table 2.8. The values of 16 pre-exponential factors and two activation energies (E_{18b}, E_{20b})

were estimated based on a fit of the NO uptake at 80°C and TPD (Figure A. 6) as reference data. The number of data points used was 2786 to estimate the 18 parameters.

The measured and predicted profiles of NO uptake at 80°C and TPD are shown in Figure A. 6. The model accurately predicts the breakthrough time of ~25 seconds as well as the two TPD peaks of NO and NO_2. The model predicts a somewhat higher temperature for the second NO_2 TPD peak (~380°C) than the measured value (~ 320°C). In the model, this NO_2 TPD peak is associated with nitrate species adsorbed on Brønsted acid sites. Two observations are worth noting. First, the high temperature NO_2 TPD peak for H-ZSM-5 lies in the range ~380°C (Figure 2.9). Since all the kinetic parameters related to H-ZSM-5 reactions were kept constant in the fit of the Pd/H-ZSM-5 data, the model not surprisingly predicts the 2nd TPD peak of NO_2 in a similar temperature range as that of H-ZSM-5. Second, and notwithstanding the first observation, the absence of the high temperature NO_2 TPD peak in the presence of H_2O (Figure 2.13) suggests that its prediction is not important for the practically important case of NO_x uptake on Pd/H-ZSM-5 in the presence of H_2O.

The model predicts the increase in area under the TPD peaks for Pd(1%)/H-ZSM-5 (Figure A. 6) as compared to H-ZSM-5 (Figure 2.9), showing higher NO_x uptake. It was observed experimentally that with an increase in flowrate the NO_x uptake decreases. Model validation was done at the total feed flowrate of 2500 sccm. The experimental and modeling results of which are shown in Figure A. 7. It can be seen the model is able to predict the uptake curve as well as the breakthrough time of ~ 8 seconds.

Water is always present in engine exhaust, thus the model with H_2O contained in the feed is of most interest. Hence, the next step was to add reaction steps associated with water to the reaction Scheme I (R2.21-R2.27). As before, activation energies for adsorption

of H_2O and NO_x species on Pd cation sites (forward reactions of reactions R2.21, R2.22, R2.25, R2.27) are taken to be 0 kJ/mole. Values are available for ΔH for R2.21 and R2.22 for Pd-BEA [53] and R2.26 for Pd-SSZ-13 [30]. These values were taken as the initial guess values of the ΔH values for R2.21, R2.22 and R2.26, respectively, while estimating the values of pre-exponential factors and the remaining seven activation energies ($E_{23f}, E_{23b}, E_{24f}, E_{24b}, E_{25b}, E_{26f}, E_{27b}$) using the same approach as before; i.e., by fitting the Pd/H-ZSM-5 model to NO uptake at 80°C and TPD data as a reference data set with water in the feed (Figure 2.13). The data comprised 1946 data points to estimate 21 unknown parameters.

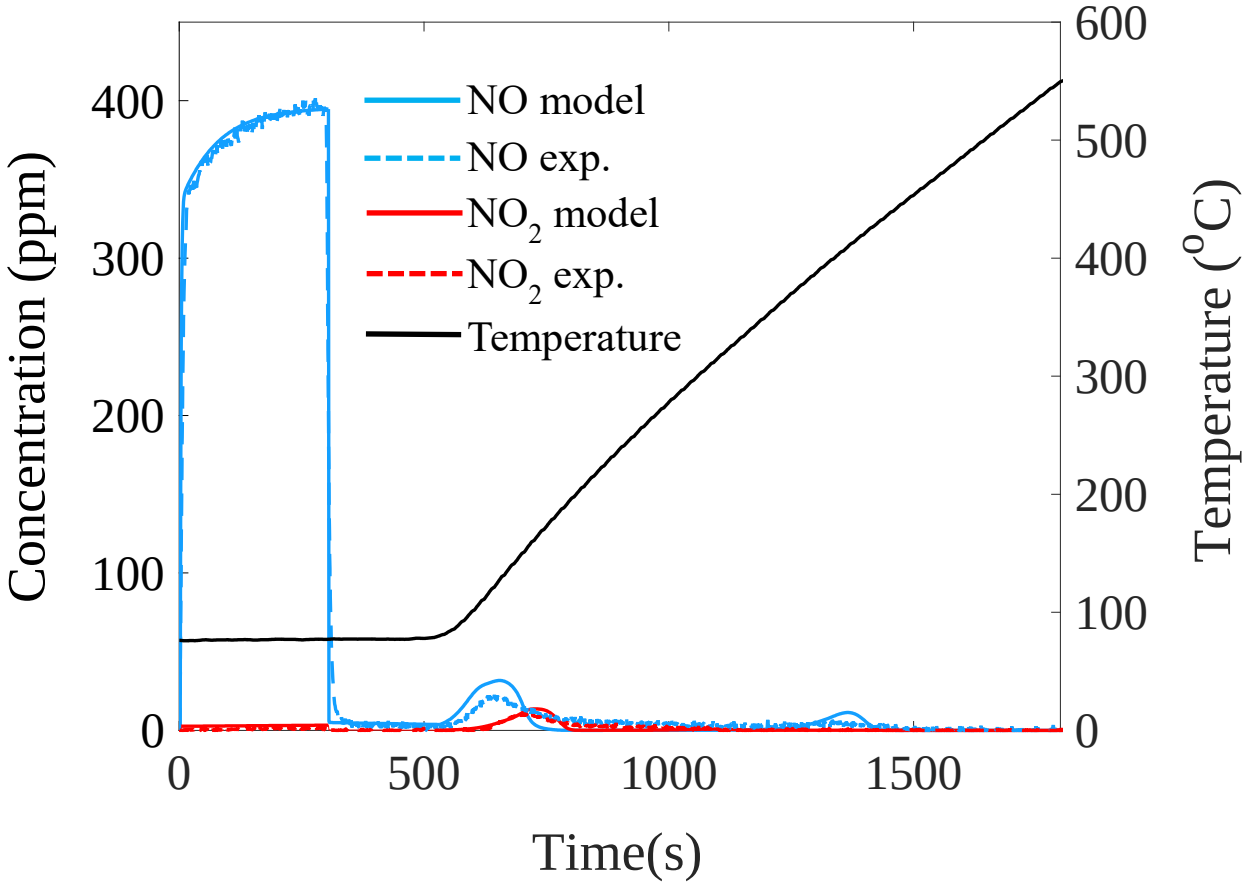

Figure 2.13 Experimental and modeling results of NO_x uptake at 80°C and TPD on Pd(1%)/H-ZSM-5 for wet-feed (7% H_2O) and feed flowrate of 1500 sccm.

The tuned model predicts the NO uptake along with the TPD data well (Figure 2.13), such as two TPD peaks for NO and one low temperature TPD peak of NO_2. The model reproduces the disappearance of the NO_2 TPD peak present for H-ZSM-5 as a result of the inhibition by water of nitrate formation on the acid sites. Similarly, the model correctly captures the significant reduction in the NO_x uptake on Pd/H-ZSM-5 as a results of water inhibition on both protonated and Pd cationic sites.

A more detailed examination is afforded with the model-predicted adsorbed species coverages spanning the uptake and desorption (Figure 2.14). Figure 2.14(a) shows the species coverages on $Z^{-}Pd^{2+}Z^{-}$. As uptake commences, most of the sites are occupied with H_2O as a result of the high feed concentration of H_2O (7%) compared to that of NO (400 ppm). During uptake the coverages of NO and NO_2 ($\theta_{(H_2O)(NO)-s2}$ and $\theta_{(H_2O)(NO_2)-s2}$) linearly increase at the expense of a linear decrease in the water coverage (θ_{H_2O-s2}). This continues until the stoppage in the NO feed at the 300 s point, as indicated by the dashed vertical line in Figure 2.14. During the constant temperature period of 5 minutes duration the species coverages remain constant. Shortly after, when temperature increases to ~150°C the NO and NO_2 adsorbed on the Pd^{2+} begin to desorb.

Most of the NO and NO_2 desorb before 200°C. Figure 2.14(b) shows the corresponding species coverages on $Z^{-}[PdOH]^{+}$. During the start of uptake, most of these sites are also occupied by H_2O ($\theta_{(H_2O)(NO)-s3}$ ~1) which quickly co-uptakes NO ($\theta_{(H_2O)(NO)-s3}$). A small, nonzero fraction of the sites is occupied by NO (θ_{NO-s3}) only. The replacement rate increases up to the 300 s mark when the feed NO is turned off. At that point the absence of NO in the feed leads to NO desorption from the $Z^{-}[PdOH]^{+}$ sites and the re-adsorption of H_2O.

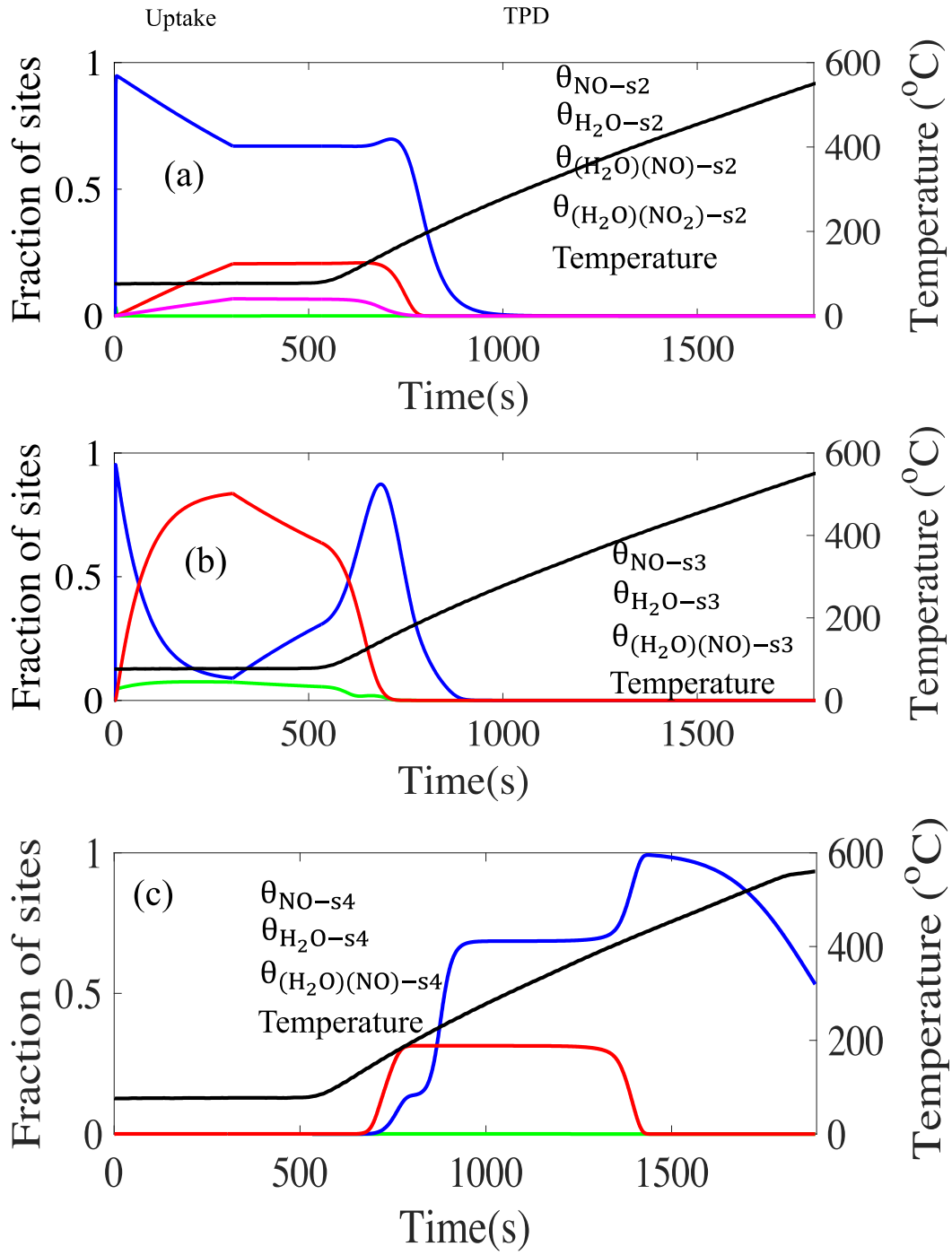

Figure 2.14 Coverage of different species on site (a) $Z^{-}Pd^{2+}Z^{-}$, (b) $Z^{-}[Pd(II)OH]^{+}$, and (c) $Z^{-}Pd^{+}$ during uptake of NO_x at 80°C and TPD for feed flow rate of 1500 sccm in presence of 7% H_2O in the feed.

As the temperature ramp commences most of the adsorbed NO desorbs by 150ºC. During this period the $[PdOH]^+$is reduced to Pd^+. This is evidenced by the increase in the coverages of co-adsorbed NO + H_2O ($\theta_{(H_2O)(NO)-s4}$) and H_2O ($\theta_{(H_2O)-s4}$) on the Pd^+ sites (Figure 2.14(c)). The model predicts that the NO that desorbs from the lower affinity Pd^{2+} and $[PdOH]^+$ sites readsorbs on Pd^+. The coverages of both NO + H_2O and H_2O achieve and sustain constant values over a wide range of temperature. Eventually NO desorbs at ~380ºC from Pd^+. All the NO and most of the H_2O are desorbed by 550ºC. After the catalyst temperature reaches 550ºC the feed of H_2O is stopped with only O_2(2%)/ Ar flowing for a duration of 30 minutes to remove the remaining adsorbed H_2O.

The Pd/H-ZSM-5 model containing Scheme I was validated for different feed flowrates, uptake temperatures, Pd loading, NO concentrations in the feed and TPD ramp rate to examine the predictive effectiveness of the model.

The model was tested for a higher uptake temperature of 150ºC, as shown in Figure 2.15. The model correctly predicts a single TPD peak for NO. In addition, the model correctly predicts the immediate generation and peak magnitude (~110 ppm) of NO_2 during the NO uptake.

The model was then tested for the higher flowrate experiment (2500 sccm). Figure 2.16 compares the measured and predicted NO and NO_2 uptake and desorption profiles. The model captures the uptake and release satisfactorily. For example, the lower desorption concentrations of NO and NO_2 that are encountered with the shorter contact time are predicted.

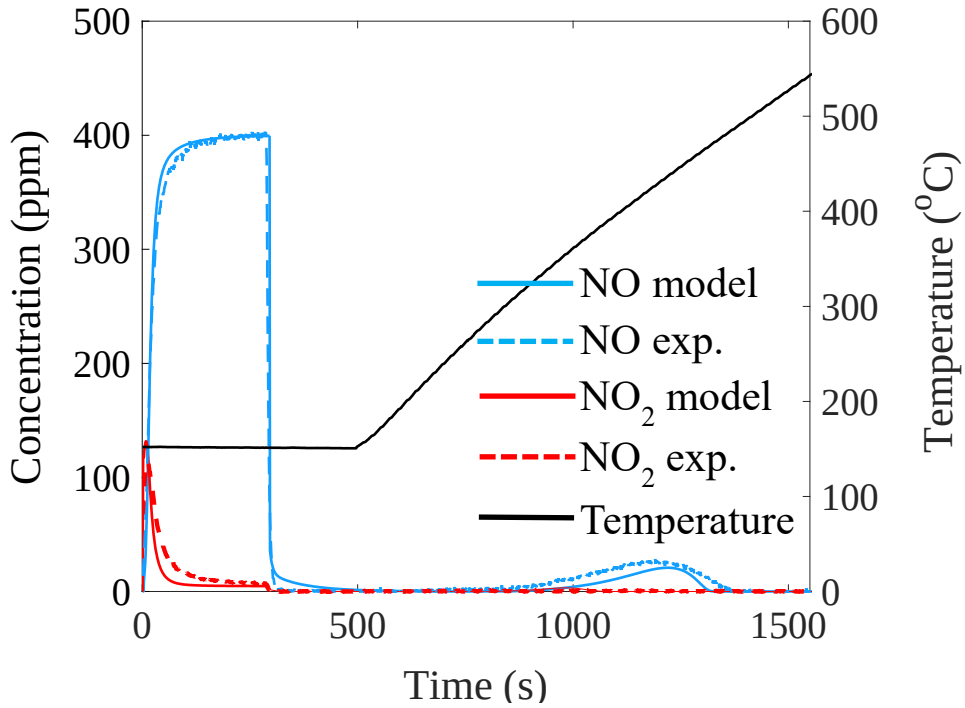

Figure 2.15 Experimental and modeling results of NO_x uptake at 150°C and TPD on Pd(1%)/H-ZSM-5 for wet-feed (7% H_2O) and feed flowrate of 1500sccm.

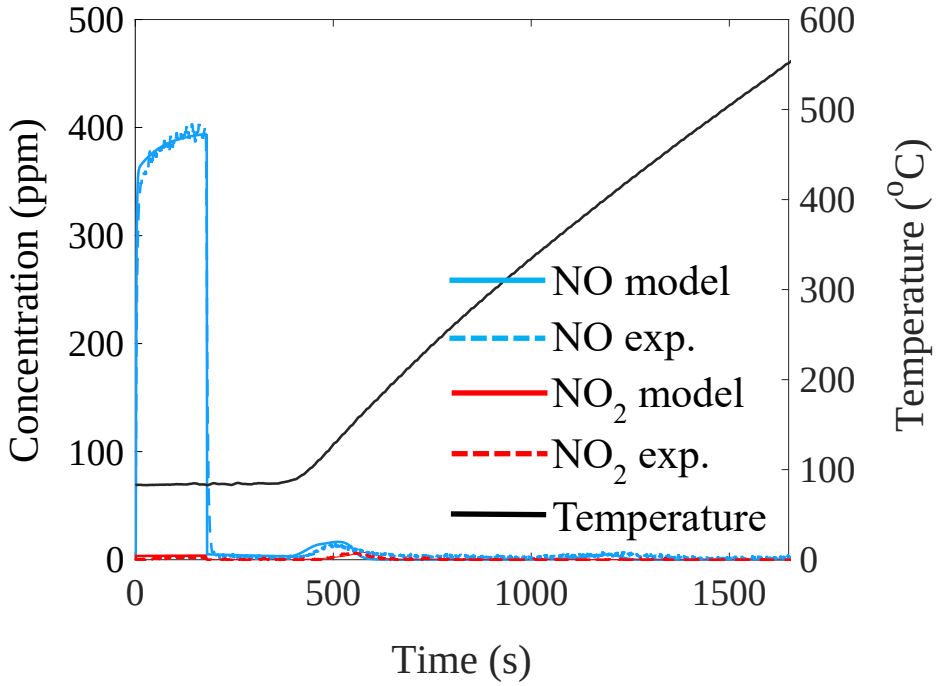

Figure 2.16 Experimental and modeling results of NO_x uptake at 80°C and TPD on Pd(1%)/H-ZSM-5 for wet-feed (7% H_2O) and feed flowrate of 2500sccm.

A third validation was carried out for the higher loading catalyst, Pd(2%)/H-ZSM-5. Figure 2.17 shows the prediction of the NO and NO_2 profiles. It is noted that chemisorption was conducted for the higher Pd loading catalyst having a fractional dispersion of 0.22, compared to 0.41 for Pd(1%)/H-ZSM-5. The model correctly predicts the minor increase in the NO_x uptake on Pd(2%)/H-ZSM-5. This is attributed to the minor increase in the dispersed Pd; i.e. ~84 mole-sites/m^3 of washcoat for Pd(2%)/H-ZSM-5 compared to ~78 mole-sites/m^3 of washcoat for Pd(1%)/H-ZSM-5.

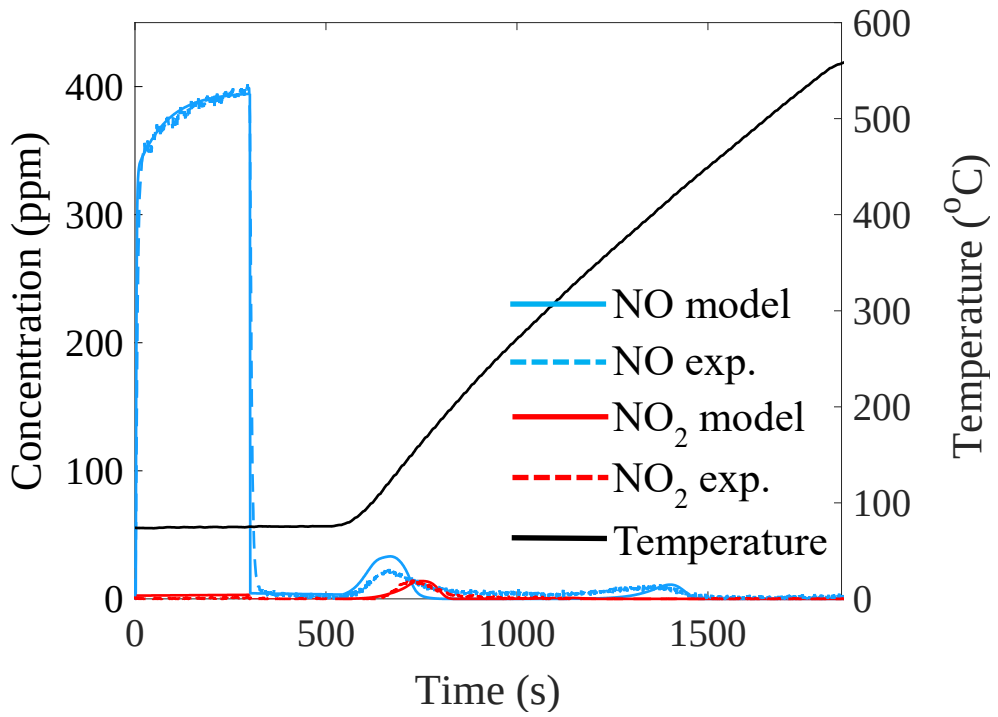

Figure 2.17 Experimental and modeling results of NO_x uptake at 80°C and TPD on Pd(2%)/H-ZSM-5 for wet-feed (7% H_2O) and feed flowrate of 1500.

The model was further validated at a different NO feed concentration during the uptake keeping all other parameters fixed. In this experiment the feed contained 350 ppm NO compared to 400 ppm in other experiments. The remaining feed components included 2% O_2 and 7% H_2O in a balance of Ar. The uptake was done at 80℃ for 5 minutes with

the subsequent TPD carried out a 22°C/min under a flow of 2% O_2/ 7%H_2O/ balance Ar. The experimental and modeling results are shown in Figure A. 8. The model is able to predict the uptake curve and the TPD peaks for NO_x for the changed NO concentration in the feed during uptake. The model was also validated at a lower TPD ramp rate of 18°C/min keeping all other variables constant. The experimental and modeling results are shown in Figure A. 9. The model is able to predict the uptake curve and the relative broadening of TPD peaks for NO_x as a result of decreasing the ramp rate.

As discussed earlier, targeted experiments indicated that the uptake is not limited by the washcoat diffusion. To check this finding, the model was used to simulate the uptake and desorption for a range of λ (= D_{fi}/D_{ei}) values between 50 to 250. The model predictions are shown in Figure A. 10. In the absence of H_2O in the feed, the uptake is nearly unaffected until λ ~100. A negligible change in NO_x uptake profile was observed by changing the value of λ in presence of H_2O in the feed. Thus, model further asserts that the uptake is not limited by the washcoat diffusion. As a check, λ values were increased to values exceeding ~150. In that impractical higher range, the model predicts a decrease in the breakthrough time and a more rapid increase in the effluent NO. Under these conditions the immediate release of NO_x shows the detrimental impact of diffusion.

Finally, using the model the distribution of NO on the different sites can be estimated using methods described earlier. For example, at an uptake temperature of 80°C with a feed containing 5ppm NO_2/ 400ppm NO/ 2% O_2/ 7% H_2O/ balance Ar in the feed, the Pd(1%)/H-ZSM-5 sample adsorbs 3.5×10^{-5} mole NO_x /g zeolite. Two different types of Pd sites are available for NO uptake at this temperature; $Z^-Pd^{2+}Z^-$ and $Z^-[PdOH]^+$. The model predicts that ~43% of NO is adsorbed on the $Z^-Pd^{2+}Z^-$sites while ~57% of NO

is adsorbed on $Z^{-}[PdOH]^{+}$. The adsorbed NO distribution on the different Pd sites at different uptake temperatures is shown in Figure A. 11.

4.5 Alternative Reaction Mechanism for NO_x Uptake on Pd/H-ZSM-5: Scheme II

The mechanism for NO_x uptake on Pd sites discussed till now (Scheme I) is capable of explaining NO_x uptake on Pd/H-ZSM-5 at different experimental conditions and is backed by FTIR experiments, DRIFTS, DFT-data and literature. Nevertheless, this model also has its limitations and the good agreement between the fit and the experimental data does not provide conclusive evidence that the underlying mechanism is correct. A potential concern is that the mechanism for Scheme I requires two $Z^{-}[PdOH]^{+}$ sites to be present in adjacent positions. This is likely for high Pd-loadings but less likely for low Pd-loading. In addition, the existence of NO adsorbed on Pd in +1 oxidation state is a disputed topic [23]. Pd on zeolites can stabilize in multiple oxidation states [15,19,20]. It can also change its oxidation state during NO_x uptake which makes it a complicated process [15,18-20]. With this in mind, an alternative mechanism for NO_x uptake on Pd sites are considered that do not require two adjacent $Z^{-}[PdOH]^{+}$ sites or Pd to be present in +1 oxidation state.

Zheng et al. experimentally found that Pd can exist as PdO_2 and PdO clusters [20]. Proposed Scheme II involves three different types of Pd sites: $Z^{-}Pd^{2+}Z^{-}$, PdO_2 and PdO. The overall reaction mechanism is shown in Table 2.7. As for Scheme I, the low temperature NO TPD peak is associated with NO adsorbed on $Z^{-}Pd^{2+}Z^{-}$. Reactions R2.28 to R2.31 account for NO_x uptake on $Z^{-}Pd^{2+}Z^{-}$ sites while reactions R2.35 to R2.37 involve H_2O uptake and combined H_2O and NO_x uptake on $Z^{-}Pd^{2+}Z^{-}$. In the presence of NO in the feed, PdO_2 is reduced to PdO, forming NO_2 (reaction R2.32) [20]. Zheng et al. observed NO_2 formation for temperatures between 150°C and 250°C [20]. This is

consistent with our data in which NO_2 was observed at ~150°C. NO in the presence of O_2 can also be stored in form of nitrates shown by reaction R2.33 [24]. Upon H_2O addition to a feed of NO and O_2 over Pd-CHA, Chen et al. [56] observed DRIFTS peak of ~1620 cm^{-1} which belongs to nitrate species. According to DFT calculations, nitrates are stable on Pd and desorb at higher temperatures and thus may be responsible for the high temperature NO TPD peak [30]. Also, H_2O can be adsorbed on PdO_2 and PdO, reducing NO_x uptake in presence of H_2O in the feed as compared to dry feed, shown by reaction R2.38 and R2.39. In the presence of O_2 in the feed, PdO can be oxidized back to PdO_2 shown by reaction R2.34.

Details of kinetic parameter tuning for Scheme II are provided in the Supplemental Material section. The estimated kinetic parameters for Scheme II are provided in Table 2.9. Model prediction of NO_x uptake at 80°C and TPD data on Pd/H-ZSM-5 with water in the feed is shown in Figure 2.18. The tuned model predicts well the NO uptake along with the TPD data, such as two TPD peaks for NO and one low temperature TPD peak of NO_2. The Pd/H-ZSM-5 model was validated for different feed flowrate, and uptake temperature to examine the predictive effectiveness of the model.

The model was tested for a higher uptake temperature of 150°C, as shown in Figure A. 12. Similar to Scheme I, Scheme II also shows a single TPD peak for NO. The model also predicts the immediate generation of NO_2 during the NO uptake. Scheme II was then validated for the higher feed flowrate experiment (2500 sccm) shown in Figure A. 13. The model is able to reproduce the lower desorption concentrations of NO and NO_2 that are encountered with the shorter contact time.

Table 2.9 Kinetic Parameters for Pd/H-ZSM-5 model- Scheme II

Reaction no.	**Pre-exponential factor**		**Activation Energy (10^3*kJ mol^{-1})**	
R2.28	A_{28f} A_{28b}	1.57e1 7.8e19	E_{28f} E_{28b}	0 160
R2.29	A_{29f} A_{29b}	1.8e3 2e14	E_{29f} E_{29b}	0 115
R2.30	A_{30f} A_{30b}	3.23e1 1e7	E_{30f} E_{30b}	0 68
R2.31	A_{31f} A_{31b}	3.15e1 1.1e10	E_{31f} E_{31b}	0 140
R2.32	A_{32f} A_{32b}	4e5 5e25	E_{32f} E_{32b}	15 240
R2.33	A_{33f} A_{33b}	7.14e9 5e17	E_{33f} E_{33b}	0 245
R2.34	A_{34f} A_{34b}	1e18 1e5	E_{34f} E_{34b}	260 80
R2.35	A_{35f} A_{35b}	1e0 1e14	E_{35f} E_{35b}	0 120
R2.36	A_{36f} A_{36b}	6e3 9.46e15	E_{36f} E_{36b}	20 140
R2.37	A_{37f} A_{37b}	7.88e1 1.57e11	E_{37f} E_{37b}	0 100
R2.38	A_{38f} A_{38b}	4.43e2 3.1e15	E_{38f} E_{38b}	0 120
R2.39	A_{39f} A_{39b}	2e1 5e14	E_{39f} E_{39b}	0 110

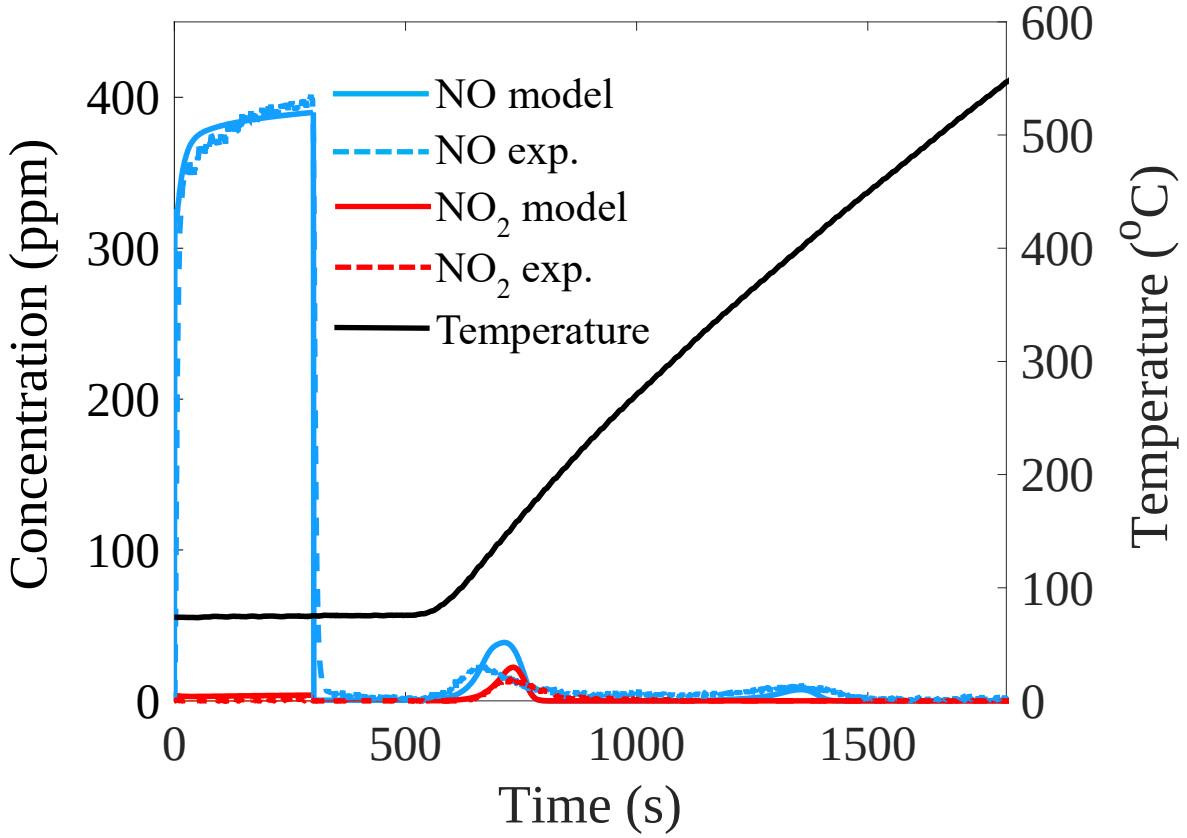

Figure 2.18 Experimental and modeling results of NO_x uptake at 80°C and TPD on Pd(1%)/H-ZSM-5 for wet-feed (7% H_2O) and feed flowrate of 1500 sccm (Scheme II).

2.3 Conclusions

The experimental findings of this study demonstrate that Pd/H-ZSM-5 shows good performance for NO uptake. NO_x uptake data reveal the process to not be washcoat diffusion limited. DRIFTS studies conducted led to the identification of different surface species present. The presence of H_2O in the feed significantly lowers NO_x uptake as a result of competition for sites between H_2O and NO_x species and the extent of inhibition is a function of temperature. Typical NO uptake in the presence of H_2O in the feed did not exceed NO/Pd ~ 0.45.

The parametric study of the H-ZSM-5 and Pd/H-ZSM-5 PNA materials provide plentiful data for the development and tuning of two prospective mechanistic microkinetic schemes contained within a monolith model of a PNA. Both of the microkinetic schemes are incorporated into a one-dimensional, two-phase transient monolith model to predict and validate NO_x uptake and temperature-programmed desorption (TPD) data for H-ZSM-5 and Pd/H-ZSM-5. Each scheme involves multi-site NO_x adsorption on multiple types of Pd cations and Brønsted acid sites (BAS), the latter of which are ineffective when water is in the feed. Scheme I involves $Z^-[PdOH]^+$, $Z^-Pd^{2+}Z^-$ and Z^-Pd^+ with the key feature being the reduction of a pair of $Z^-[PdOH]^+$ sites to two Z^-Pd^+ sites, which strongly bind NO. The site reduction generates NO_2. Scheme II involves the NO reduction of PdO_2 to PdO, also generating NO_2. Formation of Pd nitrate ($Pd(NO_3)_2$) comprises the strongly bound NO. Systematic model tuning relies on a combination of in-situ diffuse reflectance infrared Fourier transform spectroscopy (DRIFTS), literature data, and energy changes estimated from density functional theory (DFT). The model is validated at different uptake temperatures, feed flow rates, NO concentrations, ramp rate and Pd-loadings, enabling its use to identify improved catalyst formulations and operating strategies. Research is ongoing to further discriminate between the two microkinetic schemes.

Chapter 3

NO_x Adsorption with CO and C_2H_4 on Pd/SSZ-13: Experiments and Modeling

3.1 Experimental

3.1.1 Catalyst properties

The PNA monolith provided by Johnson Matthey Inc. contains 1 wt.% Pd/SSZ-13 (90%) + Al_2O_3 (10%) with a washcoat (wc) loading of 1.5 g wc/in^3 (mass: 1.76g; Pd loading of 94.0 µmole Pd/g wc). A cordierite monolith of 400 CPSI, 2.54 cm diameter, and 3.81 cm length served as the washcoat substrate.

3.1.2 Reactor setup and experimental protocol

Details of the experimental setup for evaluating the NO uptake performance on PNA materials were provided by Gupta et al. [38]. The monolith sample was loaded into the reactor and de-greened. De-greening is a pretreatment step done only once prior to using the performance testing of the catalyst. It consists of exposing the catalyst to 12% O_2/ 6% H_2O / balance N_2. This is followed by ramping from room temperature to 600°C and holding for 4 h. Prior to each experiment the catalyst was pretreated in 12% O_2/ 6% CO_2/ 6% H_2O/ balance N_2 at 600℃ for 20 minutes to remove any residual species. At the start of each experiment, the monolith sample catalyst was heated to the desired uptake temperature in the range 75℃ - 150℃, followed by adsorption for 30 min. TPD was performed at the end of adsorption period to a temperature of 600℃ in 25 min. The set point temperature of the furnace reported by Gupta et al. [38] typically differs by up to ±5℃ from the sample temperature measured by a thermocouple, the latter of which was used for modeling. Experiments were carried out at two space velocities; 30 khr^{-1} (9.65

L/min) and 45 khr^{-1} (14.5 L/min). The feed gas mixtures used for the NO-only feed experiment consisted of 200 ppm NO/ 12% O_2/ 6% CO_2/ 6% H_2O/ balance N_2. To understand the effect of reductants CO and C_2H_4 on NO uptake, experiments were performed by adding those species to the feed. For NO+CO feed experiments, 500 ppm CO was added to the NO-only feed gas mixture (without CO_2). For NO+C_2H_4 feed experiments, 200 ppm C_2H_4 was added to the NO-only feed gas mixture (without CO_2). For NO+CO+C_2H_4 experiments the feed contained 200 ppm NO/ 200 ppm CO/ 200 ppm C_2H_4/ 12% O_2/ 6% H_2O / balance N_2.

3.1.3 Characterization

In order to better understand the oxidation state of the Pd in the Pd/SSZ-13 sample, XPS was conducted. The XPS instrument used was PHI model 5700 X-ray photoelectron spectrometer. The catalyst samples were placed on the Mo cover plate which had a sample area of up to 1 in^2. The sample was loaded into the instrument chamber for analysis. The measurement probed the near surface with a depth of up to 5 nm. The effects of charging were corrected with reference to Si-2p binding energy of 103.3 eV.

Figure 3.1 shows the XPS spectra of the Pd(1%)/SSZ-13 sample which was pre-calcined (at 550℃ in presence of 21%O_2 by vol. for 4 hours). The duplet peaks ~337 eV ($3d_{5/2}$) and ~342 eV ($3d_{3/2}$) are associated with Pd in +2 state [16,20]. Thus, the XPS results shows the existence of Pd(II) in the vicinity of the catalyst sample surface. There was no evidence for Pd(I) given the oxidizing pretreatment. This is an expected result since the NO uptake experiments indicate that a mild reduction of the pre-oxidized sample is needed to obtain the lower oxidation state Pd(I).

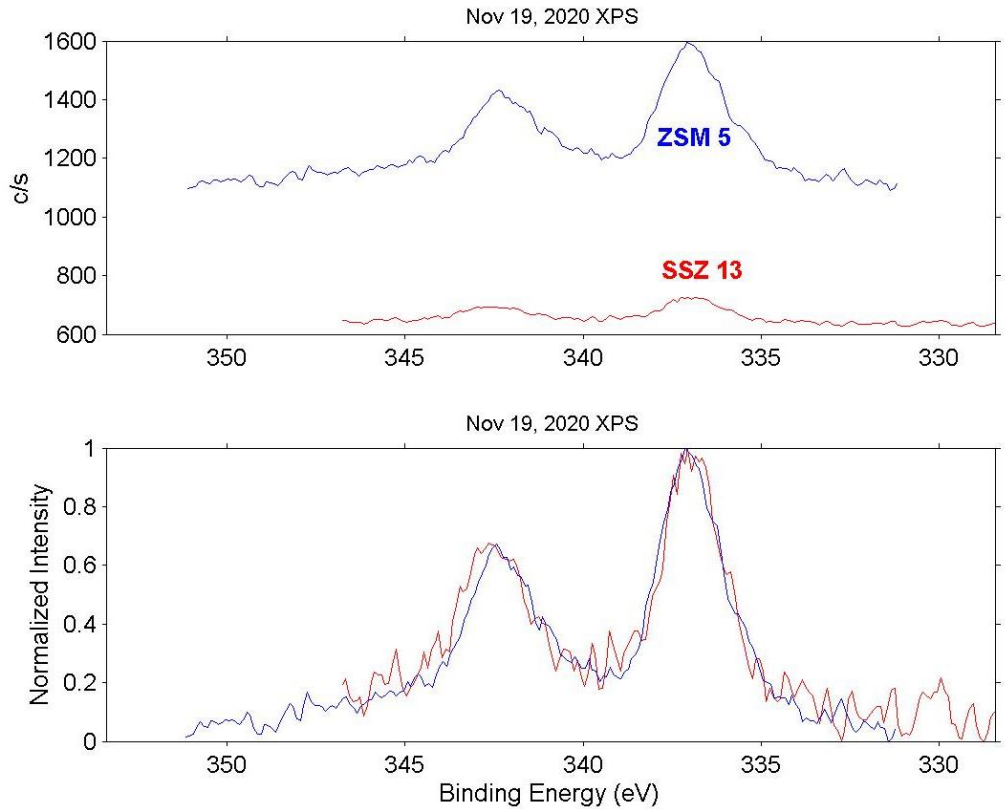

Figure 3.1 XPS spectra acquired on Pd(1%)/SSZ-13 and Pd(2%)/H-ZSM-5

Gupta et al. [38] carried out DRIFTS studies of NO uptake on SSZ-13 and Pd(1%)/SSZ-13. DRIFTS results for NO adsorption at 100℃ during NO exposure to SSZ-13 and Pd(1%)/SSZ-13 for a dry feed comprising of 1400 ppm NO/ 12 % O_2/ balance N_2 and a feed flowrate of 100 ml/min are shown in Figure 3.2. Table 2.2 lists the important IR peaks of interest provided in previous studies for NO interacting with SSZ-13 and Pd/SSZ-13. This information is used for the development of uptake mechanisms.

The presence of peaks at 1805 and 1865 cm^{-1} for Pd(1%)/SSZ-13 confirms that NO adsorbs onto Pd cations [9,18]. Peaks at 1865 and 1805 cm^{-1} are attributed to NO bound to Pd with +2 oxidation state, and NO bound to Pd with +1 oxidation state, respectively. There is an ongoing debate on the assignment of 1805 cm^{-1} [57] but several studies suggest it to

be associated with NO bound to Pd^+ [15,24,38]. We expand on that in the modeling section. Please refer to Gupta et al. [38] for DRIFTS results of NO+CO and NO+C_2H_4 feed.

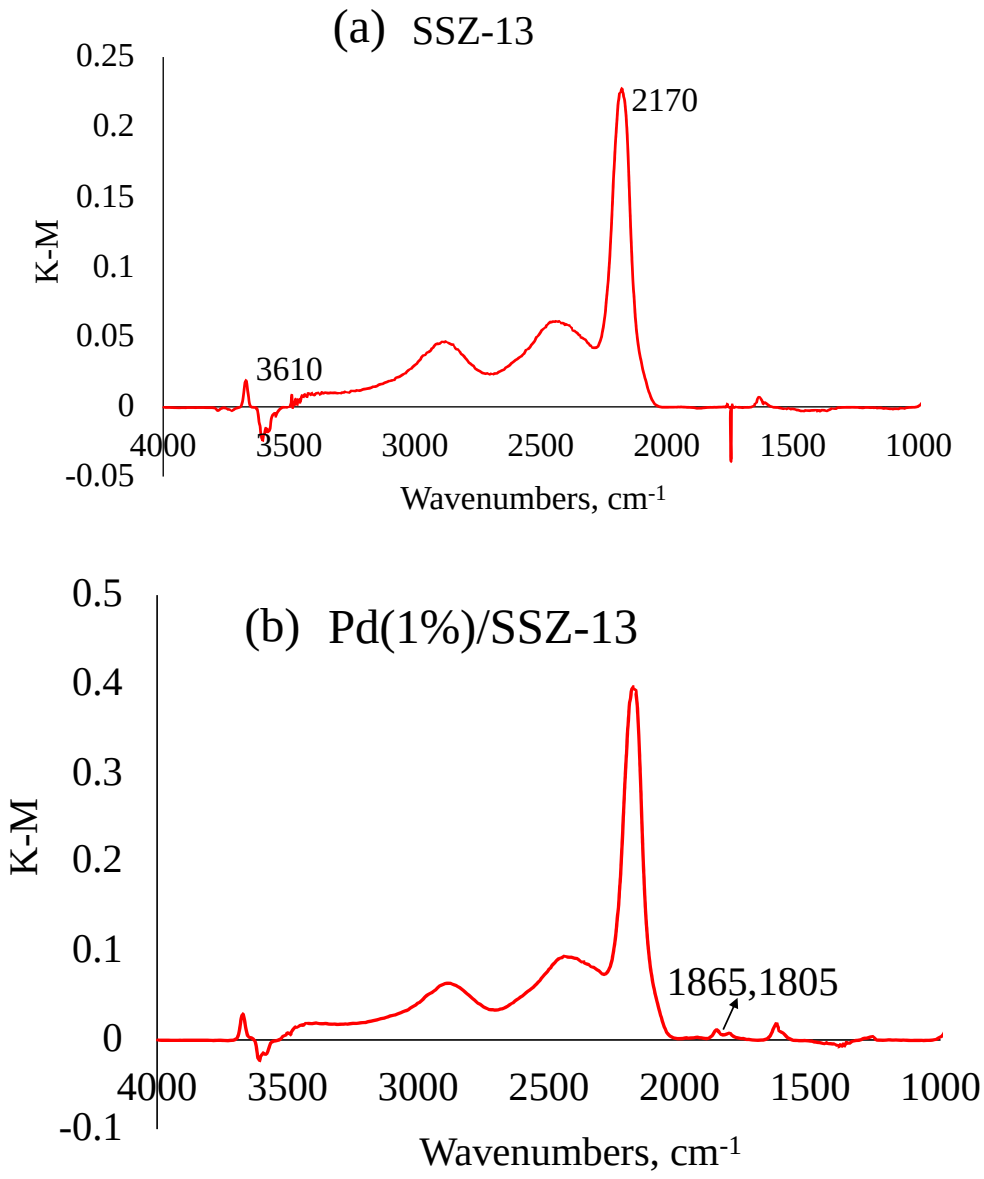

Figure 3.2 DRIFTS spectra for (a) SSZ-13 and (b) Pd(1%)/SSZ-13

Ambast et al. [37] proposed an alternative scheme for Pd/ZSM-5 that considers the redox couple involving PdO_2 and PdO, with NO uptake in the form of $Pd(NO_3)_2$. Discrimination between the two schemes is beyond the scope of the current study.

3.2 Modeling

3.2.1 Transient monolith model

We use a low dimensional 1 + 1 D, two-phase transient, single channel monolith model following Joshi et al. [52]. The model contains a mechanistic-based microkinetic scheme to predict the effluent gas concentration profiles spanning through uptake and release. The same assumptions used in [37] apply to the current study. The model equations 2.2 – 2.5 were used with model parameters and variables defined in the List of Notation. The values of non-kinetic parameters are provided in Table 3.1 and Table A. 1 of the Appendix. Additional details are provided by Ambast et al. [37].

Table 3.1 Parameters used in model

Parameter	Value
L	0.038 m
<u>	0.3548*(T/273.15) m/s
$C_{\tau m}$	$(12187.3/T)$ mol/m^3
ε_{wc}	0.4
$R_{\Omega 1}$	3×10^{-4} m
$R_{\Omega 2}$	1.5×10^{-5} m
Sh_e	4.36
$Sh_{i,\infty}$	2.37
λ	80
$C_{Z^-[Pd(II)OH]^+}$ (C_{S1})	151.5 mole-sites/m^3 of washcoat
$C_{Z^-Pd^{+2}Z^-}$(C_{S2})	1. mole-sites/m^3 of washcoat

3.2.2 Model tuning and validation procedure

A systematic approach was followed to develop the model for NO uptake on Pd/SSZ-13 with and without reductants. In this section we describe the overall approach. The model was first developed for the NO-only feed using a combination of NO uptake and desorption data, DRIFTS measurements (described in [38]), and density functional

theory (DFT) calculations. The method used for DFT calculations for Pd/SSZ-13 is described in the SM. Once the model was developed for the NO-only feed it was extended for the NO+CO and NO+C_2H_4 feeds. Parameter estimation for NO+CO and NO+C_2H_4 feed was accomplished by keeping the parameter values associated with NO-only feed fixed. At each stage the model was validated for different conditions including uptake temperature, TPD ramp rate, and feed flow rate.

Kinetic parameters were taken from DFT calculations or estimated from a fit of data sets described later. Binding energies for NO on the various Pd cation sites estimated by DFT were used. Some tuning was done to predict the precise desorption peak location and width. A broad NO desorption peak can suggest a coverage-dependent binding energy. To this end, we followed Olsson et al. [54] and Wang et al. [58] in expressing the desorption activation energy by $E_i = E_{0,i}(1 - \alpha_i\theta_j)$ for step i and adsorbate j. Here, α_i is called a repulsion coefficient or coverage dependence and $E_{0,i}$ is the coverage independent desorption activation energy. We expand on its connection to the reaction system later. These and the remaining unknown kinetic parameters were estimated using a parameter estimation algorithm (MATLAB *fmincon*) interfaced with the monolith reactor model containing the microkinetic scheme. The algorithm minimized the objective function comprising the sum of squared differences between the experimental and predicted species concentrations spanning the uptake and release. Some fine tuning was done given the complexity of the transient uptake and release data and large number of parameters. The three stages (reference sets) of the model tuning involved the following number of data points (N_d) and estimated parameters (N_p):

- NO-only feed on Pd(1%)/SSZ-13: $N_p = 27$ $N_d = 3596$

- NO+CO feed on Pd(1%)/SSZ-13: $N_p = 26$ $N_d = 1801$
- NO+C_2H_4 feed on Pd(1%)/SSZ-13: $N_p = 30$ $N_d = 1801$

The reactor model partial differential equations (PDEs) were discretized using a second-order finite difference method. The reactor length was discretized into 20 elements as a compromise between simulation time and accuracy. The resulting set of ordinary differential equations (ODEs) were solved by the MATLAB routine *ODE23s*. More details of parameter estimation are provided in the next section and by Ambast et al. [37].

3.2.3 Microkinetic model for NO-only feed

3.2.3.1 Development of reaction scheme for NO-only feed

The microkinetic model for NO uptake on Pd/SSZ-13 follows from the one recently developed for Pd/ZSM-5 [37]. Key experimental features, including multiple NO adsorption regimes, water inhibition, NO_2 generation, etc. guide development of the reaction steps. The experiment directs a gas mixture containing 200 ppm NO/ 12% O_2/ 6% CO_2/ 6% H_2O/ balance N_2 at 95℃ to the monolith (adsorption) followed by a linear temperature ramp from 95℃ to 600℃. The temporal concentration profiles of several species are shown in Figure 3.3(a). After stabilizing the feed in the bypass for 5 min, the feed is directed to the monolith sample. As soon as NO encounters the Pd/SSZ-13 coated monolith, competitive adsorption of NO and H_2O commences, a dip in the NO concentration occurs, which is followed by a slow approach to its feed concentration of 200 ppm. During the initial stage of the temperature ramp, H_2O desorbs, as seen in Figure 3.3(a); this provides additional sites onto which NO adsorbs. When the temperature reaches ~120℃, the second phase of NO uptake occurs, coinciding with the generation of NO_2. The NO_2 suggests a reduction process with NO serving as the reductant. At higher temperatures

the remaining NO desorbs from the sites. An inflection point is noted in the NO TPD peak when two apparent peaks merge together. The existence of the two overlapping peaks indicates that NO adsorbs on at least two different sites with distinct binding energies.

With the main uptake and desorption features highlighted, it is instructive to expand on the identity of the sites for NO uptake. The model considers $Z^-[PdOH]^+$, $Z^-Pd^{2+}Z^-$, and Z^-Pd^+ as active sites for NO adsorption. NO bound to the Z^-Pd^+ has the strongest binding based on DFT estimates. Brønsted acid sites (BASs) do not adsorb NO or NO_2 in the presence of excess H_2O due to blockage of sites by H_2O [21, 37] and for this reason they are not considered as active sorption sites. NO uptake experiments were conducted with and without CO_2 in the feed. The results showed that CO_2 has negligible effect on NO uptake or release (Figure A. 14), showing, in contrast to H_2O, that it does not compete with NO for the Pd sites. So, we did not consider CO_2 uptake on Pd sites in our model. Temperature programmed oxidation (TPO) experiments conducted by Friberg et al. [59] showed that Pd/SSZ-13 with SAR of 52 has a consumption peak of O_2 at 386°C. In decreasing SAR to 43, O_2 uptake becomes very less and the consumption peak shifts to a higher temperature of 456℃. Given we use a SSZ-13 sample with an even lower SAR of ~30, O_2 uptake will be not significant and at very high temperatures (T> 456℃). Almost all of the adsorbed species would be desorbed by this temperature. Our DFT calculations also backed these experimental results and showed that O_2 consumption on Pd/SSZ-13 with low SAR is unlikely. For these reasons, we have not considered O_2 adsorption.

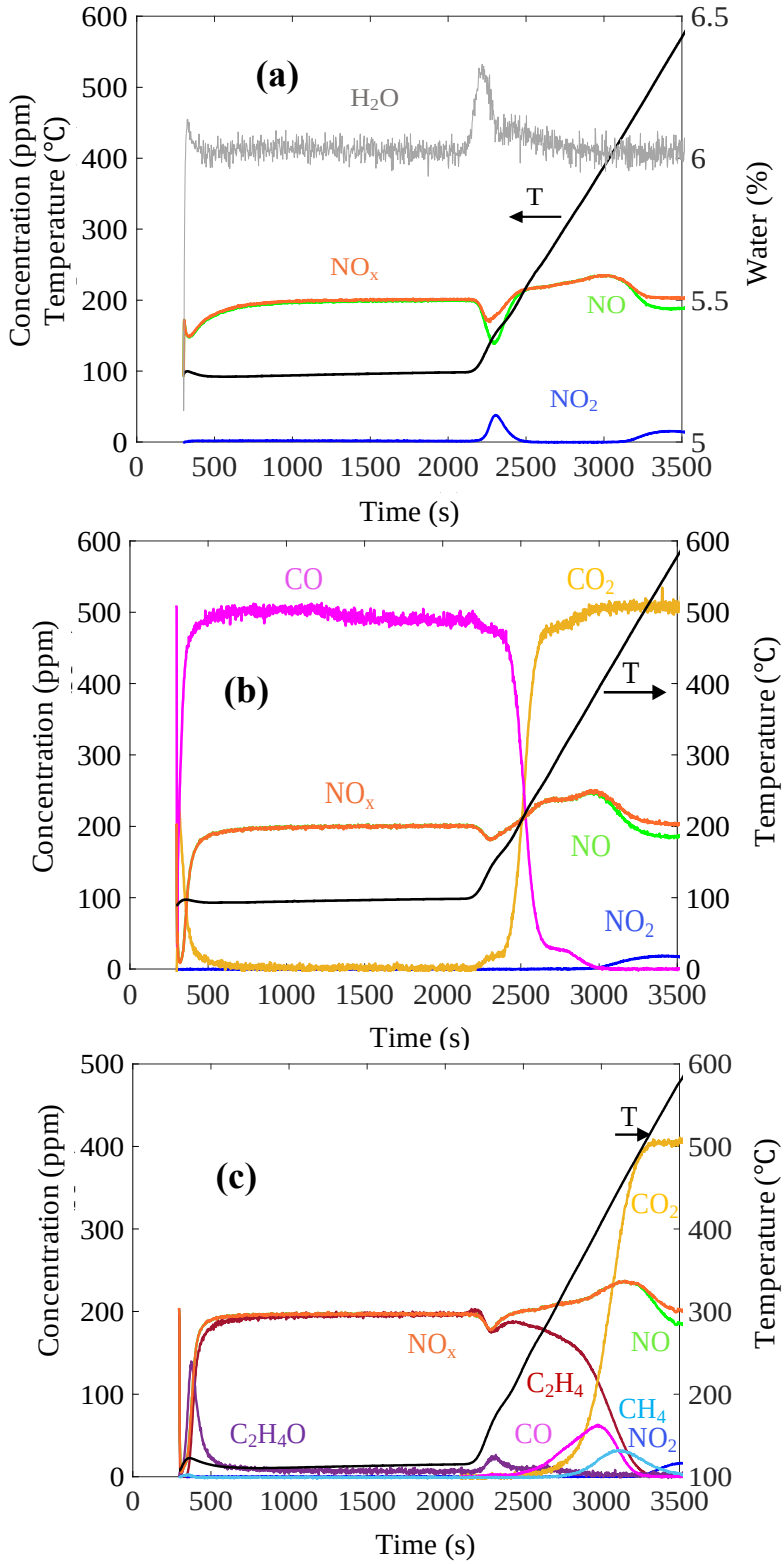

Figure 3.3 Uptake and TPD profile for feed comprising of (a) 200 ppm NO/ 12% O_2/ 6% CO_2/ 6% H_2O / balance N_2, (b) 200 ppm NO/ 500 ppm CO/ 12% O_2/ 6% H_2O / balance N_2, (c) 200 ppm NO/ 200 ppm C_2H_4/ 12% O_2/ 6% H_2O / balance N_2 on Pd(1%)/SSZ-13.

3.2.3.2 Reaction mechanism for simple NO feed

Table 3.2 provides the proposed 10-step scheme along with the rate expressions for NO uptake on Pd/SSZ-13 with H_2O in the feed. The rate of reaction is written in terms of mole fraction of the gaseous species. DFT calculated energy barriers are provided in Table 3.3 and highlighted. [Note: Most of these are estimates for Pd/SSZ-13 while a few are for Pd/BEA]. Details about the DFT calculation technique are provided in SM. Energies that were fixed during model tuning are indicated; these are described as follows. The binding energy for NO on $Z^-Pd^{2+}Z^-$ (reaction R3.1), is estimated as -122 kJ/mol. Reaction R3.2 describes the uptake of a second NO on $Z^-Pd^{2+}Z^-$ forming $(Z^-NO^+)(Z^-Pd^+\text{-}NO)$. Reaction R3.3 is the competitive adsorption of H_2O on $Z^-Pd^{2+}Z^-$; its binding energy is estimated to be -120 kJ/mol for Pd/BEA. Reactions R3.4 and R3.5 describe the two-step NO reduction of two $Z^-[PdOH]^+$ to Z^-Pd^+, generating NO_2 and H_2O. According to DFT analysis the reduction of $Z^-[PdOH]^+$ to Z^-Pd^+ occurs in a sequence of steps and sites involved in this reduction. The sequence involves two $[PdOH]^+$ complexes located in the same zeolite cage. Here, R3.4 and R3.5 represents a combination of those steps. We estimated energies for steps R3.4 (-284 kJ/mol) and R3.5 (172 kJ/mol). Reaction R3.6 is the competitive uptake of H_2O on $Z^-[PdOH]^+$. Its binding energy is estimated to be as -122 kJ/mol. Reactions R3.7 and R3.8 describe the uptake of NO and H_2O on Z^-Pd^+ sites, respectively, with binding energies estimated from DFT. Reaction R3.9 is the uptake of NO on a Z^-Pd^+ site occupied by H_2O. We estimated the binding energy of NO on the H_2O-occupied Z^-Pd^+ site to be -204 kJ/mol. R3.10 is an overall step that describes the re-oxidation of Z^-Pd^+ sites to $Z^-[PdOH]^+$ sites. It is noted that the sum R3.4+R3.5-R3.7+R3.10 gives the oxidation of NO to NO_2. The heat of reaction for NO oxidation is a known value. From this the energy of

R3.10 is calculated. The energy for forward reaction was fitted by fixing the difference between energies for forward and reverse reaction steps as twice the heat of reaction for NO oxidation which is a known value.

For the parameter estimation, a total of 20 pre-exponential factors, activation energies for forward reactions R3.10 and for reverse reaction R3.2 and adsorption coefficients α_i for steps R3.1, R3.2, R3.6, R3.7 and R3.9 were determined based on a fit of NO uptake at 95℃ and 130℃ and TPD data. A total of 3596 data points was used for the parameter estimation.

Table 3.2 Reaction mechanism for simple NO feed [S_1 - $Z^-Pd^{2+}Z^-$; S_2 - $Z^-[PdOH]^+$; S_3 - Z^-Pd^+; S_4 - $Z^-Pd^+(NO)Pd^+(NO_2)(H_2O)\,Z^-$]]

Reaction no.	Reaction step	Rate expression (R_f - R_b)
R3.1	$NO + Z^-Pd^{2+}Z^- \leftrightarrow Z^-Pd^{2+}Z^- - NO$	$k_{1f}X_{NO}\theta_{vs1}C_{S1}$- $k_{1b}\theta_{NO-S1}C_{S1}$
R3.2	$NO + Z^-Pd^{2+}Z^- - NO \leftrightarrow (Z^-NO^+)(Z^-Pd^+ - NO)$	$k_{2f}X_{NO}\theta_{NO-S1}C_{S1}$- $k_{2b}\theta_{(Z^-NO^+)(Z^-Pd^+-NO)}C_{S1}$
R3.3	$H_2O + Z^-Pd^{2+}Z^- \leftrightarrow Z^-Pd^{2+}Z^- - H_2O$	$k_{3f}X_{H_2O}\theta_{vs1}C_{S1}$- $k_{3b}\theta_{H_2O-S1}C_{S1}$
R3.4	$2NO + 2Z^-[PdOH]^+ \leftrightarrow Z^-Pd^+(NO)Pd^+(NO_2)(H_2O)\,Z^-$	$k_{4f}X_{NO}^2\theta_{vs2}^2C_{S2}^2$- $k_{4b}\theta_{S4}C_{S2}^2$
R3.5	$Z^-Pd^+(NO)Pd^+(NO_2)(H_2O)\,Z^- \leftrightarrow Z^-Pd^+ - NO + Z^-Pd^+ + NO_2 + H_2O$	$k_{5f}\theta_{s4}C_{S2}^2$- $k_{5b}\theta_{S3}\theta_{NO-S3}X_{NO_2}X_{H_2O}C_{S2}^2$
R3.6	$H_2O + Z^-[PdOH]^+ \leftrightarrow Z^-[PdOH]^+ - H_2O$	$k_{6f}X_{H_2O}\theta_{vS2}C_{S2}$- $k_{6b}\theta_{H_2O-S2}C_{S2}$
R3.7	$NO + Z^-Pd^+ \leftrightarrow Z^-Pd^+ - NO$	$k_{7f}X_{NO}\theta_{S3}C_{S2}$- $k_{7b}\theta_{NO-S3}C_{S2}$
R3.8	$H_2O + Z^-Pd^+ \leftrightarrow Z^-Pd^+ - H_2O$	$k_{8f}X_{H_2O}\theta_{S3}C_{S2}$- $k_{8b}\theta_{H_2O-S3}C_{S2}$
R3.9	$NO + Z^-Pd^+ - H_2O \leftrightarrow Z^-Pd^+ - (H_2O)(NO)$	$k_{9f}X_{NO}\theta_{H_2O-S3}C_{S2} - k_{9b}\theta_{(H_2O)(NO)-S3}C_{S2}$
R3.10	$2Z^-Pd^+ + H_2O + 0.5O_2 \leftrightarrow 2Z^-[PdOH]^+$	$k_{10f}\theta_{S3}^2X_{H_2O}X_{O_2}^{0.5}C_{S2}^2$- $k_{10b}\theta_{vS2}^2C_{S2}^2$

Table 3.3 Kinetic Parameters for simple NO feed model

Reaction no.	**Pre-exponential factor**		**Activation Energy (kJ mol^{-1})**		**α (Coverage dependence)**	**DFT calculated electronic energies (kJ mol^{-1})**	
						SSZ-13	BEA
R3.1	A_{1f} A_{1b}	3e3 1e13	E_{1f} E_{1b}	0 122	0.1	**-122**	
R3.2	A_{2f} A_{2b}	0.22e1 2e8	E_{2f} E_{2b}	0 120	0.22		
R3.3	A_{3f} A_{3b}	2e3 5.6e15	E_{3f} E_{3b}	0 110			**-120**
R3.4	A_{4f} A_{4b}	2e4 3e29	E_{4f} E_{4b}	0 284		**-284**	
R3.5	A_{5f} A_{5b}	1e20 5e3	E_{5f} E_{5b}	172 0		**172**	
R3.6	A_{6f} A_{6b}	1.8e2 4e15	E_{6f} E_{6b}	0 122	0.105	**-122**	
R3.7	A_{7f} A_{7b}	5e-2 2.5e15	E_{7f} E_{7b}	0 240	0.22	**-240**	
R3.8	A_{8f} A_{8b}	1e0 8e12	E_{8f} E_{8b}	0 87		**-87**	
R3.9	A_{9f} A_{9b}	1e2 5e15	E_{9f} E_{9b}	0 204	0.45	**-204**	
R3.10	A_{10f} A_{10b}	1e5 1e10	E_{10f} E_{10b}	105 290		*	

3.2.3.3 Estimation of site concentrations

An estimate of the loadings of the adsorption sites for Pd(1%)/SSZ-13 was conducted as follows. The sample contains 1.66×10^{-4} moles of Pd (94.0 □mol/g wc). Pd is assumed to exist in the +2 valence state ($Z^-[PdOH]^+$, $Z^-Pd^{2+}Z^-$) and +1 valence state (Z^-Pd^+). We use the measured NO uptake and TPD data to estimate the concentrations of $Z^-[PdOH]^+$, $Z^-Pd^{2+}Z^-$ and Z^-Pd^+ sites. The sum of the loadings of the three species $Z^-[PdOH]^+$, $Z^-Pd^{2+}Z^-$, and Z^-Pd^+ is 94 μmol/g wc. Following the aforementioned studies of NO uptake

on Pd/ZSM-5 [15,20,24], the reduction by NO of $Z^-[PdOH]^+$ to Z^-Pd^+ occurs according to the two-step sequence

$$2\,NO + 2\,Z^-[PdOH]^+ \leftrightarrow Z^-Pd^+(NO)Pd^+(NO_2)(H_2O)\,Z^- \quad \text{(R3.4)}$$

and $Z^-Pd^+(NO)Pd^+(NO_2)(H_2O)\,Z^- \leftrightarrow Z^-Pd^+ - NO + Z^-Pd^+ + NO_2 + H_2O.$ (R3.5)

The R3.4 + R3.5 stoichiometry shows that the generation of one mole of NO_2 occurs during the reduction of two moles of $Z^-[PdOH]^+$. At the beginning of the NO uptake experiment, which followed the standard oxidative pretreatment, the dispersed Pd cations are assumed to be present in +2 oxidation state [15,37]; Z^-Pd^+ is formed later by the reduction of $Z^-[PdOH]^+$ sites in the presence of NO. Were all of the Pd present as $Z^-[PdOH]^+$ initially and then reducted, the amount of NO_2 generated during the NO uptake would be 47 □mol/g wc. However, the experiments indicate the NO_2 generation of ~35 μmol/g wc during NO uptake at 175°C, conditions for which most of the inhibiting species H_2O has fully desorbed [38]. This gives the loading of $Z^-[PdOH]^+$ sites of 35/47 x 94 μmol/wc = 70 □mol/g wc. Therefore, at any time, the sum of the loadings of $Z^-[PdOH]^+$ and Z^-Pd^+ is 70 □mol/g wc. Assuming that the Pd is completely dispersed as isolated cations, which is in line with Khivantsev et al. [24] who reported 100% Pd cation dispersion on Pd(1%)/SSZ-13, the concentration of $Z^-Pd^{2+}Z^-$ sites is 24 μmol/g wc. Finally, the washcoat volume is estimated from SEM images to be 8.15×10^{-7} m^3; this gives a total volumetric Pd loading of 203.3 mole-site/ m^3 wc. The loading of the $Z^-Pd^{2+}Z^-$ sites (S_1) is 51.8 mole-site/ m^3 wc and that of $Z^-[PdOH]^+$ sites (S_2) is 151.5 mole-site/ m^3 wc (Table 3.1). The site balances for the NO-only feed are as follows

$$C_{NO-S1} + C_{(Z^-NO^+)(Z^-Pd^+-NO)} + C_{H_2O-S1} + C_{vS1} = 51.8 \quad (3.1)$$

and $C_{vS2} + C_{H_2O-S2} + C_{S3} + C_{NO-S3} + C_{H_2O-S3} + C_{(H_2O)(NO)-S3} + C_{S4} = 151.5.$ (3.2)

Where S_1 - $Z^-Pd^{2+}Z^-$; S_2 - $Z^-[PdOH]^+$; S_3 - Z^-Pd^+; S_4- $Z^-Pd^+(NO)Pd^+(NO_2)(H_2O)Z^-$. The surface fractions (coverages) are normalized by the total concentration of each site as

$$\theta_{NO-S1} + \theta_{(Z^-NO^+)(Z^-Pd^+-NO)} + \theta_{H_2O-S1} + \theta_{vS1} = 1 \quad (3.3)$$

and $\theta_{vS2} + \theta_{H_2O-S2} + \theta_{S3} + \theta_{NO-S3} + \theta_{H_2O-S3} + \theta_{(H_2O)(NO)-S3} + \theta_{S4} = 1.$ (3.4)

Where θ_{i-j} = fraction of sites of species i on site type j and θ_{vj} = fraction of sites of vacant site j.

3.2.3.4 *Modeling results for NO-only feed*

Experimental (Figure 3.3(a)) and modeling results of NO uptake and TPD profiles for the NO-only feed spanning uptake at 95℃ through the TPD are shown in Figure 3.4. The tuned model satisfactorily captures all of the experimental trends. The model predicts the depth and width of the first uptake peak (at 95℃) and second NO uptake peak (spanning 110 – 200℃). The model also predicts the location and magnitude of the NO_2 generation peak as well as the broad NO desorption peak spanning 200 to 480℃, including its subtle, slowly increasing feature to the left of the maximum NO concentration. Finally, the model predicts the consumption of NO and subsequent generation of NO_2 at temperatures above 500℃.

As described earlier, some of the desorption energies are dependent on uptake (coverage) which naturally expand the temperature range over which the desorption occurs. Justification at the molecular level is less obvious especially if one notes that the Pd cations are isolated from one another.

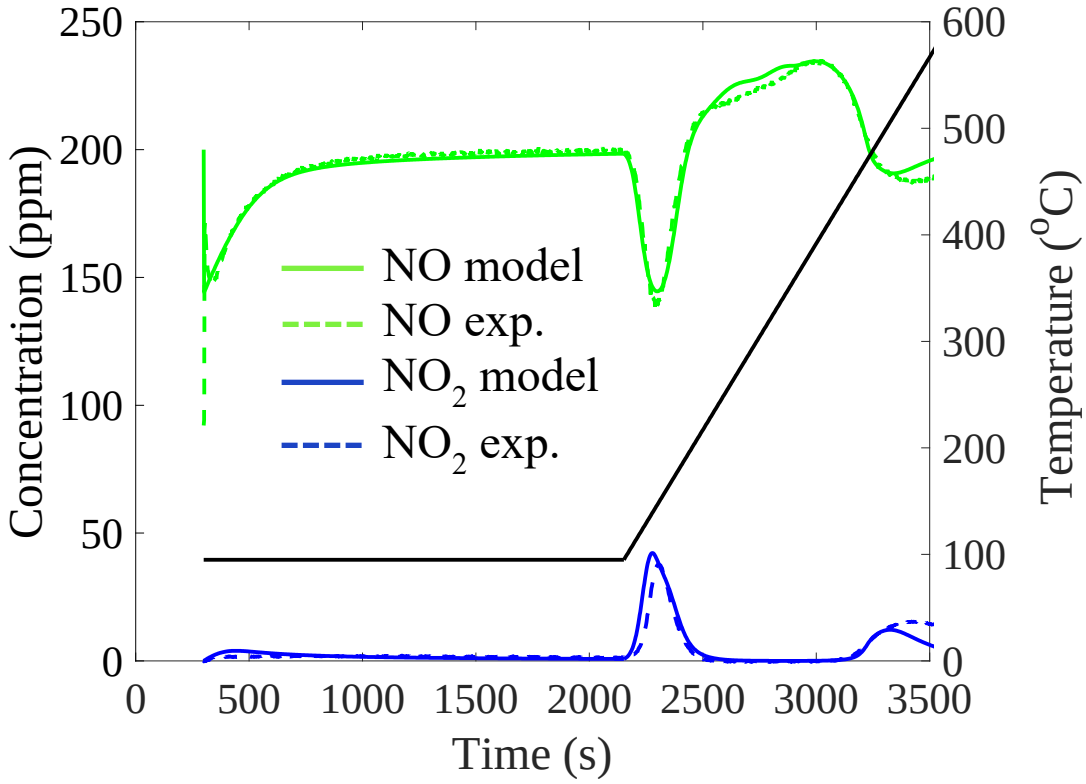

Figure 3.4 Experimental and model results of NO_x uptake at 95°C and TPD on Pd(1%)/SSZ-13 for a feed comprising of 200 ppm NO/ 12% O_2/ 6% CO_2/ 6% H_2O / balance N_2 and feed flowrate of 30 khr^{-1}.

Consider the uptake of NO on water adsorbed Z^-Pd^+ sites (reaction R3.9) as an example. The model tuning gives $E_{9b} = 204\ (1- 0.45\theta_{NO})$, which means that E_{9b} decreases from its maximum value of 204 kJ/mol to a minimum value at $\theta_{NO} \rightarrow 1$ of 112 kJ/mol. Thus, as NO coverage approaches unity, the strength of the NO binding is reduced by nearly a factor of 2. The result suggests that the local environment between proximal Pd^+ sites is impacted by the NO uptake. We speculate that crowding, possibly involving adsorbed H_2O, may be responsible.

A key utility of the model is in elucidating the main trends at the molecular level. This is accomplished by examining the predicted dependence of surface species site

fractions spanning uptake and release. Figure 3.5(a) shows the model-predicted site fraction of $Z^-Pd^+(NO)Pd^+(NO_2)(H_2O)Z^-$, $Z^-[PdOH]^+$-H_2O, $Z^-[PdOH]^+$, Z^-Pd^+; Figure 3.5(b) shows the predicted fraction of sites of Z^-Pd^+, Z^-Pd^+-NO, Z^-Pd^+-(H_2O)(NO); Figure 3.5(c) shows fraction of sites of $Z^-Pd^{2+}Z^-$, $Z^-Pd^{2+}Z^-$-NO, $(Z^-NO^+)(Z^-Pd^+$-NO), $Z^-Pd^{2+}Z^-$-(H_2O).

Figure 3.5(a) shows that just as the NO containing feed is directed to the catalyst, a large fraction of the $Z^-[PdOH]^+$ sites (~0.92) are occupied by H_2O due to the high concentration of H_2O in the feed (6%). Competitive uptake of NO (by R3.4) on the small fraction of $Z^-[PdOH]^+$ sites that are available leads to an increase in fraction of sites of the surface complex $Z^-Pd^+(NO)Pd^+(NO_2)(H_2O)Z^-$. The subsequent generation of NO_2 and H_2O (by R3.5) leads to a gradual decrease in $Z^-[PdOH]^+$-H_2O and corresponding increase in the fraction of sites of vacant reduced sites (Z^-Pd^+). At the onset of the temperature ramp (TPD), a noted, sharp decrease in the fraction of sites of $Z^-[PdOH]^+$-H_2O conveys the desorption of H_2O from $Z^-[PdOH]^+$ sites (reverse of R3.6). This frees-up sites for additional NO to adsorb, subsequently forming Z^-Pd^+ sites through R3.4 + R3.5. Above ~350℃, re-oxidation occurs of the reduced Pd sites Z^-Pd^+ back to $Z^-[PdOH]^+$ sites. In the sustained presence of NO additional NO_2 is formed by reaction R3.5 while reversibility leads to a local maximum in its production.

Figure 3.5(b) shows the model-predicted adsorbed species fraction of sites during uptake and TPD for the Z^-Pd^+ sites. Consistent with the gradual formation of the surface complex, $Z^-Pd^+(NO)Pd^+(NO_2)(H_2O)Z^-$ (via R3.4), is the gradual increase in NO adsorbed on Pd^+; i.e., Z^-Pd^+-NO (via R3.7) during the uptake at 95℃.

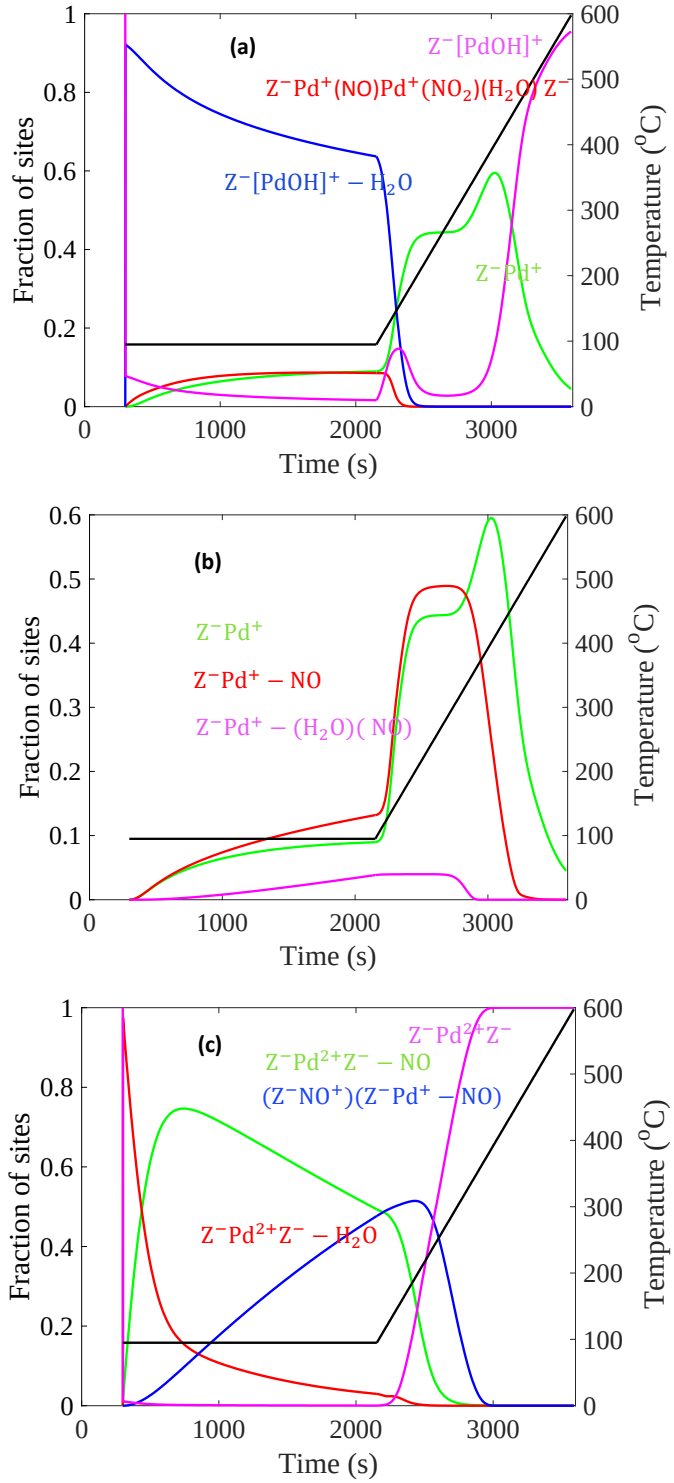

Figure 3.5 Coverage of different species on site (a) $Z^{-}[PdOH]^{+}$, (b) $Z^{-}Pd^{+}$, and (c) $Z^{-}Pd^{2+}Z^{-}$, during uptake of NO_x at 95°C and TPD for a feed comprising of 200 ppm NO/ 12% O_2/ 6% CO_2/ 6% H_2O / balance N_2 and feed flowrate of 30 khr^{-1}.

A smaller fraction of NO adsorbs on H_2O occupied Pd^+ (via R3.9). At the start of TPD, H_2O desorbs from $Z^-[PdOH]^+$ sites (via reverse of R3.6), leading to an increase in Z^-Pd^+ sites for additional NO uptake. This leads to an increase in Z^-Pd^+-NO (via R3.7). Eventually there is a sharp drop in Z^-Pd^+-NO at ~380℃ due to NO desorption from reduced sites (via reverse of R3.7 and R3.9). Further, the fraction of sites of Z^-Pd^+ decreases sharply at ~400℃ due to their re-oxidation (via R3.0). Figure 3.5(c) shows the species site fractions on isolated $Z^-Pd^{2+}Z^-$ sites. Again, just as the NO containing feed is directed to the catalyst, most of these sites (~0.98) are occupied with H_2O. There is a sequential uptake of NO onto the $Z^-Pd^{2+}Z^-$ sites. This is evidenced by the sharp increase in $Z^-Pd^{2+}Z^-$-NO at short times to a maximum, followed by a decrease at the expense of an increase in the fraction of sites occupied by two NO's, forming $(Z^-NO^+)(Z^-Pd^+\text{-NO})$. At the start of TPD, NO desorbs from $Z^-Pd^{2+}Z^-$ sites at ~150℃. The NO desorption is sharp, as evidenced by the steep decrease in sites occupied by one or two NO's. According to or DFT calculations, NO has a higher binding energy (-240 kJ/mol) on Z^-Pd^+ sites than on $Z^-Pd^{2+}Z^-$ (-122 kJ/mol). As a result, the model predicts NO desorption from $Z^-Pd^{2+}Z^-$ sites at a lower temperature (~150℃) than from Z^-Pd^+ sites (~340℃).

The uptake of NO on Pd/SSZ-13 in the presence of H_2O is a strong function of temperature [37,38]. At uptake temperatures below 100℃ most of the Pd cationic sites and essentially all of the Brønsted acid sites are occupied by H_2O [37]. Further, the increase in temperature during TPD leads to desorption of H_2O from the Pd sites at temperatures near 100℃. For this reason, at lower uptake temperatures less NO adsorbs during the first adsorption regime compared to the second adsorption regime encountered during the TPD. With increasing uptake temperature there is an increase in the amount of NO adsorbed

during first adsorption regime and a corresponding decrease in the second adsorption regime.

We conducted model validation simulations of experiments obtained under different operating conditions than used for the model tuning. Specifically, NO uptake was simulated for several uptake temperatures in the 75℃ to 150℃ range, followed by TPD. Figure 3.6 shows the measured and model-predicted NO uptake (at 75℃) and release (during TPD). None of the kinetic parameters were adjusted in this validation. At this lower uptake temperature of 75℃ most of the sites are covered with H_2O (indicated by model predicted coverages not shown here), indirectly evidenced by the negligible NO uptake during first NO uptake regime. During TPD the H_2O desorbs, resulting in the pronounced NO uptake at ~120℃. The model predicts this result and the NO_2 release during TPD. Similarly, Figure 3.7 shows the experimental and model-predicted NO uptake at 88℃ and its release during TPD. As explained above, an increase in uptake temperature from 75 to 88℃ results in a shift in some of the NO being adsorbed in the first regime, evidenced by the shallow dip at the start of the experiment. Again, the model captures these trends quite well. Figure A. 15 shows that a significant increase in uptake temperature to 125℃ results in nearly all of the NO being adsorbed in the first regime. In addition, some NO_2 is observed and predicted during this uptake. Finally, with a further increase in uptake temperature to 150℃, all the NO adsorbs during the first NO uptake regime (Figure A. 16). This is a result of the uptake of H_2O on the Pd cationic sites being low, NO does not have to compete with H_2O for the active sites. The model is able to capture it as well.

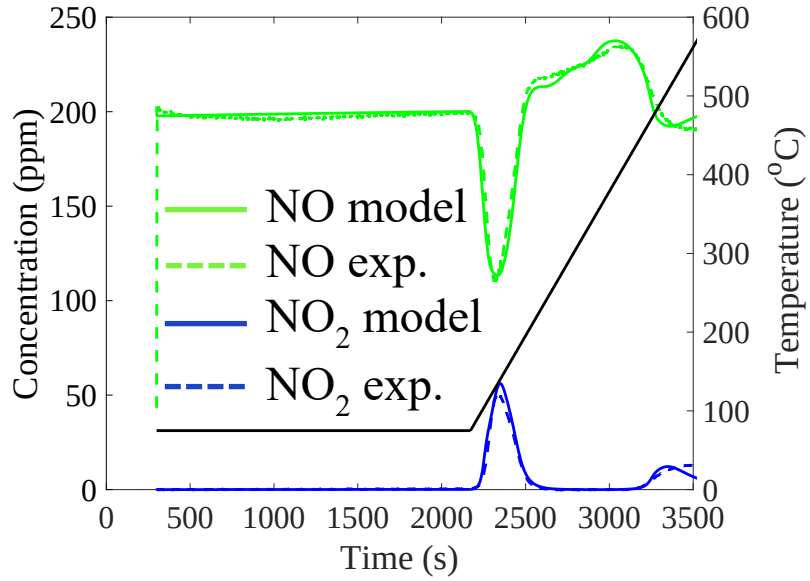

Figure 3.6 Experimental and model results of NO_x uptake at 75°C and TPD on Pd(1%)/SSZ-13 for a feed comprising of 200 ppm NO/ 12% O_2/ 6% CO_2/ 6% H_2O / balance N_2 and feed flowrate of 30 khr^{-1}.

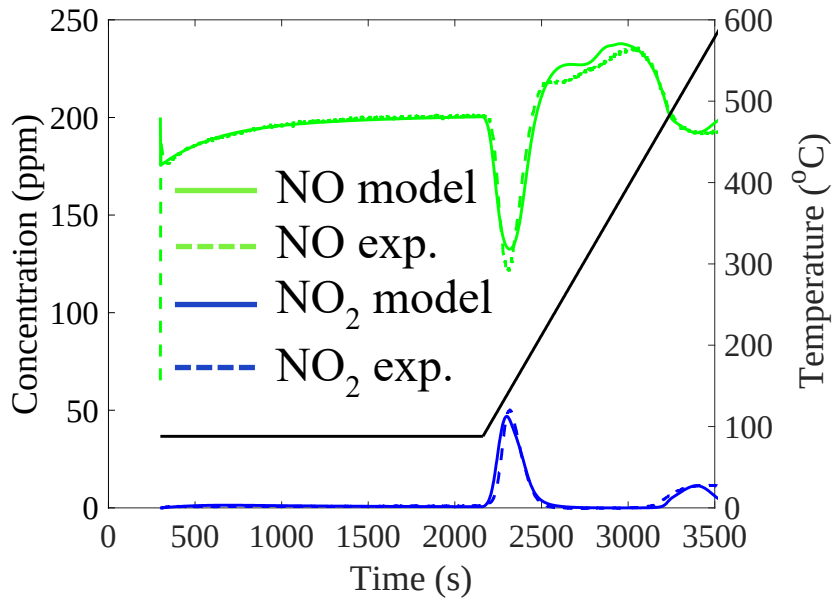

Figure 3.7 Experimental and model results of NO_x uptake at 88°C and TPD on Pd(1%)/SSZ-13 for a feed comprising of 200 ppm NO/ 12% O_2/6% CO_2/ 6% H_2O / balance N_2 and feed flowrate of 30 khr^{-1}.

To further demonstrate the model robustness, the integral NO uptake prediction of model and experimental results for both the first and second adsorption regimes are shown in Figure 3.8. The model is able to predict the experimental results within ~10%. The model

was further validated at a higher feed flowrate. Figure A. 17 compares the measured and predicted NO uptake and NO_2 generation and desorption profiles for experiment conducted at a higher feed flowrate of 45 khr^{-1} and uptake temperature of 95℃. Collectively, these validations show that that the model satisfactorily predicts NO uptake and NO_2 generation over a wide range of experimental conditions.

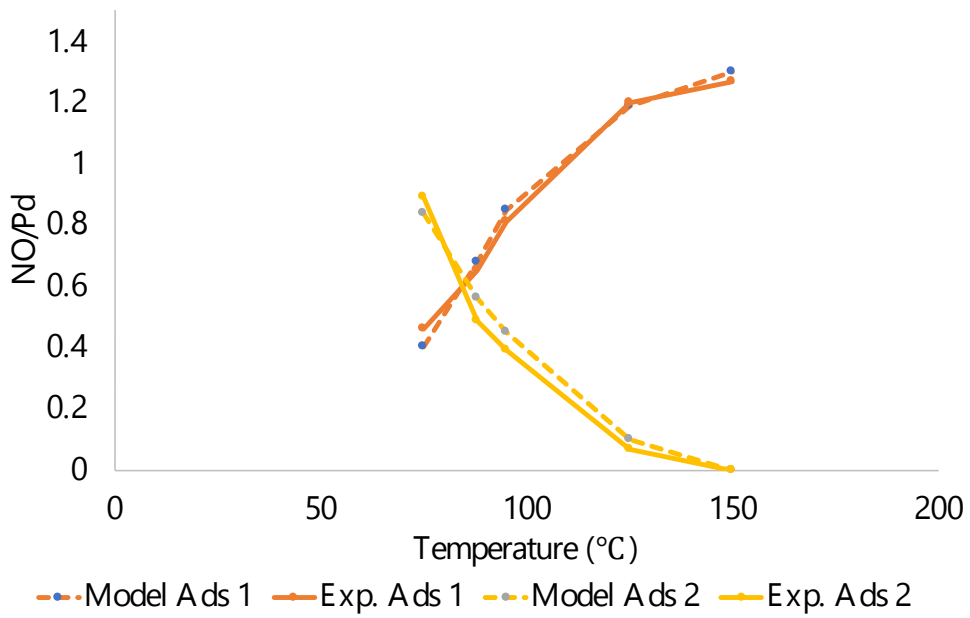

Figure 3.8 Experimental and model predicted values of NO/Pd for the two NO adsorption regimes at different uptake temperatures.

3.2.4 NO + CO feed

3.2.4.1 Development of reaction scheme for NO+CO

In this section we develop the microkinetic model for NO uptake on Pd/SSZ-13 in the presence of reductant CO.

Table 3.4 provides the proposed 9-step reaction sequence for NO uptake on Pd/SSZ-13 in the presence of CO. The proposed steps are in addition to the NO-only steps (Table 3.2). The observed CO_2 generation during NO uptake suggests the reduction of Z^-

$[PdOH]^+$ sites by CO to Z^-Pd^+ sites. Consistent with the NO-only feed, coupled $Z^-[PdOH]^+$ reduction occur as described by reactions R3.11-R3.13. Reactions R3.11 and R3.12 represent the reduction of two adjacent $Z^-[PdOH]^+$ sites to two Z^-Pd^+ sites. R3.11 and R3.12 are analogous to R3.4 and R3.5 for the NO-only feed, the difference being that CO rather than NO serves as the reductant of the $Z^-[PdOH]^+$ to Z^-Pd^+. Reaction R3.11 describes NO and CO adsorption onto proximal $Z^-[PdOH]^+$ sites, forming the surface complex $Z^-[Pd(COOH)]^+[PdOH]^+(NO)Z^-$. The complex formation is depicted as concurrent NO and CO adsorption rather a sequential addition; here the intent is to reduce the number of reactions. The reduction reaction R3.12 involves the transfer of one electron to each Pd(II) cation, contributed from the loss of two electrons during the oxidation of CO to CO_2. To examine the role of CO in more detail and to expand the scheme if needed, an experiment was carried out to analyze CO uptake on Pd/SSZ-13 without NO in the feed. The results in Figure A. 18 show that like NO, CO also adsorbs on Pd/SSZ-13. The data show an uptake of CO and generation of CO_2, suggesting a reduction process similar to the NO+CO feed. To this end, reaction R3.13 is added to the scheme; it involves the same $Z^-[PdOH]^+$ to Z^-Pd^+ reduction but with two CO molecules, leading to one bound CO and one generated CO_2. The estimated activation energies for reactions R3.11, R3.12 and R3.13 are provided in Table 3.5.

DFT calculations by us and Mei et al. [53] assess the nature of the adsorption of CO on $Z^-[PdOH]^+$, represented by reaction R3.14, while R3.15 describes the uptake of CO on $Z^-Pd^{2+}Z^-$. The calculations show that NO adsorbs more strongly on Pd than does CO; during the model tuning the binding energy of CO on $Z^-Pd^{2+}Z^-$ was constrained to be less than the binding energy of NO on $Z^-Pd^{2+}Z^-$. According to DFT calculations by Mei et al.

[53] (for Pd/BEA) and our own for Pd/SSZ-13, NO and CO co-adsorb on Z^-Pd^+ and $Z^-Pd^{2+}Z^-$ sites; these are as described by reactions R3.16 and R3.17, respectively. Both Vu et al. [22] and Khivantsev et al. [24] reported that reaction R3.17 may be responsible for an increase in low temperature NO uptake in the presence of CO. The formation of CO_2 above ~180℃ and the consumption of CO indicates that Pd/SSZ-13 catalyzes CO oxidation. Reactions R3.18 and R3.19 describes the oxidation of CO adsorbed on Pd^+ and $Z^-Pd^{2+}Z^-$ sites, respectively, by gas phase O_2.

Table 3.4 Reaction Mechanism for NO+CO feed [S_1 - $Z^-Pd^{2+}Z^-$; S_2 - $Z^-[PdOH]^+$; S_3 - Z^-Pd^+; S_5 - Z^- $[Pd(COOH)]^+[PdOH]^+(NO)Z^-$]

Reaction	Reaction step	Rate expression (R_f - R_b)
R3.11	$NO + CO + 2Z^-[PdOH]^+ \leftrightarrow Z^-[Pd(COOH)]^+[PdOH]^+(NO)Z^-$	$k_{11f}X_{NO}X_{CO}\theta_{vS2}^2C_{S2}^2$- $k_{11b}\theta_{S5}C_{S2}^2$
R3.12	$Z^-[Pd(COOH)]^+[PdOH]^+(NO)Z^- \leftrightarrow Z^-Pd^+ + Z^-Pd^+ - NO + CO_2 + H_2O$	$k_{12f}\theta_{S5}C_{S2}^2$- $k_{12b}\theta_{S3}\theta_{NO-S3}X_{CO_2}X_{H_2O}C_{S2}^2$
R3.13	$2CO + 2Z^-[PdOH]^+ \leftrightarrow Z^-Pd^+ + Z^-Pd^+ - CO + CO_2 + H_2O$	$k_{13f}X_{CO}^2\theta_{vS2}^2C_{S2}^2$- $k_{13b}\theta_{S3}\theta_{CO-S3}X_{CO_2}X_{H_2O}C_{S2}^2$
R3.14	$CO + Z^-[PdOH]^+ \leftrightarrow Z^-[PdOH]^+ - CO$	$k_{14f}X_{CO}\theta_{vS2}C_{S2}$- $k_{14b}\theta_{CO-S2}C_{S2}$
R3.15	$CO + Z^-Pd^{2+}Z^- \leftrightarrow Z^-Pd^{2+}Z^- - CO$	$k_{15f}X_{CO}\theta_{S1}C_{S1}$- $k_{15b}\theta_{CO-S1}C_{S1}$
R3.16	$NO + CO + Z^-Pd^+ \leftrightarrow Z^-Pd^+ - (NO)(CO)$	$k_{16f}X_{NO}X_{CO}\theta_{S3}C_{S2}$- $k_{16b}\theta_{(NO)(CO)-S3}C_{S2}$
R3.17	$NO + CO + Z^-Pd^{2+}Z^- \leftrightarrow Z^-Pd^{2+}Z^- - (NO)(CO)$	$k_{17f}X_{NO}X_{CO}\theta_{S1}C_{S1}$- $k_{17b}\theta_{(NO)(CO)-S1}C_{S1}$
R3.18	$Z^-Pd^+ - CO + 0.5O_2 \rightarrow CO_2 + Z^-Pd^+$	$k_{18f}\theta_{CO-S3}X_{O_2}^{0.5}C_{S2}$
R3.19	$Z^-Pd^{2+}Z^- - CO + 0.5O_2 \rightarrow CO_2 + Z^-Pd^{2+}Z^-$	$k_{19f}\theta_{CO-S1}X_{O_2}^{0.5}C_{S1}$

Model tuning was conducted for the NO + CO feed as for the NO-only feed. A total of 16 pre-exponential factors, forward activation energies of R3.12, R3.13, and R3.14 and reverse activation energies for reaction steps R3.14, R3.15, R3.17 and R3.19 along with

the adsorption repulsion coefficients for R3.14, R3.16 and R3.17 (□$_i$, i = 15, 17, 18) were estimated based on a fit of NO uptake at 98℃ and TPD data (Figure 3.9). The model was tuned for the 98℃ uptake + TPD experiment comprising the NO, CO and CO_2 effluent concentrations spanning the uptake and TPD. The results are shown in Figure 3.9(a); an enlarged view of NO and NO_2 profiles are shown in Figure 3.9. Total number of 1801 data points were used for the parameter estimation.

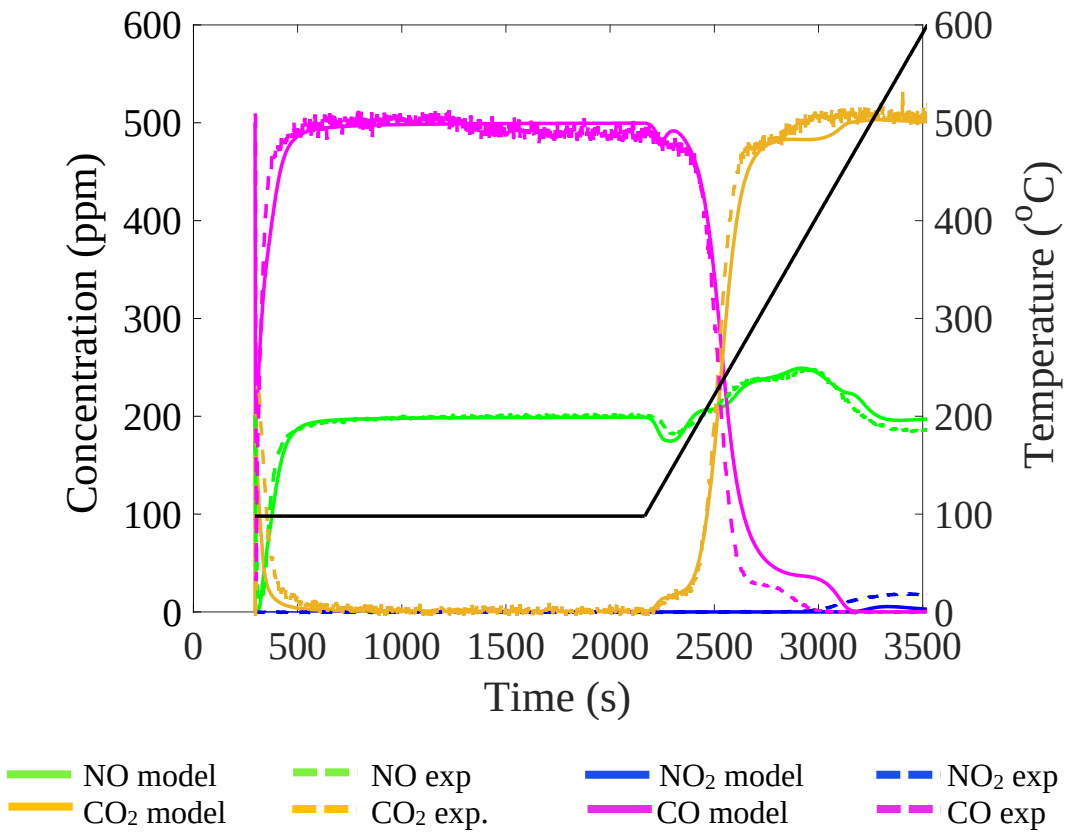

Figure 3.9 (a)Experimental and model results for uptake at 98°C and TPD on Pd(1%)/SSZ-13 for a feed comprising of 200 ppm NO/500 ppm CO/ 12% O_2/ 6% H_2O / balance N_2 and feed flowrate of 30 khr^{-1}.

Table 3.5 Kinetic Parameters for NO+CO feed model

Reaction no.	**Pre-exponential factor**		**Activation Energy (kJ mol^{-1})**		**α**	**DFT calculated electronic energies (kJ mol^{-1})**
						SSZ-13
R3.11	A_{11f} A_{11b}	1e7 2e17	E_{11f} E_{11b}	0 215		**-215**
R3.12	A_{12f} A_{12b}	1e9 2e16	E_{12f} $E1_{2b}$	39 148		**-109**
R3.13	A_{13f} A_{13b}	4e8 2e14	E_{13f} E_{13b}	30 269.5		**-239.5**
R3.14	A_{14f} A_{14b}	4e6 1e15	E_{14f} E_{14b}	30 140	0.35	
R3.15	A_{15f} A_{15b}	6e2 1e9	E_{15f} E_{15b}	0 110		
R3.16	A_{16f} A_{16b}	8e5 2e17	E_{16f} E_{16b}	0 246	0.4	**-310.8**
R3.17	A_{17f} A_{17b}	8e6 8e13	E_{17f}	0 150	0.3	
R3.18	A_{18f}	6e8	E_{18f}	134.7		**134.7**
R3.19	A_{19f}	5e7	E_{19f}	80		

3.2.4.2 Modeling results for NO+CO

Experimental and model results for NO+CO feed at an uptake temperature of 98℃ are shown in Figure 3.9. Simultaneous uptake of NO and CO occurs when the feed contacts the catalyst. The release of CO oxidation product CO_2 implies a surface reduction. Uptake experiments conducted at temperatures as low as 70℃ (Figure A. 19) show simultaneous uptake of NO and CO along with generation of CO_2. In contrast, for the NO-only feed the generation of NO_2 was not observed until ~120℃. DFT-calculated energies and activation barriers are consistent with these measurements. The DFT-calculated energy for NO_2 and H_2O production (reaction R3.5) is 172 kJ/mol (E_{5f} – E_{5b}), indicating an endothermic

reaction. In contrast, the corresponding energy for reaction R3.12 is -109 kJ/mol (E_{12f} – E_{12b}), an exothermic reaction. Using these values, the model captures the initial uptake of NO and CO and the simultaneous release of CO_2. The model also captures the observed secondary NO uptake during the TPD at a temperature of ~120℃ along with the consumption of CO and release of CO_2. Finally, interesting features from the experiments are evident in the NO+CO feeds suggest a rather complex process during the temperature ramp. Figure 3.9(a) indicates that the approach of the CO and CO_2 concentrations to 0 and 500 ppm, respectively, are somewhat protracted rather than being sharper as one would conventionally expect. According to the model this is due to the difference in CO oxidation rates of reactions R3.18 and R3.19.

To better understand the coupled uptake, desorption, and reactions, Figure 3.10(a) – (c) shows the surface species fraction of sites spanning the uptake and release. Figure 3.10 (a) shows the model-predicted fraction of sites of $Z^-[PdOH]^+$-CO, $Z^-[PdOH]^+$ -H_2O, $Z^-[PdOH]^+$, and Z^-Pd^+, Figure 3.10 (b) shows fraction of sites of Z^-Pd^+, Z^-Pd^+-NO, Z^-Pd^+-CO, and Z^-Pd^+-(CO)(NO); Figure 3.10 (c) shows fraction of sites of $Z^-Pd^{2+}Z^-$, $Z^-Pd^{2+}Z^-$-NO, $(Z^-NO^+)(Z^-Pd^+$-NO), $Z^-Pd^{2+}Z^-$-(H_2O), $Z^-Pd^{2+}Z^-$-(CO), and $Z^-Pd^{2+}Z^-$-(CO)(NO). The fractions of sites are normalized by the total concentration of each site type provided in Table 3.1.

As the NO+CO containing feed is directed to the catalyst, a large fraction of the $Z^-[PdOH]^+$ sites (~0.9) are occupied by H_2O due to the high H_2O feed concentration (6%). The uptake of CO (by R3.14) on $Z^-[PdOH]^+$ sites leads to formation of $Z^-[PdOH]^+$-CO. Competitive uptake of NO + CO (by R3.11) on $Z^-[PdOH]^+$ sites forms the complex $Z^-[Pd(COOH)]^+[PdOH]^+(NO)Z^-$, which is converted to Z^-Pd^+ (by R3.12); formation of Z^-Pd^+

sites is seen in Figure 3.10(a). The generation of CO_2 and H_2O by R3.12 and R3.13 leads to a gradual increase in the fraction of sites of Z^-Pd^+ associated sites (Figure 3.10(b)) and decrease in $Z^-[PdOH]^+$-H_2O. At the onset of TPD, the sharp decrease in the fraction of sites of $Z^-[PdOH]^+$-CO indicates the desorption of CO by from $Z^-[PdOH]^+$ sites (reverse of R3.14). At the same time, a sharp decrease in the fraction of sites of $Z^-[PdOH]^+$ -H_2O shows the release of H_2O by its desorption from $Z^-[PdOH]^+$ sites (reverse of R3.6). This frees-up sites for additional NO + CO to adsorb and subsequently form Z^-Pd^+ sites. Adsorbed species on Z^-Pd^+ sites (Figure 3.10(b)) begin desorbing above 250℃, leading to increase in vacant Z^-Pd^+ sites. Above ~400℃, the re-oxidation of the reduced Pd sites Z^-Pd^+ back to vacant $Z^-[PdOH]^+$ sites (by R3.10).

Figure 3.10(b) shows the model-predicted adsorbed species site fractions during uptake and TPD on the Z^-Pd^+ sites. The formation of Z^-Pd^+ sites by reaction R3.12 and R3.13 leads to formation of Z^-Pd^+-NO, Z^-Pd^+-CO, and Z^-Pd^+-(CO)(NO) sites during the uptake at 98℃. At the start of TPD as explained earlier, H_2O desorbs from $Z^-[PdOH]^+$ sites which forms additional Z^-Pd^+ sites by R3.12. An increase in Z^-Pd^+ sites leads to an increase in NO and CO uptake on Z^-Pd^+ sites. This leads to an increase in Z^-Pd^+-NO, and Z^-Pd^+-(CO)(NO) sites. Eventually there is a drop in Z^-Pd^+-NO, and Z^-Pd^+-(CO)(NO) sites at above ~250℃ due to desorption from reduced Z^-Pd^+ sites. In the presence of O_2 in the feed CO on Z^-Pd^+ sites are oxidized to CO_2 by reaction R3.18.

Figure 3.10(c) shows the species site fractions on isolated $Z^-Pd^{2+}Z^-$ sites. Again, as the NO+CO containing feed is switched to the catalyst, most of these sites (~0.98) become occupied with H_2O due to the high H_2O feed concentration (6%). There is uptake of NO and CO onto the $Z^-Pd^{2+}Z^-$ sites forming $Z^-Pd^{2+}Z^-$-NO, (Z^-NO^+)(Z^-Pd^+-NO), $Z^-Pd^{2+}Z^-$-CO

and $Z^-Pd^{2+}Z^-$-(CO)(NO) sites by reactions R3.1, R3.2, R3.15 and R3.17. This is evidenced by the sharp increase in $Z^-Pd^{2+}Z^-$-NO at short times to a maximum, followed by a decrease at the expense of an increase in the fraction of sites occupied by two NO's, (Z^-NO^+)(Z^-Pd^+-NO). At the start of TPD NO and CO desorbs from $Z^-Pd^{2+}Z^-$ sites at ~150℃. The sites occupied by two NO molecules desorbs at ~250℃. According to the DFT calculations, NO has a higher binding energy of -240 kJ/mol on Z^-Pd^+ sites as compared to -122 kJ/mol on $Z^-Pd^{2+}Z^-$. As a result, the model predicts NO desorption from $Z^-Pd^{2+}Z^-$ sites at a lower temperature than from Z^-Pd^+ sites (>300℃). Different binding energies of CO on Z^-Pd^+ and $Z^-Pd^{2+}Z^-$ sites results in different rates of oxidation of CO bound to these two sites. According to model this is the reason that the approach of the CO and CO_2 concentrations to 0 and 500 ppm, respectively, are somewhat protracted rather than being sharper as one would conventionally expect. In the presence of O_2 in the feed CO on $Z^-Pd^{2+}Z^-$ sites are oxidized to CO_2 by reaction R3.19.

The model was validated at the higher uptake temperature of 120℃. Experimental and modeling profiles are shown in Figure A. 20. At this higher uptake temperature more NO and CO is adsorbed during the first uptake regime along with a heightened CO_2 spike. This is due to less blocking as a result of lower H_2O coverage.

3.2.5 NO+ C_2H_4 feed

3.2.5.1 Development of reaction scheme for NO+C_2H_4

In this section we present the microkinetic scheme for NO uptake on Pd/SSZ-13 in the presence of C_2H_4. Keeping with our approach for the NO+CO feed, our intent is to devise a microkinetic scheme that predicts the main features of the data.

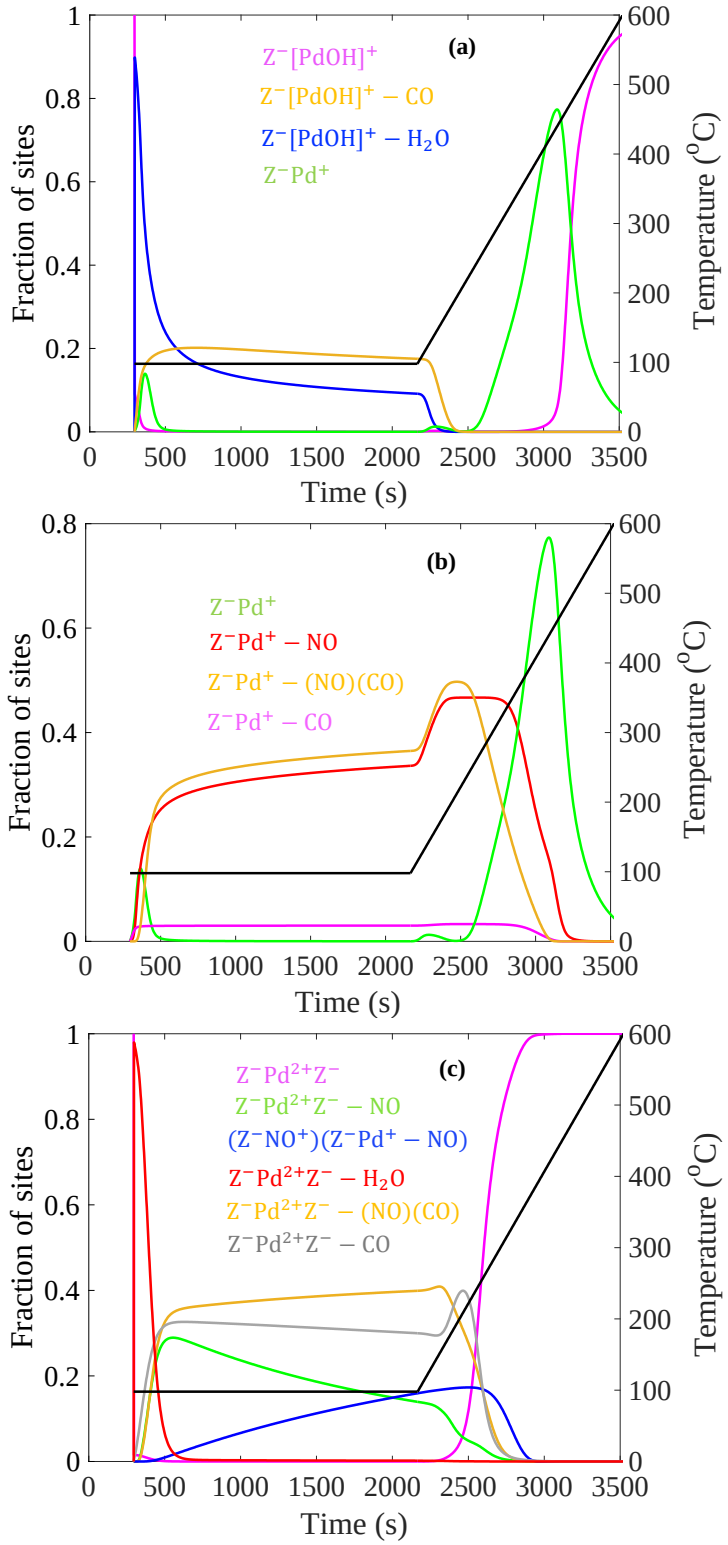

Figure 3.10 Coverage of different species on site (a) $Z^{-}[PdOH]^{+}$, (b) $Z^{-}Pd^{+}$, and (c) $Z^{-}Pd^{2+}Z^{-}$, during uptake of NO at 98°C and TPD for a feed comprising of 200 ppm NO/ 500 ppm CO/ 12% O_2/ 6% H_2O / balance N_2 and feed flowrate of 30 khr^{-1}.

The oxidation of C_2H_4 to CO (partial) and CO_2 (complete) is likely catalyzed by one or more of the several Pd cationic species. On the other hand, generation of C_2H_4O appears to be associated with the $[PdOH]^+$ to Pd^+ reduction. Absent a comprehensive molecular modeling of each of the steps along with corroborating experiments, our approach in proposing a microkinetic scheme is to capture the main features and trends in the uptake and release data. With this in mind, Table 3.6 provides a 12-step reaction sequence for NO uptake on Pd/SSZ-13 in the presence of C_2H_4; these are in addition to the steps involved for the NO-only feed (Table 3.2). Steps are added only if deemed necessary based on the data and/or availability of DFT analyses. Kinetic parameters for the related reactions are given in Table 3.7.

The uptake phase is first considered. As soon as the feed containing NO+C_2H_4 contacts the catalyst, C_2H_4O is generated. Reactions R3.20 and R3.21 describe the reduction of two adjacent $Z^-[PdOH]^+$ sites to Z^-Pd^+ sites. These reactions follow from R3.4 and R3.5 for the NO-only feed and R3.11 and R3.12 for the NO+CO feed. The difference is that instead of two NO molecules reducing $Z^-[PdOH]^+$ sites and forming NO_2, the concurrent addition of NO and C_2H_4 reduces $Z^-[PdOH]^+$ sites to Z^-Pd^+, generating C_2H_4O as the C_2H_4 oxidation product. The R3.20 + R3.21 sequence follows from the observation that NO is required for C_2H_4O formation as negligible C_2H_4O is observed without NO in the feed [63]. Further, the C_2H_4 consumed during uptake exceeds the C_2H_4O generated, suggesting that C_2H_4 is also adsorbed on Pd sites. To this end, reactions R3.22 to R3.25 describe the uptake of C_2H_4 on different Pd sites; R3.22 involves the adsorption of C_2H_4 onto H_2O occupied Z^-Pd^+; R3.23 involves the co-adsorption of NO and C_2H_4 onto $Z^-Pd^{2+}Z^-$ sites which is analogous to reaction R3.17 for NO+CO; R3.24 describes the adsorption of

C_2H_4 onto $Z^-[PdOH]^+$ sites. Reaction R3.25 describes the adsorption of C_2H_4 onto $Z^-Pd^{2+}Z^-$ sites.

Table 3.6 Reaction Mechanism for NO+C_2H_4 feed [S_1 - $Z^-Pd^{2+}Z^-$; S_2 - $Z^-[PdOH]^+$;S_3 – Z^-Pd^+; S_6 - $Z^-Pd^+(NO)Pd^+[(C_2H_4O)\ (H_2O)]Z^-$]

Reaction no.	Reaction step	Rate expression (R_f - R_b)
R3.20	$NO + C_2H_4 + 2Z^-[PdOH]^+ \leftrightarrow Z^-Pd^+(NO)Pd^+[(C_2H_4O)\ (H_2O)]Z^-$	$k_{20f}X_{NO}X_{C_2H_4}\theta_{vS2}^2C_{S2}^2$- $k_{20b}\theta_{S6}C_{S2}^2$
R3.21	$Z^-Pd^+(NO)Pd^+[(C_2H_4O)\ (H_2O)]Z^- \leftrightarrow Z^-Pd^+ - NO + Z^-Pd^+ + C_2H_4O + H_2O$	$k_{21f}\theta_{S6}C_{S2}^2$- $k_{21b}\theta_{S3}\theta_{NO-S3}X_{C_2H_4O}X_{H_2O}C_{S2}^2$
R3.22	$C_2H_4 + Z^-Pd^+ - H_2O \leftrightarrow Z^-Pd^+ - (H_2O)(C_2H_4)$	$k_{22f}X_{C_2H_4}\theta_{H_2O-S3}C_{S2}$- $k_{22b}\theta_{(H_2O)(C_2H_4)-S3}C_{S2}$
R3.23	$NO + C_2H_4 + Z^-Pd^{2+}Z^- \leftrightarrow Z^-Pd^{2+}Z^- - (NO)(C_2H_4)$	$k_{23f}X_{NO}X_{C_2H_4}\theta_{S1}C_{S1}$- $k_{23b}\theta_{(NO)(C_2H_4)-S1}C_{S1}$
R3.24	$C_2H_4 + Z^-[PdOH]^+ \leftrightarrow Z^-[PdOH]^+ - (C_2H_4)$	$k_{24f}X_{C_2H_4}\theta_{vS2}C_{S2}$- $k_{24b}\theta_{C_2H_4-S2}C_{S2}$
R3.25	$C_2H_4 + Z^-Pd^{2+}Z^- \leftrightarrow Z^-Pd^{2+}Z^- - C_2H_4$	$k_{25f}X_{C_2H_4}\theta_{S1}C_{S1}$- $k_{25b}\theta_{C_2H_4-S1}C_{S1}$
R3.26	$Z^-[PdOH]^+ - (C_2H_4) + 0.5O_2 \rightarrow Z^-[PdOH]^+ + C_2H_4O$	$k_{26f}\theta_{C_2H_4-S2}X_{O_2}^{0.5}C_{S2}$
R3.27	$Z^-Pd^{2+}Z^- - C_2H_4 + 2O_2 \rightarrow 2CO + 2H_2O + Z^-Pd^{2+}Z^-$	$k_{27f}\theta_{C_2H_4-S1}X_{O_2}^2C_{S1}$
R3.28	$Z^-Pd^+ - (H_2O)(C_2H_4) + 3O_2 \rightarrow Z^-Pd^+ + 2CO_2 + 3H_2O$	$k_{28f}\theta_{(H_2O)(C_2H_4)-S3}X_{O_2}^3C_{S2}$
R3.29	$C_2H_4O + 1.5O_2 + S \rightarrow 2CO + 2H_2O + S$	$k_{29f}X_{C_2H_4O}X_{O_2}^{1.5}C_S$
R3.30	$C_2H_4O + 0.5O_2 + S \rightarrow CH_4 + CO_2 + S$	$k_{30f}X_{C_2H_4O}X_{O_2}^{0.5}C_S$
R3.31	$C_2H_4O + 2.5O_2 + S \rightarrow 2CO_2 + 2H_2O + S$	$k_{31f}X_{C_2H_4O}X_{O_2}^{2.5}C_S$

Table 3.7 Kinetic Parameters for NO+C_2H_4 feed model

Reaction no.	Pre-exponential factor		Activation Energy (kJ mol^{-1})		α
R3.20	A_{20f} A_{20b}	2e6 1e17	E_{20f} E_{20b}	0 128	
R3.21	A_{21f} A_{21b}	5e7 2e10	E_{21f} E_{21b}	30 130	
R3.22	A_{22f} A_{22b}	5e2 7e10	E_{22f} E_{22b}	0 165	
R3.23	A_{23f} A_{23b}	1e8 1e14	E_{23f} E_{23b}	0 215	0.5
R3.24	A_{24f} A_{24b}	2e6 1e14	E_{24f} E_{24b}	30 130	
R3.25	A_{25f} A_{25b}	5e1 5e11	E_{25f} E_{25b}	0 165	
R3.26	A_{26f}	2e11	E_{26f}	100	
R3.27	A_{27f}	5e7	E_{27f}	80	
R3.28	A_{28f}	6.5e10	E_{28f}	120	
R3.29	A_{29f}	9e6	E_{26f}	40	
R3.30	A_{30f}	3.27e9	E_{30f}	70	
R3.31	A_{31f}	1e19	E_{31f}	160	

Figure 3.11 shows a complex process during the TPD. The C_2H_4 concentration starts decreasing at ~150℃ and approaches zero by ~350℃. Between those two temperature bounds there is a concurrent release of CO, C_2H_4O, CH_4 and CO_2, indicating both partial and complete C_2H_4 oxidation and C=C bond scission. C_2H_4O is observed initially, followed by CO, CO_2, and CH_4. Reactions R.26 to R3.31 are proposed to account for this sequence of products. R3.26 accounts for the oxidation of C_2H_4 adsorbed on Z^- $[PdOH]^+$ sites, forming C_2H_4O. Reaction R3.27 accounts for the oxidation of C_2H_4

adsorbed on $Z^-Pd^{2+}Z^-$ sites, forming CO while reaction R3.28 describes the oxidation of C_2H_4 adsorbed as Z^-Pd^+-(H_2O)(C_2H_4), forming CO_2. Not knowing which of the sites are responsible, we propose R3.29 as an overall reaction for oxidation of C_2H_4O to CO where S represents the sum of all the cationic Pd sites. By 350℃, the C_2H_4O is completely consumed and CH_4 is observed. Seddon et al. [60] reported that above 400℃ C_2H_4O decomposes to CH_4 and CO. In the presence of O_2, the generated CO is oxidized to CO_2. An inflection point occurs at ~ 350℃ at which the C_2H_4 profile exhibits a steeper decrease, at which point there is steep increase in CO_2 formation. To this end, CH_4 formation is proposed by a combination of C_2H_4O decomposition and CO oxidation; i.e., reaction R3.30. Reaction R3.31 is added which accounts for CO_2 from C_2H_4O.

3.2.5.2 Modeling results for NO+C_2H_4

The reactor model with NO+C_2H_4 reaction scheme was tuned using the 105℃ uptake and TPD data. Measured and model-predicted effluent concentrations of NO, C_2H_4, CO, CO_2, CH_4 and C_2H_4O (NO+C_2H_4 feed) are shown in Figure 3.11(a). The enlarged view of the NO and NO_2 profiles is shown in Figure 3.11(b). At the start of the experiment a large decrease in the NO concentration was accompanied by a decrease in C_2H_4 along with a spike of C_2H_4O. As for the NO+CO feed, more NO was adsorbed during the first uptake regime when the second reductant (C_2H_4 or CO) was present in addition to NO-only feed. This is clearly seen when comparing Figure 3.4 and 3.11(b).

The proposed microkinetic model satisfactorily reproduces most of the data features and trends. DFT calculations indicate that reactions R3.20 and R3.21 are exothermic. Fixing these DFT predicted values, the tuned model predicts NO and C_2H_4 uptake and C_2H_4O generation.

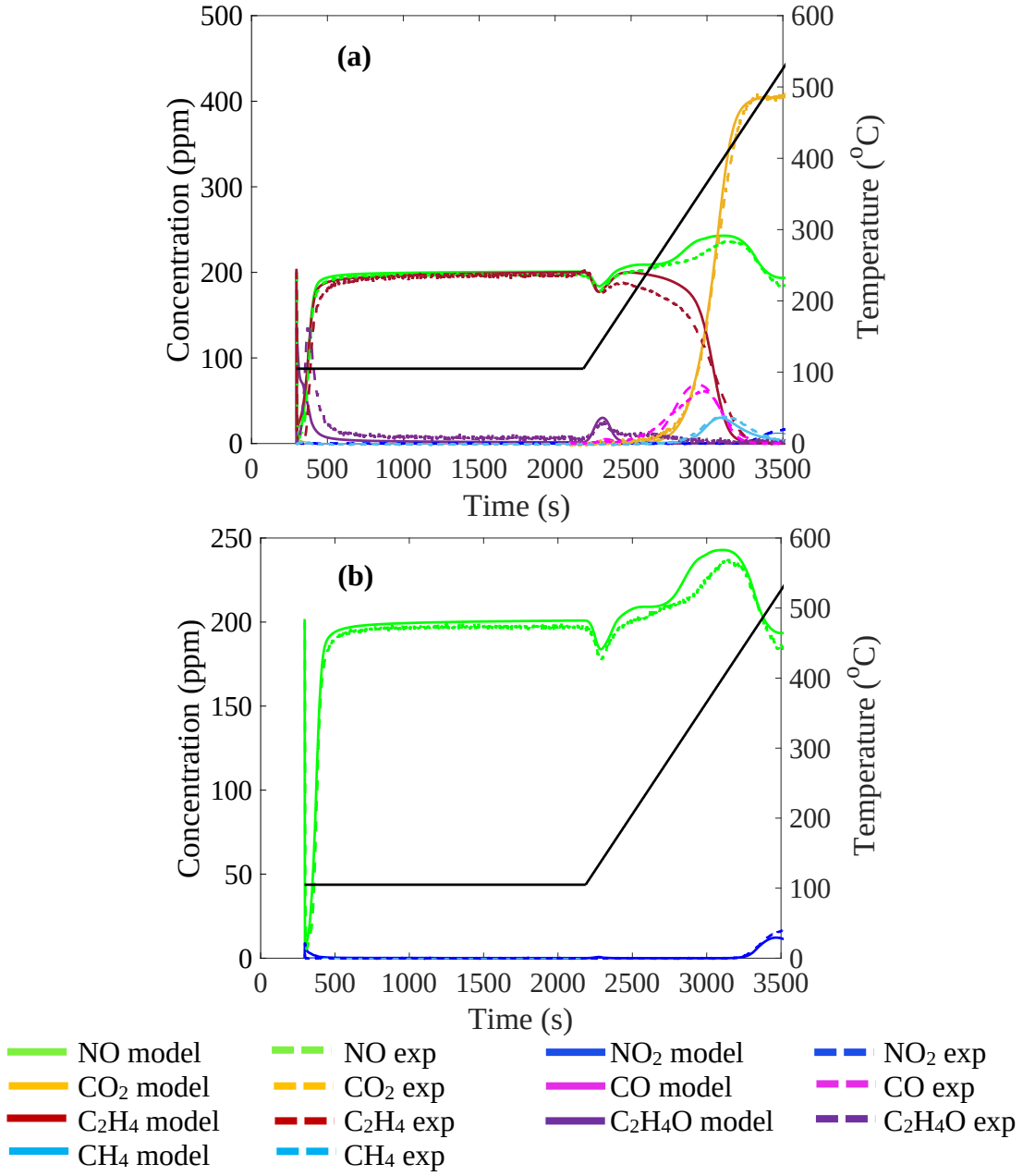

Figure 3.11 (a)Experimental and model results for uptake at 105°C and TPD on Pd(1%)/SSZ-13 for a feed comprising of 200 ppm NO/200 ppm C_2H_4/ 12% O_2/ 6% H_2O / balance N_2 and feed flowrate of 30 khr^{-1}, (b) Enlarged view of NO_x profile.

The model predicts the slightly lower NO uptake during the first regime with C_2H_4 compared to CO; compare Figure 3.9 and Figure 3.11. This is consistent with R3.11+R3.12 (CO as reductant) being more exothermic than R3.20 + R3.21 (C_2H_4 as reductant). At the

onset of the temperature ramp the model predicts the NO uptake and C_2H_4O spike at ~120°C. The oxidation of C_2H_4 to C_2H_4O, CO, and CO_2 during the TPD is also captured, along with the consumption of NO and subsequent generation of NO_2 at temperatures above 500°C, latter feature due to the combined oxidation of Z^-Pd^+ to $Z^-[PdOH]^+$ (via R3.10) and $Z^-[PdOH]^+$ reduction (via R3.4 + R3.5).

To better understand the coupled uptake, desorption, and reactions, Figure 3.12(a-c) show the predicted surface species fraction of sites spanning the uptake (at 105°C) and release (105 to 600°C). Figure 3.12(a) reports the model-predicted fraction of sites of $Z^-[PdOH]^+$-C_2H_4, $Z^-[PdOH]^+$-H_2O, $Z^-[PdOH]^+$, and Z^-Pd^+; Figure 3.12(b) shows the fraction of sites of Z^-Pd^+, Z^-Pd^+-NO, Z^-Pd^+-(C_2H_4)(H_2O), and Z^-Pd^+-(NO)(H_2O); Figure 3.12(c) shows fraction of sites of $Z^-Pd^{2+}Z^-$, $Z^-Pd^{2+}Z^-$-NO, (Z^-NO^+)(Z^-Pd^+-NO), $Z^-Pd^{2+}Z^-$-(H_2O), $Z^-Pd^{2+}Z^-$-(C_2H_4)(NO) and $Z^-Pd^{2+}Z^-$-C_2H_4. The fractions of sites are normalized by the total concentration of each site type.

As the NO+C_2H_4 containing feed is directed to the catalyst, a large fraction of the $Z^-[PdOH]^+$ (~0.88) is occupied by H_2O as earlier shown for the NO-only and NO+CO feeds (Figure 3.12(a)). The uptake of C_2H_4 on $Z^-[PdOH]^+$ sites (by R3.24) leads to the formation of $Z^-[PdOH]^+$-C_2H_4. The co-uptake of NO and C_2H_4 on $Z^-[PdOH]^+$ sites (by R3.20) forms the complex $Z^-Pd^+(NO)Pd^+[(C_2H_4O)(H_2O)]Z^-$. The predicted fraction of sites of the complex is negligible, indicating that it quickly decomposes (via R3.21), forming Z^-Pd^+ and Z^-Pd^+-NO (Figure 3.12(b)). Co-generation of C_2H_4O and H_2O (by R3.21) leads to a gradual increase in the fraction of sites of Z^-Pd^+ and decrease in $Z^-[PdOH]^+$-H_2O. Figure 3.12(b) also shows the predicted species fraction of sites during uptake and TPD on the Z^-Pd^+ sites. The formation of Z^-Pd^+ sites by reaction R3.21 leads to formation Z^-Pd^+-NO, Z^-

Pd^+-(C_2H_4)(H_2O), and Z^-Pd^+-(NO)(H_2O), sites during the uptake at 105℃. At the start of TPD as explained earlier, H_2O desorbs from $Z^-[PdOH]^+$ sites, forming additional Z^-Pd^+ sites (via R3.21).The fraction of sites of Z^-Pd^+ exhibits a maximum as NO, H_2O, and C_2H_4 are adsorbed, evidenced by the increase in Z^-Pd^+-NO, Z^-Pd^+-(C_2H_4)(H_2O), and Z^-Pd^+-(NO)(H_2O). At the onset of TPD, C_2H_4 and H_2O desorb from $Z^-[PdOH]^+$ sites, respectively via the reverse of R3.24 and R3.6. This frees-up sites for additional NO+C_2H_4 to adsorb and subsequently form Z^-Pd^+ sites through R3.20 + R3.21. Adsorbed species on Z^-Pd^+ sites (Figure 3.12(b)) starts desorbing above 300℃ leading to an increase in vacant Z^-Pd^+ sites. Above ~400℃, the re-oxidation occurs of the reduced Pd sites back to vacant $Z^-[PdOH]^+$ sites. Eventually there is a sharp drop in Z^-Pd^+-(C_2H_4)(H_2O), and Z^-Pd^+-(NO)(H_2O), sites at above ~300℃ due to desorption from reduced Z^-Pd^+ sites. Species from Z^-Pd^+-NO, sites starts desorbing at above ~350℃ leading to increase in Z^-Pd^+ sites which later gets oxidized to $Z^-[PdOH]^+$ sites.

Figure 3.12(c) shows the species coverage on isolated $Z^-Pd^{2+}Z^-$ sites. Again, as the NO+C_2H_4 containing feed is switched to the catalyst, most of these sites (~0.98) become occupied with H_2O due to the high H_2O feed concentration (6%). There is uptake of NO and C_2H_4 onto the $Z^-Pd^{2+}Z^-$ sites forming $^-$, $Z^-Pd^{2+}Z^-$-NO, (Z^-NO^+)(Z^-Pd^+-NO), $Z^-Pd^{2+}Z^-$-(C_2H_4)(NO) and $Z^-Pd^{2+}Z^-$-C_2H_4 sites by reactions R3.1, R3.2, R3.23 and R3.25. This is sharp increase in $Z^-Pd^{2+}Z^-$-NO at short time, followed by a decrease at the expense of an increase in the fraction of sites occupied by two NO's, (Z^-NO^+)(Z^-Pd^+-NO). At the start of TPD NO and C_2H_4 starts desorbing leading to increase in vacant $Z^-Pd^{2+}Z^-$ sites. By ~350℃ almost all the species are desorbed from $Z^-Pd^{2+}Z^-$ sites.

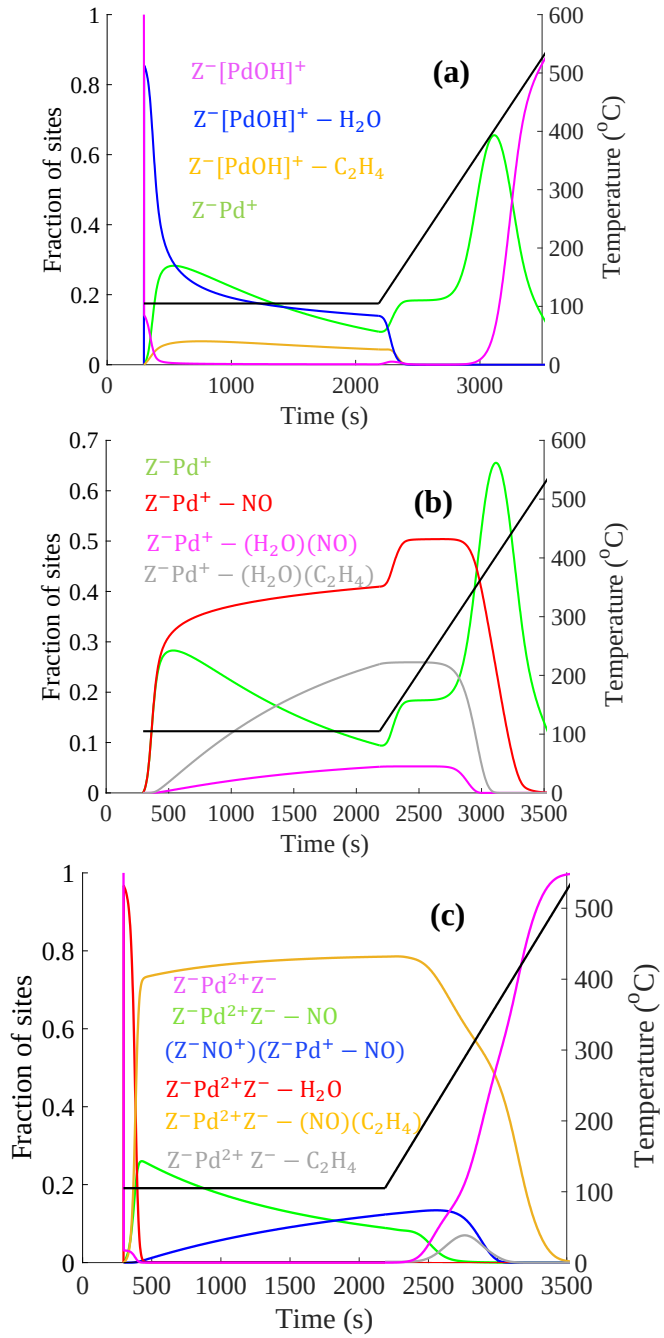

Figure 3.12 Coverage of different species on site (a) $Z^{-}[PdOH]^{+}$, (b) $Z^{-}Pd^{+}$, and (c) $Z^{-}Pd^{2+}Z^{-}$, during uptake of NO at 105°C and TPD for a feed comprising of 200 ppm NO/ 200 ppm C_2H_4/ 12% O_2/ 6% H_2O / balance N_2 and feed flowrate of 30 khr^{-1}.

The model was validated at a higher uptake temperature of 120°C. Measured and predicted profiles are shown in Figure 3.13. At the higher uptake temperature of 120°C, more NO and C_2H_4 adsorbs during the first adsorption regime with simultaneous

increase in generation of C_2H_4O compared to the second adsorption regime. This is because at high temperature of 120°C, less H_2O is adsorbed leaving more sites for the NO and C_2H_4 to be adsorbed.

Finally, the model was validated for the higher feed flowrate of 45 khr^{-1}. Figure A. 21 compares the measured and predicted NO_x, C_2H_4, CO, CO_2, CH_4 and C_2H_4O profiles spanning uptake and desorption for uptake conducted at 100°C. The model captures that experimental trend satisfactorily, conveying the robustness of the tuned model.

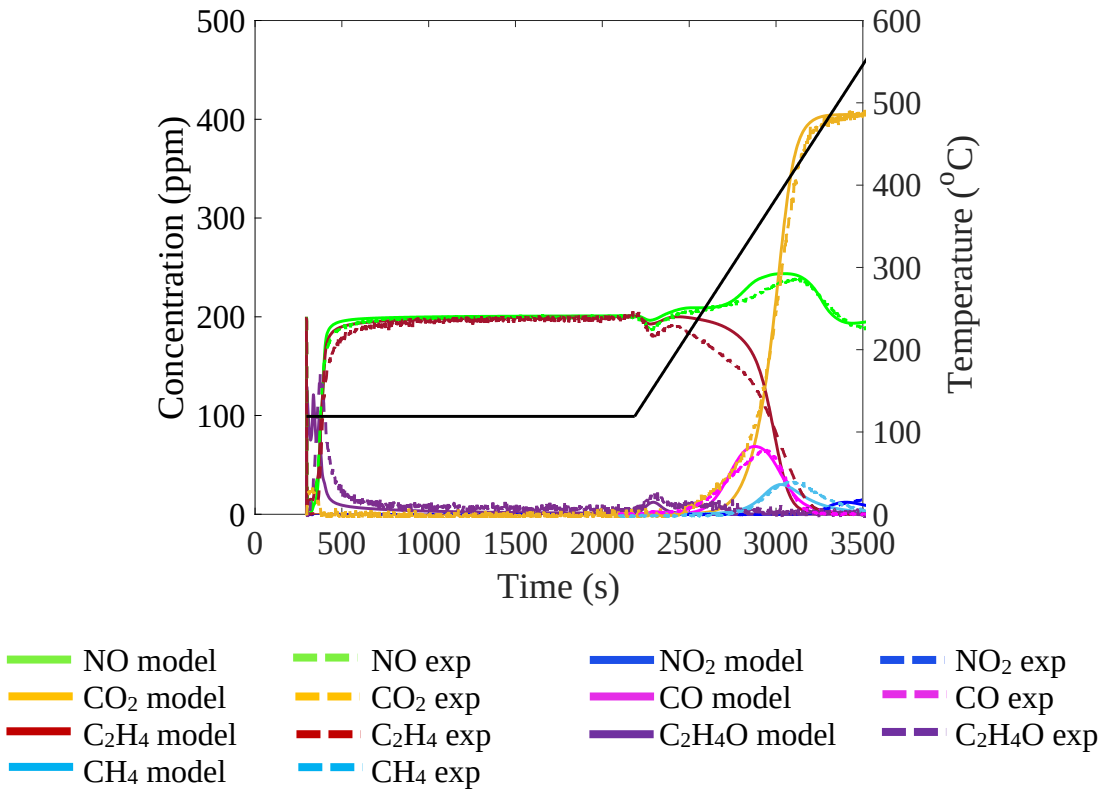

Figure 3.13 Experimental and model results for uptake at 120°C and TPD on Pd(1%)/SSZ-13 for a feed comprising of 200 ppm NO/200 ppm C_2H_4/ 12% O_2/ 6% H_2O / balance N_2 and feed flowrate of 30 khr^{-1}.

3.2.6 NO+CO+ C_2H_4 feed validation

In this section we present the model prediction for NO uptake on Pd/SSZ-13 in the presence of both CO and C_2H_4. The feed containing 200 ppm NO/ 200 ppm CO/ 200 ppm C_2H_4/12% O_2/ 6% H_2O / balance N_2 was used. The experimental and modeling uptake and

TPD profiles for several species for an uptake carried out at 118℃ are shown in Figure 3.14. All the reactions from Table 3.3, 3.4 and 3.6 were used and none of the kinetic parameters were altered in this validation. The model satisfactorily predicts the trend of uptake of NO, CO, and C_2H_4 during the uptake period of 30 min and then consecutive release of NO at higher temperatures during the TPD. The model also captures the decrease in CO and C_2H_4 concentrations at temperatures above ~220℃ along with their oxidations, resulting in generation of CO_2. The model slightly under predicts the steepness of the CO_2 curve. The likely reason is that the CO_2 is released at comparatively higher temperatures for the NO+C_2H_4 feed (Figure 3.11) compared to the NO+CO+C_2H_4 feed. Since none of the model kinetic parameters were altered for NO+CO+C_2H_4 feed (Figure 3.14), the model predicts a slightly less steep CO_2 profile.

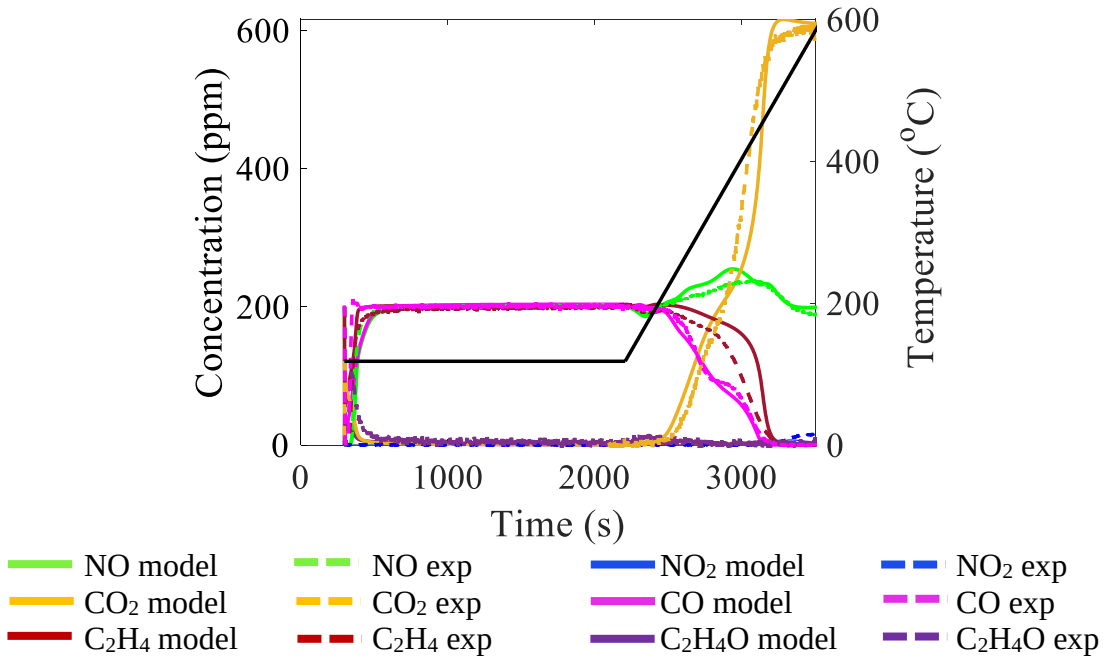

Figure 3.14 Experimental and model results for uptake at 118°C and TPD on Pd(1%)/SSZ-13 for a feed comprising of 200 ppm NO/ 200 ppm CO/ 200 ppm C_2H_4/ 12% O_2/ 6% H_2O / balance N_2 and feed flowrate of 30 khr^{-1}.

In summary, the developed model is able to predict the experimental trends of different species satisfactorily which shows the effectiveness of the model for capturing such a complex feed.

3.2.7 Integral trapping efficiency

In this section we examine the effectiveness of the model in predicting the important PNA metric, the integral NO trapping efficiency $\eta_T(t^*)$, defined as

$$\eta_T(t^*) = 100\left(1 - \frac{1}{t^* F_{NO}^o}\int_0^{t^*} F_{NO}(t)dt\right). \quad (3.5)$$

Here F_{NO}^o and F_{NO} are the NO feed and effluent molar flow rates and t^* is the exposure time. The trapping efficiency measures the percentage of NO that is retained by the unit over a specified period and is relevant to the cold-start NO of a vehicle.

Figure 3.15 compares the experimental and predicted transient dependence of $\eta_T(t^*)$ for NO only, NO+CO, and NO+C_2H_4 feeds at uptake temperatures of 95℃, 98℃ and 105℃, respectively. The model is effective in predicting the shape and magnitude of the $\eta_T(t^*)$ for each of the feeds. The comparison shows that the maximum value of $\eta_T(t^*)$ is ~88% for NO+C_2H_4 feed at an uptake temperature of 105℃ compared to ~82% for NO+CO feed at the uptake temperature of 98℃. $\eta_T(t^*)$ decreases more sharply for the NO+C_2H_4 feed, eventually becoming lower than $\eta_T(t^*)$ for the NO+CO feed after ~200 s of uptake time. In contrast, the maximum value of $\eta_T(t^*)$ for the NO-only feed at a slightly lower uptake temperature of 98℃ is only ~20% under otherwise identical conditions. This underscores the importance of the reductants in enhancing the NO uptake at lower temperatures in the presence of H_2O. $\eta_T(t^*)$ decreases monotonically with time, showing the decrease in instantaneous NO uptake due to decreasing number of available sites. Following from earlier discussion, the model predicts that CO is a more effective reductant

than C_2H_4 at the 200 ppm feed concentration. Both reductants enhance the NO uptake during the first uptake regime. The ranking is consistent with the energetics of the reduction of $Z^-[PdOH]^+$ sites to Z^-Pd^+ sites by R (R = NO, CO or C_2H_4) with adsorption of one NO on Pd^+. Specifically, for CO the predicted energy change (R3.11 + R3.12) is -324 kJ/mol. In contrast, the ΔH value for NO+C_2H_4 feed is -228 kJ/mol (R3.20 + R3.21). Finally, for NO only the □H is -112 kJ/mol for R3.4 + R3.5.

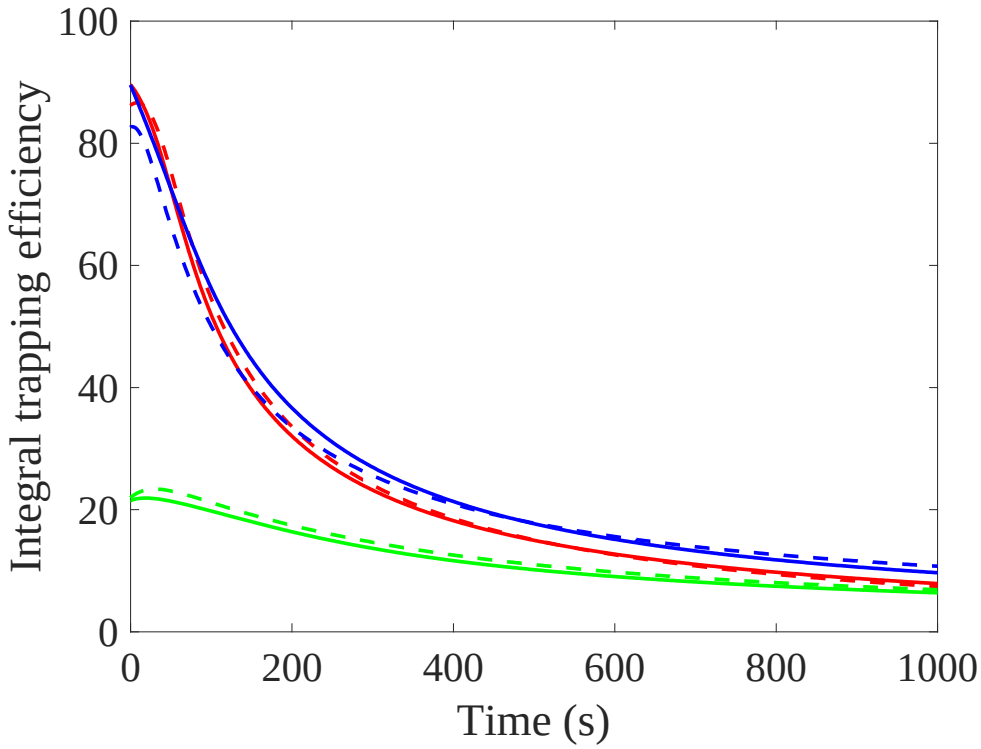

Figure 3.15 Integral trapping efficiency vs time plot for simple NO feed, NO+CO feed, and NO+C_2H_4 feed.

dashed line – experimental result, solid line – modeling results

3.2.8 Cold-start simulation: Comparison of reductants

It is also of interest to use the model to predict PNA performance under more realistic conditions. In practice, the vehicle exhaust temperature increases immediately, meaning there is no period of uptake at constant temperature. To this end, the model was run for the NO-only, NO+CO, and NO+C_2H_4 feeds during a faster temperature ramp of

40℃/min, starting at 30℃ and going to 600℃. The predicted NO effluent profiles are shown in Figure 3.16. There are a few features to note. First, for the NO-only feed there is no uptake of NO until the temperature reaches ~70℃ due to site blockage by H_2O. Second, there is only one NO uptake regime unlike the previous cases where there were two NO uptake regimes, one during the uptake and the other at the start of the TPD. Third, the effluent NO concentration reaches the feed concentration when the temperature is ~210℃ and then finally starts desorbing. The total NO absorbed is NO/Pd ~ 0.84 for the NO-only feed. For the NO+CO feed, NO starts adsorbing after the system reaches a temperature of ~45℃. The NO reaches the 200 ppm feed concentration when the temperature reaches ~200℃ at which point it begins to desorb. The total NO absorbed is NO/Pd ~1.02. For the NO+C_2H_4 feed, NO starts adsorbing after the system reaches a temperature of ~55℃. The NO increases to the feed concentration of 200 ppm when the temperature equals ~190℃. The total NO absorbed is NO/Pd ~ 0.86 for the case of NO+C_2H_4 feed. Finally, it is interesting to note that the predicted temperature of NO desorption is comparable for NO-only feed and NO+CO feeds; the desorption for both the cases continuous till ~480℃. For NO+C_2H_4 feed the desorption continues till ~510℃. These trends are consistent with the experimental results.

3.2.9 Comparison of NO uptake on Pd/SSZ-13 and Pd/ZSM-5

Here we use the model to compare the NO uptake performance of Pd-exchanged small-pore SSZ-13 and medium-pore ZSM-5 frameworks. The model developed in the current study for NO uptake on Pd/SSZ-13 and the model developed by Ambast et al. [37] for Pd/ZSM-5 were used to conduct the comparison.

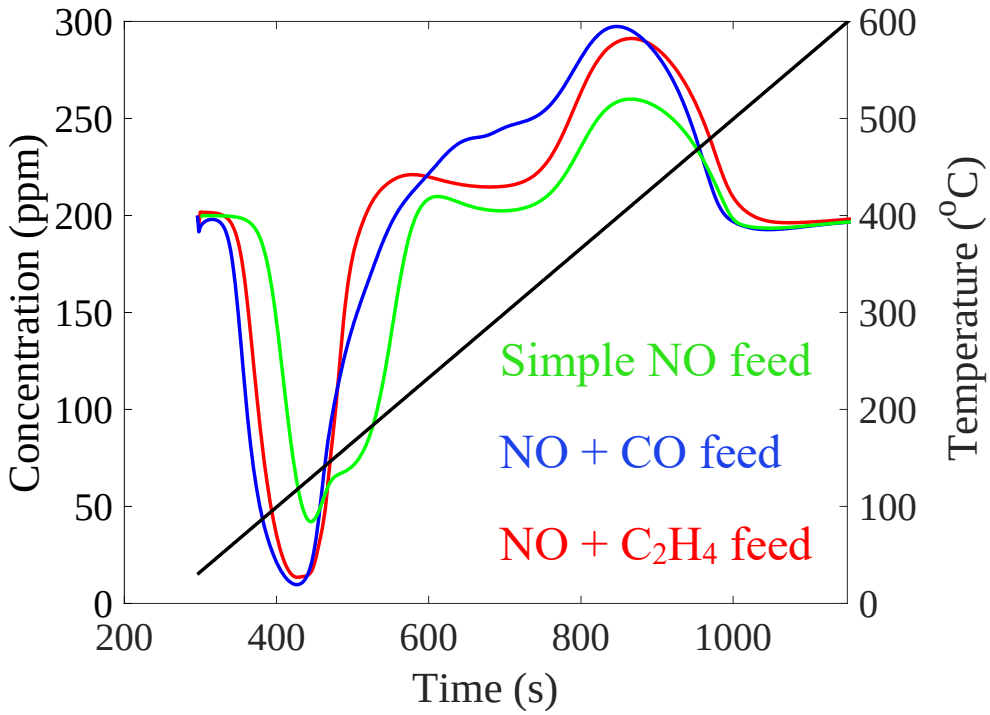

Figure 3.16 Model prediction of NO profile for simple NO feed, NO+CO feed and NO+C_2H_4 feed with a continuous temperature ramping of 40°C/min starting from 30°C to 600°C.

The instantaneous uptake profiles of NO on Pd(1%)/SSZ-13 and Pd(1%)/ZSM-5 at ~85°C and for feed containing 400ppm NO/ 2%O_2/ 7%H_2O/ balance Ar are shown in Figure 3.17. Figure also compares the predicted dependence of $\eta_T(t^*)$ on exposure time t^* for Pd(1%)/SSZ-13 and Pd(1%)/ZSM-5. The simulated comparison shows that the NO uptake during the 30 min period on Pd(1%)/SSZ-13 is NO/Pd ~ 0.78 while NO/Pd ~ 0.55 for Pd(1%)/ZSM-5. Under same Pd loading and experimental conditions Pd(1%)/SSZ-13 traps more NO as compared to Pd(1%)/ZSM-5, since the dispersion of Pd on SSZ-13 is higher than on ZSM-5 for same Pd loading leading to more number of available sites for NO adsorption. The integral trapping efficiency profile also shown in the figure underscores this feature. The predictions are consistent with experimental observations.

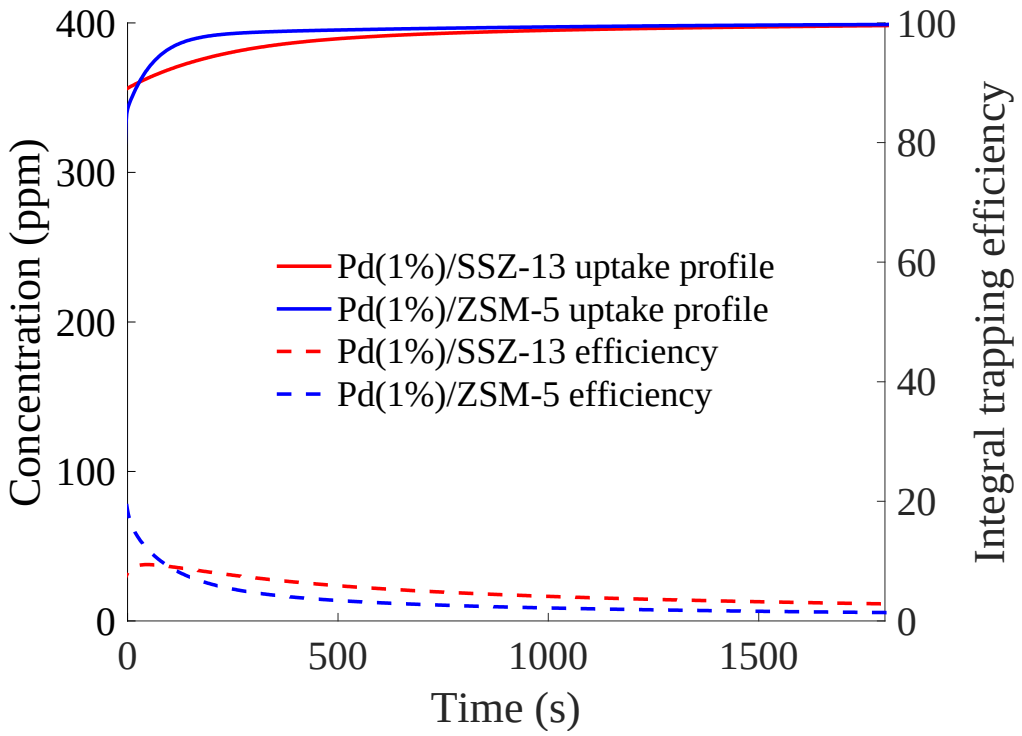

Figure 3.17 Model prediction of integral trapping efficiency and uptake profile for Pd(1%)/SSZ-13 and Pd(1%)/H-ZSM-5 for feed comprising of 400 ppm NO/ 2% O_2/ 7% H_2O / balance Ar

A more informative and practical performance comparison involves the 30 to 600℃ temperature ramp. The feed considered is the same as the one used by Ambast et al. [37]; i.e., 400ppm NO/ 2%O_2/ 7%H_2O/ balance Ar and a feed flowrate of 30k hr^{-1}. Figure 3.18(a) shows the NO profile for a TPD ramp rate of 20℃/min. Pd/ZSM-5 starts adsorbing NO at low temperatures while for Pd/SSZ-13 there is no uptake of NO until the temperature reaches ~70℃. This suggests that blocking by H_2O is more prominent on the smaller pore zeolite. Soon after an increase in the temperature the NO uptake on Pd(1%)/SSZ-13 exceeds that on Pd(1%)/ZSM-5. By 120℃ NO starts desorbing from Pd(1%)/ZSM-5 while for Pd(1%)/SSZ-13 NO starts desorbing at ~160℃. Most of the NO desorbs from Pd(1%)/SSZ-13 by ~480℃ whereas NO continues to desorb from Pd(1%)/ZSM-5 to

~500°C. These predictions are consistent with the experimental observations of Gupta et al. [38] and Ambast et al. [37]. The total NO uptake on Pd(1%)/SSZ-13 is NO/Pd ~ 1.12 while for Pd(1%)/ZSM-5 NO/Pd ~ 0.58.

The impact of the temperature ramp rate provides further insight into the nature of the NO uptake process. Figure 3.18(b) shows the NO uptake profile on Pd(1%)/SSZ-13 and Pd(1%)/ZSM-5 for a TPD ramp rate of 40°C/min. In doubling the ramp rate, the NO uptake and desorption profiles are expectedly steeper. However, the total NO uptake on Pd(1%)/SSZ-13 is NO/Pd ~ 1.05 while for Pd(1%)/ZSM-5 it is NO/Pd ~ 0.40. The decrease in NO uptake for both materials with increasing ramp rate is due to the decreased duration for NO to adsorb.

The simulated uptake and release at the higher space velocity of 45k hr^{-1} is shown in Figure A. 22(a). The total NO uptake on Pd(1%)/SSZ-13 is NO/Pd ~ 1.14 while for Pd(1%)/ZSM-5, NO/Pd is ~ 0.65. The modest increase in NO uptake with the flowrate shows that for the same duration of uptake time the catalyst is exposed to more NO. The Pd loading is an important material design variable for the PNA unit. Figure A. 22(b) shows the NO uptake profiles for Pd(2%)/SSZ-13 and Pd(2%)/ZSM-5 at a feed flowrate of 30 khr^{-1} and TPD temperature ramp rate 20°C/min. Ambast et al. [37] reported 41% and 22% dispersion for Pd(1%)/ZSM-5 and Pd(2%)/ZSM-5, respectively. Thus, in doubling the Pd loading the dispersion was reduced by 46%. The same dispersion reduction was assumed here for Pd/SSZ-13. Hence, Pd dispersion of 54% was assumed for Pd(2%)/SSZ-13. The active Pd sites therefore increase by only a factor of 1.074 which results in a ratio of NO uptake by total Pd of 0.60 NO/Pd on Pd(2%)/SSZ-13 was while 0.30 NO/Pd on Pd(2%)/ZSM-5. The decrease in NO/Pd for 2%Pd as compared to 1%Pd catalyst is because

the total Pd loading is doubled in 2%Pd catalyst but the active sites are increased only by a factor of 1.074 which leads to decrease in NO/Pd ratio.

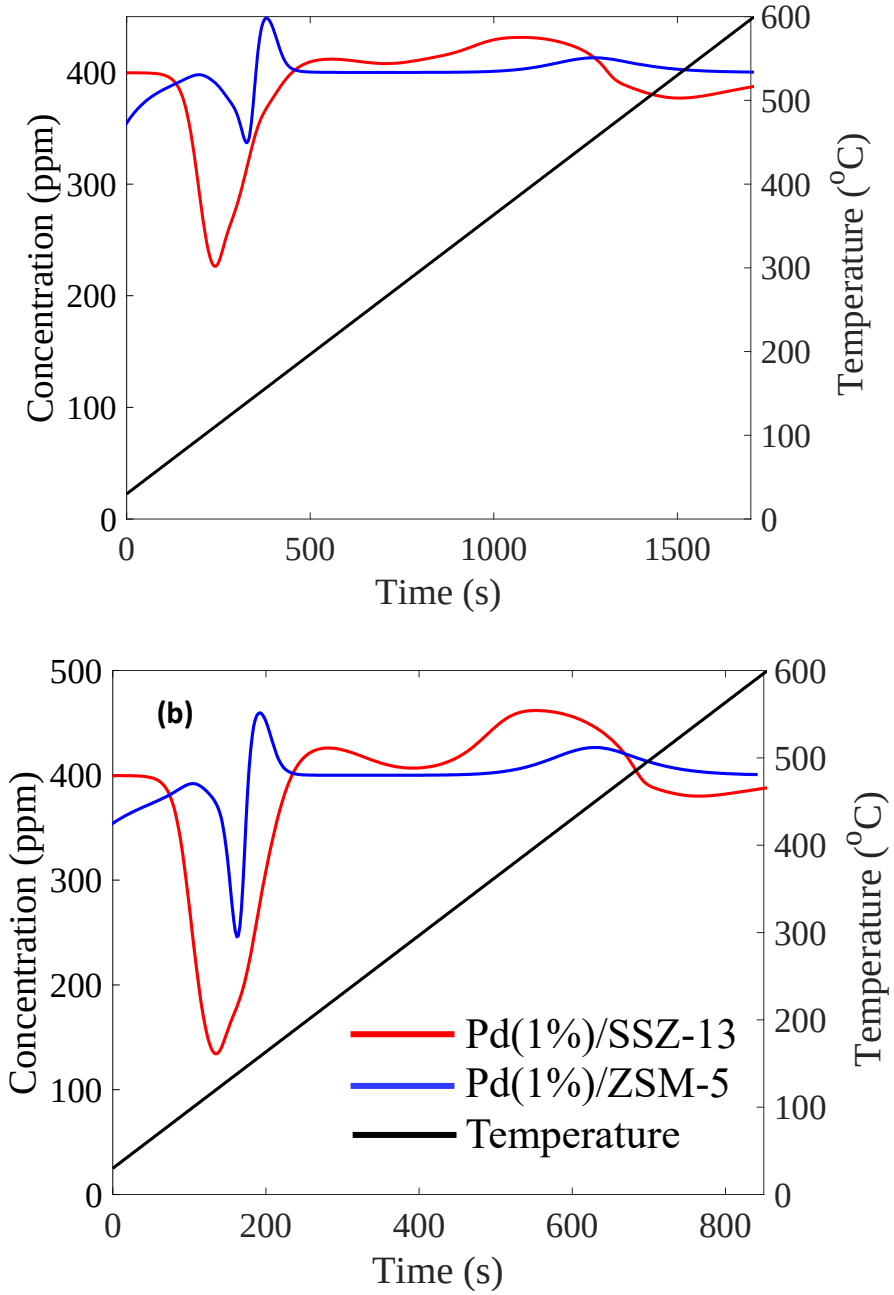

Figure 3.18 Model prediction of NO profile for Pd(1%)/SSZ-13 and Pd(1%)/ZSM-5 for a feed of 400 ppm NO/ 2% O_2/ 7% H_2O / balance Ar at 30k hr^{-1} feed flowrate with a continuous temperature ramping from 30°C to 600°C at the rate of (a) 20°C/min and (b) 40°C/min.

3.3 Degree of uptake control

Another utility of the PNA monolith model is to identify the reaction steps that limit the overall NO uptake. The transient process poses some difficulties doing this unambiguously. Here we describe and apply a sensitivity analysis to answer this question. We adopt the degree of uptake control following the well-established degree of rate control method for steady state catalytic reactions developed by Campbell et al. [61,62]. This was done by increasing both forward and reverse rate constants for each reaction step by 10% and calculating resulting fractional change in NO uptake for 300 seconds, while keeping all other parameters constant. The ratio of the forward and reverse rate constants was fixed in order to fix the reaction equilibrium constant. To this end, we define the *degree of uptake control*, denoted by $X_{uc,i}$, as the fractional change in overall NO uptake divided by the fractional change in forward rate constant for reaction step i.e.,

$$X_{uc,i} = \frac{\frac{\Delta NO\ uptake}{initial\ NO\ uptake}}{\frac{\Delta k_{fi}}{initial\ k_{fi}}}. \tag{3.6}$$

The calculation was repeated for different uptake temperatures ranging from 75℃ to 150℃. The predicted $X_{uc,i}$ are shown in Figure 3.19. The figure compares the $X_{uc,i}$ values for several reaction steps at different uptake temperatures. The reaction steps that have non-zero value of $X_{uc,i}$ are the uptake controlling steps at that particular uptake temperature [61]. Steps with negative degree of uptake control are inhibition steps.

The results show that the uptake of a first and second NO and H_2O on $Z^-Pd^{2+}Z^-$ (R3.1, R3.2, R3.3), and the uptake of NO on $Z^-[PdOH]^+$ (R3.4), each have non-zero $X_{uc,i}$ values. The order of decreasing $X_{uc,i}$ is R3.1 > R3.4 > R3.2 > R3.3 at an uptake temperature of 75℃. That is, NO uptake on $Z^-Pd^{2+}Z^-$ (R3.1) is the most important step at this

temperature. With an increase in uptake temperature to ~90℃ the $X_{uc,i}$ values for reactions R3.1-R3.3 decrease but for R3.4, with R3.4 having the highest degree of control from 90 to 150℃. This shows that the uptake of NO on $Z^-[PdOH]^+$ and the subsequent reduction to Pd^+ is critical. By 125℃ most of the H_2O (R3.3) is desorbed from the $Z^-Pd^{2+}Z^-$ so its $X_{uc,i}$ value approaches ~0 while NO desorption from $Z^-Pd^{2+}Z^-$ (R3.1) commences so its $X_{uc,i}$ value becomes negative. With further increase in uptake temperature to 150℃, reactions R3.3 and R3.4 still remains the uptake controlling steps with values of $X_{uc,i}$ for all other steps being ~0 and uptake of two NO on $Z^-[PdOH]^+$ sites being the most uptake controlling step.

In addition to providing detailed kinetic information on NO_x uptake, the degree of uptake control analysis also guides the design of improved PNA materials. In particular, the high sensitivity to R3.1, the binding of NO to $Z^-Pd^{2+}Z^-$, can be leveraged to tune the temperature window for NO_x uptake. As Thirumalai et al. [63] have shown, the binding and catalytic properties of divalent metal cations strongly depend on the local zeolite environment and framework structure. Indeed, the observed differences in NO uptake between Pd/CHA and Pd/MFI lend support to this assertion. Besides systematically evaluating different zeolite frameworks as host materials for Pd cations, it may also be possible to direct the placement of Pd to specific channel locations in a given zeolite by altering the nature of the framework heteroatom. A recent study by Zhou et al. [64] has explored this idea and introduced framework Ga atoms to alter the speciation and/or location of extra framework Lewis acid sites with marked effects on the selectivity during the aromatization of ethylene.

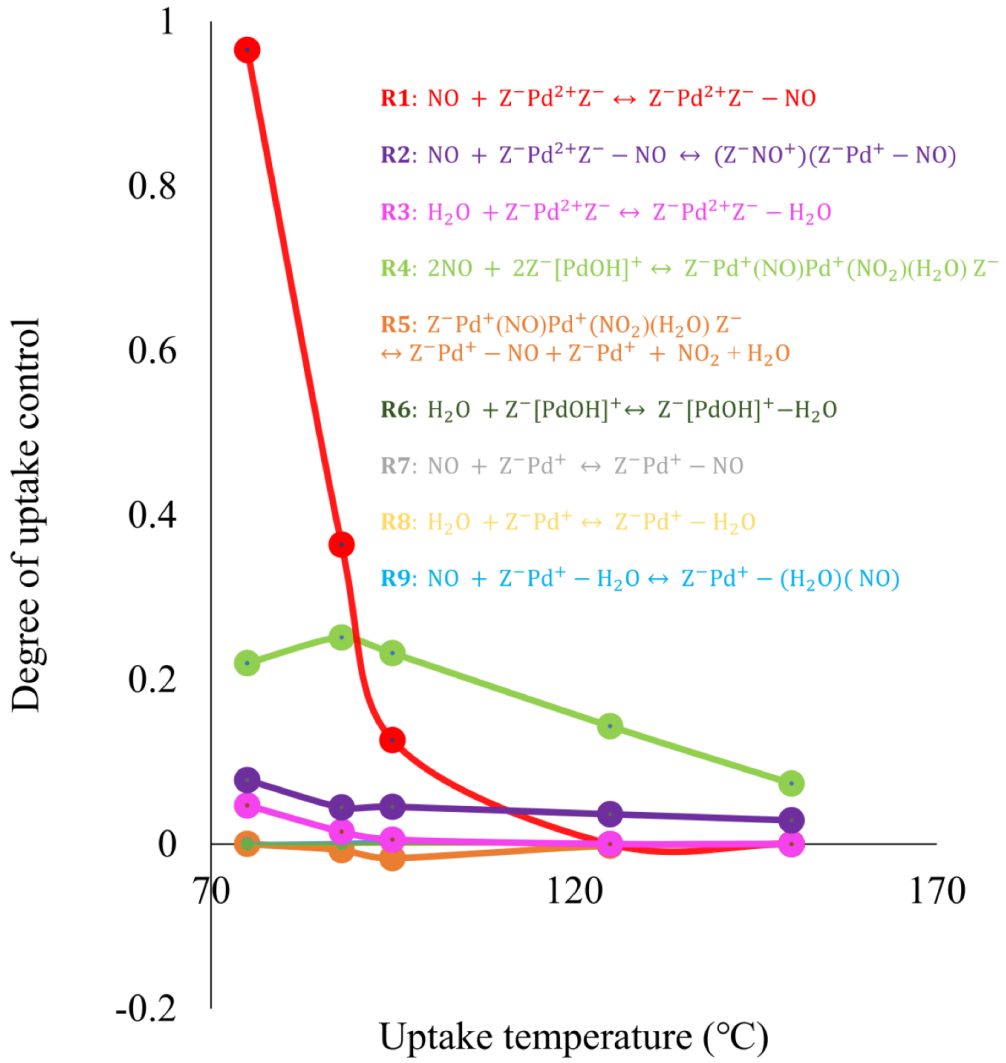

Figure 3.19 Sensitivity analysis of different reactions as a function of uptake temperature.

3.4 Conclusions

In this study we developed a two-phase transient monolith model to model NO uptake and temperature programmed desorption (TPD) data for Pd/SSZ-13 PNA with and without reductants CO and C_2H_4.

The microkinetic schemes for each of the feeds involves multi-site NO adsorption on multiple types of Pd cations $Z^-[PdOH]^+$, $Z^-Pd^{2+}Z^-$, and Z^-Pd^+, with a key feature being

the reduction of a pair of $Z^-[PdOH]^+$ sites to two Z^-Pd^+ sites. The reduced sites bind NO the strongest. The Pd(II) to Pd(I) reduction generates NO_2, CO_2 or C_2H_4O depending on the feed constituents. For NO-only feed, this endothermic reaction occurs at temperature ~120℃ and generates NO_2. In the presence of CO and C_2H_4 the exothermic reduction occurs at lower temperatures and generates CO_2 and C_2H_4O respectively. The model was validated at different uptake temperatures, feed flow rates, and ramp rates, enabling its use to identify improved catalyst formulations and operating strategies. We were also able to predict the NO uptake under a more realistic condition for NO-only feed, NO+CO feed and NO+C_2H_4 feed with a continuous temperature ramping of 40℃/min starting from 30℃ to 600℃. The model showed the maximum NO uptake for NO+CO feed.

The validated model is a quantitative tool for evaluating, understanding and optimizing NO uptake and release on Pd-exchanged small-pore zeolite under a wide range of experimental conditions. The model was used to compare the two classic PNA materials Pd/SSZ-13 and Pd/ZSM-5. The model correctly predicted the higher NO uptake on Pd/SSZ-13 under similar experimental conditions. Moreover, the model is an important tool to identify transient operating conditions that meet application-relevant performance metrics including NO trapping efficiency and NO release temperature. A sensitivity analysis shows that the NO trapping efficiency is largely determined by the NO adsorption characteristics to $Z^-Pd^{2+}Z^-$, which provides valuable guidance for the design of improved PNA materials.

Chapter 4

Coupled Uptake and Conversion of $C_{12}H_{26}$ and NO on Pd/SSZ-13: Experiments and Modeling

4.1 Experimental

4.1.1 Catalyst properties

The PNA monolith provided by Johnson Matthey Inc. containing 1 wt.% Pd/SSZ-13 (90%) + Al_2O_3 (10%) with a washcoat (wc) loading of 1.5 g wc/in^3 (Pd loading of 94 μmole Pd/g wc) was used for the experiments. A cordierite monolith of 400 CPSI (cells per in^2), 2.5 cm length, having 49 channels served as the washcoat substrate.

4.1.2 Reactor setup and experimental protocol

The experiments were carried out in a vertical quartz tube reactor. Details of the experimental setup are provided by Malamis et al. [45]. The flowing dodecane liquid feed was added to the system using a Cole-Parmer syringe pump. The liquid was vaporized in a customized unit and then injected into the flowing gas mixture. The monolith sample was loaded into the reactor and activated at 600℃ for 4 h in 5% O_2/ balance Ar prior to its first use. Before each subsequent experiment the catalyst was pretreated in 5% O_2/ balance Ar at 500℃ for 30 minutes to remove any residual species, followed by cooling to near or slightly above ambient. At the start of a typical uptake and desorption experiment, the monolith sample was heated to the desired uptake temperature in the range 100℃ - 170℃. Experiments were carried out at a flowrate of 2500 sccm, corresponding to a gas hourly space velocity (GHSV) of 75.9k h^{-1}. The feed gas mixtures used for the NO-only feed experiment consisted of 400 ppm NO/ 2% O_2/ 2% H_2O/ balance Ar.

To quantify the effect of $C_{12}H_{26}$ on NO uptake, experiments were performed with and without the addition of $C_{12}H_{26}$ to the feed. The feed was stabilized in the bypass for 5 min and then directed to the reactor. Uptake was carried out for a desired duration and then the feed was turned back to the bypass. The flows of NO and/or $C_{12}H_{26}$ and H_2O were switched off and the flowrate of Ar was adjusted to maintain a fixed total feed flowrate. The feed containing O_2 and Ar was then switched back to the reactor side. The O_2/Ar feed flowed through the reactor for ~5 min to remove loosely bound NO and $C_{12}H_{26}$ from the reactor and tube surfaces. Once the effluent concentrations of NO and $C_{12}H_{26}$ reached < 2 ppm, TPD (temperature-programmed desorption) was carried out to a temperature of 500℃ from the uptake temperature in about ~18 min. The temperature ramp which was nearly linear is reported with the uptake and release data. Species concentration profiles for only the period of time the feed was directed to the reactor side is provided. The temperatures were measured using two type K thermocouples; one was located 1 cm upstream of the front face of monolith and the other one was positioned at the axial and radial midpoint of the monolith sample. The set point temperature of the furnace typically differed by up to ±5℃ from the monolith temperature, the latter of which was used for modeling.

4.2 Results and Discussion

4.2.1 Experimental

4.2.1.1 Effect of $C_{12}H_{26}$ on NO uptake and release

To understand the effect of $C_{12}H_{26}$ on NO uptake and release, a conventional uptake experiment was conducted at 115℃ with a feed containing 395 ppm NO/ 55 ppm $C_{12}H_{26}$/ 2% O_2/ 2% H_2O/ balance Ar. Uptake was conducted for 5 min after which the flows of NO, H_2O and $C_{12}H_{26}$ were turned off. The uptake and TPD profiles shown in Figure 4.1

reveal that at the start of uptake both NO and $C_{12}H_{26}$ concentrations dip below their feed concentration levels. In addition, the simultaneous release of NO_2 is observed. The start of TPD at the 700 s mark noted by the increase in temperature is accompanied by the instantaneous release of $C_{12}H_{26}$. Carbon dioxide and a small amount of CO also desorb during the ramp; with O_2 present, this is an indication of $C_{12}H_{26}$ oxidation. NO desorption commences at about 220°C. By 500°C all of the NO is desorbed from the catalyst. There is only one NO TPD peak for this experiment of the co-feed of NO and $C_{12}H_{26}$.

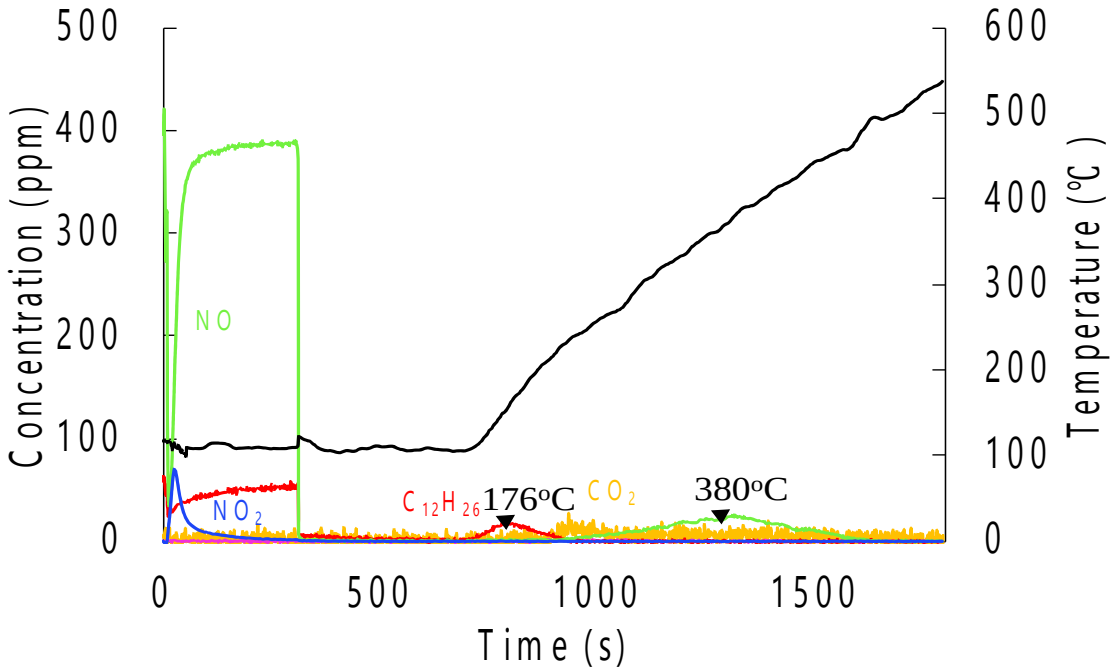

Figure 4.1 Experimental profiles for uptake at 115°C and TPD on Pd(1%)/SSZ-13 for a feed comprising of 395 ppm NO/55 ppm $C_{12}H_{26}$/ 2% O_2/ 2% H_2O/ balance Ar during uptake and 2% O_2/ Ar during TPD.

To assess the impact of $C_{12}H_{26}$, corresponding NO-only experiments were conducted. The effluent NO concentration during the uptake of the NO-only and NO + $C_{12}H_{26}$ co-feed are shown in Figure 4.2(a) (115°C) and Figure 4.2(b) (135°C). Their comparison at both temperatures indicates that the co-fed $C_{12}H_{26}$ has a negligible impact on the NO uptake, as indicated by the near overlap of the two uptake curves. It is noted that

dispersed Pd cations are active sites for NO adsorption [15,18-20,37,38]. In contrast, $C_{12}H_{26}$ adsorbs onto zeolitic sites through van der Waals interactions and therefore does not compete with NO for those sites [45,65]. That is, during the co-uptake of NO and $C_{12}H_{26}$, NO can diffuse more quickly and adsorbs with $C_{12}H_{26}$ posing no obstacle.

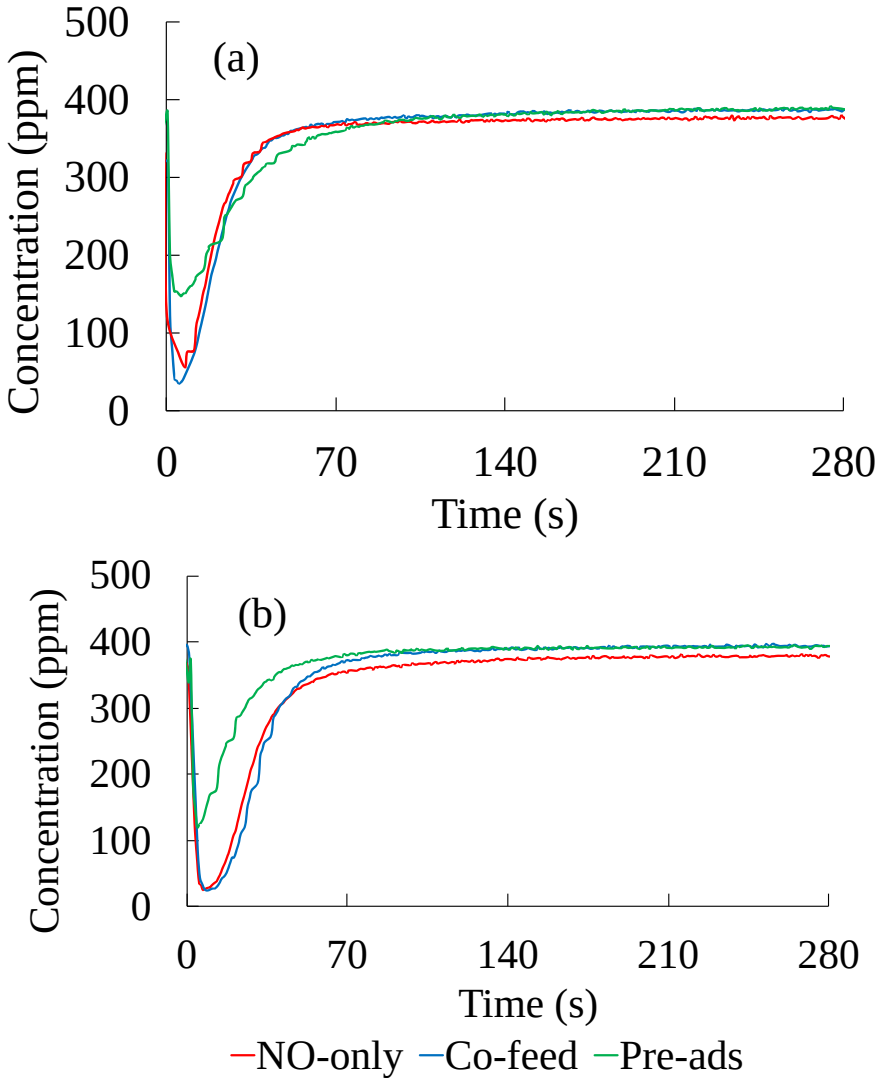

Figure 4.2 NO uptake profiles for NO only feed, co-feed of NO and $C_{12}H_{26}$ and pre-adsorption of $C_{12}H_{26}$ followed by co-feed of NO and $C_{12}H_{26}$ at uptake temperatures of (a) ~115°C and (b) ~135°C.

The NO TPD features are quite different in the presence of $C_{12}H_{26}$ co-feed; a direct comparison of the two feeds is shown in Figure 4.3. For the NO-only feed, NO starts

desorbing at lower temperatures with two peaks evident, the first at ~175°C and and second at ~408°C. For the NO + $C_{12}H_{26}$ feed, there is a delay in the release of NO to ~220°C causing the lower temperature peak to merge with the higher temperature peak. A key question to answer is why co-fed $C_{12}H_{26}$ affects the NO release but not its uptake.

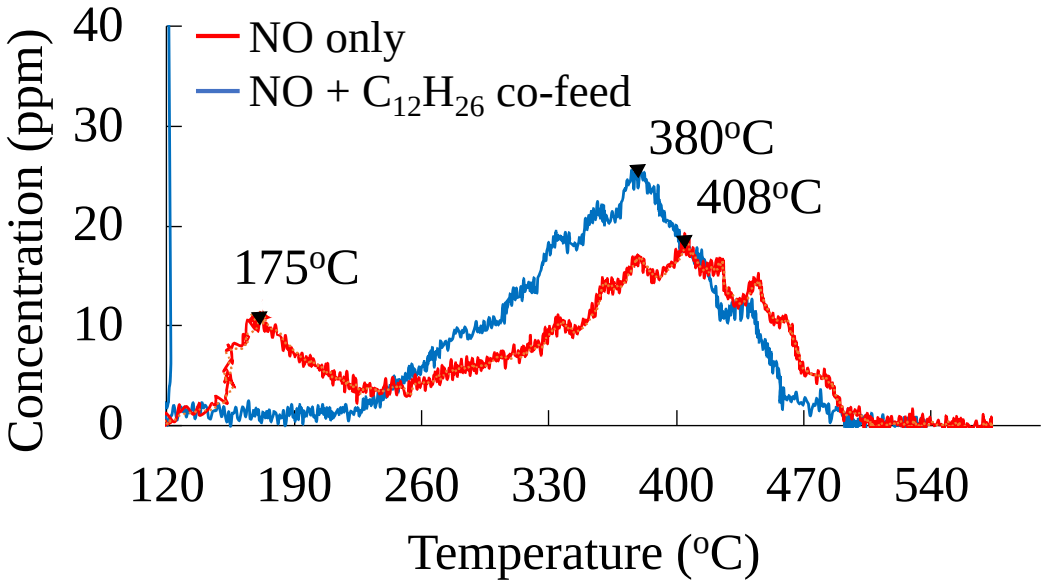

Figure 4.3 NO TPD profiles for NO only feed and co-feed of NO and $C_{12}H_{26}$ at uptake temperatures of ~115°C.

4.2.1.2 Effect of $C_{12}H_{26}$ pre-adsorption on NO uptake and release

To better understand the coupling between $C_{12}H_{26}$ and NO uptake and release, additional experiments were conducted in which $C_{12}H_{26}$ was pre-adsorbed on the Pd/SSZ-13 sample prior to NO + $C_{12}H_{26}$ co-feed. The uptake and TPD profiles for the various species are shown in Figure 4.4. In this experiment, a feed containing 55 ppm $C_{12}H_{26}$ /2% O_2/ 2% H_2O/ balance Ar was directed to the reactor at 115°C with the intent to preadsorb $C_{12}H_{26}$ (and H_2O) on the sample. Pre-adsorption was conducted for 20 min to approach saturation as evidenced by the effluent $C_{12}H_{26}$ approaching its feed value. At that point, the

feed line was switched to bypass and NO was added to the feed, giving a feed comprised of 395 ppm NO/55 ppm $C_{12}H_{26}$/ 2% O_2/ 2% H_2O/ balance Ar.

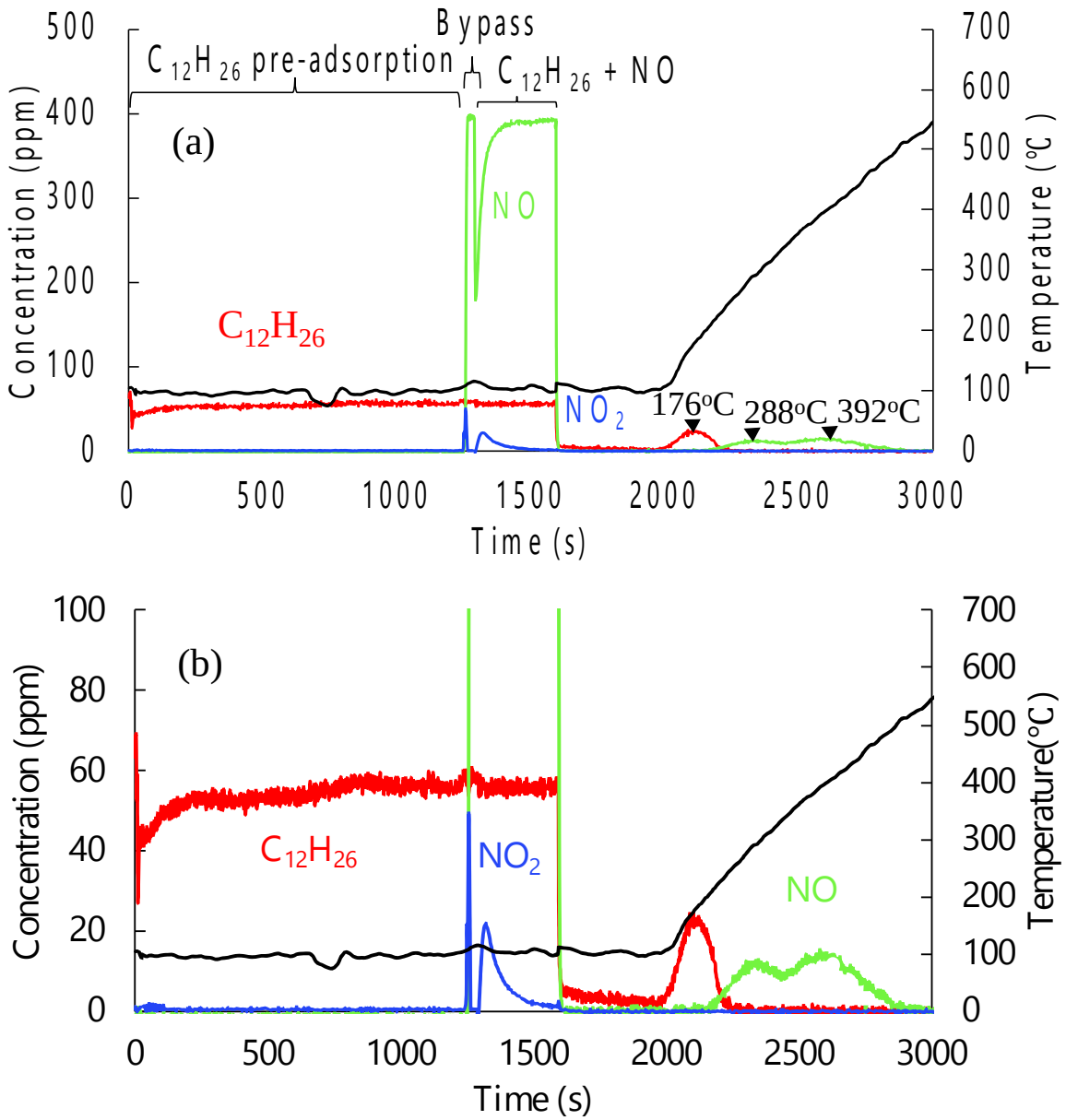

Figure 4.4 (a) Experimental profiles for pre-adsorption of $C_{12}H_{26}$ and H_2O followed by co-feed of NO and $C_{12}H_{26}$ at 115°C and TPD on Pd(1%)/SSZ-13; b) Enlarged view of uptake and TPD profiles.

The data show that, as in the earlier experiment, NO immediately adsorbs and NO_2 is generated. The data also reveal that there is no uptake of $C_{12}H_{26}$ indicating that the

sample was already saturated with $C_{12}H_{26}$ during pre-adsorption period. As before, uptake was conducted for 5 min followed by directing the feed to bypass. The flow of NO, $C_{12}H_{26}$ and H_2O were switched off and the feed was turned back to the reactor side after adjusting the flow of Ar. Once the concentrations of NO and $C_{12}H_{26}$ are below ~2 ppm, TPD starts at which point $C_{12}H_{26}$ desorption commences. Most of the $C_{12}H_{26}$ desorbs before ~220℃ and at that point NO desorption begins. A similar experiment was conducted at the somewhat higher uptake temperature of 135℃. The NO uptake and TPD profiles for that experiment are shown in Figure A. 23.

The $C_{12}H_{26}$ pre-saturation experiments also reveal an effect on the NO uptake. Figure 4.2 compares the NO uptake profiles for the NO-only feed and the NO + $C_{12}H_{26}$ co-feed without pre-saturation, along with the NO + $C_{12}H_{26}$ co-feed with pre-saturation, at uptake temperatures of ~115℃ (a) and ~135℃ (b). Compared to earlier results, the 115℃ pre-saturation data exhibit a shallower dip in the NO uptake along with a protracted approach to the NO feed concentration. This indicates that, in contrast to the NO + $C_{12}H_{26}$ co-feed experiments, pre-saturation of $C_{12}H_{26}$ and H_2O decreases the NO uptake.

Additional experiments were conducted to find out if H_2O or $C_{12}H_{26}$, or both, are responsible for the decrease in NO uptake. In the first set of experiments the catalyst was pre-adsorbed with H_2O by flowing 2% H_2O/ 2% O_2/ balance Ar for 20 min at 110℃ and 125℃, then followed by NO uptake for 5 min with a feed of 390 ppm NO/ 2% H_2O/ 2% O_2/ balance Ar. In another experiment the catalyst was pre-adsorbed with $C_{12}H_{26}$ in the absence of H_2O by flowing 55 ppm $C_{12}H_{26}$/ 2% O_2/ balance Ar for 20 min at 110℃ and 125℃. This too was followed by NO uptake for 5 min by flowing a feed of 395 ppm NO/ 2% H_2O/ 2% O_2/ balance Ar. NO uptake profiles for both the sets of experiments are shown

in Figure 4.5. For both, the NO uptake is less compared to the uptake without H_2O and $C_{12}H_{26}$ pre-adsorption (Figure 4.2), showing that both H_2O and $C_{12}H_{26}$ pre-adsorption reduce NO uptake.

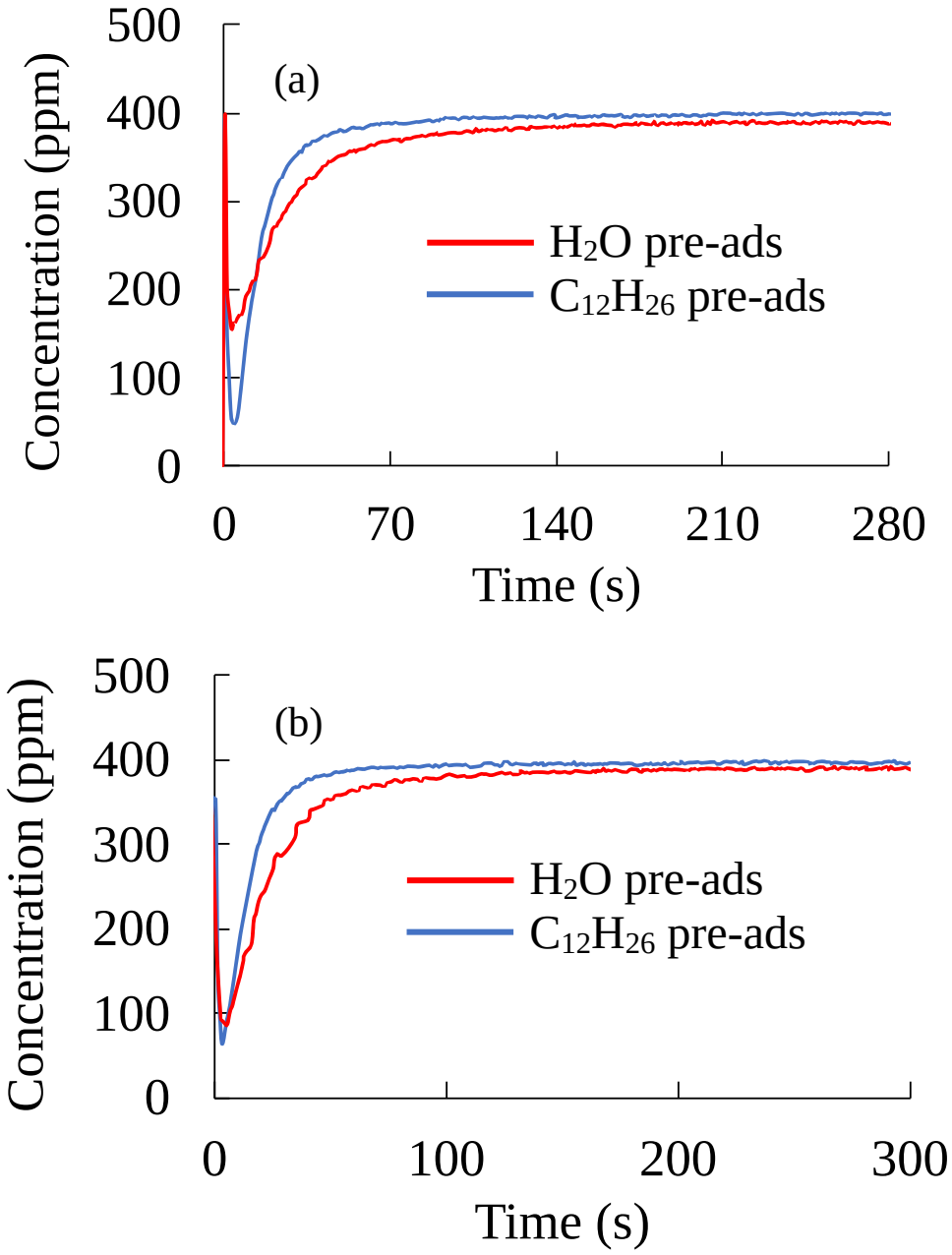

Figure 4.5 NO uptake profiles for H_2O pre-adsorption and dry $C_{12}H_{26}$ pre-adsorption followed by uptake of NO at uptake temperatures of (a) ~110°C and (b) ~125°C.

As discussed earlier, NO only adsorbs on Pd cations (when H_2O is present) while $C_{12}H_{26}$ adsorbs on zeolitic sites. Since $C_{12}H_{26}$ does not compete with NO for the Pd sites, during the co-feed of NO and $C_{12}H_{26}$, NO can diffuse more quickly to the Pd sites due to its smaller size before any restriction by $C_{12}H_{26}$ is established. On the other hand, when $C_{12}H_{26}$ is pre-adsorbed it may block zeolite pores through adsorption, making a fraction of the Pd cationic sites kinetically inaccessible for NO uptake. This reduces the NO uptake. The envisioned blockage is depicted schematically in Figure A. 24. Finally, H_2O competes with NO for adsorption on Pd sites [30,37,38]. During pre-adsorption, the rather high H_2O concentration leads to the occupancy on the sites by one or more H_2O molecules. The H_2O serves to reduce NO uptake. We return to these observations in the modeling section.

4.2.1.3 Delay in NO release

The experimental results presented to this point reveal that in the presence of $C_{12}H_{26}$, NO desorption moves at higher temperatures. Further, the pre-adsorption of $C_{12}H_{26}$ reduces the NO uptake. A closer examination of the NO TPD profile in Figure 4.1 shows that NO does not begin to desorb until all of the adsorbed $C_{12}H_{26}$ has desorbed from the catalyst. If $C_{12}H_{26}$ is effective in blocking NO from desorbing and diffusing, then as soon as $C_{12}H_{26}$ desorption starts so too should some NO desorption. However, the data shows that no NO is observed until all of the $C_{12}H_{26}$ is desorbed. This suggests that adsorbed NO blockage by $C_{12}H_{26}$ is not the cause of the delay of NO release.

In addition to NO and $C_{12}H_{26}$, there are two other species present during the TPD; namely, CO and CO_2, as shown in Figure A. 25. These are respectively formed by partial and complete oxidation of the $C_{12}H_{26}$ during the temperature ramp. The CO_2 concentration is higher than that of CO when O_2 is present as CO is oxidized to CO_2 at temperatures

higher than 200℃ [37,38]. Considering CO_2 first, we refer to our previous work [30] in which NO uptake was carried out with and without CO_2 in the feed. Those results show that CO_2 does not affect NO adsorption or desorption. We conducted a similar experiment to assess the CO impact. Figure A. 26 shows the experimental profiles for NO uptake at 105°C and TPD on Pd(1%)/SSZ-13 for a feed containing 398 ppm NO/ 760 ppm CO/ 2% O_2/ 2% H_2O/ balance Ar during uptake and 760 ppm CO/ 2% O_2/ balance Ar during TPD. The data show that NO desorption is delayed to temperatures exceeding 250℃. Moreover, there is only one NO TPD peak present. These results clearly indicate that the presence of CO delays NO desorption. Now, in the NO + $C_{12}H_{26}$ co-feed experiment CO is formed only during the TPD and is at a rather low concentration (< 25 ppm). To simulate this, another experiment was carried involving 5-min NO uptake at 105℃ in the absence of CO (395 ppm NO/ 2% O_2/ 2% H_2O/ balance Ar), followed by TPD during a feed devoid of NO and H_2O but with 25 ppm CO added (Figure 4.6). The outcome contained in Figure 4.6 (b) shows a delay in NO desorption to above 250℃. We showed earlier that CO co-adsorbs on Pd sites that are pre-exposed to NO [30,38]. Several studies have shown that co-adsorption of NO and CO may occur on the same Pd site [20,24,30,38,39,53]. According to DFT calculations, the binding energies of co-adsorbed NO and CO on Pd sites is higher than NO alone on Pd sites [30]. This suggests that the delayed NO release is a result of the formation of a more strongly held NO + CO complex on the Pd sites. Another validation was done and the experimental profiles for uptake at 105°C and TPD on Pd(1%)/SSZ-13 for a feed comprising of 395 ppm NO/ 2% O_2/ 2% H_2O/ balance Ar during uptake and 100 ppm CO/ 2% O_2/ Ar during TPD are shown in Figure A. 27.

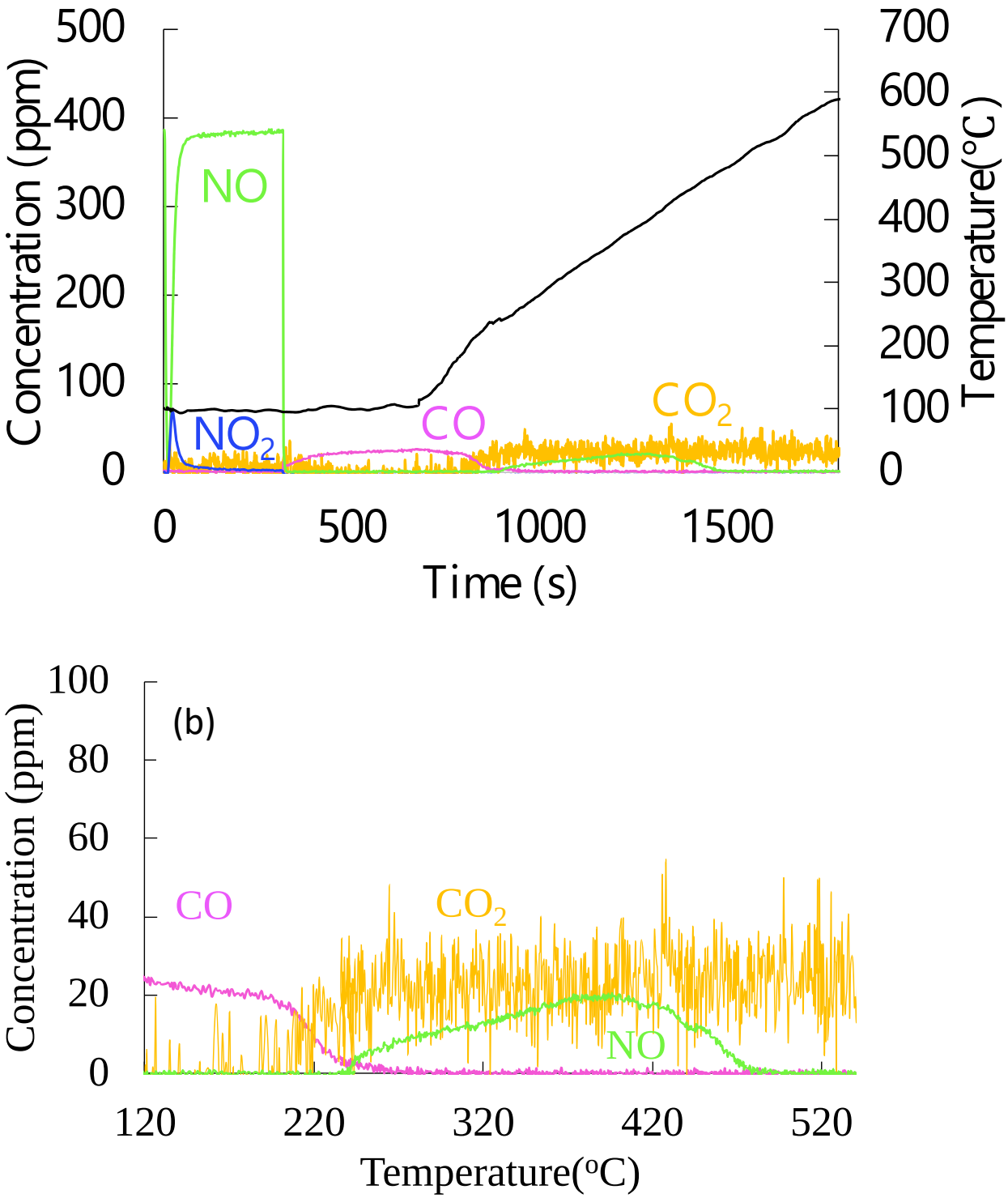

Figure 4.6 (a) Experimental profiles for uptake at 105°C and TPD on Pd(1%)/SSZ-13 for a feed comprising of 395 ppm NO/ 2% O_2/ 2% H_2O/ balance Ar during uptake and 25 ppm CO/ 2% O_2/ Ar during TPD (b) Enlarged species vs temperature profile.

4.2.2 Modeling

4.2.2.1 Model development

In this section we describe a model for NO + $C_{12}H_{26}$ uptake, conversion, and release. In our previous work we developed a model for NO-only uptake and desorption on Pd(1%)/SSZ-13 based on a set of uptake and TPD data, DRIFTS measurements, and density functional theory (DFT) calculations. Here we extend the model to include the contribution of $C_{12}H_{26}$ on NO uptake and release. The washcoated monolith model is a one-dimensional, two-phase transient, single channel monolith model. The model equations 2.2 – 2.5 were used with model parameters and variables defined in the List of Notation. The values of non-kinetic parameters are provided in Table 4.1 and Table A. 1 of the Appendix.

Table 4.1 Parameters used in model

Parameter	Value
L	0.025 m
<u>	0.527*(T/273.15) m/s
$C_{\tau m}$	$(12187.3/T)$ mol/m^3
ε_{wc}	0.4
$R_{\Omega 1}$	3×10^{-4} m
$R_{\Omega 2}$	1.5×10^{-5} m
Sh_e	4.36
$Sh_{i,\infty}$	2.37
λ	80
$C_{Z^-[Pd(II)OH]^+}$ (C_{S1})	151.5 mole-sites/m^3 of washcoat
$C_{Z^-Pd^{+2}Z^-}$(C_{S2})	51.8 mole-sites/m^3 of washcoat
C_{S_z}	360.1 mole-sites/m^3 of washcoat

Kinetic parameters were taken from literature or estimated from a fit of data sets described later. Unknown kinetic parameters were estimated using an algorithm

(MATLAB *fmincon*) interfaced with the monolith reactor model containing the microkinetic scheme. The algorithm minimized the objective function comprising the sum of squared differences between the experimental and predicted species concentrations spanning the uptake and release. Some fine tuning was done given the complexity of the transient uptake and release data and large number of parameters. The three stages (reference sets) of the model tuning involved the following number of data points (N_d) and estimated parameters (N_p):

- $C_{12}H_{26}$ dry feed on Pd(1%)/SSZ-13: $N_p = 1$ $N_d = 3482$
- $C_{12}H_{26}$ wet feed on Pd(1%)/SSZ-13: $N_p = 3$ $N_d = 2521$
- NO + $C_{12}H_{26}$ wet feed on Pd(1%)/SSZ-13: $N_p = 7$ $N_d = 1530$

The reactor model partial differential equations (PDEs) were discretized using a second-order finite difference method. The reactor length was discretized into 20 elements as a compromise between simulation time and accuracy. The resulting set of ordinary differential equations (ODEs) were solved by the MATLAB routine *ODE23s*. Parameter estimation for each successive stage was accomplished by fixing parameter values determined in earlier stages. At each stage the model was validated for different experimental conditions.

4.2.2.2 Dodecane uptake

As a first step, the addition of $C_{12}H_{26}$ to the model requires the modeling of dodecane uptake and release. $C_{12}H_{26}$ adsorption and desorption is simply described by

$$C_{12}H_{26} + S_z \leftrightarrow S_z - C_{12}H_{26}. \qquad \text{(R4.1)}$$

Where S_z represents the zeolite sites not occupied by $C_{12}H_{26}$ while S_z - $C_{12}H_{26}$ represents

zeolite sites occupied by $C_{12}H_{26}$. Again, $C_{12}H_{26}$ binds to the zeolite through van der Waals interactions [65]. The rate of forward reaction (r_{ads}) and reverse reaction (r_{des}) are given by

$$r_{ads} = k_{ads} X_{C_{12}H_{26}} \theta_{S_z} C_{S_z} \quad (0.1)$$

and $$r_{des} = k_{des} \theta_{S_z - C_{12}H_{26}} C_{S_z}. \quad (0.2)$$

Where $X_{C_{12}H_{26}}$ is the mole fraction of $C_{12}H_{26}$ in the washcoat, θ_{S_z} is the fraction of vacant zeolite sites and $\theta_{S_z - C_{12}H_{26}}$ is the fraction of zeolite sites occupied by $C_{12}H_{26}$. C_{S_z} represents the total concentration of zeolite sites available for $C_{12}H_{26}$ uptake. Assuming the adsorption and desorption rate constants are given by

$$k_{ads} = A_{ads} \quad (0.3)$$

and $$k_{des} = A_{des}\, e^{-\frac{E_{des}}{RT}}. \quad (0.4)$$

Where A_{ads} and A_{des} are pre-exponential factors for adsorption and desorption steps, respectively, and E_{des} is the activation energy for desorption. We follow the approach of Peng et al. [44] and Sampara et al. [66,67] to estimate the kinetic parameters A_{ads}, A_{des}, E_{des}, and C_{S_z}. At equilibrium $r_{ads} = r_{des}$,

$$k_{ads} X_{C_{12}H_{26}} \theta_{S_z} C_{S_z} = k_{des} \theta_{S_z - C_{12}H_{26}} C_{S_z}. \quad (0.5)$$

Using the overall site balance, i.e.

$$\theta_{S_z} + \theta_{S_z - C_{12}H_{26}} = 1, \quad (0.6)$$

eq (6) is readily rearranged to give the linearized form of the Langmuir isotherm;

$$\frac{1}{n_{eq,C_{12}H_{26}}} = \frac{1}{N_{total}} + \frac{1}{K(T) * X_{C_{12}H_{26}} * N_{total}}. \quad (0.7)$$

Where N_{total} is the total moles of available sites and K(T) is the adsorption equilibrium constant given by

$$K(T) = \frac{k_{ads}}{k_{des}}. \quad (0.8)$$

The $C_{12}H_{26}$ equilibrium fraction coverage is given by

$$\theta_{S_z-C_{12}H_{26}} = \frac{n_{eq,C_{12}H_{26}}}{N_{total}}. \quad (0.9)$$

Where $n_{eq,C_{12}H_{26}}$ can be measured from the experiments by subtracting the moles of $C_{12}H_{26}$ leaving the reactor from the moles of $C_{12}H_{26}$ fed during the uptake period.

At a fixed temperature, $C_{12}H_{26}$ uptake experiments were conducted at three different concentrations until the equilibrium was achieved. Then, $n_{eq,C_{12}H_{26}}$ was calculated for each of the experiments. This process was repeated at three different uptake temperatures of 115℃, 135℃ and 155℃, the results of which are shown in Table A. 2. Following that $1/n_{eq,C_{12}H_{26}}$ was plotted versus $1/X_{C_{12}H_{26}}$ for each of the temperatures as shown in Figure 4.7(a). The intercept of the straight lines gives a value of N_{total} of 3.36 $\times 10^{-5}$ moles. Knowing the value of N_{total}, K(T) may be calculated from the slopes. Another graph was constructed that plotted ln(K) versus 1/T as shown in Figure 4.7(b). The intercept of this curve gives the value of $\ln\frac{A_{ads}}{A_{des}}$, while the value of E_{des} can be calculated from the slope. The values of $\frac{A_{des}}{A_{ads}}$ and E_{des} were calculated as 1.01×10^3 and 53.8 kJ/mol respectively.

With the values of N_{total}, $\frac{A_{des}}{A_{ads}}$ and E_{des} known, an estimate of either A_{ads} or A_{des} is sufficient to complete the task. We estimated A_{ads} by fitting the transient $C_{12}H_{26}$ uptake and TPD data at the uptake temperature of 135℃. In this experiment the gas feed containing 103 ppm $C_{12}H_{26}$ in Ar at 135℃ was directed to the monolith for 30 min. Experimental and modeling temporal concentration profiles of $C_{12}H_{26}$ are shown in Figure 4.8(a). The data show a sharp dip in the effluent $C_{12}H_{26}$ concentration followed by a slow approach to the feed concentration. The feed is then deprived of $C_{12}H_{26}$. At the point the $C_{12}H_{26}$

concentration drops below ~2 ppm, the temperature ramp to 500℃ is initiated. The tuned model is able to capture the $C_{12}H_{26}$ uptake and desorption features. The model was validated at a different uptake temperature of 125℃ with a different concentration of $C_{12}H_{26}$; i.e., 77 ppm and is shown in Figure A. 28. The model was also validated at a different uptake temperature of 145℃ with a continuous concentration of $C_{12}H_{26}$ as 58 ppm flowing throughout uptake and TPD and is shown in Figure A. 29. Satisfactory model predictions were obtained.

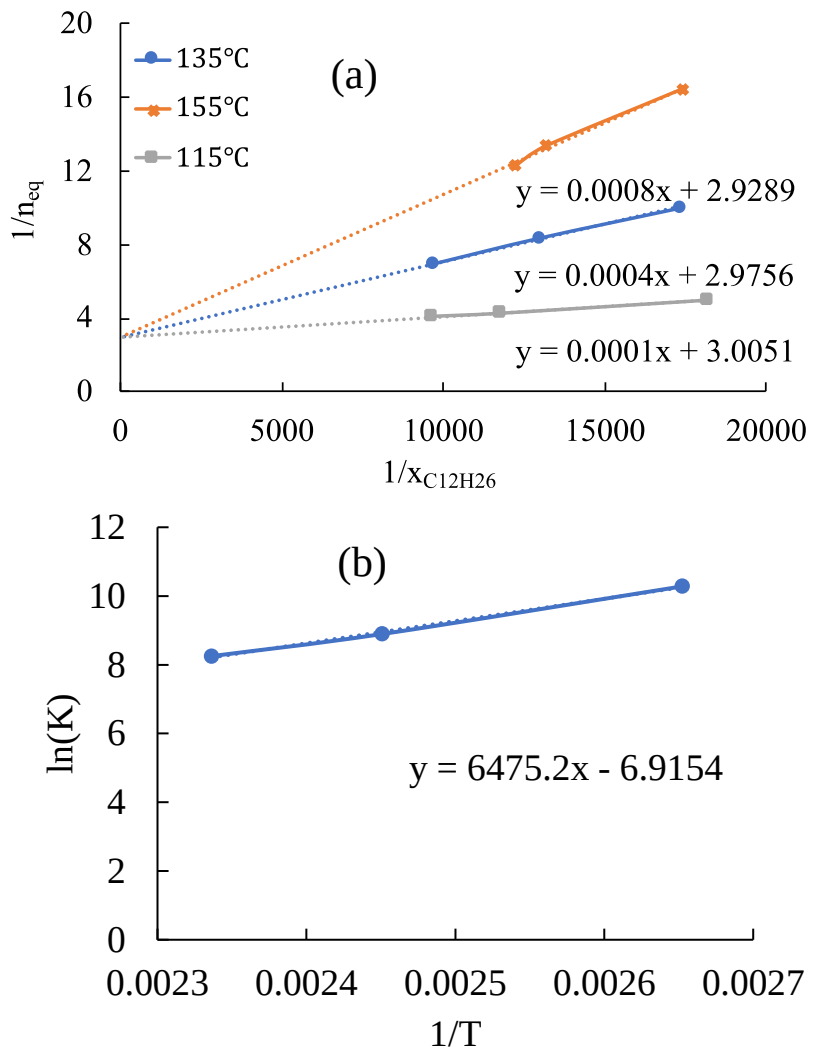

Figure 4.7 (a) Langmuir isotherms generated with the three concentration and three temperature combinations; (b) Arrhenius plot of the ratio of rate constants.

Water is always present in the exhaust so including its effect in the model is essential. Increased $C_{12}H_{26}$ uptake was observed when the $C_{12}H_{26}$ uptake was carried out in the absence of H_2O under otherwise identical conditions. This observation clearly indicates competition between $C_{12}H_{26}$ and H_2O on the zeolitic sites. Thus, we added the H_2O uptake on the S_z sites

$$H_2O + S_z \leftrightarrow S_z - H_2O. \quad \text{(R4.2)}$$

Keeping with the convention that the adsorption (forward) rate is non-activated, the pre-exponential factors and activation energy for the desorption (reverse) rate were fitted using the adsorption-desorption experiment with the uptake carried out at 135℃. The feed contained 56 ppm $C_{12}H_{26}$/ 2%H_2O/ balance Ar during uptake and only Ar during TPD. Tables 4.2 and Tables 4.3 show the rate expressions and estimated kinetic parameters, respectively. A comparison of the experimental and model predictions is shown in Figure 4.8(b). The tuned model captures the decreased $C_{12}H_{26}$ uptake as well as its release temperatures and peak concentration during TPD. Model validation was conducted at a concentration of 60 ppm $C_{12}H_{26}$ and temperature of 165℃; the results are shown in Figure A. 30. An increase in the adsorption temperature expectedly reduces $C_{12}H_{26}$ uptake. The model predicts the decrease in $C_{12}H_{26}$ uptake with increasing uptake temperature and the $C_{12}H_{26}$ desorption profile.

Table 4.2 Reaction mechanism for $C_{12}H_{26}$ feed

Reaction no.	**Reaction step**	**Rate expression (R_f - R_b)**
R4.1	$C_{12}H_{26} + S_z \leftrightarrow S_z - C_{12}H_{26}$	$k_{1f} X_{C_{12}H_{26}} \theta_{S_z} C_{S_z} - k_{1b} \theta_{S_z - C_{12}H_{26}} C_{S_z}$
R4.2	$H_2O + S_z \leftrightarrow S_z - H_2O$	$k_{2f} X_{H_2O} \theta_{S_z} C_{S_z} - k_{2b} \theta_{S_z - H_2O} C_{S_z}$

Table 4.3 Kinetic parameters for $C_{12}H_{26}$ feed

Reaction no.	Pre-exponential factor		Activation Energy (kJ mol^{-1})	
R4.1	A_{1f} A_{1b}	1.98e1 2e4	E_{1f} E_{1b}	0 53.8
R4.2	A_{2f} A_{2b}	4e-1 5e4	E_{2f} E_{2b}	0 54

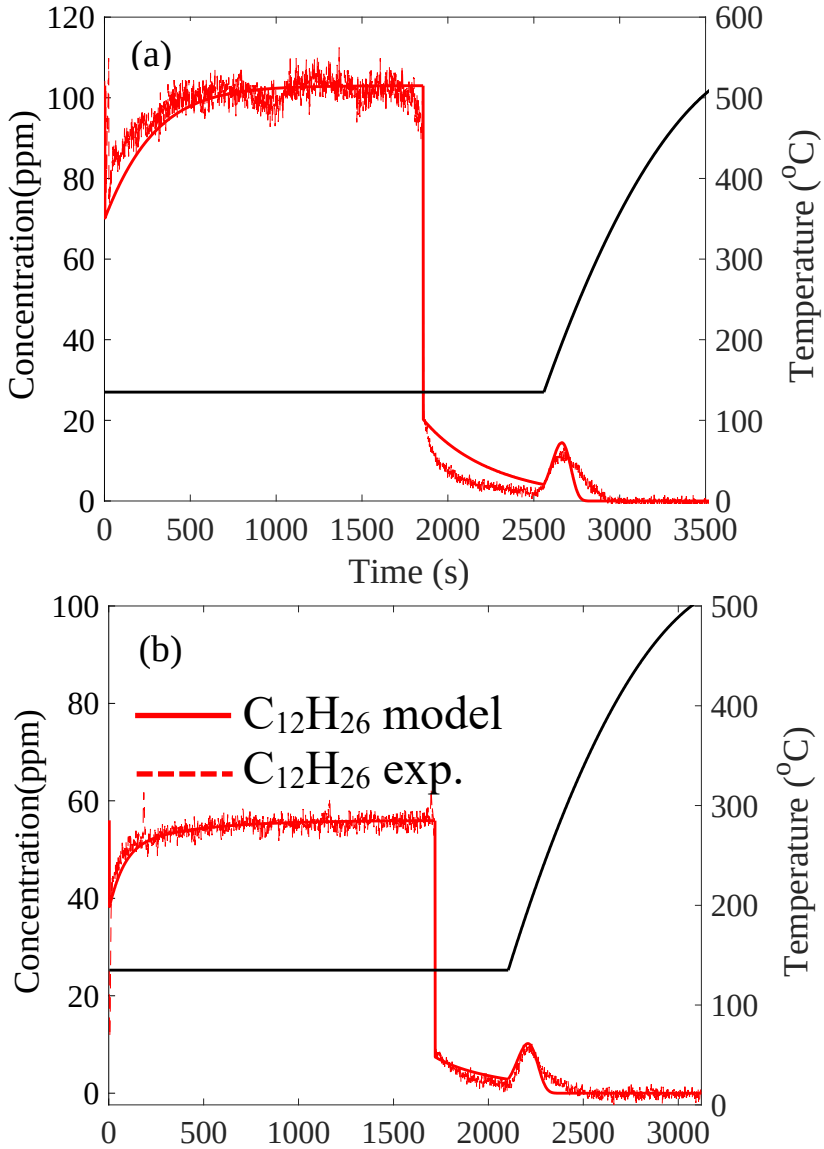

Figure 4.8 Experimental and model results for uptake at 135°C and TPD on Pd(1%)/SSZ-13 for a feed comprising of (a) 103 ppm $C_{12}H_{26}$/ balance Ar during uptake and only Ar during TPD; (b) 56 ppm $C_{12}H_{26}$/ 2%H_2O/ balance Ar during uptake and only Ar during TPD.

4.2.2.3 Microkinetic model for NO-containing feeds

The next step is to develop a model for NO uptake and release in the presence of $C_{12}H_{26}$. In our previous study we developed a model for NO uptake on Pd/SSZ-13 [30]; this is the starting point for the NO + $C_{12}H_{26}$ uptake model. The NO-only model considers $Z^-[PdOH]^+$, $Z^-Pd^{2+}Z^-$, and Z^-Pd^+ as active sites for NO adsorption. Brønsted acid sites (BASs) do not adsorb NO or NO_2 in the presence of excess H_2O due to blockage of sites by H_2O [30,37,38,53] and for this reason they are not considered as active NO sorption sites. The 10-step reaction mechanism is shown in Table 3.2 along with the rate expressions. A combination of DFT calculations and data fitting was used to estimate the unknown kinetic parameters. The kinetic parameters are given in Table 3.2. Details of DFT calculations, parameter fitting and estimation of site concentrations are provided in our earlier work [30].

The experiments in the current study were conducted on a different reactor setup that contained a different size monolith (but same composition; Pd(1%)/SSZ-13) and set of experimental conditions. Here we validate the NO-only model for a set of data from the new setup. The first validation was conducted for NO uptake at 115°C with a feed comprising 380 ppm NO/ 2% O_2/ 2% H_2O/ balance Ar during uptake and 2% O_2/ Ar during TPD. Measured and predicted profiles are shown in Figure 4.9. The developed model captures satisfactorily the NO uptake along with the TPD data without any modification of the original parameter values. The model also correctly predicts the generation of the NO_2 at the start of uptake period. At the beginning of the NO uptake experiment, which followed the standard oxidative pretreatment, the dispersed Pd cations are assumed to be present in +2 oxidation state [15,30,37]. NO_2 is produced by the two-step NO reduction of

two $Z^-[PdOH]^+$ to Z^-Pd^+, co-generating H_2O as shown by reactions R3.4 and R3.5. Finally, the model also captures the two TPD peaks for NO along with their desorption temperatures.

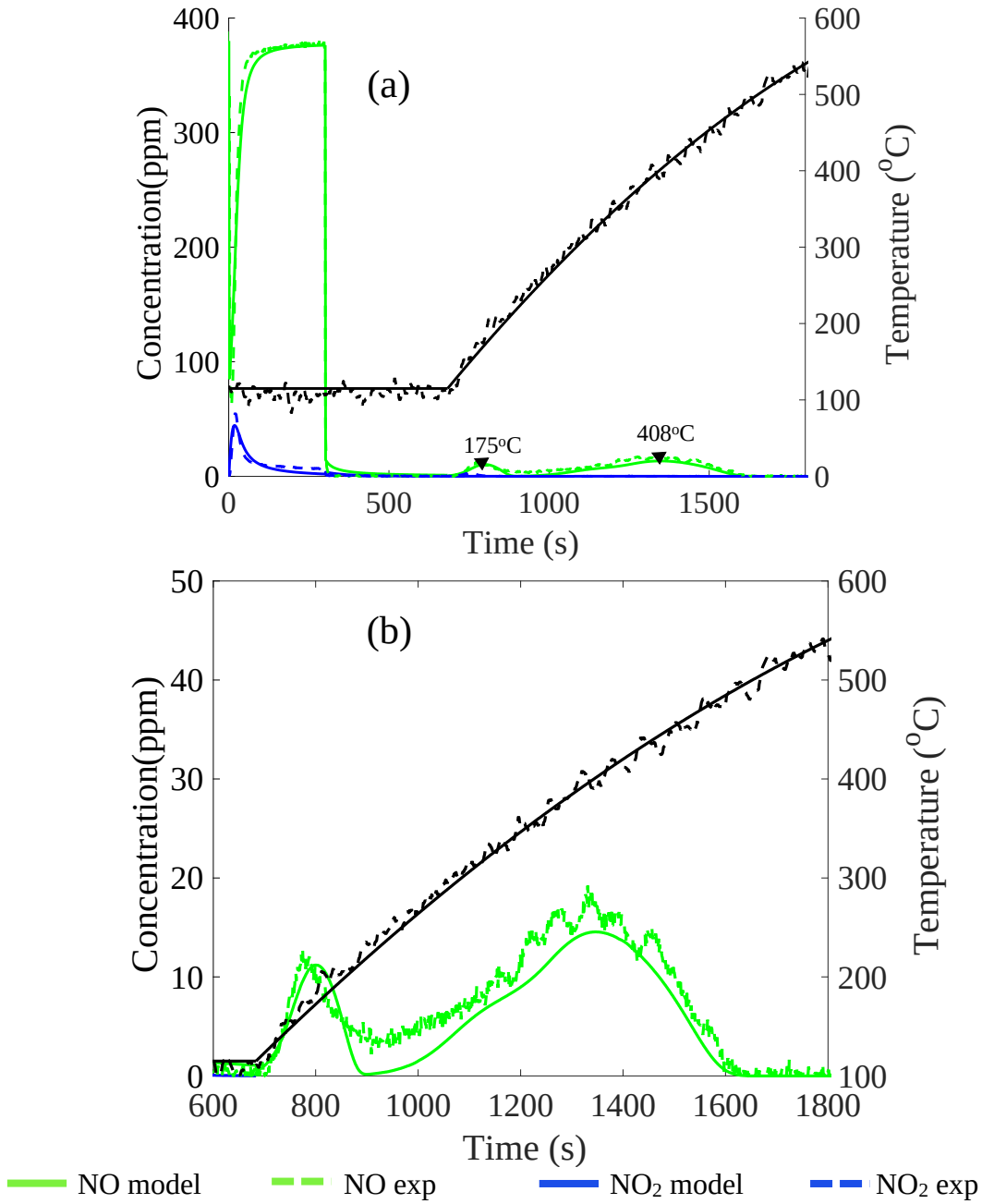

Figure 4.9 (a) Experimental and model results for uptake at 115°C and TPD on Pd(1%)/SSZ-13 for a feed comprising of 380 ppm NO/ 2% O_2/ 2% H_2O/ balance Ar during uptake and 2% O_2/ Ar during TPD; (b) Enlarged NO TPD profile.

NO uptake on Pd/SSZ-13 in the presence of H_2O is a strong function of temperature. At low uptake temperatures most of the Pd cationic sites and essentially all of the Brønsted acid sites are occupied by H_2O [30,38]. With an increase in temperature, desorption of H_2O occurs, freeing-up sites for NO adsorption. As a result, with increasing uptake temperature there is an increase in the amount of NO adsorbed. The model was tested for a higher uptake temperature of 155°C, as shown in Figure A. 31. The model correctly predicts the increased NO uptake and its TPD peak. In addition, the model correctly predicts the immediate generation and peak magnitude (~130 ppm) of NO_2 during the NO uptake.

4.2.2.4 Microkinetic model for NO and $C_{12}H_{26}$ co-feed

The next step is to combine the models of NO and $C_{12}H_{26}$ uptake into a single model for the NO + $C_{12}H_{26}$ co-feed. A complicating aspect to address is that in the presence of O_2, $C_{12}H_{26}$ catalytically oxidizes to CO and CO_2 at sufficiently high temperature. The amount of $C_{12}H_{26}$ that oxidizes versus the amount released depends on the temperature and ramp rate. In the absence of O_2 all of the $C_{12}H_{26}$ desorbs before 300℃, as seen in Figure 4.8(a), On the other hand, in the co-feed experiment containing O_2 (Figure 4.1), the oxidation product CO_2 is generated up to ~450℃. In our previous study we showed that CO_2 negligibly adsorbs onto Pd/SSZ-13 [30]. This suggest that CO_2 is observed as the partial oxidation product CO is consumed. We speculate that the protracted generation of CO_2 is linked to a trapped surface complex containing CO. We expand on this and related issues next.

Tables 4.4 provides a set of four proposed reactions that captures the coupled reactions and release for the NO + $C_{12}H_{26}$ co-feed. Reaction R4.13 is a global surface

reaction describing the partial oxidation of adsorbed $C_{12}H_{26}$ to CO. Once CO is formed, it can adsorb on the isolated $Z^-Pd^{2+}Z^-$ cations, described by reaction R4.14. According to DFT calculations by Mei et al. [53] (for Pd/BEA) and our own for Pd/SSZ-13 [30], NO and CO can co-adsorb on $Z^-Pd^{2+}Z^-$, described by reaction R4.15. Vu et al. [22] and Khivantsev et al. [24] reported the co-adsorption of NO and CO on $Z^-Pd^{2+}Z^-$ sites. Reaction R4.16 describes the oxidation of adsorbed CO to CO_2 in the presence of O_2. Rate expressions for reactions R4.13 to R4.16 are given in Tables 4.4. Kinetic parameters for R4.13 were estimated through a fit of the data while the energies for reactions R4.14 to R4.16 were taken from Ambast et al. [30]. Kinetic parameters for reactions R4.13 to R4.16 are given in Tables 4.5.

Table 4.4 Reaction mechanism for NO + $C_{12}H_{26}$ feed [S_1 - $Z^-Pd^{2+}Z^-$; S_2 - $Z^-[PdOH]^+$]

Reaction no.	**Reaction step**	**Rate expression (R_f - R_b)**
R4.3	S_z - $C_{12}H_{26}$ + 12.5 O_2 $\rightarrow$ 12 CO + 13 H_2O + S_z	$k_{3f}X_{O_2}\theta_{S_z-C_{12}H_{26}}C_{S_z}$
R4.4	$CO + Z^-Pd^{2+}Z^- \leftrightarrow Z^-Pd^{2+}Z^- - CO$	$k_{4f}X_{CO}\theta_{S1}C_{S1}$- $k_{4b}\theta_{CO-S1}C_{S1}$
R4.5	$CO + Z^-Pd^{2+}Z^- - NO \leftrightarrow Z^-Pd^{2+}Z^- - (NO)(CO)$	$k_{5f}X_{CO}\theta_{NO-S1}C_{S1}$- $k_{5b}\theta_{(NO)(CO)-S3}C_{S2}$
R4.6	$Z^-Pd^{2+}Z^- - CO + 0.5O_2 \rightarrow CO_2 + Z^-Pd^{2+}Z^-$	$k_{6f}\theta_{CO-S1}X_{O_2}^{0.5}C_{S1}$

Table 4.5 Kinetic parameters for NO + $C_{12}H_{26}$ feed

Reaction no.	**Pre-exponential factor**		**Activation Energy (kJ mol^{-1})**		**α (Coverage dependence)**
R4.3	A_{3f}	1.8e8	E_{3f}	60	
R4.4	A_{4f} A_{4b}	8e5 1e9	E_{4f} E_{4b}	0 150	
R4.5	A_{5f} A_{5b}	6e4 1e9	E_{5f} E_{5b}	0 110	0.3
R4.6	A_{6f}	1e8	E_{6f}	80	

There are likely additional reactions through which CO and NO adsorb; three possible reactions include:

$CO + Z^{-}Pd^{2+}Z^{-}\text{-}NO \leftrightarrow Z^{-}Pd^{2+}Z^{-}\text{-}(NO)(CO)$, (R4.5)

$NO + CO + Z^{-}Pd^{2+}Z^{-} \leftrightarrow Z^{-}Pd^{2+}Z^{-}\text{-}(NO)(CO)$, (R4.7)

and $NO + Z^{-}Pd^{2+}Z^{-}\text{-}CO \leftrightarrow Z^{-}Pd^{2+}Z^{-}\text{-}(NO)(CO)$. (R4.8)

CO may also adsorb on sites pre-adsorbed by H_2O. Obviously, accounting for possible reaction steps introduces a large number of unknown kinetic parameters. Rather, given the scope and complexity of the resulting system, our approach is to define a smaller set of reactions that are able to capture most of the experimental results. We have previously shown that NO adsorbed on $Z^{-}Pd^{2+}Z^{-}$ sites accounts for the low temperature NO TPD peak [30,38]. We showed earlier in the current work that the lower temperature desorption peak observed for the NO-only feed moves to higher temperature in the presence of $C_{12}H_{26}$. For this reason, we deem it sufficient to involve only the $Z^{-}Pd^{2+}Z^{-}$ sites in the $C_{12}H_{26}$ coupling.

With the kinetic scheme now defined for the NO + $C_{12}H_{26}$ feed, model tuning was carried out. A total of 6 pre-exponential factors and the activation energy for reaction R4.13 were estimated based on a fit of NO+ $C_{12}H_{26}$ uptake (at 135℃) and TPD data. A total number of 1530 of data points were used for the parameter estimation. The data included the effluent concentrations of NO, NO_2, $C_{12}H_{26}$, CO and CO_2 spanning the uptake and TPD.

The results of the model tuning are shown in Figure 4.10. The NO + $C_{12}H_{26}$ co-feed contained 395 ppm NO/ 58 ppm $C_{12}H_{26}$/ 2% O_2/ 2% H_2O/ balance Ar during uptake and 2% O_2/ Ar during TPD. The tuned model satisfactorily captures all of the experimental trends. The model predicts the simultaneous uptake of NO and $C_{12}H_{26}$ along with the generation of NO_2, a result of the reduction of Pd(II) to Pd(I).

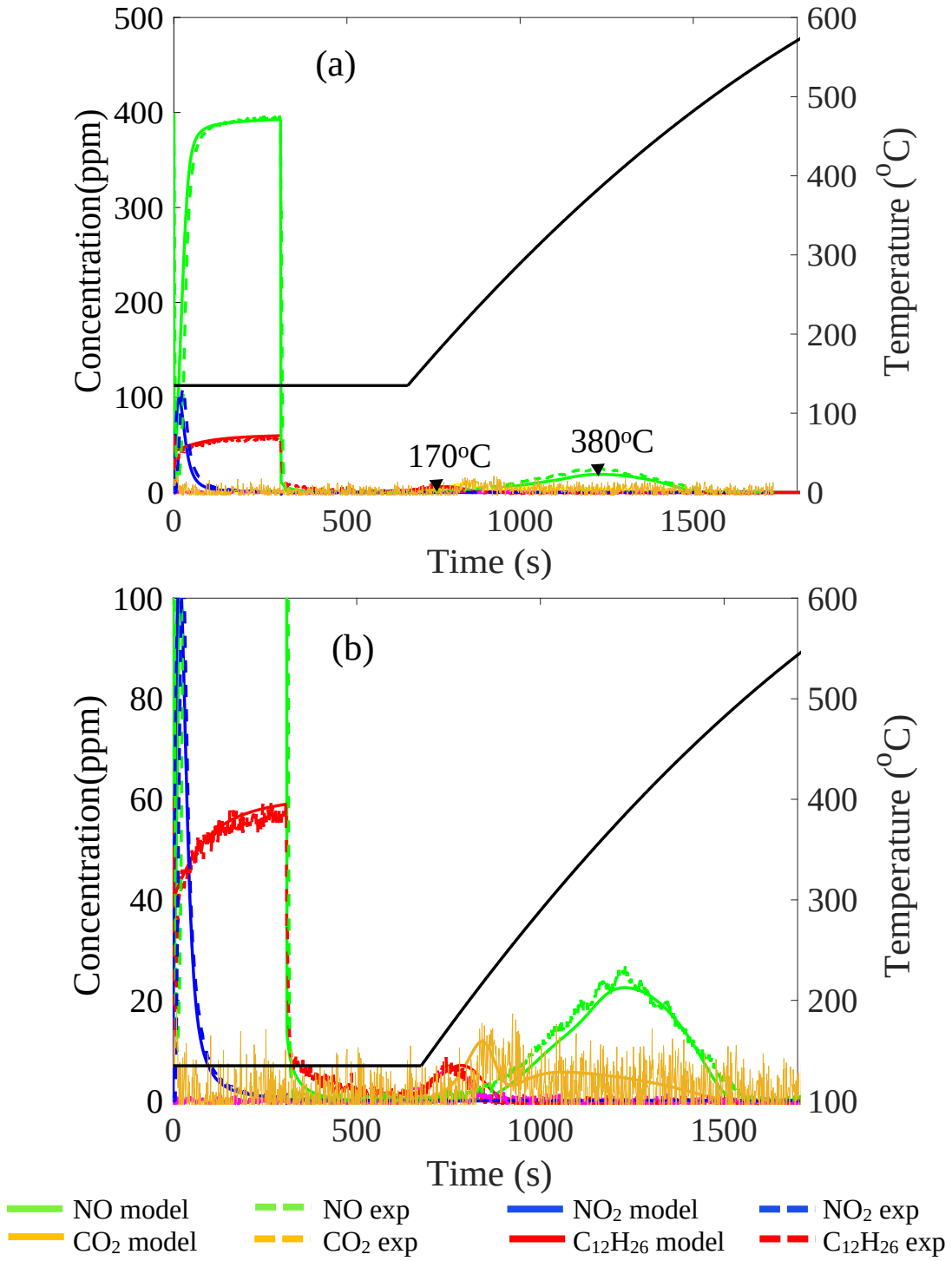

Figure 4.10 (a) Experimental and model results for uptake at 135°C and TPD on Pd(1%)/SSZ-13 for a feed comprising of 395 ppm NO/ 58 ppm $C_{12}H_{26}$/ 2% O_2/ 2% H_2O/ balance Ar during uptake and 2% O_2/Ar during TPD; (b) Enlarged uptake and TPD profiles.

At the beginning part of the TPD the model predicts the release of $C_{12}H_{26}$. In the presence of O_2, $C_{12}H_{26}$ is oxidized to CO which is adsorbed on Pd sites. According to DFT calculations [30,53], co-adsorbed CO and NO in the form of a surface complex has a higher binding energy than NO alone, which results in the release of NO at higher temperatures. Thus, the model predicts delayed NO release. Finally, in the presence of O_2, CO is oxidized to CO_2 with the model predicting the CO_2 formation.

The model was validated at the lower uptake temperature of 115℃. Experimental and modeling profiles are shown in Figure A. 32. At this lower uptake temperature less NO and $C_{12}H_{26}$ are adsorbed during the uptake regime along with a lower NO_2 spike. This is due to more blocking as a result of higher H_2O coverage at low temperatures.

4.2.2.5 Microkinetic model for $C_{12}H_{26}$ and H_2O pre-adsorption

Earlier we presented data showing that pre-adsorption $C_{12}H_{26}$ and H_2O decreases the NO uptake. The decrease in NO uptake is attributed to combined blocking by both pre-adsorbed H_2O and $C_{12}H_{26}$. Here the inhibition is examined phenomenologically by adding relevant features to the model and evaluating their impact.

First, we consider the H_2O impact. Exposure of the Pd/SSZ-13 to the large excess of H_2O in the feed leads to it blocking NO from its adsorption on Pd cations and Brønsted acid sites. NO uptake is higher in the experiment that involves co-feeding NO and H_2O compared to pre-adsorption of H_2O because when H_2O is pre-adsorbed it does not have to compete for sites with NO. At such high concentration of H_2O (~2%), sites can be surrounded by multiple H_2O molecules. Thus, following H_2O pre-adsorption, it will be difficult for the fed NO to reach to a site and get adsorbed. The number of Pd sites available for NO uptake after H_2O pre-adsorption is equal to the difference between total Pd sites

and the sites blocked with pre-adsorbed H_2O. At the start of NO uptake two different Pd active sites are present: $Z^-[PdOH]^+$ and $Z^-Pd^{2+}Z^-$. Equations (4.10) and (4.11) express the available sites for NO uptake as a function of a fraction of $Z^-[PdOH]^+$ and $Z^-Pd^{2+}Z^-$ sites that are pre-adsorbed with H_2O:

$$C_{Z^-Pd^{+2}Z^-,av} = C_{Z^-Pd^{+2}Z^-,tot} - (m_{H_2O} \times C_{Z^-Pd^{+2}Z^-,tot} \times \theta_{Z^-Pd^{+2}Z^- - H_2O}) \quad (0.10)$$

and $C_{Z^-[Pd(II)OH]^+,av} = C_{Z^-[Pd(II)OH]^+,tot} - (m_{H_2O} \times C_{Z^-[Pd(II)OH]^+,tot} \times (\theta_{[Pd(II)OH]^+ - H_2O}))$. (0.11)

m_{H_2O} is an empirical parameter that quantifies the fraction of Pd sites that are blocked by pre-adsorbed H_2O. $C_{Z^-Pd^{+2}Z^-,av}$ is the concentration of $Z^-Pd^{2+}Z^-$ sites available for NO uptake after H_2O pre-adsorption while $C_{Z^-Pd^{+2}Z^-,tot}$ is the total $Z^-Pd^{2+}Z^-$ sites in the catalyst. Similarly, $C_{Z^-[Pd(II)OH]^+,av}$ is the concentration $Z^-[PdOH]^+$ sites available for NO uptake after H_2O pre-adsorption, while $C_{Z^-[Pd(II)OH]^+,tot}$ is the total $Z^-[PdOH]^+$ sites in the catalyst. The corresponding $\theta_{Z^-Pd^{+2}Z^- - H_2O}$ and $\theta_{[Pd(II)OH]^+ - H_2O}$ are the fractions of $Z^-[PdOH]^+$ and $Z^-Pd^{2+}Z^-$ sites covered with H_2O.

We carried out a set of experiments to estimate m_{H_2O}. The NO uptake experiment was conducted at ~125°C in which the catalyst was pre-adsorbed with H_2O by flowing 2% H_2O/ 2% O_2/ balance Ar for 20 min. This was followed by NO adsorption for 5 min by flowing a feed of 390 ppm NO/ 2% H_2O/ 2% O_2/ balance Ar over the catalyst. Model tuning gives m_{H_2O} = 0.3, resulting in good agreement between the data and model predictions (Figure 4.11(a)). Model validation was done at a lower uptake temperature of ~110°C with good results as seen in Figure 4.11(b).

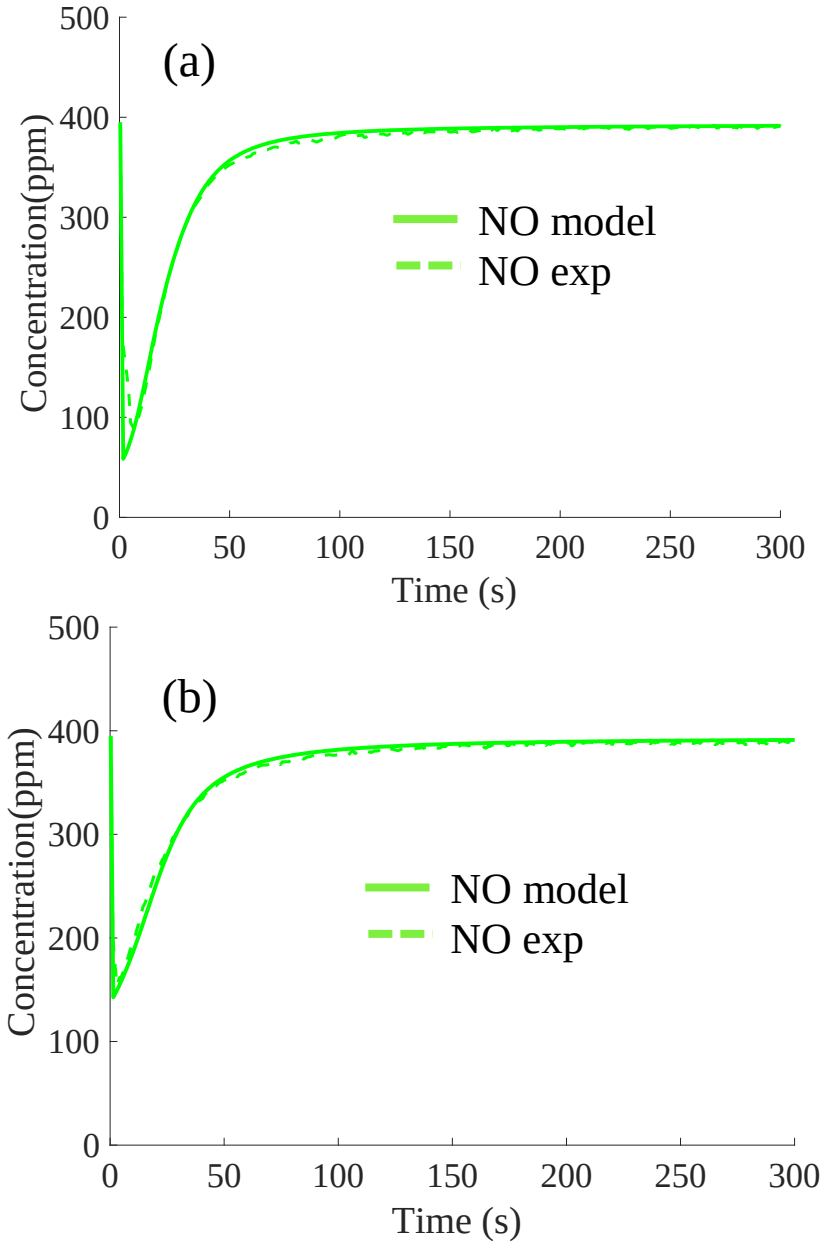

Figure 4.11 Experimental and modeling NO uptake profiles for H_2O pre-adsorption followed by NO uptake at uptake temperatures of (a) ~125°C and (b) ~110°C.

The second step is to account for the blocking of NO adsorption by pre-adsorbed $C_{12}H_{26}$. Inhibition by $C_{12}H_{26}$ is conjectured to be a kinetic (transport) process as opposed to a thermodynamic process. The 8-member ring CHA framework of SSZ-13 is a small-pore zeolite with a nominal pore size of ~ 3.8 Å. It is therefore anticipated that most of the adsorbed $C_{12}H_{26}$ will reside on the external surface of the zeolite crystallites and, as a result,

restrict access of NO to the intracrystalline adsorption sites by blocking pore mouths at the surface. In contrast, when a mixture containing NO and $C_{12}H_{26}$ is fed to a sample that is not pre-exposed to $C_{12}H_{26}$, it is anticipated that the smaller, faster diffusing NO will be able to access the unimpeded sites.

A similar approach is used to estimate the available sites for NO uptake after H_2O and $C_{12}H_{26}$ pre-adsorption. The concentration of sites available for NO uptake after H_2O and $C_{12}H_{26}$ pre-adsorption is equal to the total Pd sites present minus the sites blocked by H_2O and by $C_{12}H_{26}$. The concentrations of available $Z^-[PdOH]^+$ and $Z^-Pd^{2+}Z^-$ sites for NO uptake after pre-adsorption are as follows:

$$C_{Z^-Pd^{+2}Z^-,av} = C_{Z^-Pd^{+2}Z^-,tot} - (m_{H_2O} \times C_{Z^-Pd^{+2}Z^-,old} \times \theta_{Z^-Pd^{+2}Z^--H_2O}) - (m_{C_{12}H_{26}} \times (C_{Z^-Pd^{+2}Z^-,tot} - (m_{H_2O} \times C_{Z^-Pd^{+2}Z^-,tot} \times \theta_{Z^-Pd^{+2}Z^--H_2O})) \times \theta_{S_z-C_{12}H_{26}}) \quad (0.12)$$

and $$C_{Z^-[Pd(II)OH]^+,av} = C_{Z^-[Pd(II)OH]^+,tot} - (m_{H_2O} \times C_{Z^-[Pd(II)OH]^+,tot} \times \theta_{Z^-[Pd(II)OH]^+-H_2O}) - (m_{C_{12}H_{26}} \times (C_{Z^-[Pd(II)OH]^+,tot} - (m_{H_2O} \times C_{Z^-[Pd(II)OH]^+,old} \times \theta_{Z^-[Pd(II)OH]^+-H_2O})) \times \theta_{S_z-C_{12}H_{26}}). \quad (0.13)$$

Here $m_{C_{12}H_{26}}$ is the empirical parameter quantifies the fraction of sites made inaccessible to NO due to $C_{12}H_{26}$ pre-adsorption. The value of $m_{C_{12}H_{26}}$ is estimated by fitting the model using the measured NO uptake experiment at ~135°C for which the catalyst is pre-adsorbed with H_2O and $C_{12}H_{26}$. Given the much higher feed concentration of H_2O, the value of m_{H_2O} estimated earlier is fixed while estimating $m_{C_{12}H_{26}}$. In this experiment, the sample was exposed to a gas mixture containing 55 ppm $C_{12}H_{26}$ /2% O_2/ 2% H_2O/ balance Ar for 20 min, followed by NO adsorption for 5 min by flowing a feed of 395 ppm NO/ 55 ppm $C_{12}H_{26}$/ 2% O_2/ 2% H_2O/ balance Ar over the catalyst. The value of $m_{C_{12}H_{26}}$ was estimated to be 0.2. Experimental and modeling NO adsorption profiles for the above-mentioned

experiment are compared in Figure 4.12(a), with good agreement. The model is validated at the uptake temperature of ~115°C with good agreement, as noted in Figure 4.12(b).

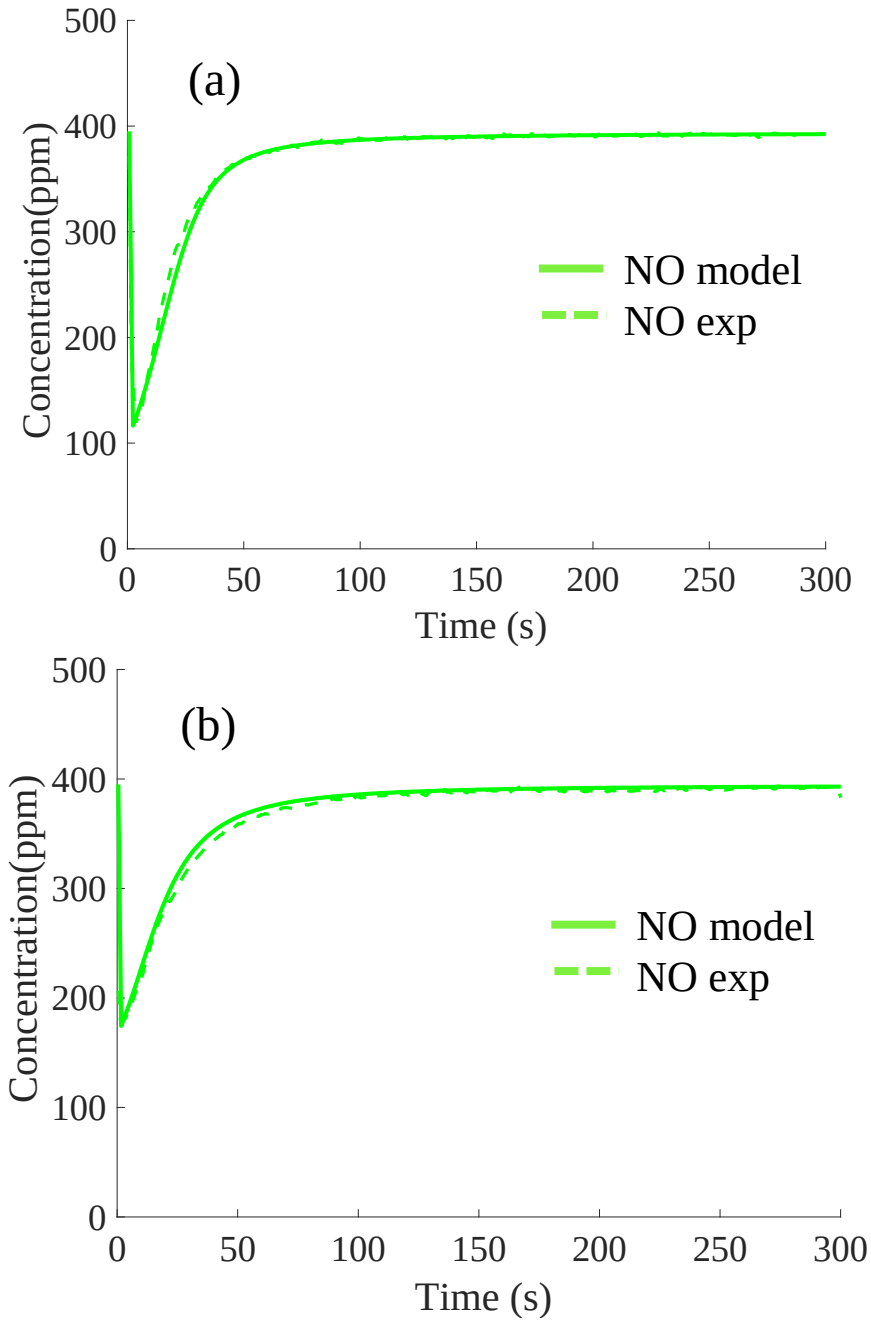

Figure 4.12 Experimental and modeling NO uptake profiles for $C_{12}H_{26}$ and H_2O pre-adsorption followed by NO uptake at uptake temperatures of (a) ~135°C and (b) ~115°C.

To check that the estimates of the blocking parameter $m_{C_{12}H_{26}}$, we estimated the NO uptake using a different, more physical approach. This involved estimating the extent

of surface coverage by pre-adsorbed $C_{12}H_{26}$ assuming that none enters the nanopores of the SSZ-13 zeolite. Consider the following. We calculated the moles of Pd per external surface area of the SSZ-13 and the external surface area of SSZ-13 covered by pre-adsorbed $C_{12}H_{26}$ molecular species. With these two values we can estimate the moles of Pd sites blocked by the adsorbed $C_{12}H_{26}$. As described in the SM section, an amount of $5.0e^{-6}$ moles Pd will be blocked by the pre-adsorbed $C_{12}H_{26}$ at 115℃ uptake temperature. This compares favorably to the amount predicted by the above-described empirical approach; i.e., 4.67e-6 moles Pd. At an uptake temperature of ~135℃, the pre-adsorbed $C_{12}H_{26}$ will block ~$4.7e^{-6}$ moles of Pd sites. This value too compares favorably to the empirical estimate of 4.4e-6 moles at the same 135℃ uptake temperature. Table A. 3 compares the results from both approaches. The close comparison of the physical and empirical estimates lends support to the envisioned blocking mechanism.

Another possible explanation for the measured decrease in NO uptake after pre-adsorption of H_2O and $C_{12}H_{26}$ may be attributed to the NO diffusion process. That is, the presence of pre-adsorbed $C_{12}H_{26}$ restricts the diffusion of NO into the zeolitic pore structure. This involved examining the model predicted NO uptake for a range of NO diffusivity values, from the original value to a value that is 4x lower; i.e. from $3.88e^{-7}$ m^2/s to $9.71e^{-8}$ m^2/s at uptake temperatures of ~115°C. The model-predicted profiles are shown in Figure A. 33. In decreasing the NO diffusivity, the depth of the NO adsorption peak begins to decrease, in agreement with the experiments. In contrast to the experimental data, the model predicts a broadening of NO uptake profile indicating a delayed NO uptake. The model, thus, was not able to predict the NO uptake profile after the pre-adsorption of H_2O and $C_{12}H_{26}$. The poor model prediction rules out the inhibition of NO uptake.

4.2.3 Model application

4.2.3.1 NO uptake with/without $C_{12}H_{26}$: Continuous temperature ramping

The tuned model was used to predict the PNA performance under the more realistic scenario in which the vehicle exhaust temperature increases immediately. This means that there is no constant uptake period followed by TPD. The model was run for the NO-only and NO + $C_{12}H_{26}$ feeds during a temperature ramp of 20°C/min, starting at 30°C and going to 600°C. For NO-only feed, the feed comprised of 400 ppm NO/ 2% O_2/ 2%H_2O/ balance Ar while 60 ppm of $C_{12}H_{26}$ was added to the NO-only feed for NO + $C_{12}H_{26}$ feed. The predicted NO profiles for both the feeds at 2500 sccm feed flowrate (GHSV = 75.9k h^{-1}) are shown in Figure 4.13.

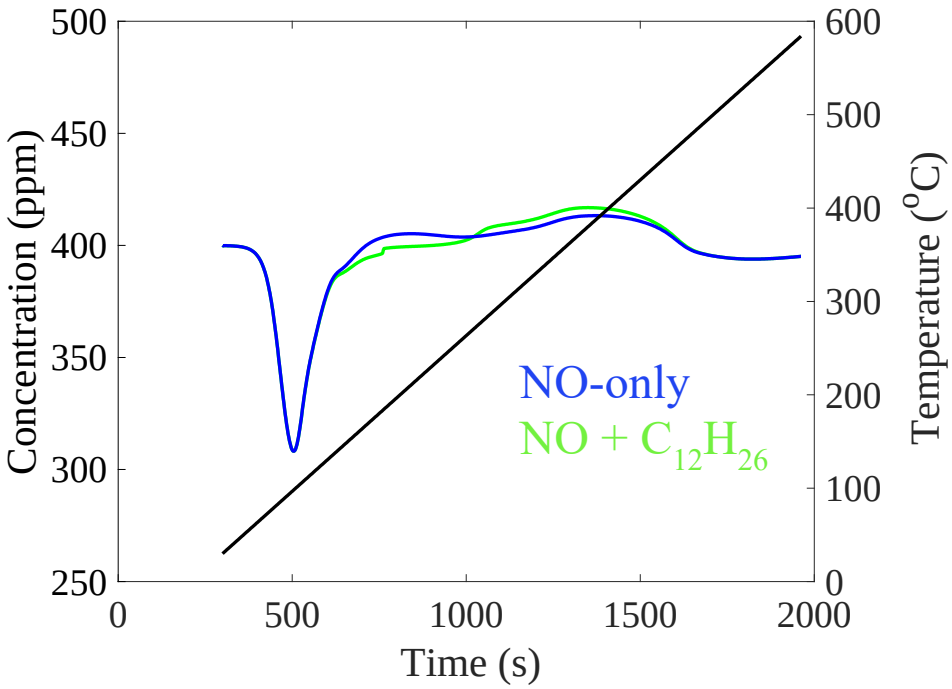

Figure 4.13 Model prediction of NO profile for feed comprising of 400 ppm NO/ 2% O_2/ 2% H_2O/ balance Ar with a continuous temperature ramping from 30°C to 600°C at the rate of 20°C/min and with and without 60 ppm $C_{12}H_{26}$ at feed flowrate of 2500 sccm .

There are a few features to note. First, for both the feeds there is no uptake of NO until the temperature reaches ~60°C due to site blockage by H_2O. Second, the NO starts

desorbing for the NO-only feed at a temperature of ~168℃ whereas for NO + $C_{12}H_{26}$ feed, NO starts desorbing at ~232℃. This is consistent with the experimental finding discussed earlier that NO desorption is delayed in the presence of $C_{12}H_{26}$. The total NO absorbed is NO/Pd ~ 1.3 for the NO-only feed while it is ~1.38 for NO + $C_{12}H_{26}$ feed. NO starts desorbing at lower temperatures for NO-only feed as compared to NO + $C_{12}H_{26}$ feed. Since the temperature is continuously increasing, therefore, the adsorption period for NO-only feed is shorter than NO + $C_{12}H_{26}$ feed and so NO uptake is higher for NO + $C_{12}H_{26}$ feed for the case of continuous temperature ramping. This shows that the presence of $C_{12}H_{26}$ is beneficial for PNA performance.

4.2.3.2 NO uptake with/without $C_{12}H_{26}$: Impact of monolith size and operating conditions

In our previous study for developing PNA model for Pd/SSZ-13 we used a different size of monolith as well as different experimental conditions [30]. Earlier we showed that the previously developed NO-only model was able to predict the experimental results for new NO-only data. Here we use the NO + $C_{12}H_{26}$ model developed to predict the NO uptake and desorption profiles with and without $C_{12}H_{26}$ for the set of experimental conditions used in our earlier study.

The NO + $C_{12}H_{26}$ feed containing 200 ppm NO/ 60 ppm $C_{12}H_{26}$/ 12% O_2/ 6% H_2O/ balance N_2 was used to generate the data. The predicted profiles for the NO-only and NO + $C_{12}H_{26}$ feeds are compared in Figure 4.14. The experiment for the NO-only feed (without the 60 ppm of hydrocarbon) directed the gas mixture to the Pd/SSZ-13 coated monolith at a GHSV of 30k hr^{-1} and temperature of 100℃ for 30 min followed by a temperature ramp from 100℃ to 600℃ in 20 min. The same predicted features as previously reported include

a dip in the NO concentration followed by a slow approach to its feed concentration of 200 ppm. During the initial stage of the temperature ramp, H_2O desorbs, providing additional sites onto which NO adsorbs. When the temperature reaches ~120°C, the second phase of NO uptake occurs, coinciding with the generation of NO_2. At higher temperatures the remaining NO desorbs from the sites. For the NO + $C_{12}H_{26}$ co-feed, 60 ppm of $C_{12}H_{26}$ was added to the feed. A comparison of the two feeds reveals the same NO uptake of NO/Pd ~1.34. The difference lies in the NO desorption profiles for both the feeds. The majority (~98%) of the NO is desorbed above 280°C for the NO + $C_{12}H_{26}$ feed while for the NO-only feed, ~76% of NO has desorbed above 280°C.

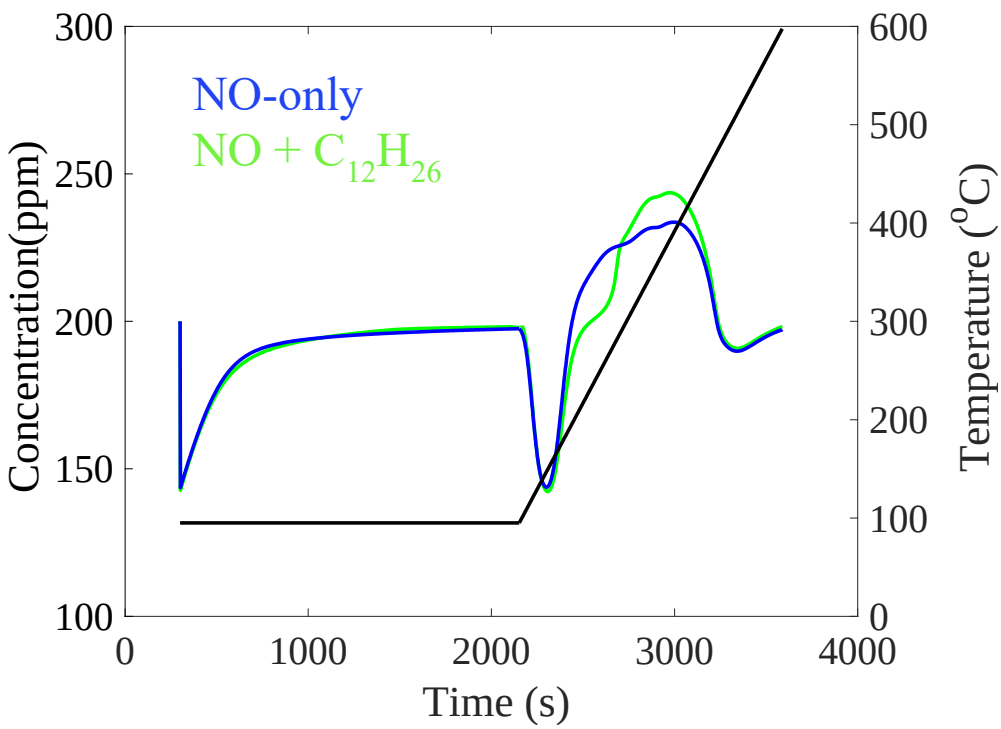

Figure 4.14 Modeling results of NO uptake at 95°C and TPD on Pd(1%)/SSZ-13 for a feed comprising of 200 ppm NO/ 12% O_2/ 6% CO_2/ 6% H_2O / balance N_2 with and without 60 ppm of $C_{12}H_{26}$.

It is of interest to quantify the benefit of $C_{12}H_{26}$ in the feed, so we used the model to predict NO uptake and desorption profiles for continuous temperature ramp starting at

30°C and going to 600°C. The model-predicted profiles for NO-only and NO + $C_{12}H_{26}$ feeds are shown in Figure 4.15. We used the model to calculate the amount of NO that is adsorbed for both feeds up to 200°C, the threshold temperature at which the SCR becomes operable. The amount of NO adsorbed per mole of Pd for NO-only feed and NO + $C_{12}H_{26}$ feed are 1.04 and 1.23, respectively. In order to trap the same amount of NO for both the feeds up to 200°C, that is 1.04 mole of NO per mole of Pd, it would require 16% less active Pd sites for NO + $C_{12}H_{26}$ feed.

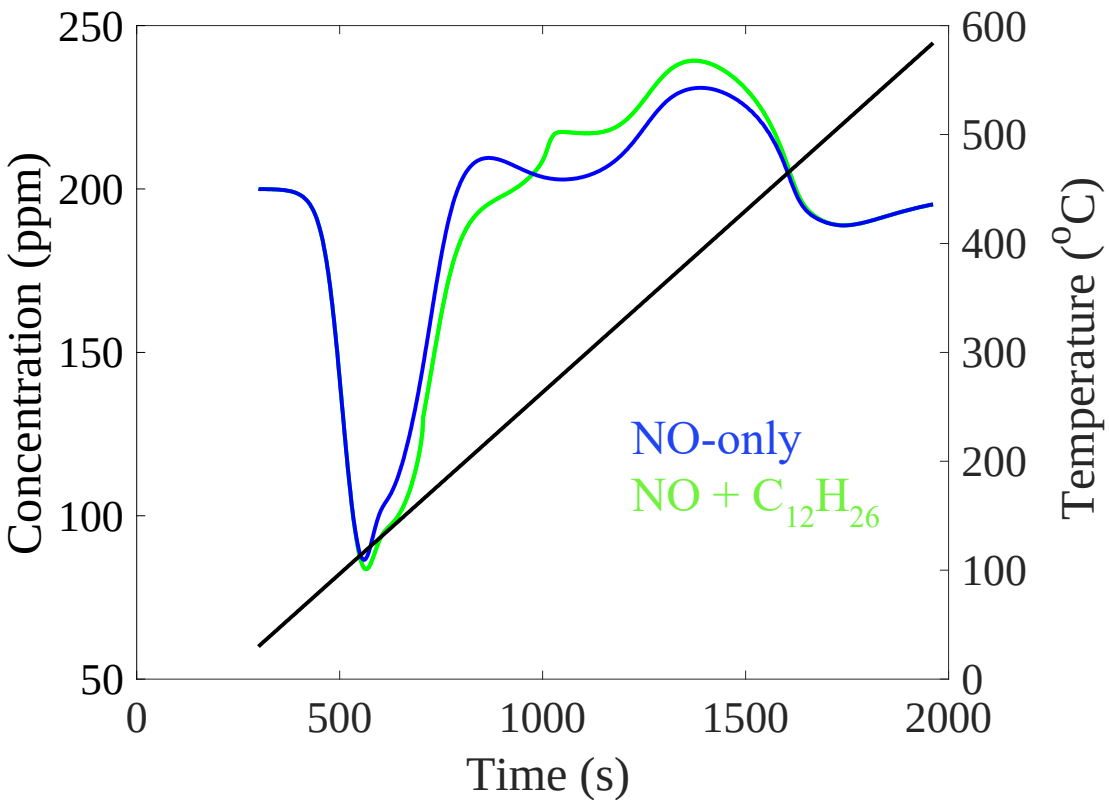

Figure 0.15 Model prediction of NO profile for a feed comprising of 200 ppm NO/ 12%O_2/ 6% H_2O/ balance Ar with and without 60 ppm of $C_{12}H_{26}$ and a continuous temperature ramping of 20ºC/min starting from 30ºC to 600ºC.

4.3 Conclusions

In this study we conducted various experiments to understand the effects of $C_{12}H_{26}$ on NO uptake and release over the classic PNA material, Pd(1%)/SSZ-13. Experiments results of co-feeding NO and $C_{12}H_{26}$ show that the presence of $C_{12}H_{26}$ does not impact NO uptake but increases NO release to above ~220℃. This is beneficial for PNA as NO_x after-treatment technologies such as SCR are ineffective at temperatures below ~200℃. After conducting several experiments to investigate the reason for delayed NO release, it was found that $C_{12}H_{26}$ oxidizes to CO which can co-adsorb with NO. The complex formed by co-adsorbing NO and CO are strongly bound to Pd sites which delays NO release to high temperatures.

Trapping of $C_{12}H_{26}$ on Pd/SSZ-13 was also examined and experiments were conducted to estimate the kinetic parameters. We used a two-phase transient monolith model containing $C_{12}H_{26}$ uptake, release, and oxidation kinetics for a variety of feeds. The model was used to predict NO + $C_{12}H_{26}$ uptake and temperature programmed desorption (TPD) data. The tuned model can be applied to identify improved catalyst formulations and operating strategies. For example, we simulated NO uptake for the NO + $C_{12}H_{26}$ feed with a continuous temperature ramping of 20℃/min starting from 30℃ to 600℃. The model predicts a higher NO uptake for the NO + $C_{12}H_{26}$ feed and that the presence of 60 ppm of $C_{12}H_{26}$ is equivalent to ~16% Pd in terms of NO trapping up to 200℃.

Chapter 5

Effects of low Pd loading, O_2 and CO on NO uptake

5.1 NO uptake for low Pd loading PNA catalyst

The reaction mechanism developed for NO uptake on PNA in this work requires 2 Pd(II) sites to be present in adjacent positions. For low Pd loading, 2 Pd(II) sites may not be present next to each other. Experiment was conducted with Pd(0.36%)/SSZ-13 catalyst containing 0.36 wt.% of Pd to study NO uptake on low Pd loading catalyst. Pre-treatment was done in 5% O_2/ 2% H_2O/ balance Ar at 550℃ for 30 min. The catalyst was then cooled to the experimental temperature under same feed and uptake was started. The uptake and TPD profiles for uptake conducted at 95℃ are shown in Figure 5. 1. Feed comprising of 390 ppm NO/ 5 ppm NO_2/ 2% O_2/ 2% H_2O/ balance Ar was fed to the reactor. Similar to our previous results, once the NO containing feed is switched to the reactor side, NO is adsorbed with simultaneous release of NO_2 indicating Pd site reduction. The uptake was conducted at 95℃ followed by TPD up to 550℃ in 18 min. With start of TPD, H_2O is desorbed leaving more sites for NO to be adsorbed on. Second NO adsorption regime occurs with simultaneous release of NO_2 and finally with further increase in temperature adsorbed NO is released. At temperatures above 400℃, NO is oxidized to NO_2.

The reaction mechanism for low Pd loading is shown in Table 5.1. For low Pd loading we are proposing the $Z^{-}Pd^{2+}Z^{-}$ sites as active NO uptake sites at the start of the uptake. The starting point is $Z^{-}Pd^{2+}Z^{-}$ sites adsorbed with 4 molecules of H_2O. According to DFT results, once NO is fed to the reactor it replaces an H_2O molecule and get adsorbed shown by reaction R5.1. A second NO molecule can then be adsorbed replacing another

H_2O molecule and forming $Z^-H^+Pd^+(HONO)(NO)Z^-$-H_2O shown by R5.2. This reaction reduces Pd from +2 oxidation state to +1.

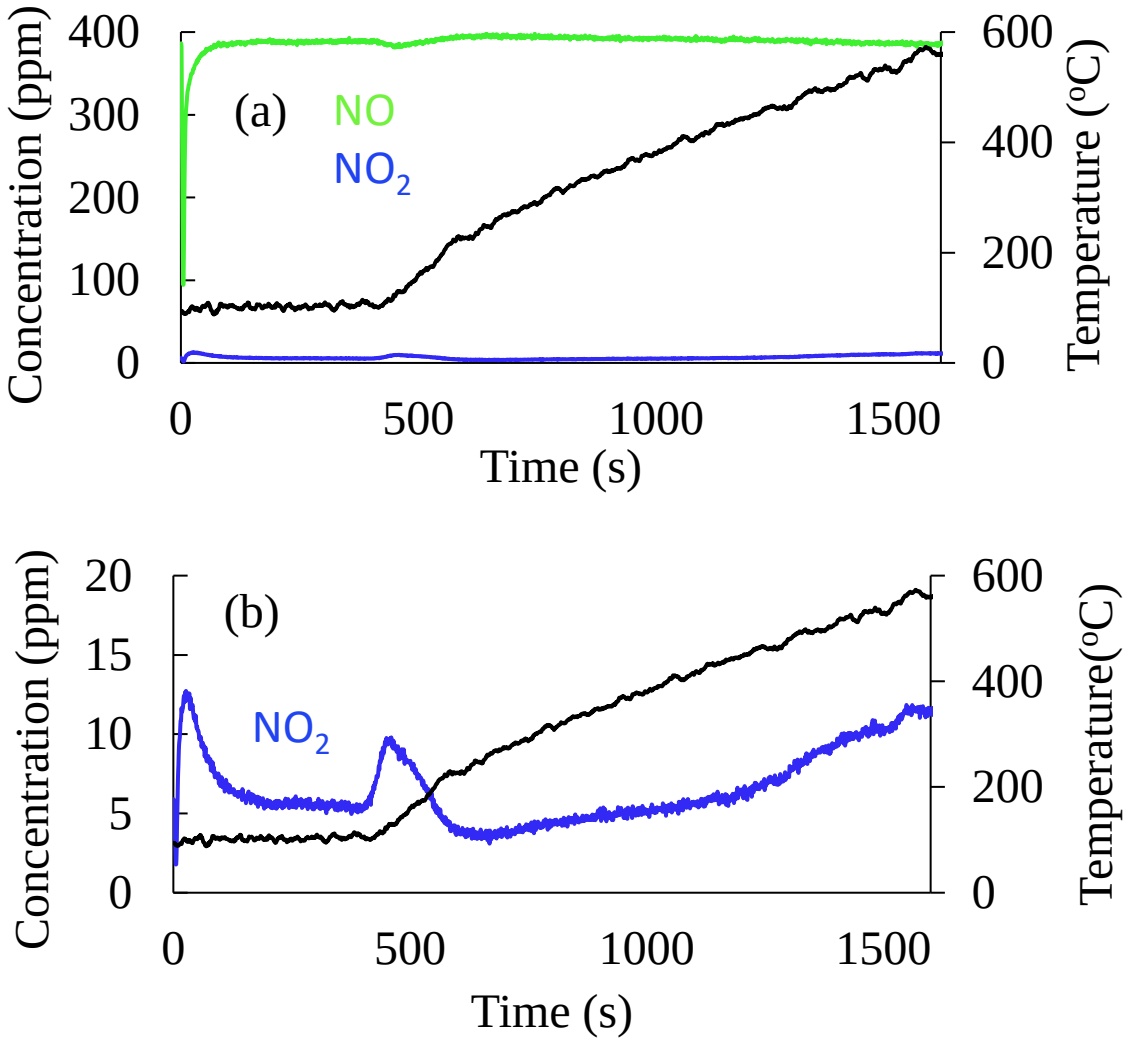

Figure 5. 1 Experimental results of NO_x uptake at 95°C and TPD on Pd(0.36%)/SSZ-13 for a feed comprising of 390 ppm NO/ 5 ppm NO_2 / 2% O_2 / 2% H_2O / balance Ar.

HONO can then be desorbed (R5.3) and form NO, NO_2 and H_2O (R5.4). Like discussed earlier according to DFT calculations Pd is strongly bound to Pd with +1 oxidation state. At high temperatures (> 350°C), NO is desorbed from Pd^+ sites shown by

reaction R5.5. Reactions R5.6 to R5.8 shows the re-oxidation of Pd^{1+} to Pd^{2+} in the presence of O_2 and NO. At high temperature O_2 oxidizes Pd^{1+} to Pd^{2+} forming $Z^-Pd^{2+}(OOH)Z^-(H_2O)_3$ (R5.6), which in the presence of 2 moles of NO forms $Z^-Pd^{2+}(HONO)(ONO)Z^-(H_2O)_2$ shown by reaction R5.7. Finally, HONO and NO_2 is desorbed from $Z^-Pd^{2+}Z^-$ site (R5.8).

Table 5.1 Reaction mechanism for simple NO feed for low Pd loading

Reaction no.	Reaction step
R5.1	$NO + Z^-Pd^{2+}Z^- - (H_2O)_4 \leftrightarrow Z^-H^+Pd^{2+}(OH^-)(NO)Z^- - (H_2O)_2 + H_2O$
R5.2	$NO + Z^-H^+Pd^{2+}(OH^-)(NO)Z^- - (H_2O)_2 \leftrightarrow Z^-H^+Pd^+(HONO)(NO)Z^- - H_2O + H_2O$
R5.3	$Z^-H^+Pd^+(HONO)(NO)Z^- - H_2O + 2H_2O \leftrightarrow HONO + Z^-H^+Pd^+Z^- - (NO)(H_2O)_3$
R5.4	$2HONO \leftrightarrow NO + NO_2 + H_2O$
R5.5	$Z^-H^+Pd^+Z^- - (NO)(H_2O)_3 \leftrightarrow NO + Z^-H^+Pd^+Z^- - (H_2O)_3$
R5.6	$Z^-H^+Pd^+Z^- - (H_2O)_3 + O_2 \leftrightarrow Z^-Pd^{2+}(OOH)Z^- - (H_2O)_3$
R5.7	$Z^-Pd^{2+}(OOH)Z^- - (H_2O)_3 + 2NO \leftrightarrow Z^-Pd^{2+}(HONO)(ONO)Z^- - (H_2O)_2 + H_2O$
R5.8	$Z^-Pd^{2+}(HONO)(ONO)Z^- - (H_2O)_2 \leftrightarrow HONO + NO_2 + Z^-Pd^{2+}Z^- - (H_2O)_2$

5.2 Effects of Oxygen

To understand the impact of O_2 on NO uptake and release, experiments were conducted with and without O_2 in the feed during pre-treatment, uptake and TPD. Before each subsequent experiment, the catalyst was pre-treated in 2% H_2O/ balance Ar/ with or without 5% O_2 at 500℃ for 30 minutes to remove any residual species, followed by cooling

to slightly above ambient. At the start of a typical uptake and desorption experiment, the monolith sample was heated to the desired uptake temperature while flowing of 2% H_2O/ balance Ar/ with or without 2% O_2. Experiments were carried out at a flow rate of 2500 sccm, corresponding to a gas hourly space velocity (GHSV) of 75.9k h^{-1}. Uptake was conducted for desired duration followed by temperature programmed desorption (TPD) up to a temperature of 500℃ from the uptake temperature in about ~18 min.

As discussed earlier our proposed mechanism shows that only water reacts with NO to form NO_2 at low temperature which leads to reduction of Pd. To validate this hypothesis, we carried out NO_x uptake on Pd(1%)/SSZ-13 at 95℃ with and without O_2 in the feed. The uptake and TPD profiles of which are shown in Figure 5.2 and 5.3 respectively. When a feed comprising of 386 ppm NO/ 5 ppm NO_2/ 2% H_2O/ (w and w/o) 2% O_2/ Ar flows through the reactor, there is uptake of NO and a simultaneous release of NO_2. Uptake was followed by TPD. With the start of TPD as temperature increases, H_2O starts desorbing from the sites leaving more sites for the NO to be adsorbed on and so, a second NO adsorption regime is observed with simultaneous release of NO_2. With further increase in temperature adsorbed NO is desorbed. Finally, at temperatures above 400˚C, NO is oxidised to NO_2 in the presence of O_2 in the feed. The NO_2 desorption peak at low temperature is present even without oxygen in the feed. This justifies that only H_2O reacts with NO to form NO_2. The desorption profile is also similar to the one which is observed even in the presence of O_2, implying Pd active site transformation is happening because of the presence of H_2O in the feed. Interestingly there is also no high-temperature NO_2 formation in the absence of O_2, suggesting the high-temperature oxidation is a result of NO oxidation by O_2 only. Combination of reactions R5.4, R5.6 and R5.7 shows the re-oxidation

of Pd(I) sites to Pd(II) in the presence of NO and O_2 forming NO_2. Removing O_2 from the pre-treatment state also didn't affect the result and NO oxidation is still observed at low temperature in presence of H_2O (Figure 5.4).

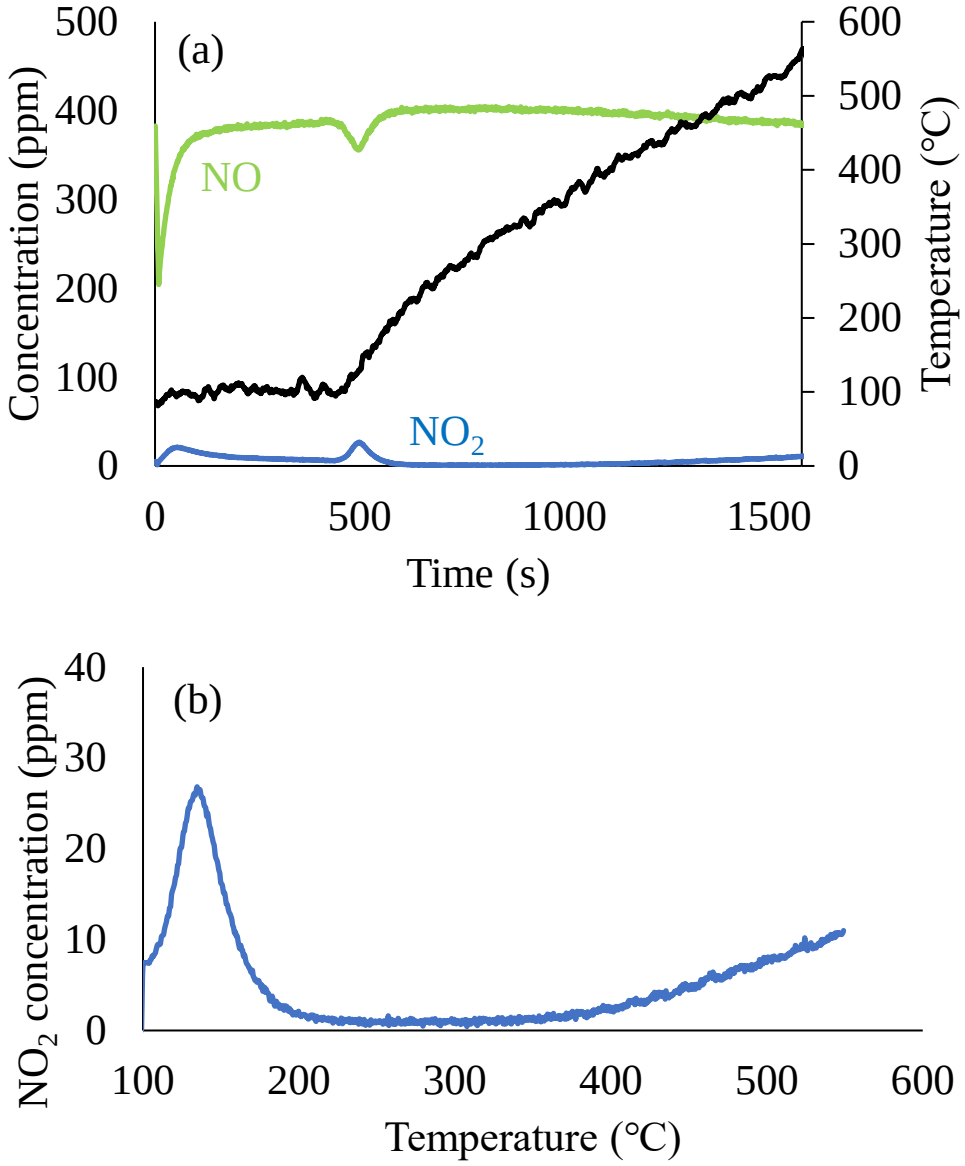

Figure 5. 2 (a) Experimental profiles for uptake at 95°C and TPD for a feed comprising of 386 ppm NO/ 5 ppm NO_2/ 2% O_2/ 2% H_2O/ balance Ar during uptake and TPD on catalyst pre-treated with 5% O_2/ 2% H_2O/ balance Ar; (b) Enlarged view of NO_2 TPD profile.

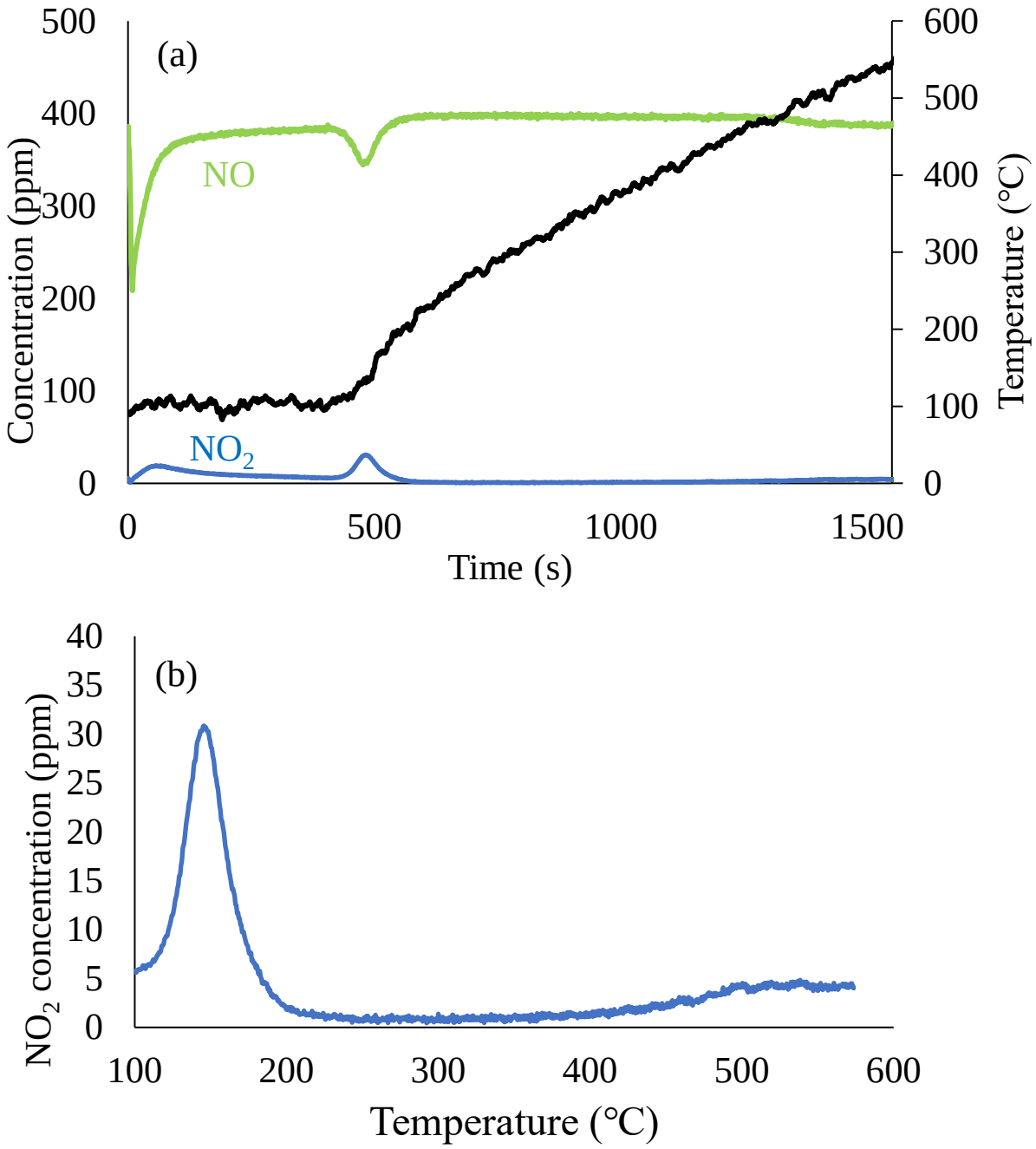

Figure 5.3 (a) Experimental profiles for uptake at 95°C and TPD for a feed comprising of 386 ppm NO/ 5 ppm NO_2/ 2% H_2O/ balance Ar during uptake and TPD on Pd(1%)/SSZ-13 pre-treated with 5% O_2/ 2% H_2O/ balance Ar; (b) Enlarged view of NO_2 TPD profile.

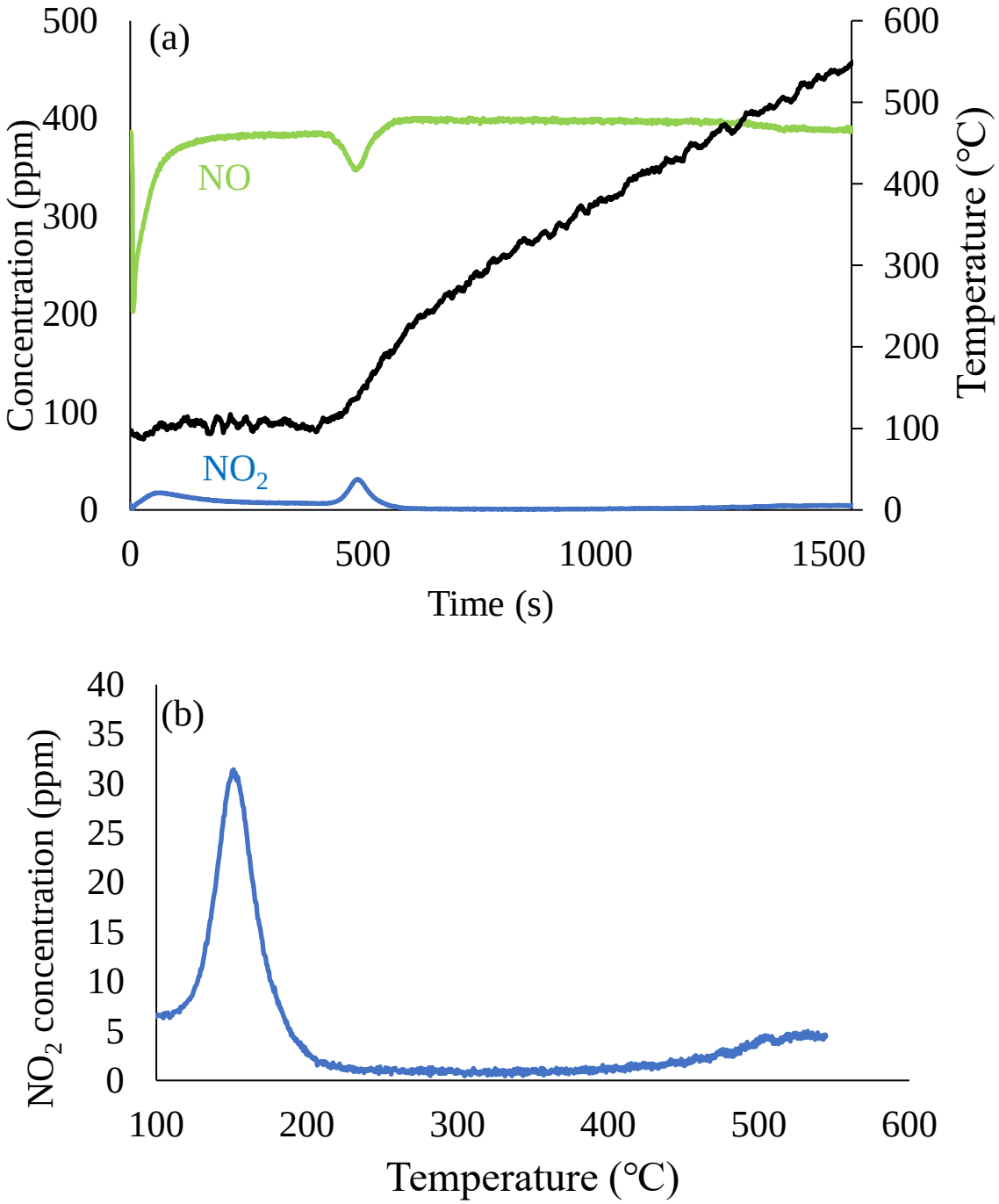

Figure 5.4 (a) Experimental profiles for uptake at 95°C and TPD for a feed comprising of 386 ppm NO/ 5 ppm NO_2/ 2% H_2O/ balance Ar during uptake and TPD on Pd(1%)/SSZ-13 pre-treated with 2% H_2O/ balance Ar; (b) Enlarged view of NO_2 TPD profile.

5.3 Alternate mechanism for CO uptake

Alternate mechanism was developed for CO uptake on Pd/SSZ-13 with and without O_2 in the presence of H_2O in the feed. This mechanism also describes a possible pathway for deactivation of catalyst in the presence of CO in the feed. Reaction R5.9 in table 5.2 shows the uptake of CO on Pd^{2+} sites adsorbed with 4 molecules of H_2O, replacing one H_2O molecule. Reaction R5.10 shows the formation of PdOH sites by moving one H^+ to Z^-. Finally, reaction R5.11 shows the formation of $HOCO^-$ i.e., $Z^-H^+Pd^{2+}(HOCO^-)Z^- - (H_2O)_2$. If O_2 is present in the feed, then the successive reaction steps are shown in table 5.3. Oxygen can be adsorbed on $Z^-H^+Pd^{2+}(HOCO^-)Z^- - (H_2O)_2$ sites forming $Z^-H^+Pd^{2+}(OCO)(OOH^-)Z^- - (H_2O)_2$ shown by reactions R5.12 and R5.13. In the presence on one mole of H_2O, $Z^-H^+Pd^{2+}(OOH^-)Z^- - (H_2O)_3$ is formed and one mole of CO_2 is released shown by reaction R5.14. NO can then be adsorbed on the sites if present by replacing a H_2O molecule as shown by reaction R5.15.

Table 5.2 Alternate reaction mechanism for CO uptake on Pd(1%)/SSZ-13

Reaction no.	Reaction step
R5.9	$CO + Z^-Pd^{2+}Z^- - (H_2O)_4 \leftrightarrow Z^-Pd^{2+}Z^- - (CO)(H_2O)_3 + H_2O$
R5.10	$Z^-Pd^{2+}Z^- - (CO)(H_2O)_3 \leftrightarrow Z^-H^+Pd^{2+}(OH^-)(CO)Z^- - (H_2O)_2$
R5.11	$Z^-H^+Pd^{2+}(OH^-)(CO)Z^- - (H_2O)_2 \leftrightarrow Z^-H^+Pd^{2+}(HOCO^-)Z^- - (H_2O)_2$

Table 5.3 Alternate reaction mechanism for CO uptake on Pd(1%)/SSZ-13 in the presence of O_2

Reaction no.	Reaction step
R5.12	$Z^-H^+Pd^{2+}(HOCO^-)Z^- - (H_2O)_2 + O_2 \leftrightarrow Z^-H^+Pd^{2+}(HOCO^-)(O_2)Z^- - (H_2O)_2$
R5.13	$Z^-H^+Pd^{2+}(HOCO^-)(O_2)Z^- - (H_2O)_2 \leftrightarrow Z^-H^+Pd^{2+}(OCO)(OOH^-)Z^- - (H_2O)_2$
R5.14	$Z^-H^+Pd^{2+}(OCO)(OOH^-)Z^- - (H_2O)_2 + H_2O \leftrightarrow Z^-H^+Pd^{2+}(OOH^-)Z^- - (H_2O)_3 + CO_2$
R5.15	$Z^-H^+Pd^{2+}(OOH^-)Z^- - (H_2O)_3 + NO \leftrightarrow Z^-H^+Pd^{2+}(OOH^-)(NO)Z^- - (H_2O)_2 + H_2O$

If O_2 is not present in the feed, then the successive reactions after R5.11 are shown in the table 5.4. Another molecule of H_2O can be adsorbed on $Z^-H^+Pd^{2+}(HOCO^-)Z^- - (H_2O)_2$ reducing Pd (II) to Pd(I) by forming $Z^-H^+Pd^+(OCO^-)H^+Z^- - (H_2O)_3$shown by reactions R5.16 and R5.17. The Pd (I) sites then reduces to Pd(0) sites forming $Z^-H^+Pd^0H^+Z^- - (H_2O)_2$, H_2O and CO_2, shown by reaction R5.18. Up to 2 moles of CO can then be adsorbed on Pd(0) sites shown by reactions R5.19 and R5.20. Once Pd(0) is formed it can also sinter which deactivates the catalyst.

Table 5.4 Alternate reaction mechanism for CO uptake on Pd(1%)/SSZ-13 in the absence of O_2

Reaction no.	Reaction step
R5.16	$Z^-H^+Pd^{2+}(HOCO^-)Z^- - (H_2O)_2 + H_2O \leftrightarrow Z^-H^+Pd^{2+}(HOCO^-)Z^- - (H_2O)_3$
R5.17	$Z^-H^+Pd^{2+}(HOCO^-)Z^- - (H_2O)_3 \leftrightarrow Z^-H^+Pd^+(OCO^-)H^+Z^- - (H_2O)_3$
R5.18	$Z^-H^+Pd^+(OCO^-)H^+Z^- - (H_2O)_3 \leftrightarrow Z^-H^+Pd^0H^+Z^- - (H_2O)_2 + H_2O + CO_2$
R5.19	$Z^-H^+Pd^0H^+Z^- - (H_2O)_2 + CO \leftrightarrow Z^-H^+Pd^0H^+Z^- - (H_2O)(CO) + H_2O$
R5.20	$Z^-H^+Pd^0H^+Z^- - (H_2O)(CO) + CO \leftrightarrow Z^-H^+Pd^0H^+Z^- - (CO)_2 + H_2O$

Chapter 6

Conclusions

The main contribution of this work is the development of first predictive microkinetic model of PNA: H/ZSM-5, Pd/HZSM-5 and Pd/SSZ-13. The model can provide a quantitative tool for evaluating NO uptake and release. The model was developed for NO-only feed with and without H_2O in the feed for HZSM-5 and Pd/HZSM5. The model was extended for NO uptake on Pd/SSZ-13 for NO-only feed, NO + CO feed, NO + C_2H_4 feed as well as for NO + $C_{12}H_{26}$ feed. The model was finally used to compare two classic PNA materials: Pd/SSZ-13 and Pd/ZSM-5.

In this study we developed a one-dimensional, two-phase transient monolith model to predict and validate NO uptake and TPD data for H/ZSM-5, Pd/HZSM-5 and Pd/SSZ-13. One of the schemes involve NO adsorption on multiple types of Pd cations and BAS, the latter of which are ineffective when water is in the feed. It involves $Z^-[PdOH]^+$, $Z^-Pd^{2+}Z^-$, and Z^-Pd^+ with the key feature being the reduction of a pair of $Z^-[PdOH]^+$ sites to two Z^-Pd^+ sites, which strongly bind NO. The site reduction generates NO_2, CO_2 or C_2H_4O depending on the feed constituents. For NO-only feed, this occurs at temperature ~150℃ for Pd/HZSM-5 and at ~120℃ for Pd/SSZ-13 which according to DFT estimates is endothermic reaction. But in the presence of reductants such as CO and C_2H_4, this reduction is enhanced at lower temperatures followed by release of CO_2 or C_2H_4O respectively. This is because the reduction of $Z^-[PdOH]^+$ sites is exothermic reaction in presence of reductants CO and C_2H_4 according to DFT estimates. The model we developed satisfactorily capture these results.

When a co-feed containing $C_{12}H_{26}$ and NO is supplied to an unsaturated (with $C_{12}H_{26}$) sample, $C_{12}H_{26}$ does not impact NO uptake but delays NO release from 175℃ to over 220℃. The release delay is beneficial for PNA performance as the SCR, used for reducing NO_x to N_2 is active above 200℃. Oxidation of $C_{12}H_{26}$ generates CO. Carbon monoxide binds strongly to Pd sites with NO and can delay NO release. Pre-saturation of $C_{12}H_{26}$ followed by the same NO and $C_{12}H_{26}$ co-feed results in a decrease in the NO uptake compared to the NO + $C_{12}H_{26}$ co-feed. We conjecture that $C_{12}H_{26}$ pre-adsorbed on the exterior surface of the sample blocks NO access to the pores, decreasing the number of available sites for NO uptake. Through a systematic combination of judicious experiments, model tuning, and validation, we provided evidence for the underlying NO uptake and release mechanisms in the presence of $C_{12}H_{26}$.

The above-mentioned reaction scheme involves 2 Pd sites to be present in adjacent position which may not be possible for low Pd loading. Alternate mechanism for low Pd loading catalyst was also proposed with the help of DFT calculations which considers $Z^-Pd^{2+}Z^-$ as the starting active sites. Distinguishing between the two mechanism is out of scope of the study. Also, prolonged use of CO in the feed causes catalyst deactivation. Deactivation mechanism was also proposed in the study. Carbon monoxide in the feed can reduce Pd(II) sites to Pd(0) sites which then can sinter and thus deactivates the catalyst.

The model was validated at different uptake temperatures, feed flow rates, and ramp rate, enabling its use to identify improved catalyst formulations and operating strategies. Hence, we were then able to utilize the model to predict the NO uptake under a more realistic condition for NO-only feed, NO+CO feed, NO+C_2H_4 feed and NO + $C_{12}H_{26}$ feed with a continuous temperature ramping of 20℃/min starting from 30℃ to 600℃. The

model showed the maximum NO uptake for NO+CO feed. We also used the model to compare Pd/SSZ-13 and Pd/ZSM-5 catalysts under different experimental conditions and the model correctly predicts more NO uptake on Pd/SSZ-13 under similar experimental conditions. The model developed here provides an important tool for evaluating PNA catalysts: Pd/HZSM-5 and Pd/SSZ-13 under wide range of experimental conditions which is vital to identify operating conditions to meet application-relevant performance metrics including NO_x trapping efficiency and NO_x release temperature.

Chapter 7

Future Work

Malamis et al. [45] conducted NO + $C_{12}H_{26}$ uptake, release and conversion experiments on sequential (Pt+Pd/BEA → Pd/SSZ-13; Pd/SSZ-13 → Pt+Pd/ BEA) and dual layer (Pt+Pd/BEA top, Pd/SSZ-13 bottom) configurations in an attempt to improve the trapping and conversion performance. They reported a decrease in overall monolith volume achieved by dual layer configuration without significantly compromising performance. Pd/SSZ-13 adsorbs NO at low temperatures [9-11] whereas Pt+Pd/BEA adsorbs HCs [30-35] as well as oxidizes NO to NO_2. Formation of NO_2 is beneficial as it results is fast SCR reaction [6-8].

We have developed the model for NO uptake on Pd/SSZ-13 with and without $C_{12}H_{26}$. The next work would be to develop model for HC uptake and NO oxidation on Pt+Pd/BEA catalyst. The Pd/SSZ-13 model and Pt+Pd/BEA model can then be combined to develop the overall model for sequential (Pt+Pd/BEA → Pd/SSZ-13; Pd/SSZ-13 → Pt+Pd/ BEA) and dual layer (Pt+Pd/BEA top, Pd/SSZ-13 bottom) configurations.

The combination of HCT and PNA poses a number of questions about materials selection, adsorption-reaction-transport coupling, device configuration, and operating strategy to achieve emission targets. A combined experimental and modelling study will help to understand the transient coupling and to converge on the best configurations for combined NO_x and HC trapping, release, and conversion.

References

[1] Melville, J. E., Brisley, R. J., Keane, O., Phillips, P. R., Mountstevens, E. H. US Patent US8105559B2, 2012.

[2] Cole, J. A., US Patent US5656244A, 1997.Russell, W.S. Epling, Diesel oxidation catalysts, Catal. Rev. 53 (4) (2011) 337–423.

[3] G. N. Pontikakis, G. S. Konstantas, and A. M. Stamatelos, ASME. *J. Eng. Gas Turbines Power*, 2004; 126(4): 906–923.

[4] G.C. Koltsakis, P.A. Konstantinidis, A.M. Stamatelos, *Applied Catalysis B: Environmental*, Volume 12, Issues 2–3, 1997, Pages 161-191, ISSN 0926-3373.

[5] S. Siemund, J. P. Leclerc, D. Schweich, M. Prigent, F. Castagna, *Chem. Eng. Sci.*, 51(15), pp. 3709–3720, 1996.

[6] I. Nova, E. Tronconi, Urea_SCR Technology for deNOx after Treatment of Diesel Exhausts, Springer, New York, 2014.

[7] J.W. Girard, G. Cavataio, C.K. Lambert, The Influence of Ammonia Slip catalyst on NH3, N2O and NO Emissions for Diesel Engines, SAE Technical Paper (2007) 2007-01-1572.

[8] E.V. Hunnekes, P.V.V.M. van der Heijden, J.A. Patchett, Ammonia Oxidation Catalysts for Mobile SCR Systems, SAE Technical Paper (2006) 2006-01-0640.

[9] F. McKenna, “NOx trap composition,” United States Patent US9005560 B2, 14 April 2015.

[10] H. Chen and S. Mulla, “Cold start catalyst and its use in exhaust systems,” United States Patent US20120308439 A1, 6 December 2012.

[11] R.R. Rajaram, F. M. McKenna, H.Y. Chen, D. Liu, U.S. Patent US20150157982 A1, (2014).

[12] J. Lee, J. R. Theis, E. A. Kyriakidoua, *Applied Catalysis B: Environmental*, 243, 397–414, 2019.

[13] Y. Gu, W.S. Epling, *Applied Catalysis A, General*, 570, 1–14, 2019.

[14] H.-Y. Chen, S. Mulla, U.S. Patent US20120308439 A1, (2011).

[15] C. Descorme, P. Gelin, M. Primet and C. Lecuyer, *Catalysis Letters*, vol.41, pp. 133-138, 1996.

[16] J. Lee, Y. Ryou, S. J. Cho, H. Lee, C. H.Kim, D. H. Kim, *Applied Catalysis B: Environmental*, 226, 71–82, 2018.

[17] Y. Murata, T. Morita, K. Wada, H. Ohno, *SAE Int. J. Fuels Lubr.* 8, pp.454–459, 2015.

[18] K. Okumura, J. Amano, N. Yasunobu and M. Niwa, *Journal of Physical Chemistry B*, vol.104, pp.1050-1057, 2000.

[19] B. Pommier and P. Gelin, *Phys. Chem. Chem. Phys*., 3, pp. 1138-1143, 2001.

[20] Y. Zheng, L. Kovarik. M. H. Engelhard, Y. Wang, F. Gao and J. Szanyi, *The Journal of Physical Chemistry*, 2017.

[21] A. Porta, T. Pellegrinelli, L.Castoldi, R. Matarrese, S. Morandi, S. Dzwigaj, L. Lietti, *Topics in Catalysis* 61:2021–2034, 2018.

[22] A. Vu, J. Luo, J. Li, W.S. Epling, *Catal. Lett.* 147, pp. 745–750, 2017.

[23] K. Chakarova, E. Ivanova, K. Hadjiivanov, D. Klissurski and H. Kno¨zinger, *Phys. Chem. Chem. Phys*., pp. 3702-3709, 2004.

[24] K. Khivantsev, F. Gao, L. Kovarik, Y. Wang, and J. Szanyi, *J. Phys. Chem. C*, 122, 10820−10827, 2018.

[25] Y. Ryou, J. Lee, H. Lee, C.H. Kim, D.H. Kim, *Catal. Today*, 320, 175-180, 2019.

[26] Y. Ryou, J. Lee, S.J. Cho, H. Lee, C.H. Kim, D.H. Kim, Appl. Catal. B 212 (2017) 140–149.

[27] S.T. Homeyer, W.M.H. Sachtler, *J. Catal.* 118 (1989) 266–274.

[28] B.J. Adelman, W.M.H. Sachtler, *Appl. Catal. B* 14 (1997) 1–11.

[29] Y. Ryou, J. Lee, Y. Kim, S. Hwang, H. Lee, C. H. Kim, Do H. Kim, *Applied Catalysis A*, General 569 (2019) 28–34

[30] M. Ambast, A. Gupta, B. M. M. Rahman, L. Grabow, M. P. Harold, *NO_x Adsorption with CO and C_2H_4 on Pd/SSZ-13: Experimental and Modeling*, Appl. Catal. B Environment, 2021, Vol 286, 119871, ISSN 0926-3373.

[31] R.R. Rajaram, F. M. McKenna, H.Y. Chen, D. Liu, U.S. Patent US20150157982 A1, (2014).

[32] H. Chang, Gasoline cold start concept (gCSC™) technology for low temperature emission control, SAE Int. J. Fuels Lubr. 7 (2) (2014) 480–488.

[33] H.-X. Li, Application of zeolites as hydrocarbon traps in automotive emission controls, Stud. Surf. Sci. Catal. 158 (2005) 1375–1382.

[34] Murakami, K., Development of a high-performance catalyzed hydrocarbon trap using Ag-zeolite, 2004, SAE Technical Paper.

[35] S. Elangovan, A comparative study of zeolites SSZ-33 and MCM-68 for hydrocarbon trap applications, Microporous Mesoporous Mater. 96 (1) (2006) 210–215.

[36] M.-F. Hsieh, Y. Zhou, H. Thirumalai, L. C. Grabow, J. D. Rimer, *Chem Cat Chem*, 2017, *9*, 1675.

[37] M. Ambast, K. Karinshak, B. M. Rahman L. Grabow, and M.P. Harold, "Passive NOx Adsorption on Pd/H-ZSM-5: Experiments and Modeling," *Appl. Catal. B. Environ*., 269, 118802, 2020.

[38] A. Gupta, S. B. Kang, M. P. Harold, *Catalysis Today*, 360, 411-425, 2021.

[39] R.M. Serra, Experimental and theoretical studies about the adsorption of toluene on ZSM5 and mordenite zeolites modified with Cs, Microporous Mesoporous Mater. 147 (1) (2012) 17–29.

[40] M. Navlani-García, CuH-ZSM-5 as hydrocarbon trap under cold start conditions, Environ. Sci. Technol. 47 (11) (2013) 5851–5857.

[41] B. Puertolas, Optimizing the performance of catalytic traps for hydrocarbon abatement during the cold-start of a gasoline engine, J. Hazard. Mater. 279 (2014) 527–536.

[42] M. Navlani-García, BETA zeolite thin films supported on honeycomb monoliths with tunable properties as hydrocarbon traps under cold-start conditions, ChemSusChem 6 (8) (2013) 1467–1477.

[43] M. Ogura, T. Okubo, S.P. Elangovan, Hydrocarbon reformer trap by use of transition metal oxide-incorporated beta zeolites, Catal. Lett. 118 (1–2) (2007) 72–78.

[44] P. Y. Peng, M. P. Harold, D. Luss, *Chemical Engineering Journal*, 355 (2019) 661–670.

[45] S. A. Malamis, M. P. Harold, *Catalysis Today*, 360, 388-400, 2021.

[46] H.-Y. Chen, J.E. Collier, D. Liu, L. Mantarosie, D. Dur.n-Mart.n, V. Nov.k, R.R. Rajaram, D. Thompsett, Low temperature NO storage of zeolite supported Pd for low temperature diesel engine emission control, Catal. Lett. 146 (2016) 1706–1711.

[47] T. Armaroli, T. Bécue and S. Gautier, *Oil & Gas Science and Technology – Rev. IFP*, Vol. 59, No. 2, 2004.

[48] B.Adelman, W. Sachtler, *Apll. Catal. B Environ*, 14, 1-11, 1997.

[49] T. E. Hoost, K. A. Laframboise and K. Otto, *Catalysis Letters*, vol.33, pp. 105-116, 1995.

[50] I. Perdana, D. Creaser, I. M. Bendiyasa, Rochmadi, B. W. Tyoso, *Chemical Engineering Science* 62, pp. 3882-3893, 2007.

[51] P. S. Metkar, M. P. Harold, V. Balakotaiah, *Chemical Engineering Science*, vol.87, pp.51-66, 2013.

[52] S. Y. Joshi, M. P. Harold, and V.Balakotaiah, *AIChE Journal* Vol. 55, No. 7, 2009.

[53] D. Mei, F. Gao, J. Szanyi and Y. Wang, *Applied Catalysis A, General* (2017).

[54] L. Olsson, H. Sjovall, R. J. Blint, *Applied Catalysis B: Environmental*, vol.87, pp. 200-210, 2009.

[55] Hanna Sjövall, Richard J. Blint, and Louise Olsson, *J. Phys. Chem.* C, Vol. 113, No. 4, 2009.

[56] H. Y. Chen, J. E. Collier, D. Liu, L. Mantarosie, D. D. Martín, V.Novák, R. R. Rajaram, D. Thompsett, *Catal Lett*, DOI 10.1007/s10562-016-1794-6, 2016.

[57] K. Mandal, Y. Gu, K. S. Westendorff, S. Li, J.A.Pihl, L.C. Grabow, W. S. Epling, and C. Paolucci, , under preparation.

[58] T.J. Wang, S. W. Baek, H. J. Kwon, Y. J. Kim, I. S. Nam, M. S. Cha, G. K. Yeo, *Ind. Eng. Chem*, Res 50, 2850-2864, 2011.

[59] I. Friberg, N. Sadokhina, L. Olsson, *Applied Catalysis B: Environmental*, 250, Pg. 117-131, 2019.

[60] R. V. Seddon and M. W. Travers, *Proc. R. Soc. Lond. A* 156, 234–269, 1997.

[61] C. T. Campbell, *Topics in Catalysis I*, (1994) 353-366.

[62] H. Ma and W. F. Schneider, *ACS Catal.*, 2019, 9, 2407−2414.

[63] Thirumalai, H.; Rimer, J. D.; Grabow, L. C. Quantification and Statistical Analysis of Errors Related to the Approximate Description of Active Site Models in Metal-Exchanged Zeolites. *ChemCatChem* **2019**, *11* (20), 5055–5067.

[64] Zhou, Y.; Thirumalai, H.; Smith, S. K.; Whitmire, K. H.; Liu, J.; Frenkel, A. I.; Grabow, L. C.; Rimer, J. D. Ethylene Dehydroaromatization over Ga-ZSM-5 Catalysts: Nature and Role of Gallium Speciation. *Angew. Chemie Int. Ed.* **2020**, anie.202007147.

[65] B. Azambre, A. Westermann, G. Finqueneisel, F. Can, J.D. Comparot, Adsorption and Desorption of a Model Hydrocarbon Mixture Over HY Zeolite Under Dry and Wet Conditions, *J. Phys. Chem. C*, 119, 1, 315–331,2015.

[66] C. S. Sampara, E. J. Bissettb, D. Assanis, Chemical Engineering Science 63 (2008) 5179 – 5192.

[67] C. S. Sampara, E. J. Bissett, and M. Chmielewski, Ind. Eng. Chem. Res., Vol. 47, No. 2, 2008.

[68] I. Song, S. Youn, H. Lee, D. H. Kim, *Korean J. Chem. Eng.* 33, 2547-2554, 2016.

[69] V. Pashkova, K. Mlekodaj, P. Klein, L. Brabec, R. Zouzelka, J. Rathousky, V. Tokarova, and J. Dedecek, Chem. Eur. J. 2019, 25, 12068 – 12073.

Appendix

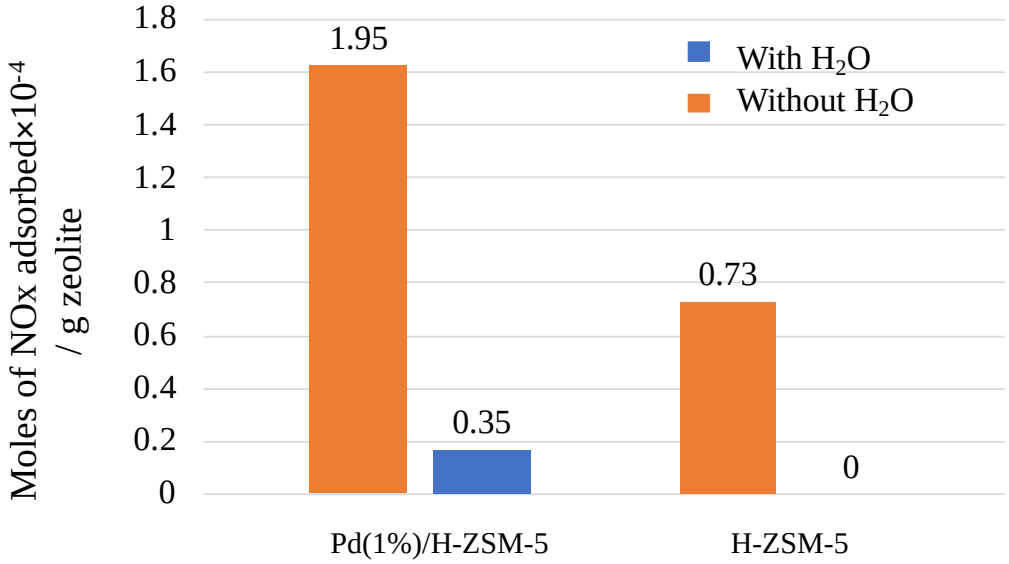

Figure A. 1 Comparison of moles of NO_x adsorbed per gram washcoat for Pd(1%)/H-ZSM-5 and H-ZSM-5 with and without H_2O in the feed (uptake at 80°C).

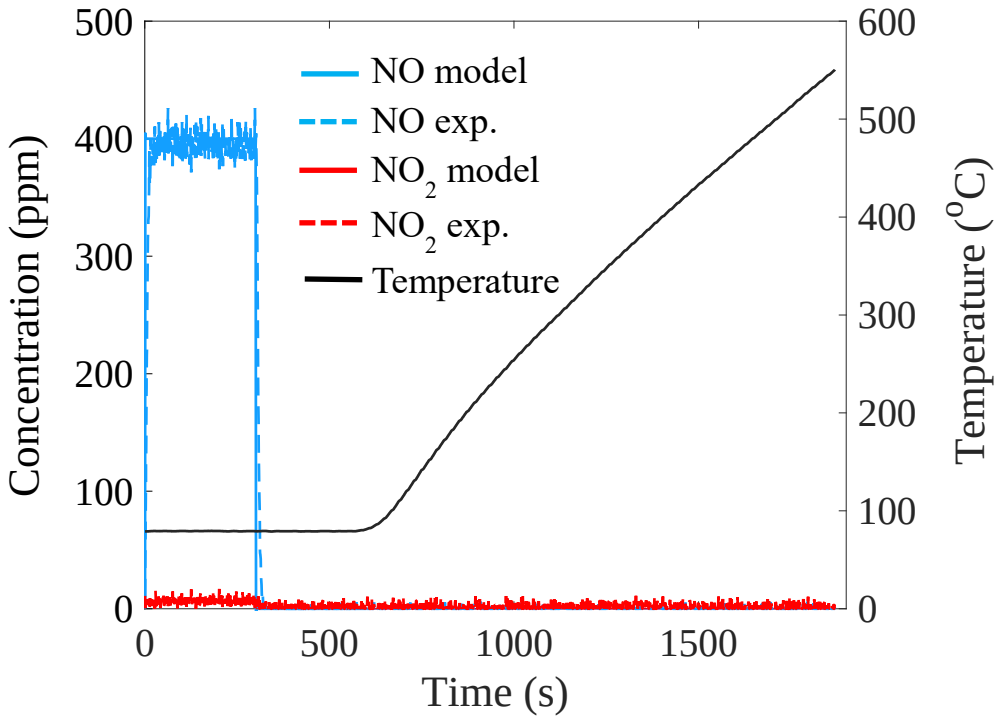

Figure A. 2 Experimental and modeling results of NO_x uptake at 80°C and TPD on H-ZSM-5 for wet-feed (7% H_2O) and feed flowrate of 1500sccm.

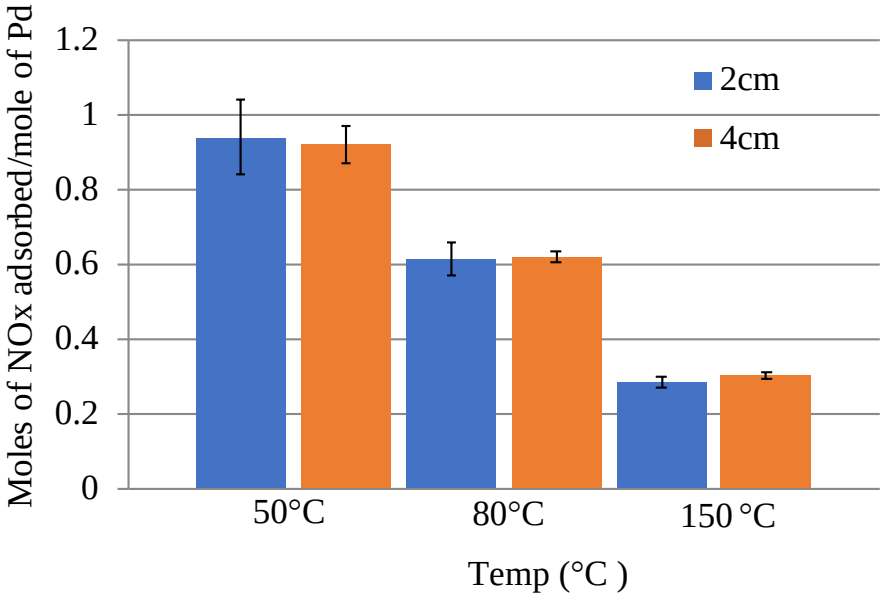

Figure A. 3 Comparison of moles of NO_x adsorbed per mole of Pd for dry feed at different uptake temperatures for monoliths of length 2cm and 4cm with same ratio of space velocity to mass of catalyst.

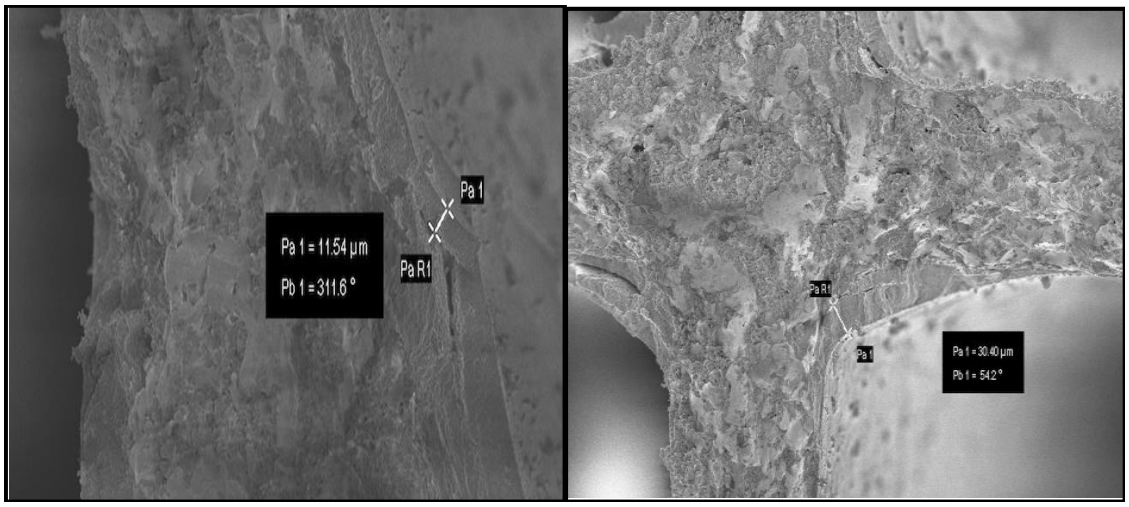

Figure A. 4 Washcoat SEM images of 1%Pd/H-ZSM-5.

Table A. 1 Diffusivity values in fluid phase (m^2/s)

$D_{f,NO}$	$1.13e\text{-}9T^{1.7148}$
D_{f,NO_2}	$0.91e\text{-}9T^{1.7148}$
D_{f,O_2}	$1.13e\text{-}9T^{1.7019}$
D_{f,H_2O}	$1.62e\text{-}9T^{1.7033}$
$D_{f,CO}$	$1.13e\text{-}9T^{1.7019}$
D_{f,CO_2}	$0.825e\text{-}9T^{1.7148}$
D_{f,CH_4}	$1.13e\text{-}9T^{1.7019}$
D_{f,C_2H_4}	$3.39e\text{-}7T^{0.75}$
D_{f,C_2H_4O}	$3.18e\text{-}7T^{0.75}$
$D_{f,C_{12}H_{26}}$	$3.39e\text{-}7T^{0.75}$

Estimation of Brønsted Acid Sites (BAS) on H-ZSM-5 Catalyst

Total weight of washcoat = 0.3811 g

Mass of H-ZSM-5 in washcoat = 82% of 0.3811 g

= 0.3125 g

Formula of H-ZSM-5 = $H_nAl_nSi_{96-n}O_{192}.{}_{16}H_2O$

For Si/Al_2 = 30, n = 6 gives:

= $H_6Al_6Si_{90}O_{192}.{}_{16}H_2O$

Molecular weight of H-ZSM-5 = 8935.08

Moles of H-ZSM-5 = 3.498e-5 moles

Moles of BAS (C_s) = 6 x 3.498e-5 moles

=2.099e-4moles

= 1406 moles/m^3

Estimation of Site Concentrations for Pd(1%)/H-ZSM-5 Catalyst

An estimation scheme that uses knowledge of the Pd loading, Pd dispersion, Silica to Alumina ratio (Si/Al_2), and selected features of the TPD profile is described. Each of the dispersed Pd cation types can adsorb NO at low temperature based on experimental and DFT calculations [30,53]. With the acid site loading known and the TPD peaks identified, the loadings of $Z^-[Pd(II)OH]^+, Z^-Pd^{2+}Z^-$ and Z^-Pd^+ can be calculated. The total moles of Pd in the washcoat can be calculated since a known amount of Pd is added to the H-ZSM-5 by wetness impregnation method.

Total mass of washcoat	= 0.3673 g
Mass of Pd(1%)/H-ZSM-5 in washcoat	= 82% of 0.3673 g = 0.3011 g
Mass of Pd in washcoat	= wt% of Pd * total mass of catalyst in washcoat
	= 1% of 0.3011 g
	= 3.01186e-3 g = 2.8306e-5 moles

The chemisorption measurement of the Pd(1%)-H-ZSM-5 sample gives a Pd fractional dispersion (d_{Pd}) of 0.41. It is assumed that this represents the fraction of Pd in the form of isolated cations, with the remainder associated with PdO_x. (The loading of PdO can likely be gotten by TPR at sub-zero Centigrade; alternatively, the loading of dispersed metal cations may be estimated by H_2 TPR.) The total moles of dispersed Pd is the product of d_{Pd} and the total Pd loading; i.e.,

n_{Pd} = d_{Pd} × total moles of Pd (= 2.83e-5 moles) = 1.16e-5 moles Pd cations.

Where n_{Pd} is the total moles of Pd cations; i.e.

$$n_{Pd} = n_{Z^-Pd^{2+}Z^-} + n_{Z^-[Pd(II)OH]^+} + n_{Z^-Pd^+}. \quad \text{(A. 1)}$$

As per the earlier discussion, the incremental NO_x uptake areas in the first and second NO TPD peaks in Figure 2.12 (ΔA_1 and ΔA_2) enable an estimate of the loading of $Z^-[Pd(II)OH]^+$, $Z^-Pd^{2+}Z^-$ and Z^-Pd^+, respectively; i. e.,

$$\Delta A_1 \propto n_{Z^-Pd^{2+}Z^-} + n_{Z^-[Pd(II)OH]^+} \quad \text{(A. 2)}$$

and $\Delta A_2 \propto n_{Z^-Pd^+}$. (A. 3)

Assuming equal proportionality constants in eqns. (2) and (3), and dividing the two equations gives the area ratio

$$\frac{\Delta A_1}{\Delta A_2} = \frac{n_{Z^-Pd^{2+}Z^-} + n_{Z^-[Pd(II)OH]^+}}{n_{Z^-Pd^+}} = \frac{n_{Pd} - n_{Z^-Pd^+}}{n_{Z^-Pd^+}}. \quad \text{(A. 4)}$$

With n_{Pd} known and the ratio of $\frac{\Delta A_1}{\Delta A_2}$ estimated from Figure 2.12, the value of $n_{Z^-Pd^+}$ can be calculated from Eq. (4). Next, we know that Z^-Pd^+ is formed from $Z^-[Pd(II)OH]^+$ by the reduction reaction R2.18 (Table 2.6). Further, $n_{Z^-Pd^+} = y \times n_{Z^-[Pd(II)OH]^+}$, where, y is a function of temperature and $0 < y < 1$. It is assumed that all of the $Z^-[Pd(II)OH]^+$ is reduced to Z^-Pd^+ at temperatures above 150°C and therefore y is taken to be unity. At any time, sum of $Z^-[Pd(II)OH]^+$ and Z^-Pd^+ will be constant and the value will be equal to the value of $n_{Z^-Pd^+}$ calculated from equation 4, since we are assuming the value of y to be 1. Knowing $n_{Z^-Pd^+}$ and $n_{Z^-[Pd(II)OH]^+}$, $n_{Z^-Pd^{2+}Z^-}$ can be calculated from eq. (1). It is noted that two Al sites are required to stabilize Pd species which decrease the Brønsted acid sites that are available for NO_x uptake on Pd/H-ZSM-5 [16,68]. For this reason, two times the total moles of Pd are subtracted from the total Brønsted acid site loading to estimate the loading of Brønsted acid sites that are available for NO_x uptake. Finally, it is assumed that after the pretreatment with O_2 at the beginning of experiments, Pd cations are in the +2 oxidation state [15].

This analysis scheme gives estimates of the loading of available Brønsted acid sites (C_{s1}), $Z^{-}Pd^{2+}Z^{-}$ (C_{s2}) and $Z^{-}[Pd(II)OH]^{+}$(C_{s3}) on Pd(1%)-H-ZSM-5 as 1016, 49 and 29 mole-sites/m^3 of washcoat, respectively (Table 2.3). With the loadings estimated, unknown kinetic parameters can then be estimated from a fit of selected uptake and desorption data.

Model Tuning and Validation Procedure

The model contains both non-kinetic and kinetic parameters. Values of non-kinetic parameters are provided in Table 2.3 and are primarily concerned with the monolith geometry and operating conditions. Where possible, values of kinetic parameters available from the literature or from DFT calculations were used. The remaining unknown kinetic parameters were estimated by fitting selected data using a parameter estimation algorithm (MATLAB *fmincon*) interfaced with the monolith reactor model containing the microkinetic scheme. This involved defining an objective function comprising the sum of squared differences between the experimental and predicted NO_x (NO, NO_2) concentrations spanning the uptake and release.

The procedure of estimating the kinetic parameters was an iterative one for H-ZSM-5 and Pd/H-ZSM-5. The procedure is highlighted here for NO_x uptake on H-ZSM-5. First, the reactor model was used to predict uptake and release as dictated by *fmincon* for a selected set of experimental data. For H-ZSM-5 we used the NO_x uptake at 80°C and 1500 sccm feed flowrate without H_2O in the feed. With adsorption parameters being more important for uptake and desorption being more important during TPD, the data fitting was divided into two steps.

First, the objective function was defined as the sum of squared differences between the experimental and predicted NO concentrations only during uptake. The *fmincon* tool enabled the estimation of the unknown kinetic parameters related to the adsorption steps, while fixing the unknown desorption parameters set to zero. This led to a satisfactory fit of the uptake.

The next step was to keep the adsorption parameters fixed while estimating the desorption parameters in the fit of the TPD data. In this step the objective function was the sum of squared differences between the experimental and predicted NO concentrations only during the TPD. At this point the set of estimated parameter values were used as an initial guess and *fmincon* was run again with the objective function being the sum of squared differences between the experimental and predicted NO concentrations during the entire experiment; spanning uptake and TPD. This third step resulted in a set of estimated kinetic parameters which were able to predict the NO_x uptake at 80°C and TPD data on H-ZSM-5.

In the next step the same kinetic parameters were used as initial guess value to predict the experimental data (uptake +TPD) at a different uptake temperature of 150°C. The estimated kinetic parameter values for both the set of experiments (80°C and 150°C) were compared. The kinetic parameter values of some of the reactions were same for both the set of experiments while some of the parameters were different. We require a set of kinetic parameters which can predict both of these experimental results. So, the next step was then to run *fmincon* for a different objective function which was a combination of both uptake at 80°C and its TPD data set along with uptake at 150°C and its TPD data set. For this run, the values of kinetic parameters which were estimated to be same by *fmincon* for both the

experiments were kept constant and only the parameters which were estimated to have different values for 80°C and 150°C experiments were taken as variables. The set of kinetic parameters thus estimated were able to predict both the experimental profiles (80°C and 150°C). This step by step process was adopted rather than using only one objective function (a large set of data which is a combination of both the set of experiments (80°C and 150°C)) to decrease the computational time. The next step was then to select another set of experimental data for example NO_x uptake and TPD data set for uptake at 80°C and at a different feed flowrate of 2500 sccm. Similar procedure was repeated to estimate a set of kinetic parameters which were able to predict all three experimental profiles (80°C/1500sccm, 150°C/1500sccm and 80°C/2500sccm)). This process was repeated till a single set of kinetic parameters were able to predict all of the different experimental profiles.

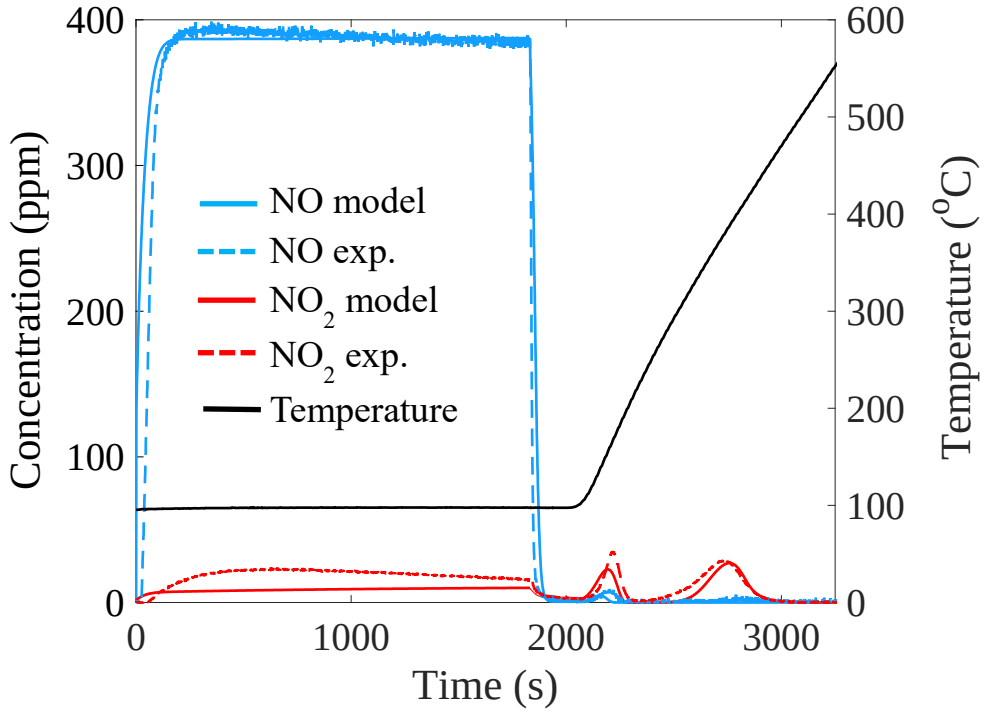

Figure A. 5 Experimental and modeling results of NO_x uptake at 95°C and TPD on H-ZSM-5 for dry feed and feed flowrate of 1500sccm.

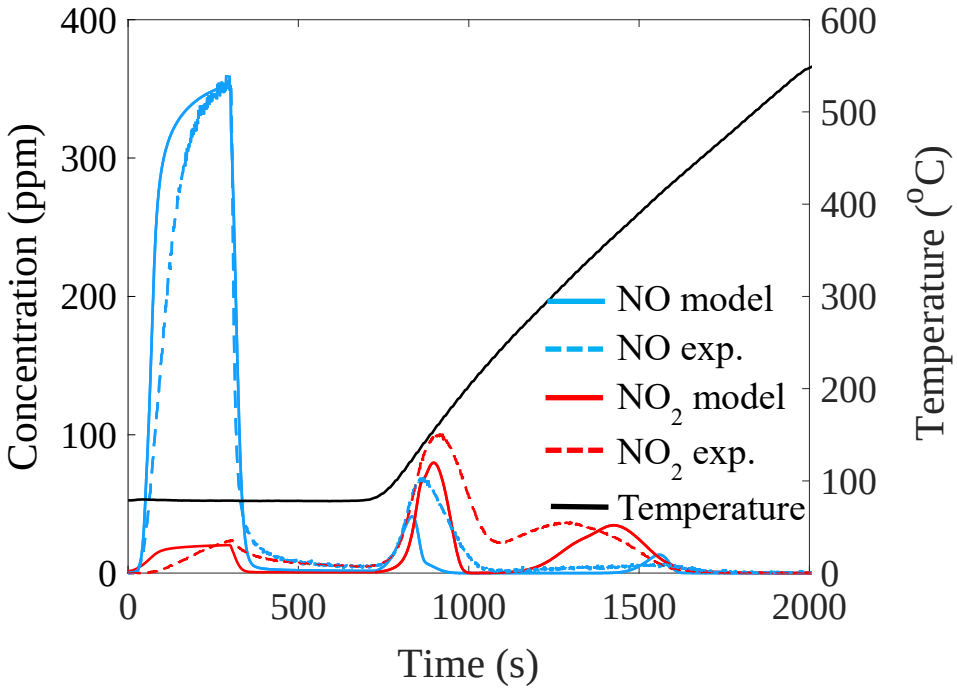

Figure A. 6 Experimental and modeling results of NO_x uptake at 80°C and TPD on 1%Pd-H-ZSM-5 for dry feed and feed flowrate of 1500sccm (Scheme I).

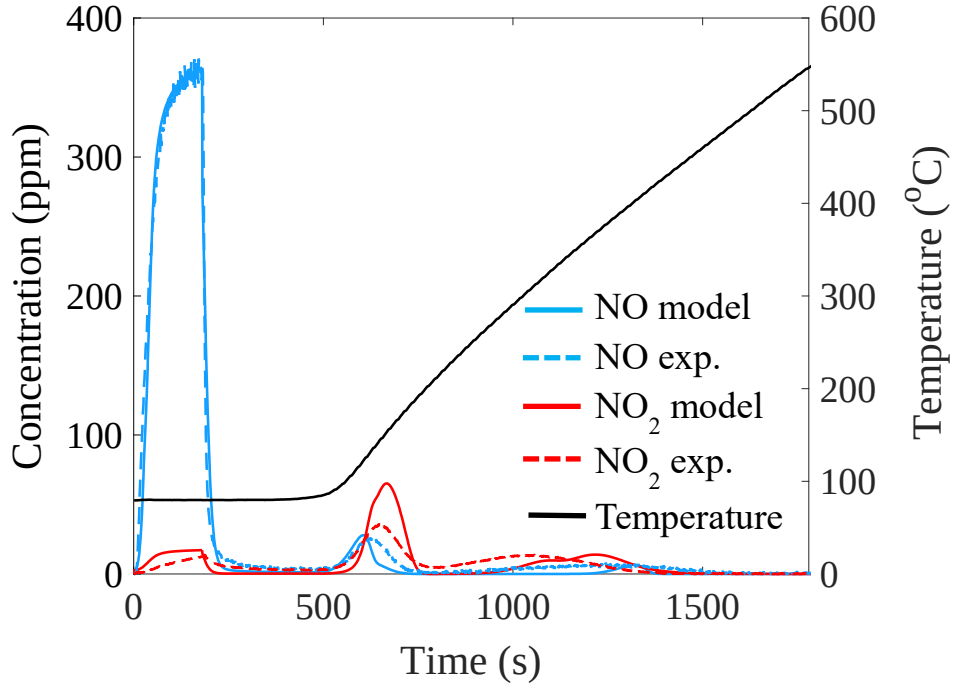

Figure A. 7 Experimental and modeling results of NO_x uptake at 80°C and TPD on 1%Pd-H-ZSM-5 for dry feed and feed flowrate of 2500sccm (Scheme I).

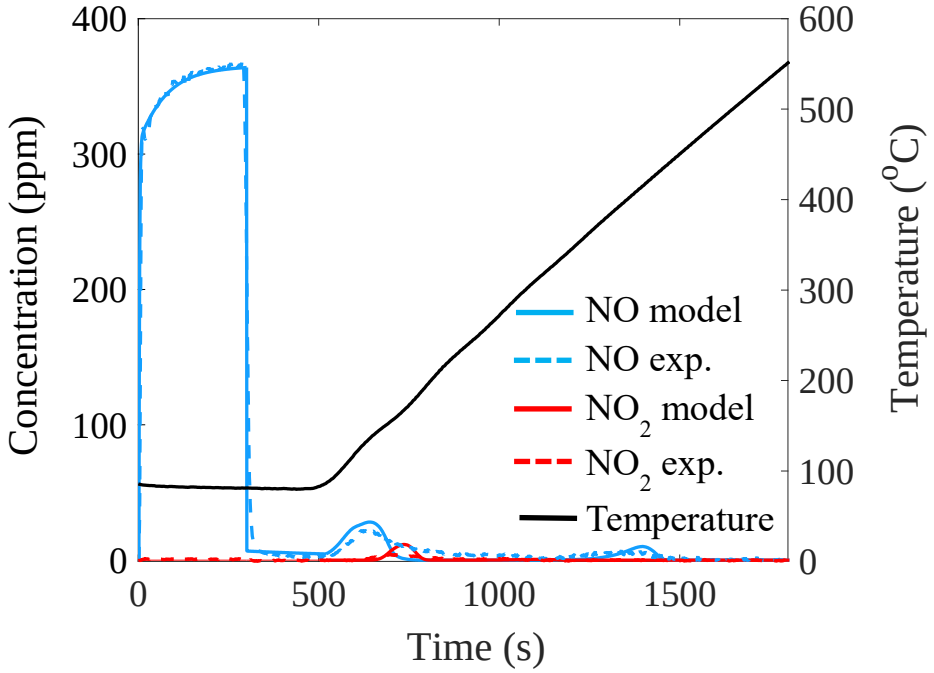

Figure A. 8 Experimental and modeling results of NO_x uptake at 80°C and TPD on Pd(1%)/H-ZSM-5 for wet-feed (7% H_2O) and feed containing 350 ppm of NO during uptake (Scheme I).

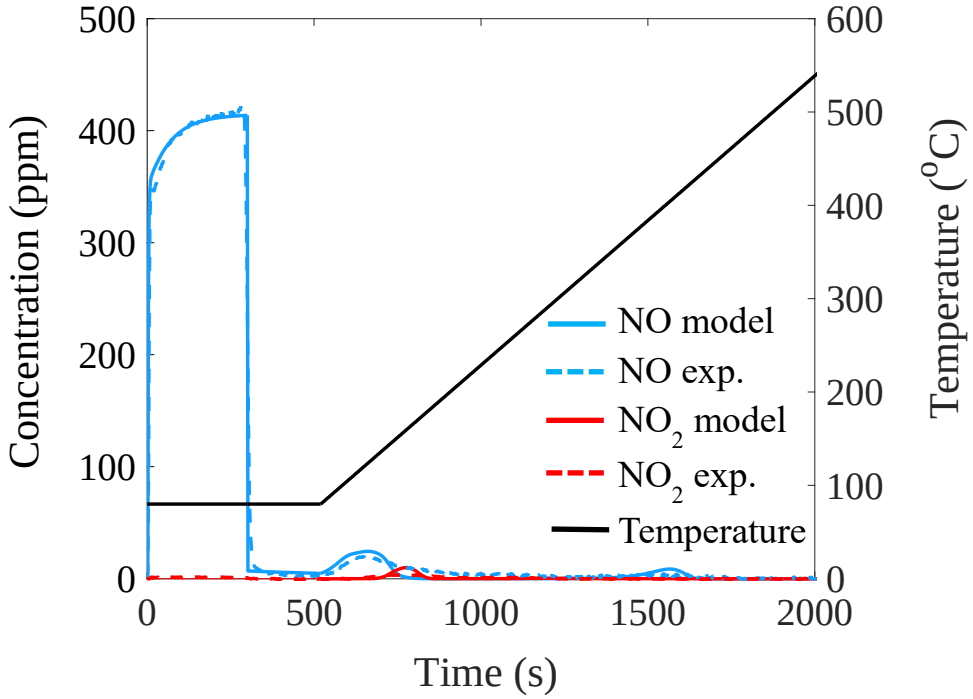

Figure A. 9 Experimental and modeling results of NO_x uptake at 80°C and TPD on Pd(1%)/H-ZSM-5 for wet-feed (7% H_2O) and ramp rate of 18°C/min (Scheme I).

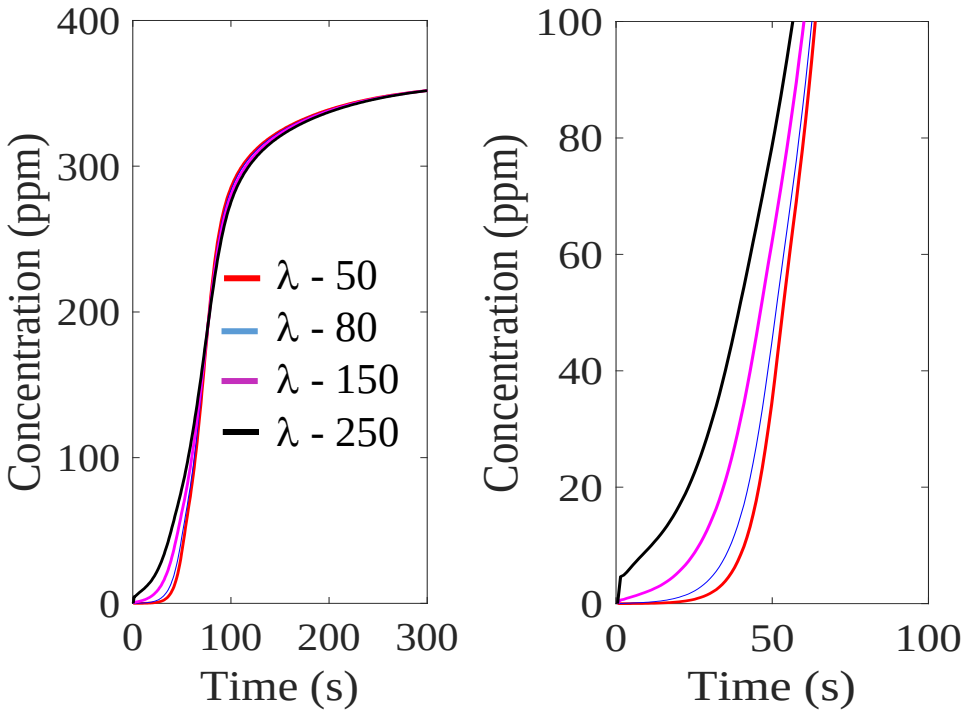

Figure A. 10 Effect of diffusivity on NO_x uptake on Pd(1%)/H-ZSM-5 at uptake temperature of 80°C and in absence of H_2O in the feed.

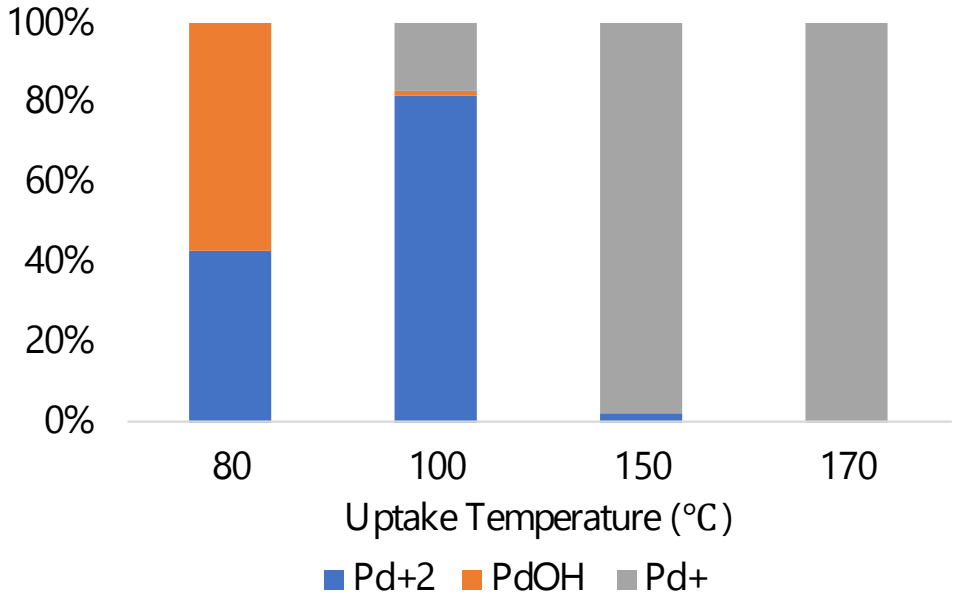

Figure A. 11 Normalized amounts of adsorbed NO on different Pd sites at different uptake temperatures.

Calculation of Site Concentrations and Parameter Estimation for Pd/H-ZSM-5-Scheme II

Water is always present in the exhaust system. So, modeling results in the presence of water in the feed is of practical importance. Therefore, modeling using scheme II is only done for feed with water present in it. For scheme II, we are proposing that NO uptake on $Z^{-}Pd^{2+}Z^{-}$is associated with low temperature NO TPD peak whereas NO adsorbed as nitrates on Pd are associated with high temperature NO TPD peak. Similar approach as scheme I is taken to calculate the concentrations of different types of Pd sites. As per the earlier discussion, the incremental NO_x uptake areas in the first and second NO TPD peaks in Figure 2.12 ($\Delta A_1$and ΔA_2) enable an estimate of the loading of $Z^{-}Pd^{2+}Z^{-}$, PdO_2 and PdO respectively. Since two moles of NO are adsorbed on PdO to form nitrates which are associated with second peak:

$$\Delta A_1 \propto n_{Z^{-}Pd^{2+}Z^{-}} \quad \text{(A. 5)}$$

and $$0.5\Delta A_2 \propto n_{PdO}. \quad \text{(A. 6)}$$

Further, $n_{PdO_2} = y \times n_{PdO}$, where, y is a function of temperature and $0 < y < 1$. It is assumed that all of the PdO_2 is reduced to PdO at temperatures above 150°C and therefore y is taken to be unity. At any time, sum of PdO_2 and PdO will be constant and the value will be equal to the value of n_{PdO} calculated from equation 6, since we are assuming the value of y to be 1. This analysis scheme gives estimates of the loading of $Z^{-}Pd^{2+}Z^{-}$ (C_{s2}) and PdO_2 (C_{s5}) on Pd(1%)-H-ZSM-5 as 63 and 15 mole-sites/m^3 of washcoat, respectively.

The values of activation energies for NO_x, H_2O and combined NO_x and H_2O uptake on $Z^{-}Pd^{2+}Z^{-}$ is kept similar to scheme I (R2.28-R2.31, R2.35-R2.37). Explanations for

these are already presented. As before, activation energies for adsorption of H_2O and NO_x species on Pd sites (forward reactions of reactions R2.33, R2.38-R2.39) are taken to be 0 kJ/mole. The values of all the pre-exponential factors and remaining 7 activation energies were estimated by using MATLAB tool *fmincon* and NO uptake (@ 80ºC) and TPD data as a reference data set with water in the feed (Figure 2.18). The data comprised 1946 data points to estimate unknown parameters. The validations for the model are shown in Figure A. 12 and Figure A. 13.

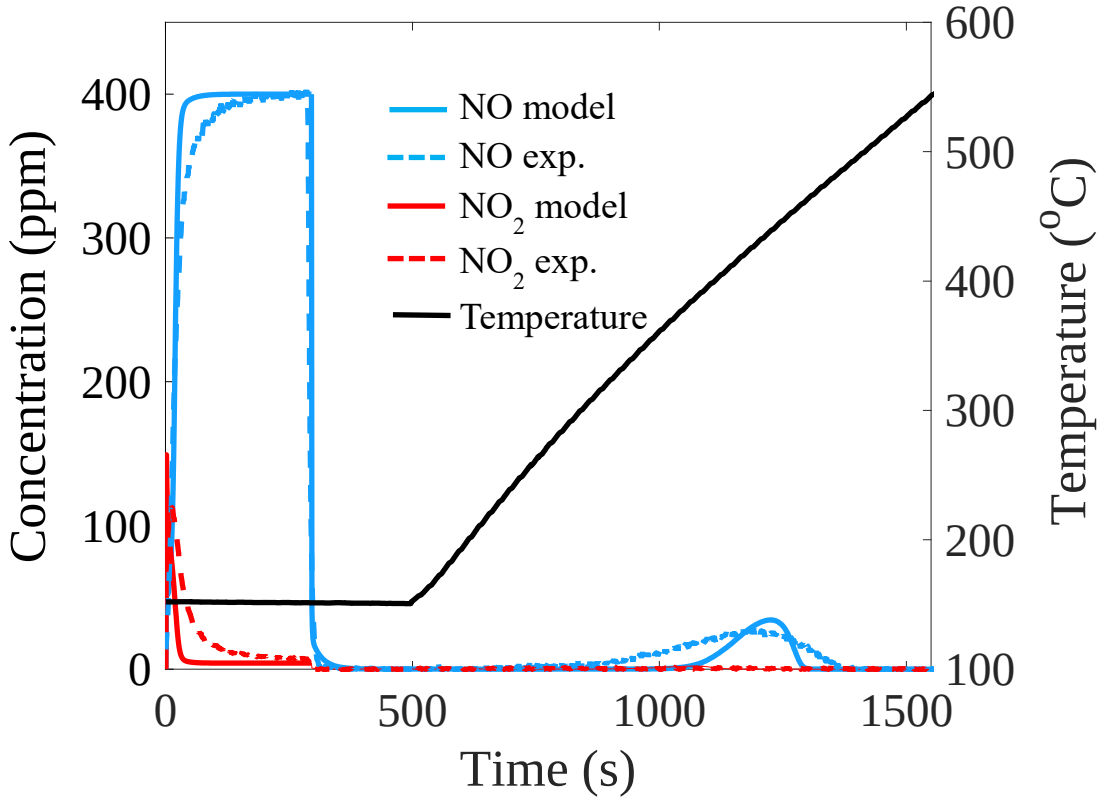

Figure A. 12 Experimental and modeling results of NO_x uptake at 150°C and TPD on Pd(1%)/H-ZSM-5 for wet-feed (7% H_2O) and feed flowrate of 1500sccm (Scheme II).

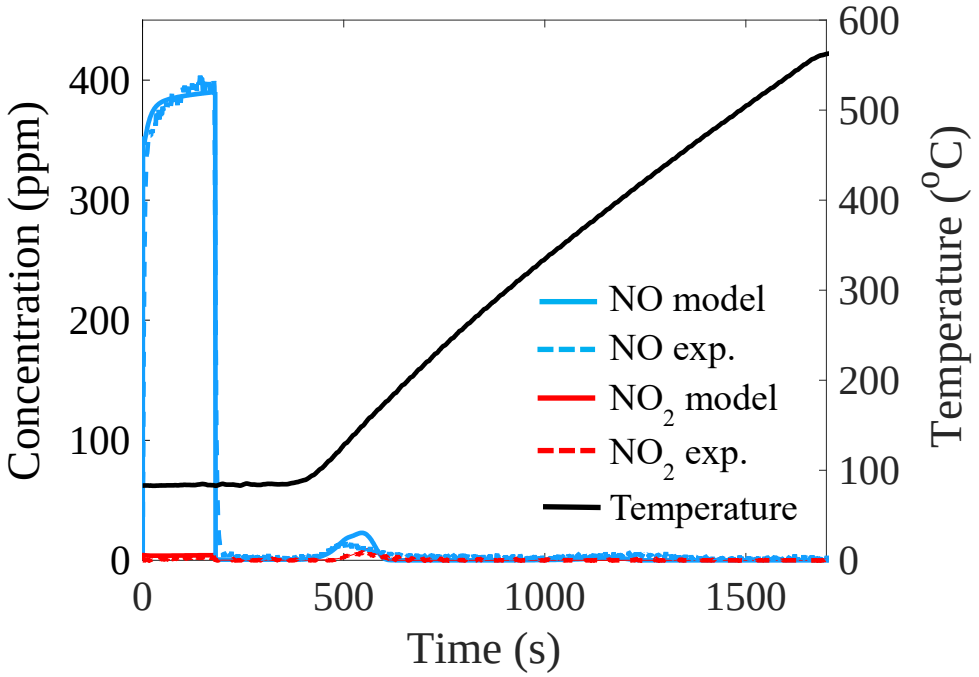

Figure A. 13 Experimental and modeling results of NO_x uptake at 80°C and TPD on Pd(1%)/H-ZSM-5 for wet-feed (7% H_2O) and feed flowrate of 2500sccm (Scheme II).

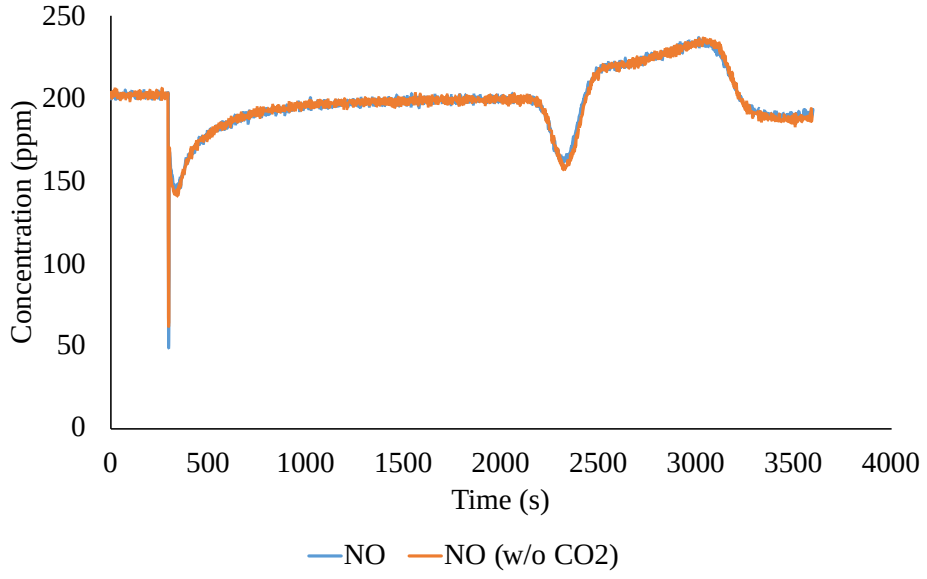

Figure A. 14 NO uptake and TPD profiles for feed comprising of 200 ppm NO/ 12% O_2/ 6% H_2O/ balance N_2 with and without 6% CO_2.

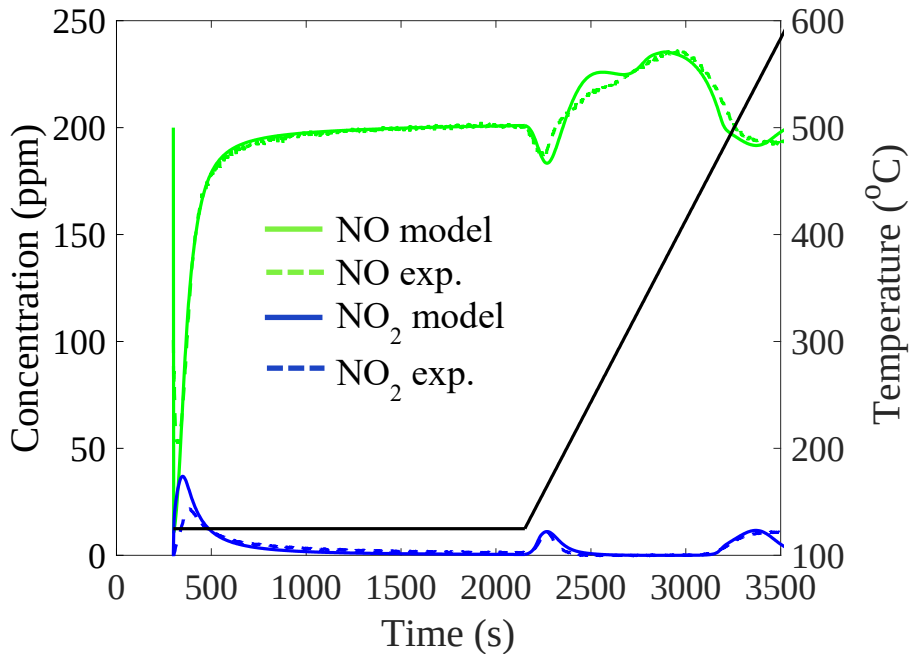

Figure A. 15 Experimental and model results of NO_x uptake at 125°C and TPD on Pd(1%)/SSZ-13 for a feed comprising of 200 ppm NO/ 12% O_2/6% CO_2/ 6% H_2O / balance N_2 and feed flowrate of 30 khr^{-1}.

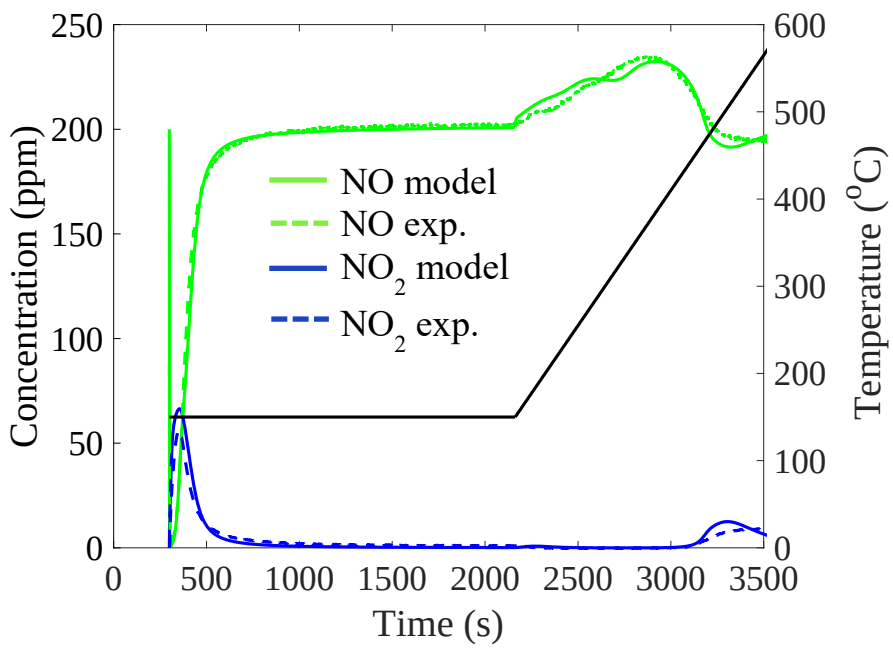

Figure A. 16 Experimental and model results of NO_x uptake at 150°C and TPD on Pd(1%)/SSZ-13 for a feed comprising of 200 ppm NO/ 12% O_2/ 6% CO_2/ 6% H_2O / balance N_2 and feed flowrate of 30 khr^{-1}.

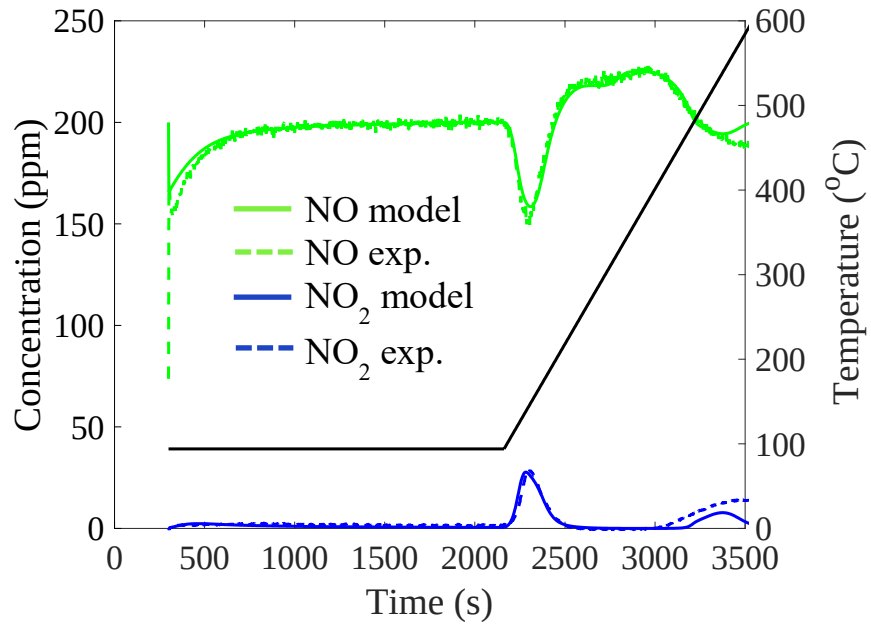

Figure A. 17 Experimental and model results of NO_x uptake at 94°C and TPD on Pd(1%)/SSZ-13 for a feed comprising of 200 ppm NO/ 12% O_2/ 6% CO_2/ 6% H_2O / balance N_2 and feed flowrate of 45 khr^{-1}.

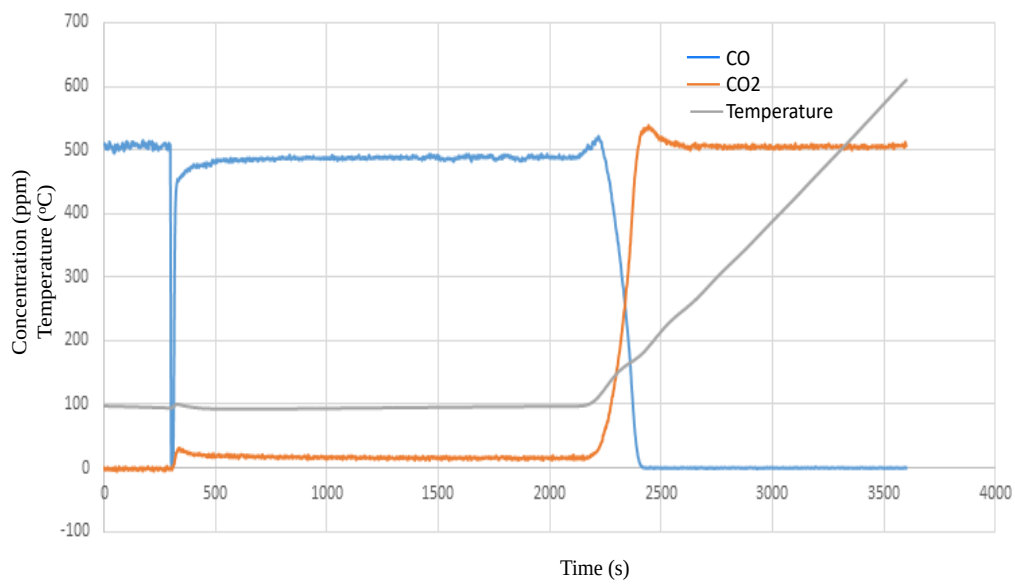

Figure A. 18 Experimental results for uptake at 100°C and TPD on Pd(1%)/SSZ-13 for a feed comprising of 500 ppm CO/ 12% O_2/ balance N_2 and feed flowrate of 45 khr^{-1}.

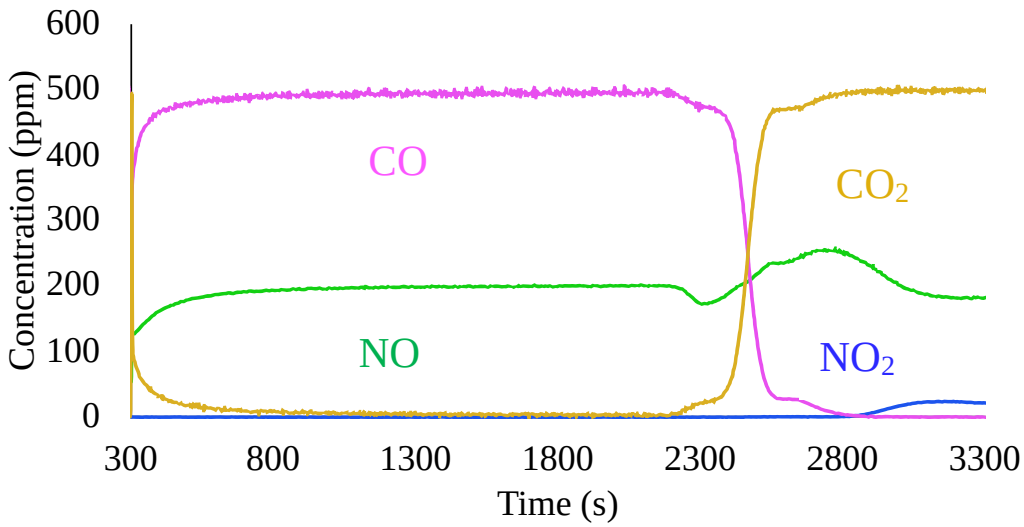

Figure A. 19 Experimental results for uptake at 70°C and TPD on Pd(1%)/SSZ-13 for a feed comprising of 200 ppm NO/500 ppm CO/ 12% O_2/ 6% H_2O / balance N_2 and feed flowrate of 45 khr^{-1}.

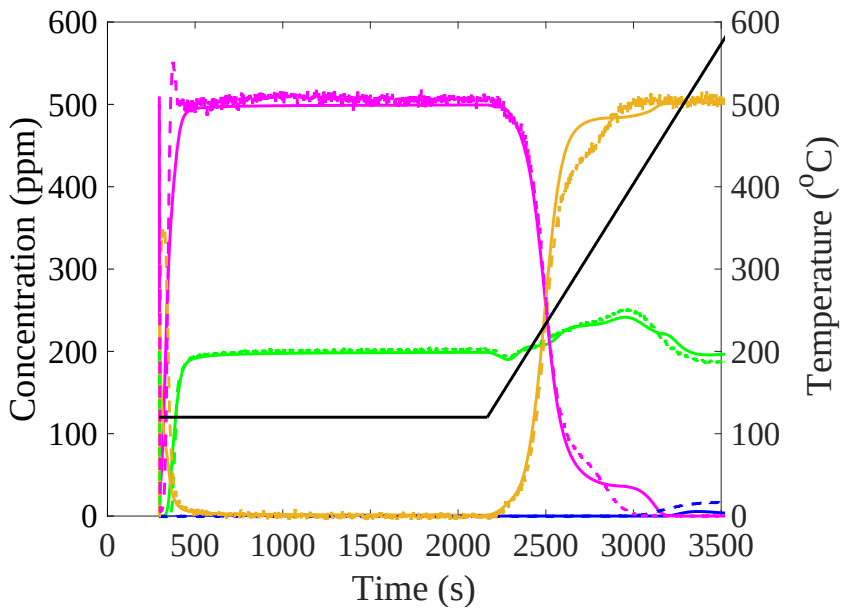

Figure A. 20 Experimental and model results for uptake at 120°C and TPD on Pd(1%)/SSZ-13 for a feed comprising of 200 ppm NO/500 ppm CO/ 12% O_2/ 6% H_2O / balance N_2 and feed flowrate of 30 khr^{-1}.

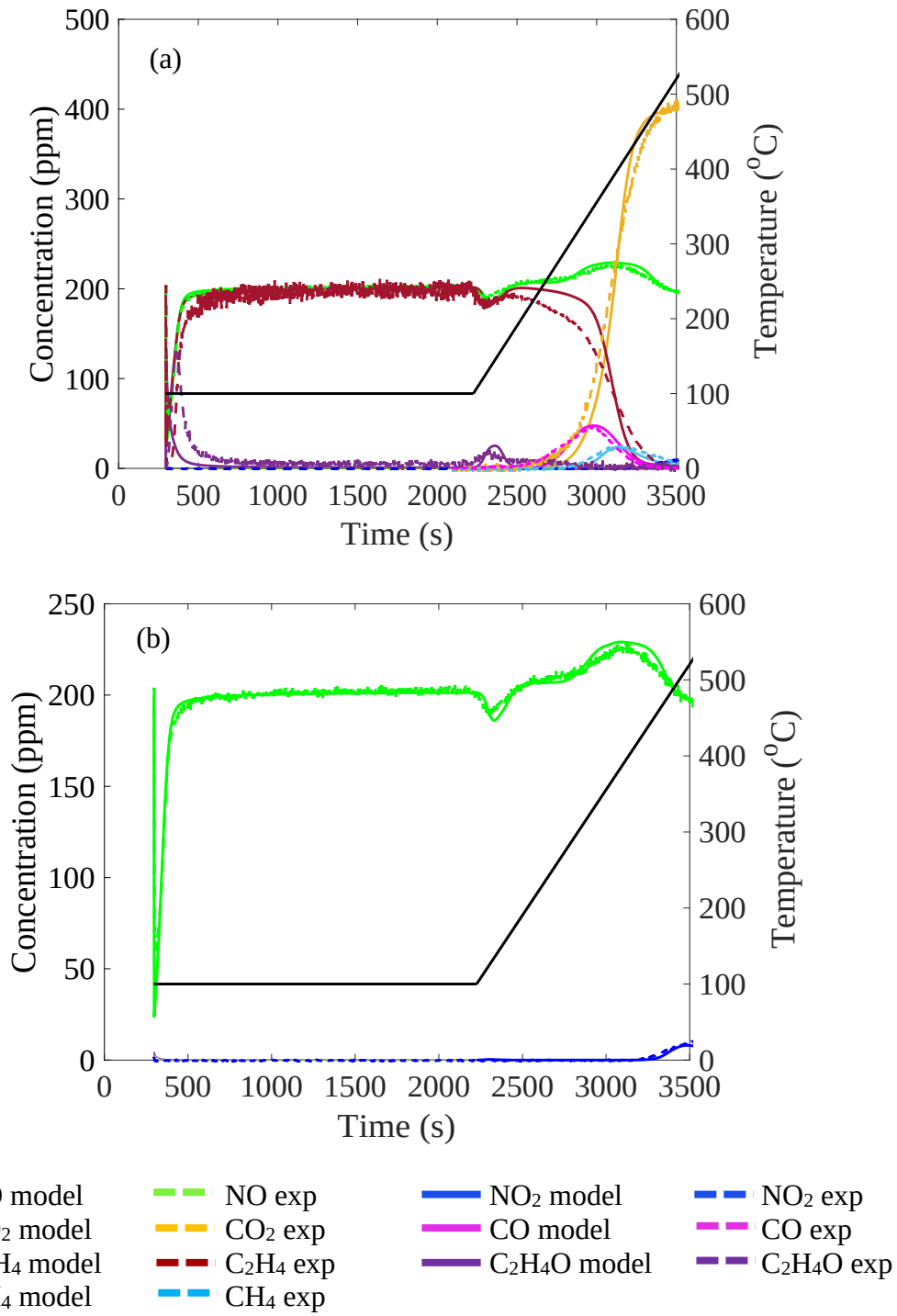

Figure A. 21 (a)Experimental and model results for uptake at 100°C and TPD on Pd(1%)/SSZ-13 for a feed comprising of 200 ppm NO/200 ppm C_2H_4/ 12% O_2/ 6% H_2O / balance N_2 and feed flowrate of 45 khr^{-1}, (b) Enlarged view of NO_x profile.

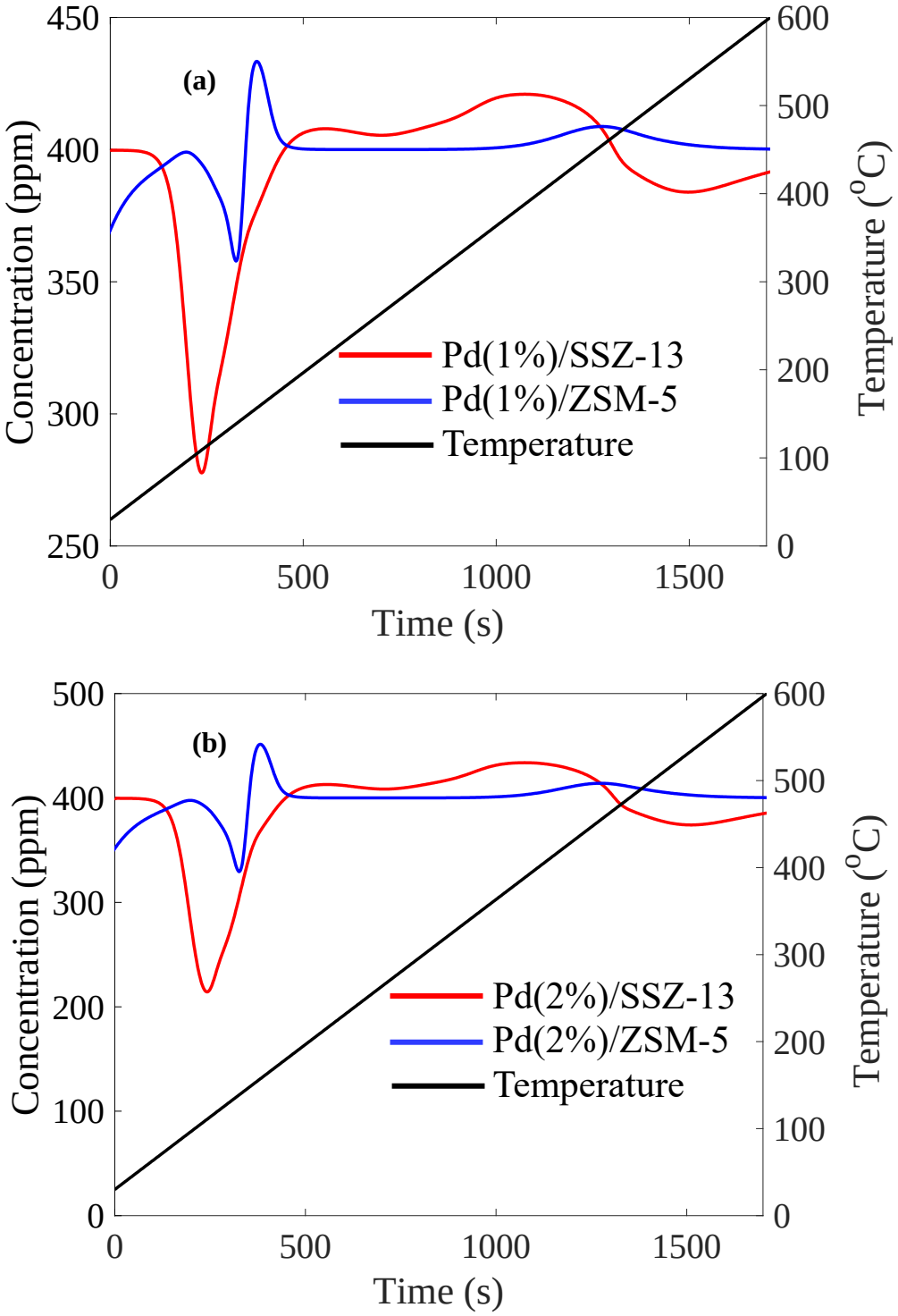

Figure A. 22 Model prediction of NO profile for a continuous temperature ramping from 30°C to 600°C at the rate of 20°C/min and (a) 45k hr^{-1} feed flowrate for Pd(1%)/SSZ-13 and Pd(1%)/ZSM-5 and (b) 30k hr^{-1} feed flowrate for Pd(2%)/SSZ-13 and Pd(2%)/ZSM-5.

Table A. 2 $n_{eq,C_{12}H_{26}}$ calculated for different experimental of temperature and n-dodecane concentration

Temperature (°C)	$\mathbf{X_{C_{12}H_{26}}}$	$\mathbf{n_{eq,C_{12}H_{26}}}$
115	5.50E-05	2.00E-05
115	8.50E-05	2.35E-05
115	1.04E-04	2.45E-05
135	5.78E-05	1.00E-05
135	7.70E-05	1.20E-05
135	1.03E-04	1.45E-05
155	5.75E-05	6.10E-06
155	7.60E-05	7.50E-06
155	8.20E-05	8.17E-06

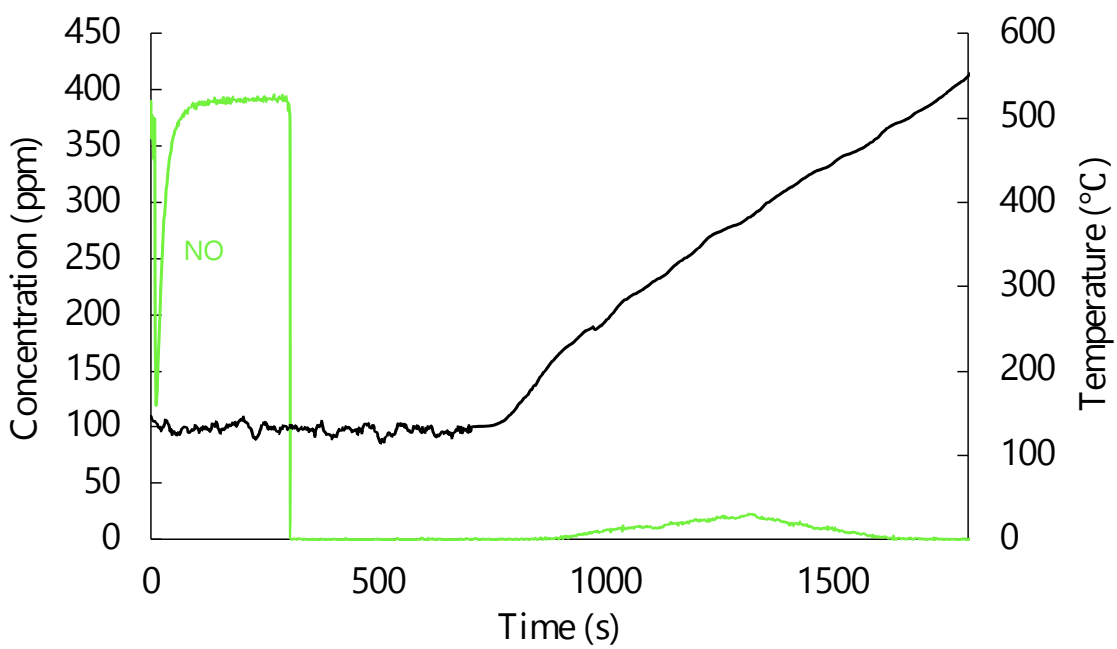

Figure A. 23 NO experimental profile for pre-adsorption of $C_{12}H_{26}$ followed by co-feed of NO and $C_{12}H_{26}$ at 135°C and TPD on Pd(1%)/SSZ-13.

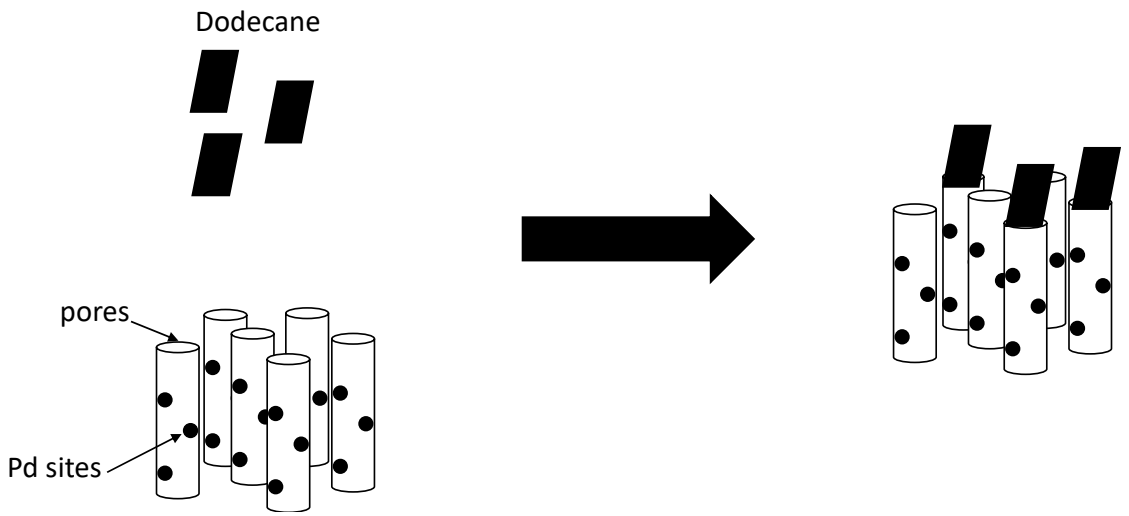

Figure A. 24 Schematic showing reduction of available sites for NO uptake by $C_{12}H_{26}$ pre-adsorption.

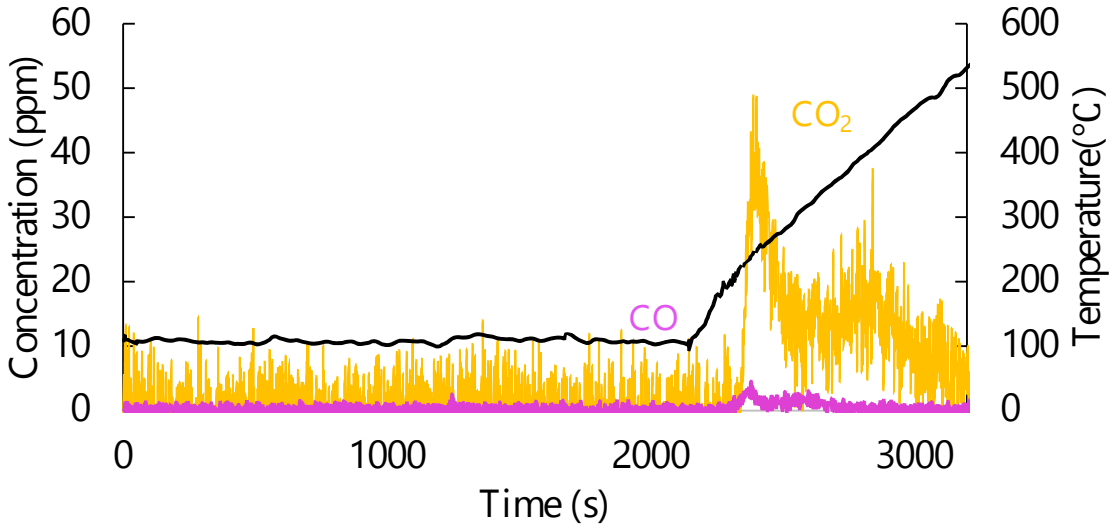

Figure A. 25 Experimental profiles for CO and CO_2 uptake at 100°C and TPD on Pd(1%)/SSZ-13 for a feed comprising of 395 ppm NO/ 58 ppm $C_{12}H_{26}$/ 2% O_2/ 2% H_2O/ balance Ar during uptake and 2% O_2/ Ar during TPD.

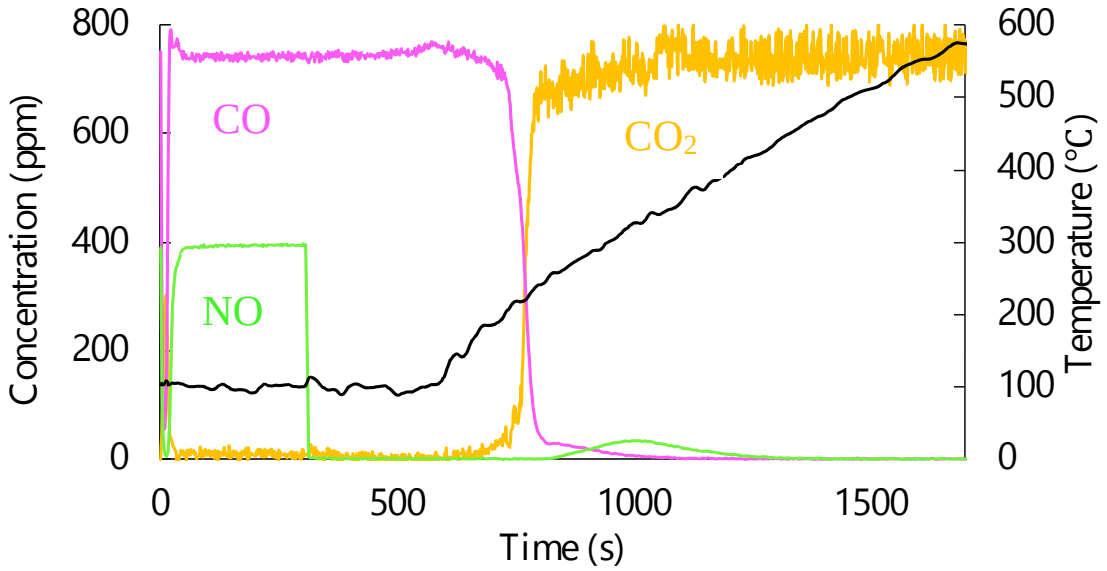

Figure A. 26 Experimental profiles for uptake at 105°C and TPD on Pd(1%)/SSZ-13 for a feed comprising of 398 ppm NO/ 760 ppm CO/ 2% O_2/ 2% H_2O/ balance Ar during uptake and 760 ppm CO/ 2% O_2/ Ar during TPD.

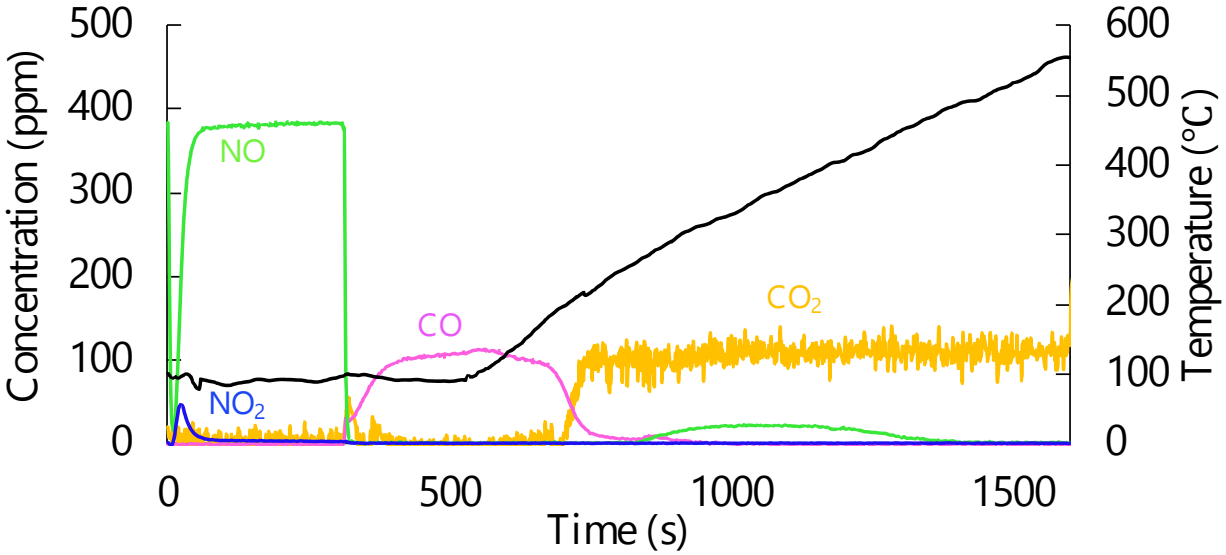

Figure A. 27 Experimental profiles for uptake at 105°C and TPD on Pd(1%)/SSZ-13 for a feed comprising of 395 ppm NO/ 2% O_2/ 2% H_2O/ balance Ar during uptake and 100 ppm CO/ 2% O_2/ Ar during TPD.

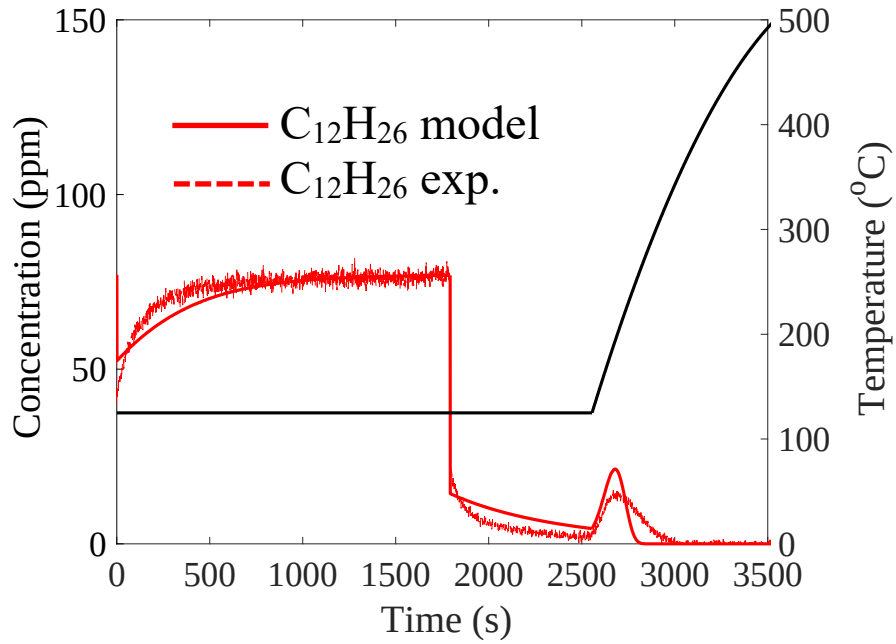

Figure A. 28 Experimental and model results for uptake at 125°C and TPD on Pd(1%)/SSZ-13 for a feed comprising of 77 ppm $C_{12}H_{26}$/ balance Ar during uptake and only Ar during TPD.

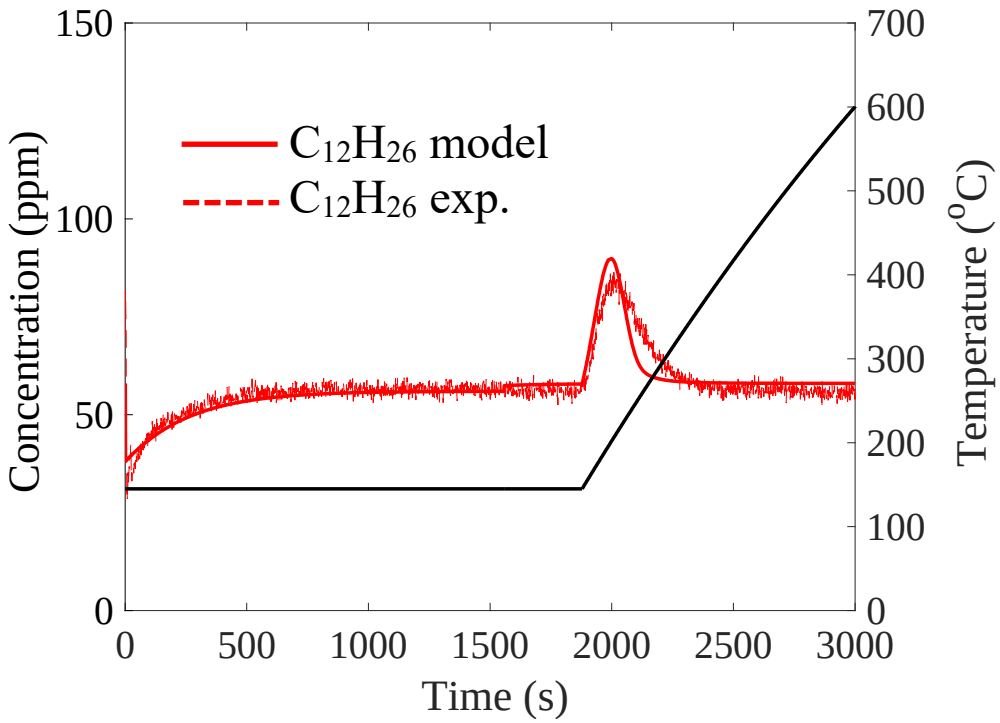

Figure A. 29 Experimental and model results for uptake at 145°C and TPD on Pd(1%)/SSZ-13 for a feed comprising of 58 ppm $C_{12}H_{26}$/ balance Ar during uptake and TPD.

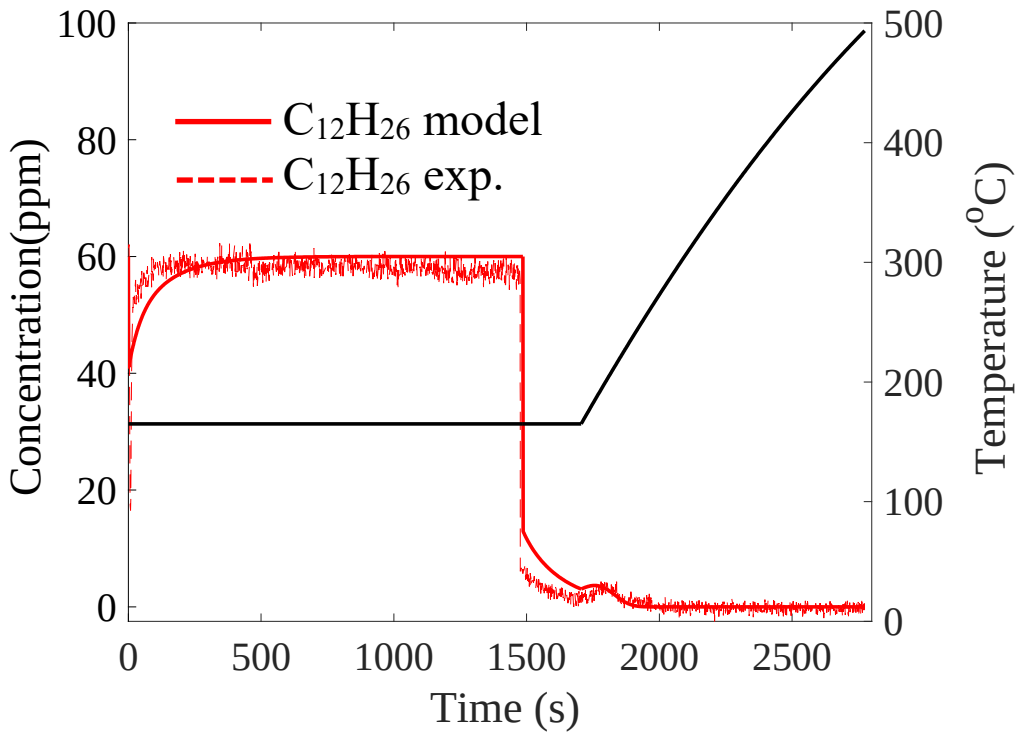

Figure A. 30 Experimental and model results for uptake at 165°C and TPD on Pd(1%)/SSZ-13 for a feed comprising of 60 ppm $C_{12}H_{26}$/ 2%H_2O/ balance Ar during uptake and only Ar during TPD.

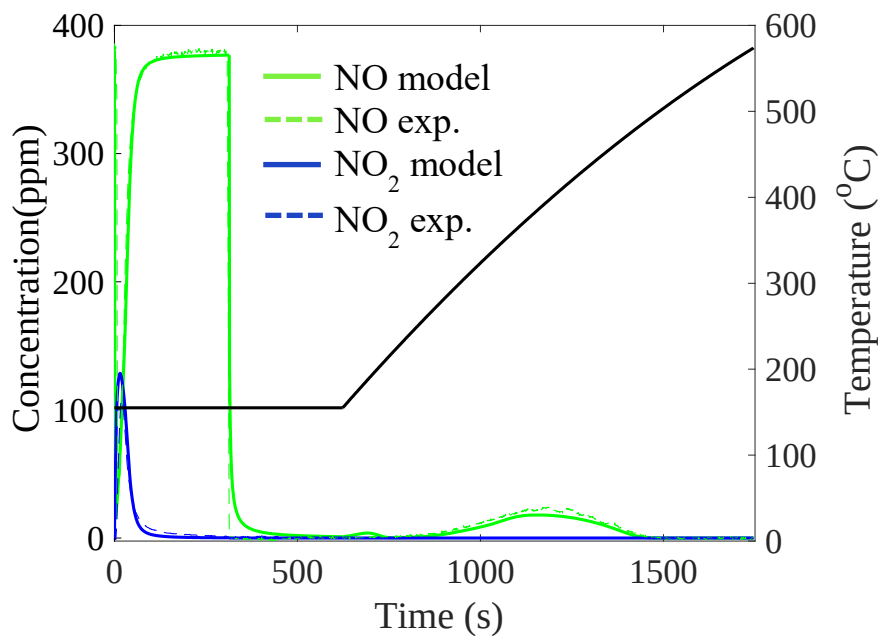

Figure A. 31 Experimental and model results for uptake at 155°C and TPD on Pd(1%)/SSZ-13 for a feed comprising of 380 ppm NO/ 2% O_2/ 2% H_2O/ balance Ar during uptake and 2% O_2/ Ar during TPD.

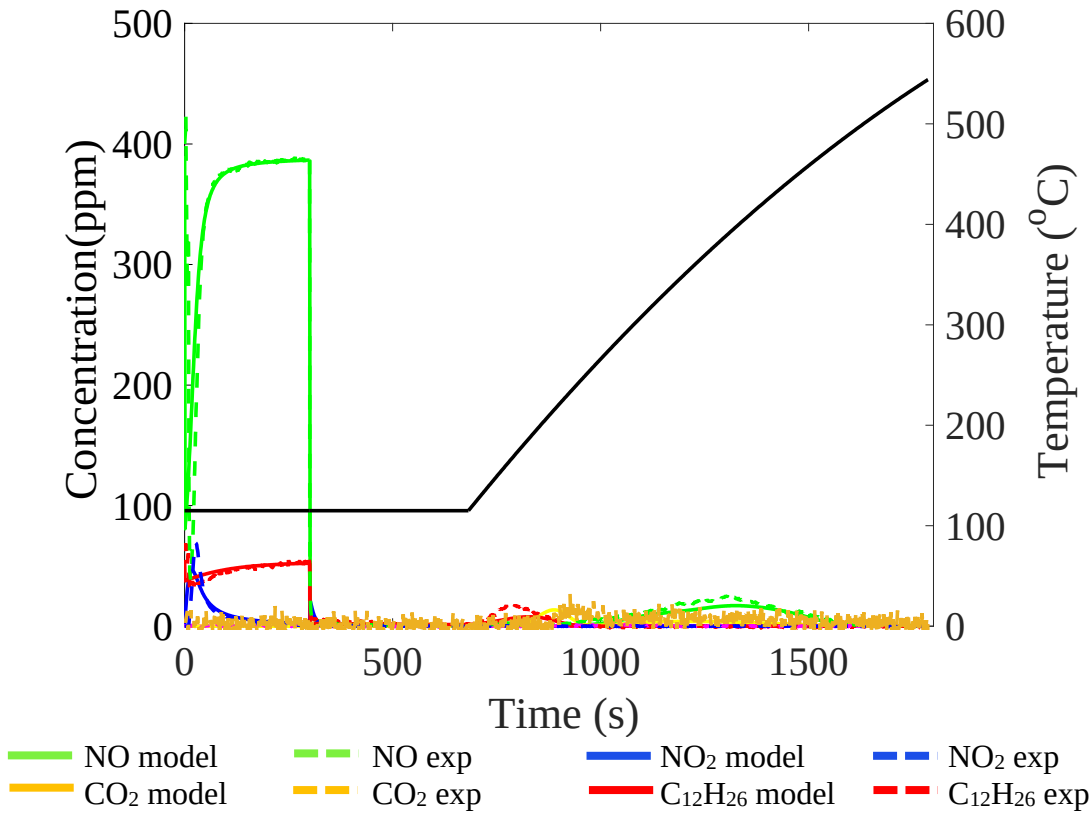

Figure A. 32 Experimental and model results for uptake at 115°C and TPD on Pd(1%)/SSZ-13 for a feed comprising of 395 ppm NO/ 58 ppm $C_{12}H_{26}$/ 2% O_2/ 2% H_2O/ balance Ar during uptake and 2% O_2/ Ar during TPD.

Estimate of External Crystallite Area Coverage by Adsorbed Dodecane

The amount of zeolite present in the monolith sample is 0.162 g and the amount of Pd is 1.043e-4 moles/g zeolite. We use an external surface area of SSZ-13 as 34 m^2/g cat; this is based on the study of Pashkova et al. who reported the value of external surface area of 34 m^2/g cat for SSZ-13 crystallites of 1-2 μm size [69]. The crystallite size of the SSZ-13 zeolite used in the current study is also1-2 μm. Assuming a uniform distribution of Pd sites, the surface concentration of Pd is ~3.0e-6 moles/ m^2. A n-dodecane molecule has 11 C-C bonds and 2 C-H bonds in axial direction and 2 C-H bonds in transverse direction.

This gives a total length of 19.01 Å and width of 2.18 Å, and a projected area of 3.95e-19 m^2.

The next step is to calculate the Pd sites blocked for NO adsorption by pre-adsorbed $C_{12}H_{26}$. For the uptake temperature of ~115°C and for a feed containing 55 ppm $C_{12}H_{26}$ /2% O_2/ 2% H_2O/ balance Ar during pre-adsorption, the amount of $C_{12}H_{26}$ adsorbed is 7.12e-6 moles (4.28e^{18} atoms). The area covered by 4.28e^{18} $C_{12}H_{26}$ atoms is 1.69 m^2. An amount of 5.0e^{-6} moles Pd will be blocked by the pre-adsorbed $C_{12}H_{26}$ at 115℃ uptake temperature. This compares favorably to the amount predicted by the above-described empirical approach; i.e., 4.67e-6 moles Pd. At an uptake temperature of ~135℃, 6.62e-6 moles (3.98e^{18} atoms) of $C_{12}H_{26}$ are pre-adsorbed. The area covered by 3.98e^{18} atoms of $C_{12}H_{26}$ is 1.57 m^2. This will block ~4.7e^{-6} moles of Pd sites. This value too compares favorably to the empirical estimate of 4.4e-6 moles at the same 135℃ uptake temperature. Table A. 3 compares the estimated amount of NO blocked through the dodecane coverage analysis and the empirical m value method.

Table A. 3 Moles of Pd sites blocked for NO uptake due to $C_{12}H_{26}$ blockage after 20 min of pre-exposure to $C_{12}H_{26}$ and H_2O

Temperature (℃)	**Decrease in available Pd site (area calculation)**	**Decrease in available Pd site (empirical m value calculation)**
115	5.0e-6 moles	4.67e-6 moles
135	4.7e-6 moles	4.40e-6 moles

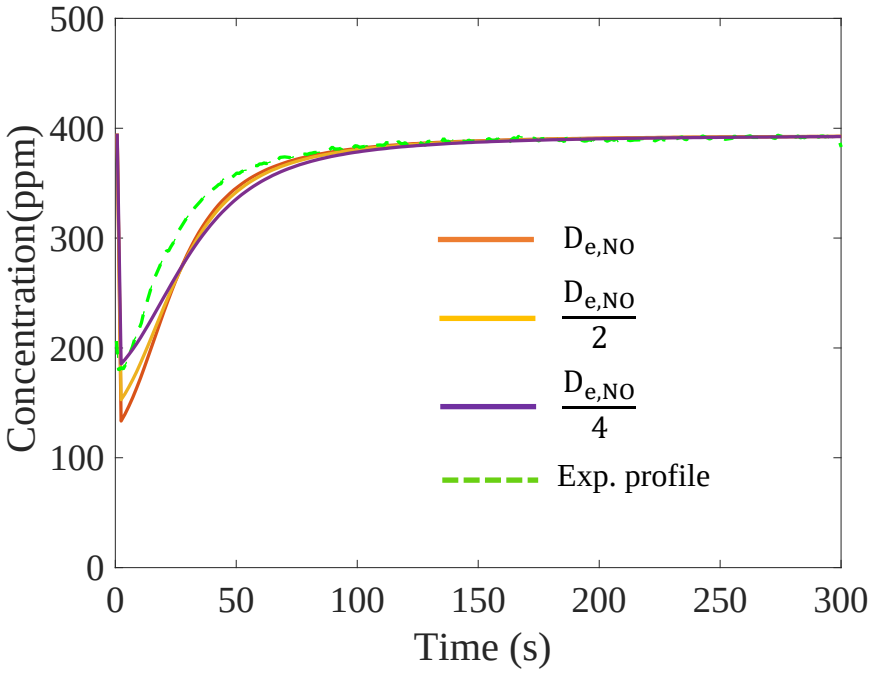

Figure A. 33 Experimental and modeling results of NO uptake profiles for $C_{12}H_{26}$ and H_2O pre-adsorption followed by NO uptake at uptake temperatures of ~115°C and with different values of NO washcoat diffusivity ($D_{e,NO}$= 3.88e^{-7} m^2/s).